ZnCdMgSe and AlGaInP multi-quantum well films for colour conversion and optically-pumped visible lasers

A thesis presented in fulfilment of the requirements for the degree of Doctor of Philosophy

by

Brynmor Edward Jones

Department of Physics
University of Strathclyde

2015

This thesis is the result of the author's original research. It has been composed by the author and has not been previously submitted for examination which has led to the award of a degree.

Signed: _____

Date: _____

Ar gyfer fy mam a thad, a fy nghariad Barbora

Acknowledgements

To begin, I would like to especially thank my supervisor Dr Jennifer Hastie, whose help, guidance and support have kept me on the path through all stages of this PhD. My thanks also to our collaborators in the group of Prof Maria Tamargo in CCNY, their collaboration and growth of the II-VI samples enabled my project to exist, and they offered me a superbly warm welcome on my visit to their lab and city.

I would like to thank Dr Peter Schlosser, for his guidance and laying down of the VECSEL law when I started, and for all the help and discussions throughout my time. I would also like to thank Joel de Jesus in New York, for his assistance and efforts in the growth and characterisation of the II-VI samples.

To the PhD students of the IoP, I would like to acknowledge the years of fun and often perplexing conversation we have had, which made the Institute a great place to be: the shoppage crew with whom I must have walked miles up and down the hill; the cleanroom gang who made working in a loud, hot yellow room actually fun; the lunch club for broadening my culinary horizons. Particularly I would like to thank Antonio for all the advice and conversation over innumerable cups of The Earl, and Caroline for providing an inspirational challenge over who can have the messiest desk. Deserving significant mention outside the Institute, friends far and near: Derek, James and Ant, for providing an avenue for me to escape from life every once in a while.

A special thanks to my parents for their continued and ever-present moral support, and for giving me the courage to get out there and do things.

Finally, to Barbora, who has had to put up with late night working (especially during thesis writing) and occasional bouts of extreme grumpiness (ditto) – my absolute thanks for providing the support and companionship that I treasure.

Abstract

II-VI semiconductor material ZnCdMgSe has the potential to enable optical devices emitting throughout the visible spectrum. While difficulties in doping of this material have hindered its development for conventional electrically-injected semiconductor lasers, the recent availability of efficient, high power InGaN-based laser diodes has created the opportunity for optically-pumped devices, and this work primarily focusses on the progression towards realising vertical external-cavity surface-emitting lasers (VECSELs) based on this material system. Challenges in the growth of a ZnCdMgSe distributed Bragg reflector (DBR), such as low refractive index contrast and limited growth thickness for maintaining material quality, lead to the design of novel thin-film VECSEL structures, and the development of epitaxial transfer techniques to overcome the absorptive InP growth substrate and buffer. Transfer of thin-film (few microns thick) multi-quantum well heterostructures is demonstrated for samples with areas of a few mm^2, successfully transferring and liquid-capillary-bonding the films to diamond heat-spreaders for thermal management. Continued challenging growth, namely heterostructure layer inaccuracies, mean that laser threshold is not yet reached, however extensive characterisation and analysis is carried out to inform future progress in realising the ZnCdMgSe thin-film VECSEL.

The thin-film VECSEL architecture offers advantages beyond allowing for the use of novel materials, opening the potential for novel laser cavities and optical pumping schemes. The thin-film transfer method developed for the II-VI VECSEL is adapted for the transfer of III-V AlGaInP epitaxial structures from GaAs growth substrates, and AlGaInP thin-film VECSELs are demonstrated operating continuous wave at red wavelengths at room temperature. Laser operation is currently limited by pump-induced de-bonding from the diamond, with attempts made to counter this through the refinement of structure design (including strain balancing) and transfer method. Until thermal rollover occurs, performance is relatively comparable with the ‘conventional’

gain-mirror AlGaInP VECSELs, with a maximum output power of 21 mW recorded at both 682 nm and 670 nm for low output coupling.

Using the transfer method developed for the II-VI material, ZnCdMgSe multi-quantum well structures are used as colour conversion films for micron-size LED arrays. The resulting hybrid devices are demonstrated to have high modulation bandwidths, limited only by the LED modulation bandwidth, suitable for application in visible-light communication.

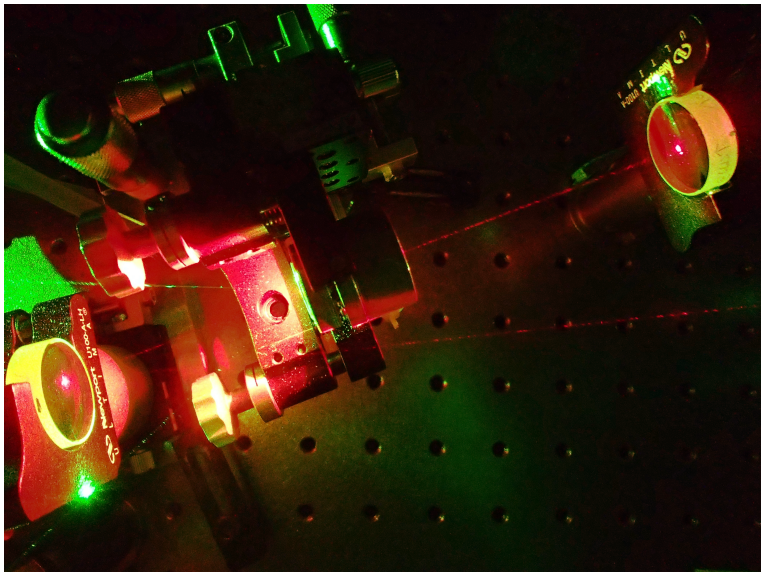

Laser operation of a thin-film AlGaInP VECSEL.

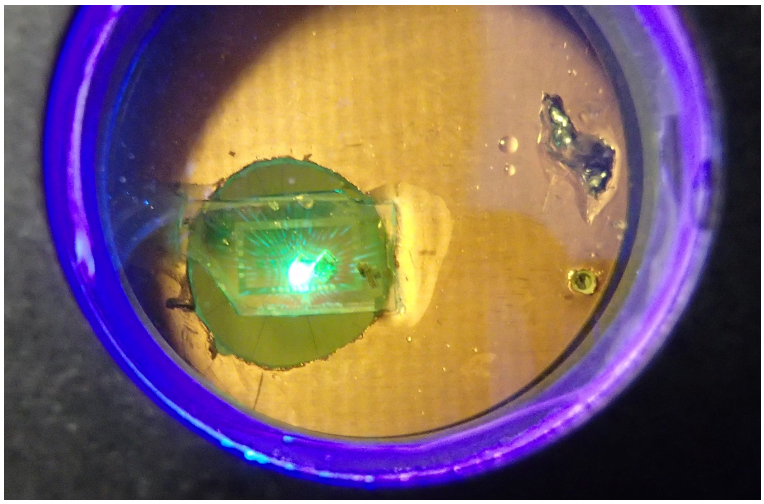

Demonstration of the hybrid micro-scale LED with II-VI colour-conversion film.

Contents

Declaration of Authorship i

Acknowledgements iii

Abstract iv

Contents vi

1 Introduction 1
- 1.1 The laser . . . 1
- 1.2 Semiconductors . . . 2
  - 1.2.1 Semiconductor band-structure . . . 2
  - 1.2.2 Quantum confinement and wells . . . 4
  - 1.2.3 Semiconductor lasers . . . 6
- 1.3 Visible spectrum lasers . . . 7
  - 1.3.1 Applications of visible lasers . . . 8
  - 1.3.2 Types of visible laser . . . 9
    - 1.3.2.1 Large bandgap semiconductor materials . . . 11
- 1.4 Introduction to the VECSEL . . . 13
  - 1.4.1 Distributed Bragg reflector . . . 16
  - 1.4.2 Pump schemes and power scaling . . . 16
  - 1.4.3 External cavity arrangements . . . 17
- 1.5 Fundamental spectral coverage of reported VECSELs . . . 18
- 1.6 Frequency conversion . . . 20
- 1.7 Thin-films and applications . . . 21
- 1.8 Thesis overview . . . 22
- 1.9 References . . . 23

2 Semiconductor and VECSEL design 35
- 2.1 Introduction . . . 35

2.2 Semiconductor materials and band-gap engineering . . . 35
2.2.1 Lattice constant and band-gap . . . 37
2.2.2 Strain effects in semiconductors . . . 37
2.2.3 Accommodating strain . . . 41
2.2.4 Temperature dependence . . . 43
2.2.5 Refractive index calculation . . . 44
2.3 Quantum well emission . . . 44
2.3.1 Schrödinger equation ground state solution . . . 45
2.4 Multi-layer structures . . . 47
2.4.1 Simulation of stratified media . . . 48
2.5 DBR design and limitations . . . 49
2.6 VECSEL structures and layer placement . . . 51
2.6.1 The Kuznetsov model of VECSEL performance . . . 51
2.6.2 Designing for temperature effects . . . 54
2.6.3 Pump absorption . . . 55
2.6.4 VECSEL design . . . 56
2.7 Thermal management of VECSEL devices . . . 59
2.8 Design challenges and thin-film devices . . . 63
2.8.1 Thermal considerations in a thin-film design . . . 64
2.9 Summary . . . 66
2.10 References . . . 68

3 II-VI ZnCdMgSe VECSEL structures 73
3.1 Introduction . . . 73
3.1.1 ZnCdMgSe material system . . . 74
3.2 II-VI ZnCdMgSe growth . . . 75
3.2.1 Molecular beam epitaxy . . . 75
3.2.1.1 RHEED measurement . . . 76
3.2.2 Structure growth procedure . . . 77
3.2.2.1 Growth challenges . . . 78
3.3 Material properties . . . 79
3.3.1 ZnCdMgSe quaternary characteristics . . . 80
3.3.2 Band-gap and absorption: Hattori et al. 1998 . . . 81
3.3.3 Band-gap and refractive index: Morita et al. 1997 . . . 82
3.3.4 Conduction band offset . . . 85
3.4 ZnCdSe/ZnCdMgSe Quantum well design . . . 85
3.4.1 Bulk material band-gap . . . 85
3.5 Quantum well thickness . . . 86
3.5.1 Strain effects in a quantum well . . . 87
3.5.2 Simulated quantum wells . . . 88
3.6 Thin-film epitaxial lift-off . . . 90
3.6.1 Development of a processing method for ELO of thin-film II VI ZnCdMgSe structures . . . 92

3.6.1.1 Photoresist mask via-hole . . . 92
3.6.1.2 Adhesive mask for via-hole . . . 96
3.6.2 Thin-film transfer method . . . 96
3.6.3 Sample preparation . . . 97
3.6.3.1 Substrate and buffer etch . . . 99
3.7 Structure designs . . . 100
3.7.1 Generation 1: 5 quantum well structures . . . 101
3.7.2 Generation 2: 9 quantum well structures with partial DBR . . . 102
3.7.3 Generation 2.5: 9 quantum well structures with partial DBR . . . 104
3.7.4 Generation 3: 14 QW structures with no DBR . . . 104
3.8 Structure photoluminescence & reflectivity studies and SEM thickness measurements. . . . 105
3.8.1 Generation 1 . . . 106
3.8.2 Generation 2 . . . 109
3.8.3 Generation 2.5 – 5-period DBR structures . . . 111
3.8.4 Generation 2.5 – 10 period DBR structures . . . 117
3.8.5 Generation 3: 14 QW no-DBR structures. . . . 118
3.9 20 period DBR . . . 121
3.10 Structure strain and transfer . . . 122
3.10.1 Generation 1 . . . 123
3.10.2 Generation 2 . . . 124
3.10.3 Generation 2.5 . . . 126
3.10.4 Generation 3 . . . 128
3.11 Conclusions and future work . . . 131
3.12 References . . . 132

4 III-V AlGaInP thin-film VECSEL 139
4.1 Introduction . . . 139
4.1.1 III-V structure growth . . . 140
4.2 Material characteristics for design . . . 141
4.3 Thin-film processing and considerations . . . 141
4.3.1 Substrate removal and transfer . . . 143
4.3.2 Strain balancing . . . 145
4.4 Thin-film structure designs . . . 146
4.4.1 Structure design A . . . 146
4.4.2 Structure design B . . . 147
4.4.3 Structure design C . . . 149
4.5 VECSEL mount and cavity . . . 150
4.6 Structure characterisation . . . 151
4.6.1 Initial characterisation: Design A . . . 153
4.6.2 Initial characterisation: Design B . . . 155
4.6.3 Initial characterisation: Design C . . . 156
4.7 Laser and transfer characterisation . . . 159
4.7.1 Processed laser gain regions . . . 159

4.7.2 Power loss issues . . . 160
4.7.3 Laser characterisation: design A . . . 162
4.7.4 Etch & transfer tests: designs B and C . . . 165
4.7.5 Laser characterisation: design C . . . 168
4.8 Summary and future work . . . 169
4.9 References . . . 171

5 II-VI quantum well films for colour conversion 174
5.1 Introduction to visible light communication . . . 174
5.2 White light generation . . . 175
5.3 Characterisation for colour conversion . . . 175
5.4 Transfer and testing of II-VI films . . . 177
5.4.1 Power and efficiency . . . 178
5.4.2 Bandwidth measurements . . . 180
5.5 Designing for colour conversion . . . 182
5.6 Transfer printed LEDs . . . 183
5.7 Conclusions . . . 184
5.8 References . . . 185

6 Conclusions and outlook 187
6.1 II-VI ZnCdMgSe thin-film VECSELs . . . 188
6.2 III-V AlGaInP thin-film VECSELs . . . 190
6.3 Colour conversion . . . 192
6.4 References . . . 194

A Quantum well transition energy simulation 196

B Simulation of E-field propagation in stratified media 198

List of Publications 200

Chapter 1

Introduction

This introductory chapter begins by briefly describing the laser, its applications, and the material technologies used to achieve laser oscillation. Visible light emission is discussed, and the advantages that visible light technologies can bring, along with the associated material considerations. There follows a discussion on vertical external-cavity surface-emitting lasers (VECSELs) and their properties, and in turn how these lasers could be fabricated for visible light emission using materials allowing for thin-film epitaxial lift-off (ELO) and substrate removal. Thin-film devices can have several advantages, and these are discussed. Finally the thesis is outlined, following this same general order of subjects.

1.1 The laser

A laser operates by amplifying light in an optical resonator through the action of stimulated emission. The result is an output beam of light with normally low to moderate divergence and high directionality, and a high degree of spatial coherence. Lasers can also demonstrate other extremely useful properties as required, e.g. high temporal coherence, continuous or pulsed operation, and well-defined polarisation.

Lasers are used widely and enable technologies necessary for the modern world. Key is the telecommunications industry, where the internet, fundamental to the information age, is enabled by fibre lasers and amplifiers. Laser use within medicine is

being embraced, with diagnosis and treatment technologies based on lasers becoming commonplace. In industry lasers are used in manufacturing, to mark, cut, and weld material. In entertainment, laser projection and displays have the potential to make major changes to everyday consumer technologies, and advances in efficiency, size and design of lasers allow for the introduction of new applications (e.g. focus-aiding lasers in new generation smartphones).

In this thesis, novel configurations of VECSELs are investigated using two semiconductor material systems for accessing the visible spectrum: AlGaInP for red emission lasers, and ZnCdMgSe which holds promise for enabling devices spanning the rest of the visible spectrum. The motivations for visible spectrum lasers and the need for further semiconductor material development are discussed in Section 1.3, while the VECSEL is introduced in Section 1.4.

1.2 Semiconductors

Semiconductor lasers have become ubiquitous in recent decades, enabling consumer products and industrial technologies with their low cost and rapid large-scale manufacture. Their method of operation is through charge-carrier excitation and recombination transitions within the material energy band-structure.

1.2.1 Semiconductor band-structure

While individual atoms can be described as having discrete energy levels, in crystal structures where atoms are in close proximity these levels split into bands, due to the Pauli-exclusion principle [1]. Knowledge of these energy bands is key to understanding and manipulating band-structure in the design and operation of semiconductor devices.

Figure 1.1 shows a generalised explanation of semiconductor material bands, based on a diagram in ref. [2]. Conductive materials have the Fermi level of the material within an energy band (the ground state), resulting in a band partially filled with charge carriers at room temperature allowing free movement. In contrast to this, the energy

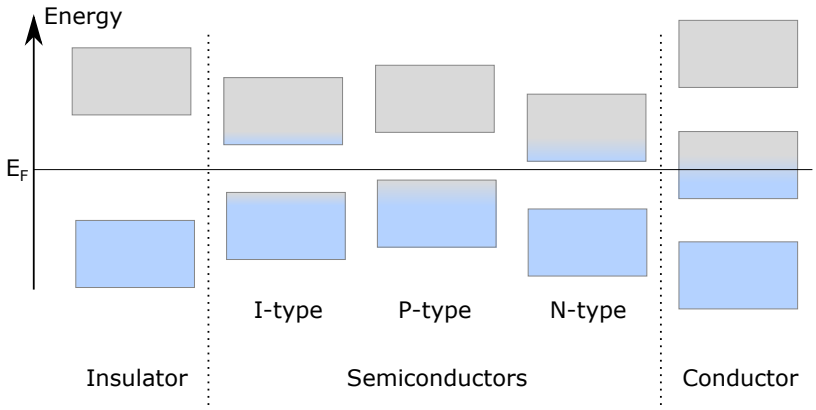

Figure 1.1: Basic diagram demonstrating the generalised band-structures of insulators, semiconductors and conductors (metals). Blue shading indicates electron distribution within the band. The y axis E denotes energy, with the the Fermi-energy Ef indicated. Intrinsic I-type semiconductors are undoped, while P-type and N-type are doped to have the majority of carriers in the valence and conduction bands respectively.

bands of insulators have a wide energy *band-gap* between ground and excited states such that the states do not intersect the Fermi level, a fully filled band below and fully empty above, and the gap is sufficiently wide that excitation of electrons cannot easily occur. The band-gap is defined as the forbidden area in energy-momentum space where there are no available states, between the band-edges. Semiconductors, as the name describes, are halfway between the two, the Fermi-level within the band-gap, but the gap small enough for excitation of some electrons to occur (e.g. thermal energy at room temperature).

Excitation of electrons from a ground state to an excited state (from the valence band to the conduction band) requires an energy greater than the gap. The recombination of a conduction band electron and a hole (a positively charged gap between electrons, acting as a positive particle) in the valence band across the band-gap results in the emission of a photon.

Doping introduces additional carriers to the valence or conduction bands (p- and n-type doping respectively), shifting the Fermi-level closer to the band. Through manipulation of multiple materials with different doping, electronic devices are produced using the effects of band bending (e.g. P-N junction, first demonstrated semiconductor lasers in 1962 [3,4]). For electrically pumped lasers, control of doping is essential, and the diode laser is entirely dependent on it by its nature, hence the relatively low research

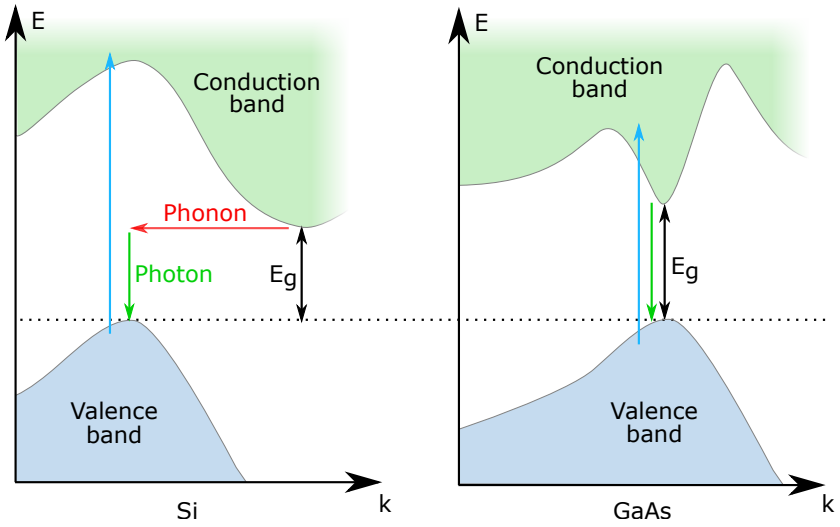

Figure 1.2: Indirect and direct semiconductor energy band-structure of Si and GaAs. Transition between conduction and valence bands in Si requires a transfer of momentum k in the form of a phonon. Conduction and valence band edges as indicated.

volume into difficult-to-dope materials such as ZnCdMgSe [5]. In optically pumped devices such as the VECSEL, doping is not necessary, and the accurate growth of high quality material with specific band-gap according to design is paramount.

The relation between conduction band minima and valence band maxima in terms of crystal momentum k determines whether a semiconductor is described as direct or indirect. As examples, shown schematically in Figure 1.2, GaAs is a direct semiconductor where the conduction and valence band-edges have equal crystal momentum, while Si is an indirect semiconductor with a difference in momentum between the conduction and valence band-edge states. Recombination across the band-gap for GaAs requires no change in momentum to emit a photon, while recombination for Si also requires a phonon for every photon, thus lowering efficiency. Laser devices are nearly always based on direct band-gap devices.

1.2.2 Quantum confinement and wells

When a semiconductor of smaller band-gap is surrounded by a semiconductor of higher energy band-gap such that the charge-carriers within the inner material have insufficient energy to leave the material, these charge carriers are *confined* in a potential

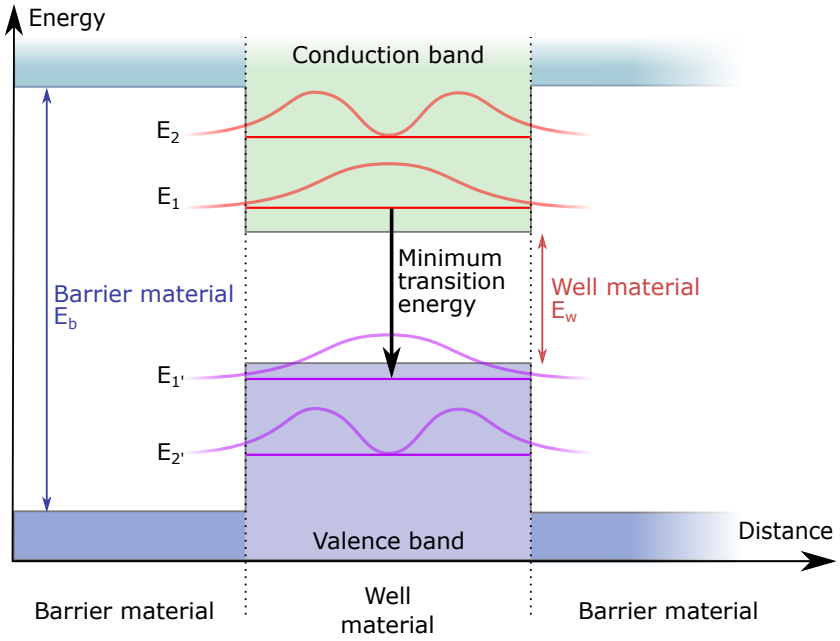

Figure 1.3: Schematic diagram indicating the first (ground) and second quantised energy states within the QW conduction band, E_1 and E_2, and the equivalent first and second states within the valence band $E_{1'}$ and $E_{2'}$. Indicated in red and purple above these are the probability distribution functions for the electrons and holes for each respective energy state. The black arrow shows the minimum transition energy of the quantum well, from the ground conduction band state to the ground valence band state. E_w and E_b are the material energy band-gaps for the well and barrier material respectively.

well. Charge-carriers from the surrounding material, or barrier material, will move to the lower energy states within the well.

When the thickness of the potential well is lowered, in one dimension, to the magnitude of the de Broglie wavelength of the carriers, the energy states in the conduction and valence bands become quantised, as shown in Figure 1.3. As the thickness of the potential well is reduced, i.e. the confinement increases, the energy of the states in the band increases. This one-dimensionally confined potential well is known as a quantum well (QW), and is discussed in detail in Section 2.3. The QW allows for control of transition energies through the thickness of the well layer. It should be noted that as device temperature increases, the energy required to excite the carriers from the well becomes available and carriers will escape the well.

Confinement in two and three dimensions produces further confinement of the carriers and control of the energy states available to the carriers, and these configurations are

known as quantum wires and quantum dots respectively. The structures and designs considered within this thesis are however based on QWs only

Quantum confinement delivers advantages when used in a semiconductor laser device, causing increased localisation of the density of states and removal of valence band degeneracy, resulting in higher material gain, reduced threshold, higher thermal stability and increased device efficiency [6,7]. In complex laser structures, such as those discussed in this work, confinement allows for control of emission wavelength beyond band-gap modification through material composition.

1.2.3 Semiconductor lasers

Semiconductor lasers can technically be described as solid-state lasers (hence diode-pumped semiconductor lasers being described as *all-solid-state*), however they are conventionally given their own category. Gain normally results from stimulated emission in inter-band transitions, where electrons are promoted from the valence band to the conduction band (leaving a *hole* in the valence band), with electron and hole recombination through the stimulated emission process. An exception to this is the intrasubband transition based quantum cascade lasers, e.g. ref. [8]. Through the design of the material and thus the energy band-gap and transition wavelengths between conduction and valence bands, structures can be designed for operation at specific output wavelengths.

Generally, semiconductor lasers have two distinct configurations for light output: in the plane of the gain layer (edge-emission) or perpendicular to the plane (surface-emission), shown in Figure 1.4.

Edge-emitters have the advantage of long gain regions (the width of the device) and so have high gain and can endure high losses. The cleaved facets of the structure are often sufficiently reflective to act as the end mirrors of the laser cavity due to the high gain, although edge emitters are sometimes used in external cavity configurations. The output power can be increased to high powers in multimode operation. Disadvantages

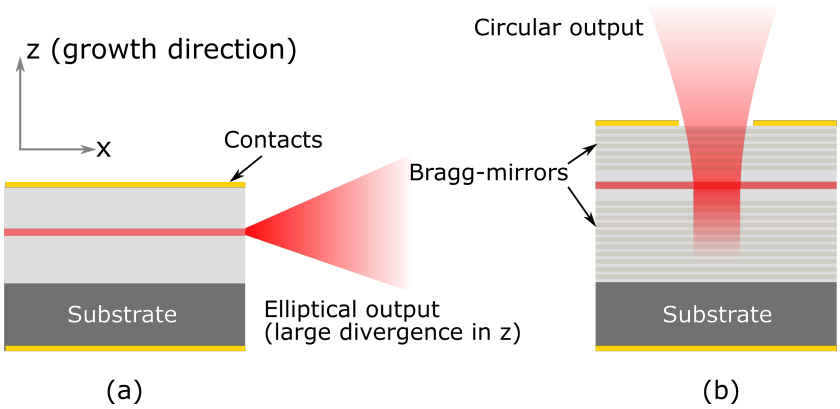

Figure 1.4: Basic configuration of edge- and surface-emission semiconductor lasers, with gain regions in red. (a) Edge emission semiconductor laser configuration, with waveguides (light grey) and elliptical emission through end facets. (b) Surface emission laser configuration, with on-chip Bragg mirrors and circular top emission.

are that the beam quality is normally low, and with a strong vertical divergence producing an elliptical beam and requiring beam-shaping optics.

Surface-emitters have short gain regions (defined by the thickness of gain layers) so are more sensitive to losses, but when optically-pumped over a wide area produce scalable output power in a single transverse mode. An example of a surface emitting laser is the electrically pumped vertical-cavity surface-emitting laser (VCSEL). VCSELs consist of an active region of QW or quantum dot layers, with high reflectivity mirrors above and below. The VCSEL is commonly electrically-pumped and has a low threshold with high beam quality, but cannot produce high output powers and the intracavity field is inaccessible.

1.3 Visible spectrum lasers

Visible lasers emit in the visible part of the spectrum, from approximately 390 nm-wavelength violet light to 700 nm red.

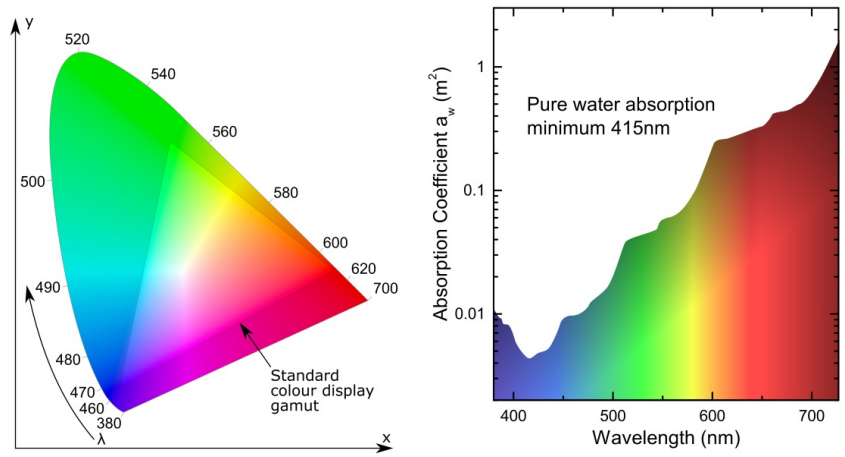

Figure 1.5: (a) CIE Chromaticity diagram, showing the standard sRGB colour gamut for displays. Around the plot are indicated the wavelengths that direct laser light could provide. Using laser emission at 540 nm, 460 nm and 660 nm would provide a colour gamut covering a significantly higher quantity of the spectrum. (b) Absorption coefficient for pure water, showing a minimum at 415 nm. Salinity and other factors will shift this minimum position throughout the blue-green region, dependant on water quality (absorption data from [10]).

1.3.1 Applications of visible lasers

Lasers in the visible region are in high demand. For the display market, laser projectors have the ability to display a high colour gamut (see Figure 1.5 (a) for chromaticity plot of standard gamut) and the potential for significantly longer device lifetimes than current metal-halide or high-pressure mercury arc lamps (approximately 10,000 hours) [9].

While rear-projection laser displays are no longer desirable with the increasing quality and availability of slim organic-LED displays, large scaling front-projection laser displays (long- and short-throw) are now commercially available and are an area of active industrial development (e.g. for cinema projection [11]). The devices are highly priced, so investigating alternative potential laser sources is essential for reducing manufacturing costs and bringing them to the consumer market at a significant level.

Away from entertainment applications, specific visible wavelengths are often required for sensitive medical procedures, e.g. yellow lasers for ophthalmology [12,13]. By easing the restrictions on wavelength imposed by solid-state and gas lasers, medical

researchers could optimise the wavelength rather than compromise the procedure. Lowering unit cost is also important for the use of laser-based medical equipment and techniques to penetrate beyond specialised treatment centres.

Spectroscopy applications require tunable sources around specific transition wavelengths of target elements and molecules, and an external laser cavity allowing for highly accurate intracavity laser absorption spectroscopy [14]. UV-visible absorption and luminescence spectroscopy are used in analytical chemistry [15,16], and for medical diagnosis [17,18].

While visible lasers are well suited for free-space communication through air (near-IR also being suitable) [19], for communication in water (e.g. submarine communication) the blue-green spectral region provides the lowest absorbance conveniently achievable, shown in Figure 1.5 (b), and a laser beam allows for the elimination of much of the noise from sunlight through filters [20].

1.3.2 Types of visible laser

There are multiple laser types for operation within the visible spectrum with advantages and disadvantages to each, and a general overview of the spectral coverage of common lasers emitting in the visible spectrum is shown in Figure 1.6.

Gas lasers are an often-used method for reaching visible-spectrum wavelengths, using gases of elemental atoms or molecules as the gain medium. Gas lasers provide high beam quality and are normally electrically pumped. The transitions in the gain medium are fixed by the atomic transitions, and so are not tunable, although multiple transition wavelengths can be accessed with one laser system. Helium-Neon lasers emit mainly at 632.8 nm, 611.9 nm, 594.1 nm and 534.5 nm, and are a relatively compact laser source with a gain-region size of approx. 20 cm. Another visible-wavelength gas laser, Argon ion lasers have their main emission wavelengths at 514.5 nm, 488.0 nm and 457.9 nm, and the gain region is of significant lengths of 1 m or more. Of similar size to the Argon ion laser, Krypton ion lasers emit mainly at 647.1 nm, although have emission wavelengths from 406.7 nm to 676.4 nm. An obvious disadvantage of these lasers is

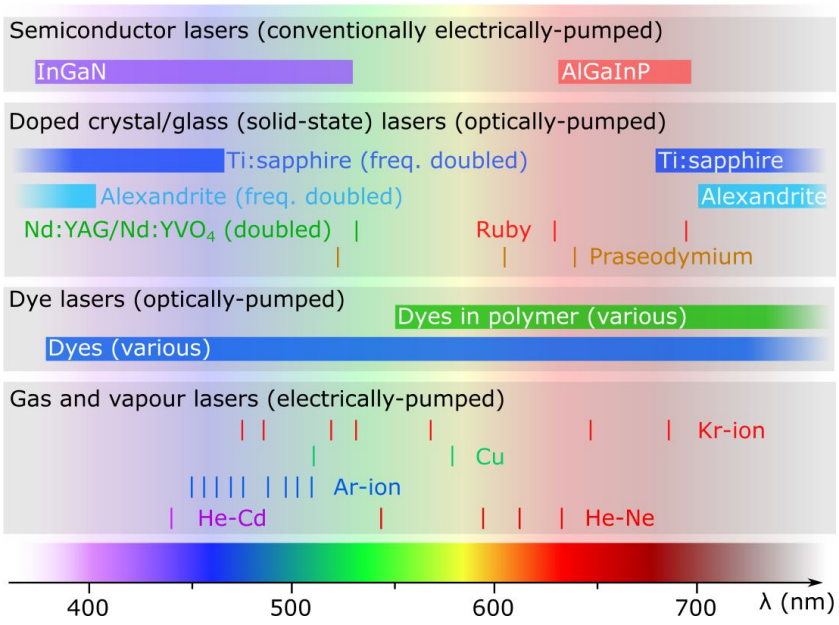

Figure 1.6: Graph showing significant examples of laser coverage across the visible spectrum. Dye laser coverage is indicated for various overlapping laser dyes rather than specific gain media. InGaN and AlGaInP are semiconductor materials that allow for fundamental visible wavelength operation.

the inability to design for different wavelengths, and for specific applications this can be significant. Another disadvantage is the inability for the devices to be scaled to smaller sizes for incorporation into efficient, compact devices for practical use outside a research lab environment.

Specific wavelengths within the visible spectrum are also commonly reached through either direct emission or non-linear frequency conversion of solid-state (doped glass or crystal) lasers with fundamental emission in the near-IR region (e.g. frequency doubling of a Nd:YVO_4 solid-state laser from 1064 nm to 532 nm). With a few exceptions, notably Ti:sapphire lasers, most solid-state lasers emit at discrete, fixed wavelengths, as with gas lasers. Praseodymium doped solid-state lasers provide direct emission in the visible spectrum , with recent advances in GaN diode pump lasers capable of targeting their high absorption at 442 nm improving their practicality [21].

Dye lasers, on the other hand, can provide tunable emission throughout the visible spectrum [22]. Using a dye as the laser gain medium, normally organic molecules in liquid, allows for gain from the ultra-violet to the near-IR spectral regions through choice of dye. However, dye lasers have the safety and environmental disadvantages

that the use of organic dyes bring, often using carcinogens as either the gain molecules or for the liquid suspension. In terms of laser performance they are similar to semiconductor lasers, in that the individual device can be designed for addressing a specific target wavelength and broad gain bandwidth allows for large tuning ranges. Dye lasers also share other characteristics with semiconductor lasers, with upper-state lifetimes in the order of nanoseconds.

Where dye lasers are largely impractical outside the research laboratory however, semiconductor lasers in the visible region are highly desirable for their flexibility in wavelength, mass-producibility, lower environmental impact and cost, while maintaining some of the positive characteristics that dye lasers bring. The spectral coverage of semiconductor materials is increasing from both long- and short-wavelengths of the visible spectrum, with InGaN in the blue-green and AlGaInP in the red as shown in Figure 1.6.

1.3.2.1 Large bandgap semiconductor materials

As discussed in Section 1.2, semiconductor band-gaps determine the potential operational wavelengths for a semiconductor laser. Through the alloying of different binary semiconductor materials (e.g. the Nitride materials GaN and InN) the band-gap can be designed and controlled for the production of laser devices. Materials with a band-gap in the visible or UV spectra are said to be large band-gap or wide band-gap materials. Figure 1.7 shows a plot of binary materials and their corresponding lattice constant (atomic spacing within the crystal structure) and energy-band gap, while the *ternary* alloy materials (e.g. InGaN) are indicated by the joining lines. Further alloying can occur to produce quaternary materials (e.g. an alloy of AlP, GaP and InP to produce AlGaInP), and possible *quaternary* materials exist within the areas created by the surrounding ternary lines in the figure.

Semiconductor materials are defined by their elemental group numbers, with materials such as GaAs denoted as III-V, and materials such as ZnSe as II-VI. As can be seen from Figure 1.7 and as discussed in the previous section, the III-V material systems of

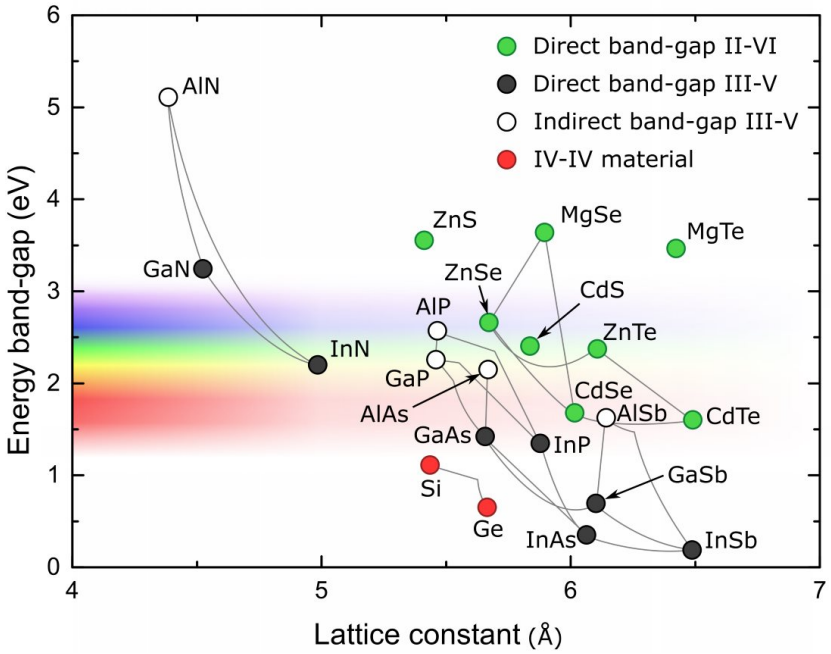

Figure 1.7: Diagram showing III-V and II-VI materials, along with group IV Si and Ge. The band-gap of each binary is indicated as direct or indirect. Example ternary alloys are indicated by the joining lines between binary materials.

InGaN and AlGaInP cover the blue and red regions of the visible spectrum respectively, with only the extremes of each material system reaching towards the green-yellow emission region. A 'gap' is evident in the III-V semiconductor spectrum, however II-VI materials broadly cover this gap.

II-VI materials have been investigated in the past as blue-emission laser materials, but difficulties in doping, along with rapid advances in Nitride-based technologies caused research interests to move away from II-VI investigations. Nitride lasers faced similar research problems in growth quality and p-type doping to the II-VI, with ZnSe devices grown on GaAs initially showing equal promise of blue-emission semiconductor devices, and it was only during the period 1986–1996 that the material was demonstrated to be the clear route to blue-emission devices and lasers with the introduction of AlN growth buffers [23] and successful p-type doping [24], closely followed by demonstrations of LED [25] and laser [26] devices.

The portion of the spectrum from approximately 625 nm to 700 nm can be reached using AlGaInP-based semiconductor lasers [27], while Nitride-based lasers allow for

access to the blue (and recently green, e.g. ref. [28]) regions of the spectrum [29], up to approximately 530 nm. A coverage gap in the spectrum exists in semiconductor lasers, from 530 nm to 625 nm, and new materials and methods are required to access this. InGaN devices are making progress to longer wavelengths, however the difficulty and complexity increases with material strain causing reductions in efficiency due to the piezoelectric effect in strained nitride material, and the resultant quantum-confined Stark effect [30].

The result is that there is still an area of the spectrum not covered by fundamental emission semiconductor laser devices, with the upper wavelength limits of InGaN and lower limits of AlGaInP providing barriers to full spectral coverage within a single material system. This gap in the spectrum encompasses desirable wavelengths to target with semiconductor lasers, especially for astronomy and biomedical applications, some examples being: 589.2 nm for sodium guide stars for astronomical adaptive optics; 561 nm, 592 nm for bio-medical imaging and cytometry; 577 nm for medical treatment of the eye, absorbed by melanin and hemoglobin; 581 nm for laser therapy and photodynamic cancer therapy.

With the advent of high power GaN pump lasers, II-VI materials such as ZnCdMgSe show promise as the solution to coverage across the centre gap of the visible spectrum if they can be incorporated into an optically-pumped laser architecture.

1.4 Introduction to the VECSEL

An optically-pumped VECSEL is a type of laser that has been the subject of a large amount of research and development over the past 2 decades, combining power scalability and high beam quality via uniform wide area optical pumping and vertical emission.

At its simplest, a VECSEL can be described as an optically-pumped semiconductor gain mirror with an external resonator. The VECSEL is commonly compared to two other laser types: the similarly named vertical-cavity surface-emitting laser (VCSEL)

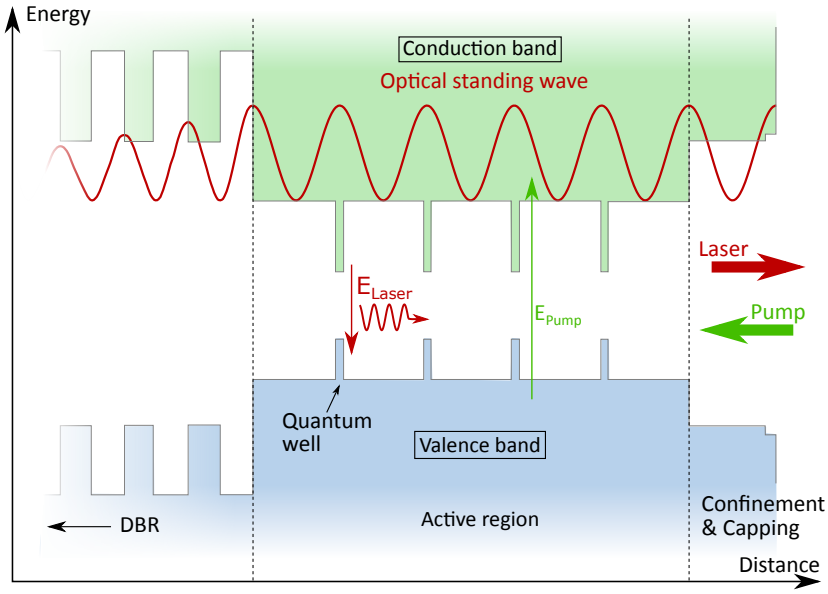

Figure 1.8: Standard design of a QW VECSEL gain structure, with DBR shown to the left of the gain region, surface barrier for carrier confinement to the right. The quantum wells are placed at the antinodes of the laser optical standing wave for RPG.

and optically-pumped doped-dielectric thin-disk lasers, hence its alternative name the semiconductor disk laser.

The external cavity surface-emitting semiconductor laser was first demonstrated in 1991 by W.B. Jiang et al. in pulsed operation [31]. This initial demonstration was based on an InGaAs/InP multi-QW structure, with a gold-coating on the structure acting as a cavity end mirror. The 'external-cavity' in the name was provided by an external dielectric output coupler mirror with 10 % transmission.

The modern design of an optically-pumped continuous-wave semiconductor VECSEL with a distributed Bragg reflector (DBR) was demonstrated in 1997 by Kuznetsov et al. [32]. A number of gain layers, usually QWs but sometimes layers of quantum dots, are placed within the semiconductor subcavity to provide gain. An optical standing wave is set up with the QWs placed at the electric field antinodes for maximum efficiency. This arrangement of the active layers is called resonant periodic gain (RPG) [33]. A design of a standard VECSEL gain structure is shown in Figure 1.8.

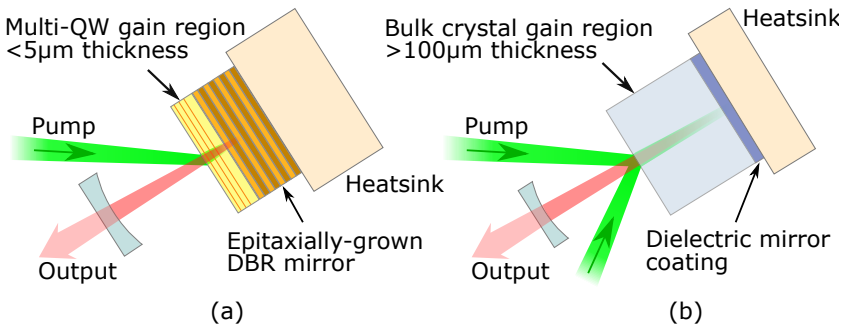

Figure 1.9: Comparison between the laser architecture of (a) a VECSEL and (b) a solid-state thin-disk laser. VECSELs have significantly shorter gain regions due to high pump absorption, while thin-disk lasers often require mult-pass pump schemes. Diagrams not to scale.

Since then the progress has been made with subtle advances in structure design and thermal management to increase the maximum power and VECSEL spectral coverage; reported VECSEL powers exceeding 20 W continuous-wave (CW) in TEM00 [34,35] and >100 W multimode [36] from a single structure.

Comparing to the similar solid-state doped-dielectric disk laser (as in Figure 1.9) which is also able to produce high powers with an external cavity for intracavity field access, the disk-laser does not have the flexibility of wavelength engineering possible with a semiconductor gain region. Reduced pump absorption also complicates the configuration of a disk-laser, necessitating multi-pass arrangements [37], usually not necessary with semiconductor structures with intrinsic high pump absorption.

The VECSEL can be thought of as a hybrid: it has the bottom DBR and bandgap engineered gain structure of the VCSEL (shown in Figure 1.4 (b)), but the external cavity and (normally) optical pump of the doped dielectric thin-disk. Their similarity to the doped dielectric lasers means that VECSELs are beginning to replace vanadate lasers due to their compact nature and low noise characteristics. There have been demonstrations of electrically pumped VECSELs (known as NECSELs [38]) with recent visible wavelength applications in projection and display technologies [11], however these are a different category of device and are not discussed further in this thesis .

1.4.1 Distributed Bragg reflector

While an edge-emission laser (e.g. diode laser) has high gain and can simply rely on reflection from the cleaved end-facets of the semiconductor, the low gain vertical-emission structures require that loss be minimised. For visible wavelength lasers where the substrate tends to be highly absorptive for the laser light (e.g. GaAs, InP, although not for blue lasers grown on sapphire), reflection of the light before reaching the substrate is crucial for the operation of VECSELs. The high reflectivity of a DBR, >99.9 % allows for low loss to the rear of the structure.

The DBR is based on the constructive and destructive interference experienced by light undergoing a series of Fresnel reflections at sub-wavelength distance scales. The optical path-length between each interface is calibrated for a target wavelength λ to be $\lambda/4$, with path lengths of the DBR pairs $\lambda/2$ such that light with wavelength λ undergoes maximum constructive interference for the reflected component of the wave and maximum destructive interference for the transmitted component.

The addition of multiple layer pairs contributes to the final reflectivity, and increased refractive index contrast for the Fresnel reflections reduces the number of interfaces required for a given reflectivity. DBR design is discussed in detail in Section 2.5.

1.4.2 Pump schemes and power scaling

A VECSEL is optically pumped and, in contrast to conventional solid-state lasers, does not require high pump beam-quality due to the thin pump absorption region. The VECSEL output can have a high beam-quality with single transverse mode so the VECSEL can be described as a brightness converter from a high power optical pump with low beam-quality to high power with high beam-quality [39].

The thin (micrometre scale), high absorption gain region of a VECSEL effectively renders insignificant the effects of thermal lensing that must be accounted for in solid state lasers, where thermal gradients within the material caused by pump absorption

in the gain region produce a variation in refractive index and a corresponding lens effect.

The external cavity of a VECSEL allows for the mode size at the active region to be varied through manipulation of the external resonator, and this allows for the matching of pump spot size with mode-size, or mode-matching. Through proper mode matching of the pump spot with cavity mode-size, the pump spot can be large enough to avoid un-pumped regions of the laser mode, while not overly large such that higher-order transverse modes cause multimode operation.

In contrast, increasing the pumped spot in an electrically pumped scheme can cause a shortage of carriers in the centre of the mode, limited by the effectiveness of the carrier-spreading layer.

An increase in optical pump spot size provides a linear increase in VECSEL output power , known as *power scaling*. This spot size increase has the advantage of maintaining pump intensity and therefore avoiding thermal limitations. VECSEL output powers have been reported in excess of 100 W for multimode operation [36], and the state-of-the-art are further discussed in Section 1.5.

For small areas (and thin-devices), thermal extraction is essentially a one-dimensional process from pumped region to heatsink through the substrate, where wider-pumped regions effectively act as separated laser elements in parallel [39,40]. As the pump spot size increases beyond a certain point, lateral heat transfer begins impact on laser performance as heat transfers through the active region.

1.4.3 External cavity arrangements

The external cavity of a VECSEL is designed for mode-matching of the pumped area at the gain region, with additional beam waists as required. The external cavity allows for access to the intracavity field to integrate intracavity optical elements, for performing efficient intracavity frequency doubling, Raman conversion, frequency selection and tuning.

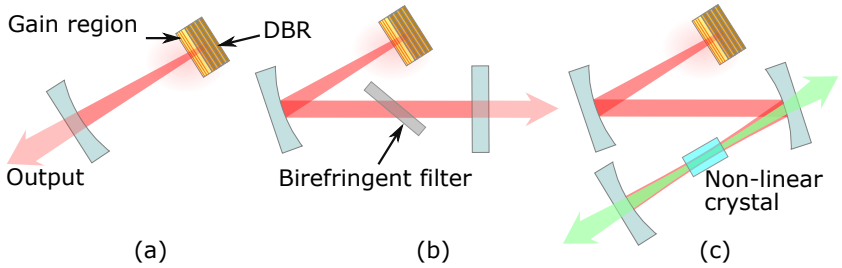

Figure 1.10: Examples of VECSEL cavity arrangements. (a) 2-mirror, (b) 3-mirror with intracavity birefringent filter at Brewster's angle, (c) 4-mirror with non-linear crystal positioned at a beam focus for intracavity frequency conversion (e.g. second-harmonic generation).

The most basic cavity configuration is the 2-mirror shown in Figure 1.10 (a), with a simple curved mirror acting as cavity end-mirror. More cavity-mode control can be obtained by adding another mirror to the cavity, producing the 3-mirror cavity, an example of which (with birefringent filter for wavelength selection and tuning) is shown in Figure 1.10 (b). Where intracavity non-linear elements are desired, such as frequency doubling crystals (Figure 1.10 (c)), additional cavity mirrors can control focus locations and sizes, and coupled cavities can be set up with the inclusion of narrow-band high-reflection/high-transmission mirrors .

Flexibility in the external cavity allows for further application of the VECSEL output using the intracavity field, e.g. single frequency operation through the addition of an intracavity etalon and Lyot filter as in ref. [41], active modelocked operation with an intracavity acousto-optic modulator as in ref. [42], and passive modelocked operation with a semiconductor saturable absorber mirror as in ref. [43].

1.5 Fundamental spectral coverage of reported VECSELs

While VECSEL devices are well suited for intracavity frequency conversion (discussed in Section 1.6), there are significant advantages to direct emission: higher efficiency, simplified external cavity, short pulse operation and modelocking, and intracavity frequency conversion. This section discusses the direct emission coverage of reported

VECSELs. Figure 1.11 shows a selection of reports of continuous-wave VECSEL devices.

The most mature area in VECSEL emission is the infrared (IR) region, most notably at λ 1 μm with >20 W TEM00 output [34] and >106 W multimode operation [36] reported with InGaAs QW gain structures.

Visible QW devices have been demonstrated in the red portion of the spectrum with the GaInP/AlGaInP material system [44–48] to as low as 645 nm [49], the minimum wavelength limited when compared to the edge-emission devices in ref. [50] due to the requirement for compressive strain in the QWs for TE-polarised gain. Pulsed operation in the blue-violet and near-UV have been demonstrated for VECSELs of GaN/InGaN grown on sapphire [51–53].

As discussed in Section 1.3, there is little direct green-yellow emission in semiconductor lasers and there are no reported direct emission green VECSELs. While nitride lasers continue to increase in wavelength into the green region, alternative material systems allow for emission within the visible spectrum. This, together with the recent availability of high power GaN blue diode-lasers for pumping, provides the motivation for investigating II-VI materials with bandgaps in this region, these diodes recently having been used to pump red GaInP/AlGaInP VECSELs [54]. The gap in fundamental emission coverage is closing, with green VCSELs based on ZnCdSSe having been reported [55], as well as green-emission VCSELs based on GaN [56].

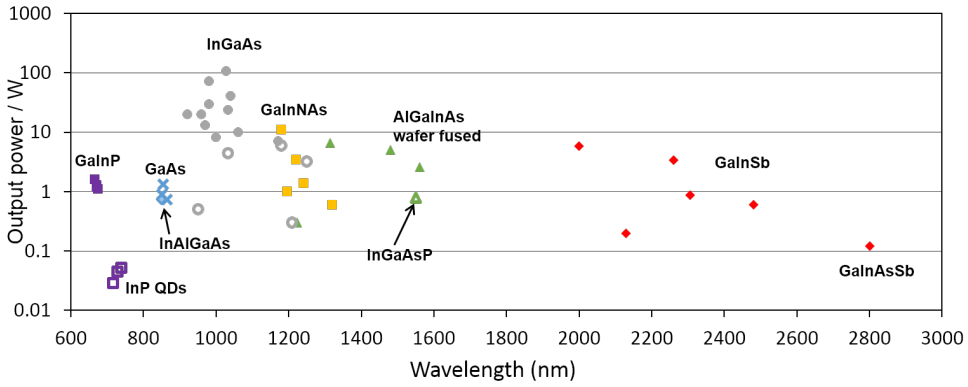

Figure 1.11: Fundamental spectral coverage of CW VECSELs. Selected results are plotted to illustrate the maximum continuous wave output power and spectral range of all materials used and refer to QWs unless otherwise indicated. GaInP [44–48]; InP QDs [57]; GaAs [58,59]; InAlGaAs [60]; InGaAs [34–36,61–65]; InAs QDs [66–69]; GaInNAs [70–74]; InGaAsP [75]; AlGaInAs wafer fused, (where the gain region and DBR are grown on different substrates) [76–79]; GaInSb [80]; GaInAsSb [80–83]; bulk PbTe [84].

1.6 Frequency conversion

Non-linear frequency conversion allows lasers to reach wavelengths that are difficult to reach via direct emission. A common conversion technique used to reach the visible spectrum is second harmonic generation (SHG), e.g. the conversion from light at 1064 nm to green wavelengths at 532 nm as in ref. [85] and commercial green laser systems. Frequency doubling was first observed in 1961 with single-crystal quartz with a ruby laser [86] and has rapidly grown to prominence in extending the wavelengths reachable. This is achieved using a two photon 'mixing' process to produce a third photon with double the frequency. Other non-linear frequency conversion techniques are sum and difference frequency generation and Raman conversion [87–89].

Frequency conversion techniques are particularly effective within VECSELs, as the high circulating intracavity field allows for high efficiency conversion. Intracavity SHG was demonstrated in a VECSEL in 1999 [90], and the frequency-doubling of VECSELs to the visible spectrum is sufficiently commonplace that there are commercial devices on the market (e.g. visible spectrum lasers in ref. [91]). Each conversion will however reduce overall efficiency, and fundamental emission at the wavelength of interest has the advantage of potentially higher efficiency, simplified cavity and the ability to

perform further frequency conversion to other difficult to reach spectral regions, e.g. frequency doubling a red laser allows emission in the UV [44].

1.7 Thin-films and applications

In the course of this thesis, the novel approach that must be taken to realise a II-VI ZnCdMgSe VECSEL, away from the standard format gain-mirror laser structures, is described. A DBR in the ZnCdMgSe material system is limited by refractive index contrast, with the high Mg content layers and total device thickness limited by growth quality concerns. To overcome the lack of reliable integrated DBR, the idea of thin-film VECSELs composed of fully discrete components are investigated, moving onto substrate removal and thin-film transfer. There are also advantages to the removal and transfer of semiconductor structures and the demonstration of transfer of II-VI and III-V AlGaInP multi-QW films are a major result of this body of work, apart from the consideration of the VECSEL devices.

Epitaxial lift-off (ELO) and transfer of semiconductor structures from their growth substrates allows structures, grown lattice-matched on top of a high quality substrate, to be moved to substrates where the lattice mismatch would otherwise prevent high quality growth or which would not be suitable for growth, e.g. flexible substrates; or as with the case of rear-emission visible emitters on InP, the transfer of devices from growth substrates that preclude the device from operation.

The investigation into stratified or layered devices, combining monolithically grown heterostructures and non-related bulk substrates, is already an area of active research. ELO and semiconductor transfer is a field of growing importance in research applications [92,93], in the production of thin film transistors [94], light emitting diodes (LEDs) [95], solar cells [96], sensing arrays [97], complementary metal oxide semiconductor (CMOS) circuits [98], etc.

Additional applications of ELO lie in areas where a band-gap engineered transferrable semiconductor film offers advantages over similar methods (e.g. the production of

low noise III-V distributed Bragg reflector (DBR) mirrors with significant performance increase over the previous highest performing dielectric SiO2/Ta2O5 mirror [99]). Standard ELO in III-V and III-N semiconductor devices is performed on structures with a sacrificial layer of fast etching material underneath the device which, once removed, allows for the structure to be lifted and transferred.

1.8 Thesis overview

This thesis covers the progression towards thin-device VECSELs, from design to testing. The overall progression of this body of work leads from the description of the gain-mirror VECSEL devices, which have been heavily investigated since the key work by Kuznetsov et al. in 1997 [32]. Further development of VECSEL devices in a range of material systems, enables the spectral coverage and output powers of the VECSEL family of lasers to grow to a custom laser solution for multiple applications. Chapter 2 discusses the key features of VECSEL structures, and the considerations and calculations necessary to produce state-of-the-art vertical semiconductor laser devices.

The primary investigation is into the ZnCdMgSe material system, which promises lattice-matched material with band-gaps throughout the visible spectrum, and reported edge-emission QW lasers in red, green and blue wavelengths [100]. Material growth limits the opportunities for the standard gain-mirror VECSEL design, and the structures are designed for operation in a thin-film VECSEL scheme. Further details of this material system and the design, growths, structure processing and preparation, and structure characterisation are described in Chapter 3.

The thin-film VECSEL device is not only a method for achieving laser action with challenging material systems, but has advantages of its own thanks to the separation of the gain region from the cavity end-mirror. Possibilities open for novel cavity configurations and pump schemes, and the demonstration and optimisation of the basic thin-film VECSEL is a first step to this. The thin-film VECSEL described in

Chapter 4 is based on AlGaInP grown on and transferred from GaAs, and to our knowledge is the first thin-film VECSEL of this kind demonstrated.

The structure transfer techniques developed for the thin-film VECSEL project have applications in other areas, and Chapter 5 discusses one such application. Colour conversion of GaN LEDs to produce white light for visible light communication is an area receiving much attention in recent years, with a significant boost in the area due to the high-profile demonstration of high-definition video transmitted from a light-bulb in 2011 [101]. Material with high modulation speeds is needed to convert the blue-violet GaN emission to white light, while allowing for high-bandwidth data transfer. The transfer and testing of a ZnCdMgSe multi-QW structure for colour conversion is demonstrated, and the results discussed in relation to alternative colour conversion methods.

1.9 References

[1] O. Svelto, Principles of lasers, 2010. doi:10.1007/978-1-4419-1302-9.

[2] C. Kittel, Introduction to solid state physics, 2005. http://www.wiley.com/WileyCDA/WileyTitle/productCd-EHEP000803.html.

[3] R.N. Hall, G.E. Fenner, J.D. Kingsley, T.J. Soltys, R.O. Carlson, Coherent light emission from GaAs junctions, Phys. Rev. Lett. 9 (1962) 366–368. doi:10.1103/PhysRevLett.9.366.

[4] M.I. Nathan, W.P. Dumke, G. Burns, F.H. Dill, G. Lasher, Stimulated emission of radiation from GaAs p-n junctions, Appl. Phys. Lett. 1 (1962) 62–64. doi:10.1063/1.1777371.

[5] P. Prete, N. Lovergine, Novel precursors for the growth of device-quality ZnSe-based compounds, III-Vs Rev. 14 (2001) 44–47. doi:10.1016/S0961-1290(01)80516-0.

[6] M. Asada, Y. Miyamoto, Y. Suematsu, Gain and the threshold of three-dimensional quantum-box lasers, IEEE J. Quantum Electron. 22 (1986) 1915–1921. doi:10.1109/JQE.1986.1073149.

[7] Y. Arakawa, H. Sakaki, Multidimensional quantum well laser and temperature dependence of its threshold current, Appl. Phys. Lett. 40 (1982) 939–941. doi:10.1063/1.92959.

[8] J. Faist, F. Capasso, D.L. Sivco, C. Sirtori, A.L. Hutchinson, A.Y. Cho, Quantum cascade laser., Science. 264 (1994) 553–556. doi:10.1126/science.264.5158.553.

[9] G. Derra, H. Moench, E. Fischer, H. Giese, U. Hechtfischer, G. Heusler, et al., UHP lamp systems for projection applications, J. Phys. D. Appl. Phys. 38 (2005) 2995–3010. doi:10.1088/0022-3727/38/17/R01.

[10] R.M. Pope, E.S. Fry, Absorption spectrum (380-700 nm) of pure water. II. Integrating cavity measurements., Appl. Opt. 36 (1997) 8710–8723. doi:10.1364/AO.36.008710.

[11] IMAX, IMAX Announces Exclusive Global Laser Technology Partenership With Necsel, (2014). http://necsel.com/news/2014/imax-announces-exclusive-global-laser-technology-partenership-with-necsel (accessed April 17, 2015).

[12] C.F. Blodi, S.R. Russell, J.S. Pulido, J.C. Folk, Direct and feeder vessel photocoagulation of retinal angiomas with dye yellow laser., 1990. doi:10.1016/S0161-6420(90)32509-5.

[13] S.B. Bressler, T. Almukhtar, L.P. Aiello, N.M. Bressler, F.L. Ferris, A.R. Glassman, et al., Green or yellow laser treatment for diabetic macular edema: exploratory assessment within the Diabetic Retinopathy Clinical Research Network., Retina. 33 (2013) 2080–8. doi:10.1097/IAE.0b013e318295f744.

[14] A. Garnache, A.A. Kachanov, F. Stoeckel, R. Planel, High-sensitivity intracavity laser absorption spectroscopy with vertical-external-cavity surface-emitting semiconductor lasers, Opt. Lett. 24 (1999) 826–828. doi:10.1364/OL.24.000826.

[15] W. Haiss, N.T.K. Thanh, J. Aveyard, D.G. Fernig, Determination of Size and Concentration of Gold Nanoparticles from UV–Vis Spectra, Anal. Chem. 79 (2007) 4215–4221. doi:10.1021/ac0702084.

[16] H.K. Lichtenthaler, C. Buschmann, Chlorophylls and Carotenoids : Measurement and Characterization by UV-VIS, Curr. Protoc. Food Anal. Chem. F4.3.1-F4. (2001) 1–8. doi:10.1002/0471142913.

[17] R. Alfano, D. Tata, J. Cordero, P. Tomashefsky, F. Longo, M. Alfano, Laser induced fluorescence spectroscopy from native cancerous and normal tissue, IEEE J. Quantum Electron. 20 (1984) 1507–1511. doi:10.1109/JQE.1984.1072322.

[18] I.J. Bigio, J.R. Mourant, Ultraviolet and visible spectroscopies for tissue diagnostics: fluorescence spectroscopy and elastic-scattering spectroscopy., Phys. Med. Biol. 42 (1997) 803–814. doi:10.1088/0031-9155/42/5/005.

[19] K.-D. Langer, J. Grubor, Recent Developments in Optical Wireless Communications using Infrared and Visible Light, 2007 9th Int. Conf. Transparent Opt. Networks. 3 (2007) 146–151. doi:10.1109/ICTON.2007.4296267.

[20] W.P. Risk, T.R. Gosnell, A. V Nurmikko, Compact blue–green lasers, Cambridge University Press, Cambridge, UK, 2003.

[21] A. Richter, E. Heumann, G. Huber, V. Ostroumov, W. Seelert, Power scaling of semiconductor laser pumped Praseodymium-lasers., Opt. Express. 15 (2007) 5172–5178. doi:10.1364/OE.15.005172. [22] F.P. Schafer, Dye lasers, (1990).

[23] H. Amano, N. Sawaki, I. Akasaki, Y. Toyoda, Metalorganic vapor phase epitaxial growth of a high quality GaN film using an AlN buffer layer, Appl. Phys. Lett. 48 (1986) 353. doi:10.1063/1.96549.

[24] H. Amano, M. Kito, K. Hiramatsu, I. Akasaki, P-Type Conduction in Mg-Doped GaN Treated with Low-Energy Electron Beam Irradiation (LEEBI), Jpn. J. Appl. Phys. 28 (1989) L2112–L2114. doi:10.1143/JJAP.28.L2112.

[25] S. Nakamura, M. Senoh, T. Mukai, High-power InGaN/GaN double-heterostructure violet light emitting diodes, Appl. Phys. Lett. 62 (1993) 2390–2392. doi:10.1063/1.109374.

[26] S. Nakamura, M. Senoh, S. ichi Nagahama, N. Iwasa, T. Yamada, T. Matsushita, et al., InGaN-based multi-quantum-well-structure laser diodes, Japanese J. Appl. Physics, Part 2 Lett. 35 (1996). doi:10.1143/JJAP.35.L74.

[27] T. Nishida, N. Shimada, T. Ogawa, M. Miyashita, T. Yagi, Short wavelength limitation in high power AlGaInP laser diodes, SPIE LASE. 7918 (2011) 791811–791811–7. doi:10.1117/12.872939.

[28] Y. Enya, Y. Yoshizumi, T. Kyono, K. Akita, M. Ueno, M. Adachi, et al., 531 nm Green lasing of InGaN based laser diodes on semi-polar 2021 free-standing GaN substrates, Appl. Phys. Express. 2 (2009) 82101. doi:10.1143/APEX.2.082101.

[29] F.A. Ponce, D.P. Bour, Nitride-based semiconductors for blue and green light-emitting devices, Nature. 386 (1997) 351–359. doi:10.1038/386351a0.

[30] J.H. Ryou, P.D. Yoder, J. Liu, Z. Lochner, H.S. Kim, S. Choi, et al., Control of quantum-confined stark effect in InGaN-based quantum wells, IEEE J. Sel. Top. Quantum Electron. 15 (2009) 1080–1091. doi:10.1109/JSTQE.2009.2014170.

[31] W. Jiang, S. Friberg, High powers and subpicosecond pulses from an external cavity surface emitting InGaAs/InP multiple quantum well laser, Appl. Phys. .... 807 (1991). doi:10.1063/1.104495.

[32] M. Kuznetsov, F. Hakimi, High-power (> 0.5-W CW) diode-pumped vertical-external-cavity surface-emitting semiconductor lasers with circular TEM/sub 00/beams, IEEE Photonics Technol. Lett. 9 (1997) 1063–1065. http://ieeexplore.ieee.org/xpls/abs_all.jsp?arnumber=605500 (accessed February 5, 2014).

[33] M.Y.A. Raja, S.R.J. Brueck, M. Osinski, C.F. Schaus, J.G. McInerney, T.M. Brennan, et al., Resonant periodic gain surface-emitting semiconductor lasers, IEEE J. Quantum Electron. 25 (1989) 1500–1512. doi:10.1109/3.29287.

[34] B. Rudin, A. Rutz, M. Hoffmann, D.J.H.C. Maas, A.-R. Bellancourt, E. Gini, et al., Highly efficient optically pumped vertical-emitting semiconductor laser with more than 20 W average output power in a fundamental transverse mode., Opt. Lett. 33 (2008) 2719–2721. doi:10.1364/OL.33.002719.

[35] T.L. Wang, Y. Kaneda, J.M. Yarborough, J. Hader, J. V. Moloney, A. Chernikov, et al., High-power optically pumped semiconductor laser at 1040 nm, IEEE Photonics Technol. Lett. 22 (2010) 661–663. doi:10.1109/LPT.2010.2043731.

[36] B. Heinen, T.-L. Wang, M. Sparenberg, a. Weber, B. Kunert, J. Hader, et al., 106 W continuous-wave output power from vertical-external-cavity surface-emitting laser, Electron. Lett. 48 (2012) 516. doi:10.1049/el.2012.0531.

[37] A. Giesen, J. Speiser, Fifteen Years of Work on Thin-Disk Lasers: Results and Scaling Laws, Sel. Top. Quantum Electron. IEEE J. 13 (2007) 598–609. doi:10.1109/JSTQE.2007.897180.

[38] J.G. McInerney, A. Mooradian, A. Lewis, A. V Shchegrov, E.M. Strzelecka, D. Lee, et al., High-brightness 980-nm pump lasers based on the Novalux extended cavity surface-emitting laser (NECSEL) concept, Proc. SPIE. 4947 (2003) 240–251. doi:10.1117/12.476231.

[39] O.G. Okhotnikov, Semiconductor disk lasers: physics and technology, John Wiley & Sons, 2010.

[40] A. MacLean, Power scaling and wavelength control of semiconductor disk lasers, University of Strathclyde, 2008. http://ethos.bl.uk/OrderDetails.do?uin=uk.bl.ethos.487871 (accessed February 5, 2014).

[41] M.A. Holm, D. Burns, A.I. Ferguson, M.D. Dawson, Actively stabilized single-frequency vertical-external-cavity AlGaAs laser, IEEE Photonics Technol. Lett. 11 (1999) 1551–1553. doi:10.1109/68.806843.

[42] M.A. Holms, P. Cusumano, D. Burns, A.I. Ferguson, M.D. Dawson, Mode-locked operation of a diode-pumped, external-cavity GaAs/AlGaAs surface emitting laser, Tech. Dig. Summ. Pap. Present. Conf. Lasers Electro-Optics. Postconf. Ed. CLEO '99. Conf. Lasers Electro-Optics (IEEE Cat. No.99CH37013). (1999) 153–154. doi:10.1109/CLEO.1999.834017.

[43] S. Hoogland, S. Dhanjal, A.C. Tropper, J.S. Roberts, R. Häring, R. Paschotta, et al., Passively mode-locked diode-pumped surface-emitting semiconductor laser, IEEE Photonics Technol. Lett. 12 (2000) 1135–1137. doi:10.1109/68.874213.

[44] J.E. Hastie, L.G. Morton, A.J. Kemp, M.D. Dawson, A.B. Krysa, J.S. Roberts, Tunable ultraviolet output from an intracavity frequency-doubled red vertical-external-cavity surface-emitting laser, Appl. Phys. Lett. 89 (2006) 061114. doi:10.1063/1.2236108.

[45] T. Schwarzbäck, M. Eichfelder, W. Schulz, R. Roßbach, M. Jetter, P. Michler, Short wavelength red-emitting AlGaInP-VECSEL exceeds 1.2 W continuous-wave output power, Appl. Phys. B. 102 (2010) 789–794. doi:10.1007/s00340-010-4213-5.

[46] T. Schwarzbäck, M. Eichfelder, W.M. Schulz, R. Roßbach, M. Jetter, P. Michler, Short wavelength red-emitting AlGaInP-VECSEL exceeds 1.2W continuous-wave output power, Appl. Phys. B Lasers Opt. 102 (2011) 789–794. doi:10.1007/s00340-010-4213-5.

[47] T. Schwarzbäck, R. Bek, F. Hargart, C.A. Kessler, H. Kahle, E. Koroknay, et al., High-power InP quantum dot based semiconductor disk laser exceeding 1.3 W, Appl. Phys. Lett. 102 (2013) 092101. doi:10.1063/1.4793299.

[48] S. Baumgärtner, H. Kahle, R. Bek, T. Schwarzbäck, M. Jetter, P. Michler, Comparison of AlGaInP-VECSEL gain structures, J. Cryst. Growth. 414 (2015) 219–222. doi:10.1016/j.jcrysgro.2014.10.016.

[49] S. Calvez, J.E. Hastie, M. Guina, O.G. Okhotnikov, M.D. Dawson, Semiconductor disk lasers for the generation of visible and ultraviolet radiation, Laser Photonics Rev. 3 (2009) 407–434. doi:10.1002/lpor.200810042.

[50] T. Tanaka, H. Yanagisawa, M. Takimoto, S. Yano, S. Minagawa, Low-threshold operation of tensile-strained GaInP/AlGaInP MQW LDs emitting at 625 nm, Electron. Lett. 29 (1993) 722. doi:10.1049/el:19930483.

[51] S.-H. Park, J. Kim, H. Jeon, T. Sakong, S.-N. Lee, S. Chae, et al., Room-temperature GaN vertical-cavity surface-emitting laser operation in an extended cavity scheme, Appl. Phys. Lett. 83 (2003) 2121. doi:10.1063/1.1611643.

[52] T. Wunderer, J.E. Northrup, Z. Yang, M. Teepe, A. Strittmatter, N.M. Johnson, et al., In-well pumping of InGaN/GaN vertical-external-cavity surface-emitting lasers, Appl. Phys. Lett. 99 (2011) 201109. doi:10.1063/1.3663575.

[53] R. Debusmann, N. Dhidah, V. Hoffmann, L. Weixelbaum, U. Brauch, T. Graf, et al., InGaN–GaN Disk Laser for Blue-Violet Emission Wavelengths, IEEE Photonics Technol. Lett. 22 (2010) 652–654. doi:10.1109/LPT.2010.2043668.

[54] A. Smith, J.E. Hastie, A.J. Kemp, H.D. Foreman, M.D. Dawson, T. Leinonen, et al., GaN diode-pumping of a red semiconductor disk laser, in: Conf. Proc. - Lasers Electro-Optics Soc. Annu. Meet., 2008: pp. 404–405. doi:10.1109/LEOS.2008.4688661.

[55] S. Klembt, M. Seyfried, T. Aschenbrenner, K. Sebald, J. Gutowski, D. Hommel, et al., Blue monolithic II-VI-based vertical-cavity surface-emitting laser, Appl. Phys. Lett. 100 (2012) 121102. doi:10.1063/1.3696029.

[56] D. Kasahara, D. Morita, T. Kosugi, K. Nakagawa, J. Kawamata, Y. Higuchi, et al., Demonstration of blue and green GaN-based vertical-cavity surface-emitting lasers by current injection at room temperature, Appl. Phys. Express. 4 (2011). doi:10.1143/APEX.4.072103.

[57] P.J. Schlosser, J.E. Hastie, S. Calvez, A.B. Krysa, M.D. Dawson, InP/AlGaInP quantum dot semiconductor disk lasers for CW TEM00 emission at 716 - 755 nm., Opt. Express. 17 (2009) 21782–21787. doi:10.1364/OE.17.021782.

[58] J.E. Hastie, High Power Surface Emitting Semiconductor Lasers, University of Strathclyde, 2004.

[59] S.S. Beyertt, U. Brauch, F. Demaria, N. Dhidah, A. Giesen, T. Kübler, et al., Efficient gallium-arsenide disk laser, IEEE J. Quantum Electron. 43 (2007) 869–875. doi:10.1109/JQE.2007.904074.

[60] S.J. McGinily, R.H. Abram, K.S. Gardner, E. Riis, A.I. Ferguson, J.S. Roberts, Novel gain medium design for short-wavelength vertical-external-cavity surface-emitting laser, IEEE J. Quantum Electron. 43 (2007) 445–450. doi:10.1109/JQE.2007.895666.

[61] J.L.A. Chilla, S.D. Butterworth, A. Zeitschel, J.P. Charles, A.L. Caprara, M.K. Reed, et al., High-power optically pumped semiconductor lasers, Proc. SPIE 5332. (2004) 143. doi:10.1117/12.549003.

[62] F. Demaria, S. Lorch, S. Menzel, M.C. Riedl, F. Rinaldi, R. Rösch, et al., Design of highly efficient high-power optically pumped semiconductor disk lasers, IEEE J. Sel. Top. Quantum Electron. 15 (2009) 973–977. doi:10.1109/JSTQE.2008.2011372.

[63] S. Lutgen, T. Albrecht, P. Brick, W. Reill, J. Luft, W. Späth, 8-W high-efficiency continuous-wave semiconductor disk laser at 1000 nm, Appl. Phys. Lett. 82 (2003) 3620–3622. doi:10.1063/1.1579137.

[64] K.S. Kim, J.R. Yoo, S.H. Cho, S.M. Lee, S.J. Lim, J.Y. Kim, et al., 1060 nm vertical-external-cavity surface-emitting lasers with an optical-to-optical efficiency of 44

[65] L. Fan, M. Fallahi, J. Murray, Tunable high-power high-brightness linearly polarized vertical-external-cavity surface-emitting lasers, Appl. Phys. Lett. (2006) 10–12. doi:10.1063/1.2164921.

[66] T.D. Germann, A. Strittmatter, U.W. Pohl, D. Bimberg, J. Rautiainen, M. Guina, et al., Quantum-dot semiconductor disk lasers, J. Cryst. Growth. 310 (2008) 5182–5186. doi:10.1016/j.jcrysgro.2008.07.004.

[67] M. Butkus, K.G. Wilcox, J. Rautiainen, O.G. Okhotnikov, S.S. Mikhrin, I.L. Krestnikov, et al., High-power quantum-dot-based semiconductor disk laser., Opt. Lett. 34 (2009) 1672–1674. doi:10.1364/OL.34.001672.

[68] A.R. Albrecht, C.P. Hains, T.J. Rotter, A. Stintz, K.J. Malloy, G. Balakrishnan, et al., High power 1.25 μm InAs quantum dot vertical external-cavity surface-emitting laser, J. Vac. Sci. Technol. B Microelectron. Nanom. Struct. 29 (2011) 03C113. doi:10.1116/1.3555379.

[69] M. Hoffmann, O.D. Sieber, V.J. Wittwer, I.L. Krestnikov, D.A. Livshits, Y. Barbarin, et al., Femtosecond high-power quantum dot vertical external cavity surface emitting laser., Opt. Express. 19 (2011) 8108–8116. doi:10.1364/OE.19.008108.

[70] V.-M. Korpijärvi, T. Leinonen, J. Puustinen, A. Härkönen, M.D. Guina, 11 W single gain-chip dilute nitride disk laser emitting around 1180 nm., Opt. Express. 18 (2010) 25633–25641. doi:10.1364/OE.18.025633.

[71] S. Vetter, S. Calvez, M.D. Dawson, F. Fusari, A.A. Lagatsky, W. Sibbett, et al., 1213nm semiconductor disk laser pumping of a Tm3+-doped tellurite glass laser, in: IEEE Lasers Electro-Optics Soc. 2008. LEOS 2008. 21st Annu. Meet., 2008: pp. 840–841. doi:10.1109/LEOS.2008.4688883.

[72] J. Rautiainen, V.-M. Korpij'nrvi, P. Tuomisto, M. Guina, O.G. Okhotnikov, others, 2.7 W tunable orange-red GaInNAs semiconductor disk laser, Opt. Express. 15 (2007) 18345–18350.

[73] J. Konttinen, A. Härkönen, P. Tuomisto, M. Guina, J. Rautiainen, M. Pessa, et al., High-power (> 1 W) dilute nitride semiconductor disk laser emitting at 1240 nm, New J. Phys. 9 (2007) 140.

[74] J. Hopkins, S. Smith, C. Jeon, H. Sun, 0.6 W CW GaInNAs vertical external-cavity surface emitting laser operating at 1.32 μm, Electron. Lett. 40 (2004) 30–31. doi:10.1049/el.

[75] H. Lindberg, M. Strassner, E. Gerster, A. Larsson, 0.8 W optically pumped vertical external cavity surface emitting laser operating CW at 1550 nm, Electron. Lett. 40 (2004) 601–602.

[76] A. Rantamäki, A. Sirbu, A. Mereuta, E. Kapon, O.G. Okhotnikov, 3 W of 650 nm red emission by frequency doubling of wafer-fused semiconductor disk laser, Opt. Express. 18 (2010) 21645–21650.

[77] J. Lyytikainen, J. Rautiainen, A. Sirbu, V. Iakovlev, A. Laakso, S. Ranta, et al., High-Power 1.48- μm Wafer-Fused Optically Pumped Semiconductor Disk Laser, Photonics Technol. Lett. IEEE. 23 (2011) 917–919. doi:10.1109/LPT.2011.2143399.

[78] J. Rautiainen, J. Lyytikäinen, A. Sirbu, A. Mereuta, A. Caliman, E. Kapon, et al., 2.6 W optically-pumped semiconductor disk laser operating at 1.57-μm using wafer fusion, Opt. Express. 16 (2008) 21881–21886.

[79] J. Rautiainen, I. Krestnikov, J. Nikkinen, O.G. Okhotnikov, 2.5 W orange power by frequency conversion from a dual-gain quantum-dot disk laser, Opt. Lett. 35 (2010) 1935–1937.

[80] D. Burns, J.-M. Hopkins, A.J. Kemp, B. Rösener, N. Schulz, C. Manz, et al., Recent developments in high-power short-wave mid-infrared semiconductor disk lasers, in: Proc. SPIE, 2009: pp. 719311–719311–13. doi:10.1117/12.811977.

[81] J.-M. Hopkins, A.J. Maclean, D. Burns, E. Riis, N. Schulz, M. Rattunde, et al., Tunable, Single-frequency, Diode-pumped 2.3 μm VECSEL, Opt. Express. 15 (2007) 8212–8217.

[82] J. Nikkinen, J. Paajaste, R. Koskinen, S. Suomalainen, O.G. Okhotnikov, GaSb-Based Semiconductor Disk Laser With 130-nm Tuning Range at 2.5 m, Photonics Technol. Lett. IEEE. 23 (2011) 777–779.

[83] B. Rösener, M. Rattunde, R. Moser, S. Kaspar, T. Töpper, C. Manz, et al., Continuous-wave room-temperature operation of a 2.8 μm GaSb-based semiconductor disk laser, Opt. Lett. 36 (2011) 319–321.

[84] M. Rahim, A. Khiar, F. Felder, M. Fill, H. Zogg, M.W. Sigrist, 5-μm vertical external-cavity surface-emitting laser (VECSEL) for spectroscopic applications, Appl. Phys. B. 100 (2010) 261–264.

[85] H.E. Jing-Liang, H. Wei, Z. Heng-li, W. Ling-an, X. Zu-yan, Y. Guo-zhen, et al., Continuous-wave output of 5.5 W at 532 nm by intracavity frequency doubling of an Nd: YVO4 laser, Chinese Phys. Lett. 15 (1998) 418.

[86] P.A. Franken, A.E. Hill, C.W. Peters, G. Weinreich, Generation of optical harmonics, Phys. Rev. Lett. 7 (1961) 118–119. doi:10.1103/PhysRevLett.7.118.

[87] C. V. Raman, K.S. Krishnan, A New Type of Secondary Radiation, Nature. 121 (1928) 501–502. doi:10.1038/121501c0.

[88] E.O. Ammann, C.D. Decker, 0.9-W Raman oscillator, J. Appl. Phys. 48 (1977) 1973–1975. doi:10.1063/1.323904.

[89] D. Parrotta, W. Lubeigt, A. Kemp, Continuous-wave Raman laser pumped within a semiconductor disk laser cavity, Opt. Lett. 36 (2011) 1083–1085. http://www.opticsinfobase.org/abstract.cfm?URI=ol-36-7-1083 (accessed February 5, 2014).

[90] T.D. Raymond, W.J. Alford, M.H. Crawford, A.A. Allerman, Intracavity frequency doubling of a diode-pumped external-cavity surface-emitting semiconductor laser, Opt. Lett. 24 (1999) 1127. doi:10.1364/OL.24.001127.

[91] Coherent inc., Optically Pumped Semiconductor Laser (OPSL) Technology, (n.d.). http://www.coherent.com/products/?771/Optically-Pumped-Semiconductor-Laser-OPSL-Technology.

[92] M. Madsen, K. Takei, R. Kapadia, H. Fang, H. Ko, T. Takahashi, et al., Nanoscale semiconductor “x” on substrate “y” - Processes, devices, and applications, Adv. Mater. 23 (2011) 3115–3127. doi:10.1002/adma.201101192.

[93] A. Carlson, A.M. Bowen, Y. Huang, R.G. Nuzzo, J.A. Rogers, Transfer printing techniques for materials assembly and micro/nanodevice fabrication, Adv. Mater. 24 (2012) 5284–5318. doi:10.1002/adma.201201386.

[94] E. Menard, K.J. Lee, D.Y. Khang, R.G. Nuzzo, J.A. Rogers, A printable form of silicon for high performance thin film transistors on plastic substrates, Appl. Phys. Lett. 84 (2004) 5398–5400. doi:10.1063/1.1767591.

[95] S.H. Park, H. Jeon, Microchip-type InGaN vertical external-cavity surface-emitting laser, Opt. Rev. 13 (2006) 20–23. doi:10.1007/s10043-006-0020-y.

[96] J. Yoon, A.J. Baca, S.-I. Park, P. Elvikis, J.B. Geddes, L. Li, et al., Ultrathin silicon solar microcells for semitransparent, mechanically flexible and microconcentrator module designs., Nat. Mater. 7 (2008) 907–915. doi:10.1038/nmat2287.

[97] Y.M. Song, Y. Xie, V. Malyarchuk, J. Xiao, I. Jung, K.-J. Choi, et al., Digital cameras with designs inspired by the arthropod eye., Nature. 497 (2013) 95–99. doi:10.1038/nature12083.

[98] D.H. Kim, Y.S. Kim, J. Wu, Z. Liu, J. Song, H.S. Kim, et al., Ultrathin silicon circuits with strain-isolation layers and mesh layouts for high-performance electronics on fabric, vinyl, leather, and paper, Adv. Mater. 21 (2009). doi:10.1002/adma.200900405.

[99] G.D. Cole, W. Zhang, M.J. Martin, J. Ye, M. Aspelmeyer, Tenfold reduction of Brownian noise in high-reflectivity optical coatings, Nat. Photonics. 7 (2013) 644–650. doi:10.1038/nphoton.2013.174.

[100] L. Zeng, B.X. Yang, A. Cavus, W. Lin, Y.Y. Luo, M.C. Tamargo, et al., Red-green-blue photopumped lasing from ZnCdMgSe/ZnCdSe quantum well laser structures grown on InP, Appl. Phys. Lett. 72 (1998) 3136–3138. doi:10.1063/1.121571.

[101] H. Haas, Harald Haas: Wireless data from every light bulb, TED Talks Dir. (2011). http://www.ted.com/talks/harald_haas_wireless_data_from_every_light_bulb (accessed March 18, 2015).

Chapter 2

Semiconductor and VECSEL design

2.1 Introduction

This chapter details the underlying materials science required for producing a design for the gain structure of a VECSEL laser, after the general introduction in Chapter 1 to the structure and external cavity and their advantages and disadvantages. Material composition, strain and temperature, and their effects on the design are discussed. Methods for calculating the electric field (E-field) within and the reflectivity of the gain structure are given, along with the considerations for VECSEL design. Detailed calculation of the layer thicknesses are provided for the design of the VECSEL gain structure. The last section introduces the design of thin-film VECSEL structures, both how they can help to circumvent the challenges presented by the II-VI material ZnCdMgSe, and provide advantages for laser cavity engineering even with well-established VECSEL materials, e.g. the III-V material AlGaInP.

2.2 Semiconductor materials and band-gap engineering

The design and growth of semiconductor structures depends on the control of various material parameters for different purposes. For semiconductor materials, this means

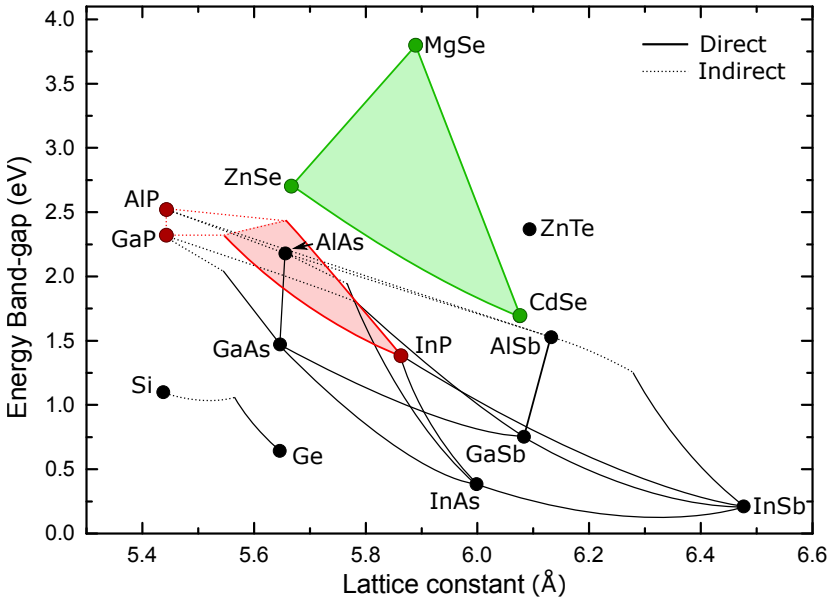

Figure 2.1: Band-gap of common binary and ternary (joining lines) semiconductor materials, plotted against lattice constant. Direct and indirect band-gap materials indicated by solid and dotted lines respectively. Red and green regions indicate the material systems investigated for thin-film VECSEL devices in this thesis, AlGaInP and ZnCdMgSe respectively.

finding a way to reach a targeted band-gap energy within the constraints of lattice constants and material strains. By producing alloys of different semiconductor materials, complex designs can be produced, from junctions and quantum wells (QWs) to quantum cascade lasers.

Binary semiconductor materials such as GaAs, AlAs, AlP and GaP, generally have well-defined (although temperature dependant) lattice constants and energy band-gaps, but can be mixed to produce ternary alloys, e.g. AlGaAs, AlAsP, AlGaP. The basic ternary alloys are shown by the lines in Figure 2.1. The solid lines indicate ternaries with direct band-gaps, while the dotted lines indicate indirect band-gap semiconductors. Further, the materials can be mixed to quaternary (e.g. AlGaInP), or even quinternary (e.g. InGaAsSbN [1]) alloys, to reach the combination of desired band-gap and lattice constant. To grow semiconductor heterostructures with high crystal quality, the lattice constant must be within close proximity to that of the growth substrate, so the range of bandgaps that may be attainable is limited by the particular substrate.

2.2.1 Lattice constant and band-gap

The calculation of lattice constant for ternary materials is achieved through linear interpolation, described by the empirical Vegard's law [2] which states that for two binary materials AC and BC with lattice constants a_{AC} and a_{BC} alloyed with a material composition x to make the material $A_xB_{(1-x)}C$, the lattice constant is:

$$a_{A_xB_{(1-x)}C} = a_{AC}x + a_{BC}(1-x) \tag{2.1}$$

The calculation of the energy band-gap is similar, but includes a bowing parameter in its calculation [3]:

$$E_{(A_xB_{(1-x)}C)} = E_{AC}{\cdot}x + E_{BC}{\cdot}(1-x) + x(1-x)b \tag{2.2}$$

where b is the bowing parameter for the ternary material.

This can be generalised for most semiconductor parameters for ternary material, and a similar case applies for finding parameters of quaternary materials [3]. For quaternary alloys of the form $(A_xB_{(1-x)})_{(1-y)}C_yD$, the parameter is first calculated for the ternary material $T(x) = A_xB_{(1-x)}D$, as in Equation 2.1, followed by re-inserting $T(x)$ repeating as $T(x)_{(1-y)}C_yD$. For quaternaries of the form $A_{x'}B_{y'}C_{(1-x'-y')}D$, the simplest method is to convert to the $(A_xB_{(1-x)})_{(1-y)}C_yD$ form before calculation.

2.2.2 Strain effects in semiconductors

Strain in a semiconductor lattice is caused by a material of one lattice size a_0 being used as the growth substrate of another material with different lattice size a_1. If $a_1 > a_0$, the grown material will be compressed such that the lattice grown is the size of a_0. For $a_1 < a_0$, the grown material is 'stretched', or put under tensile strain. These are shown in Figure 2.2 respectively. The strain in directions parallel to the substrate surface,

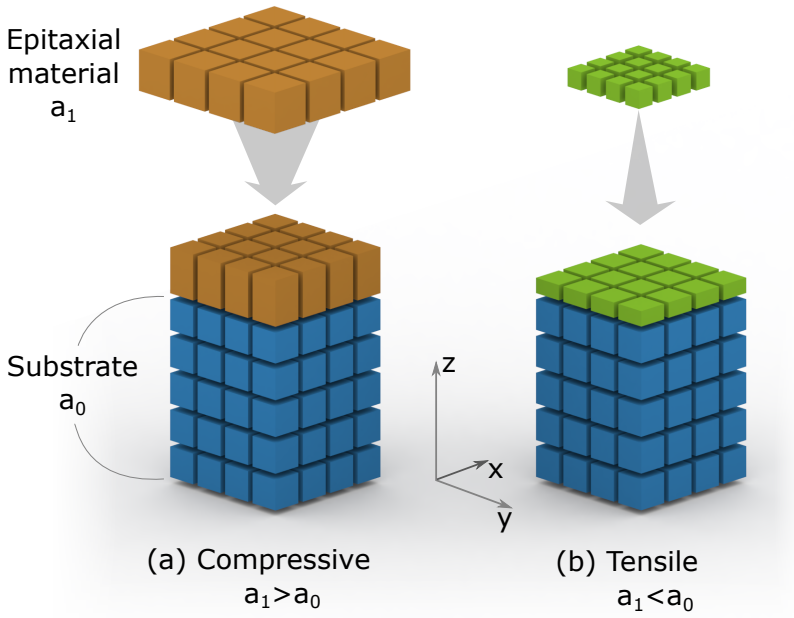

Figure 2.2: Lattice deformation causing compressive and tensile strain of material grown on a substrate with lattice constant a_0, adapted from [4]: (a) for material with lattice constant a_1 larger and (b) smaller than a_0.

shown as x and y in Figure 2.2, are given by Equation 2.3:

$$\epsilon_x = \epsilon_y = \frac{(a_0 - a_1)}{a_1} \equiv \epsilon \tag{2.3}$$

where ϵ_x and ϵ_y are the strains parallel to the substrate surface, a_0 is the substrate lattice constant, a_1 the lattice constant of the grown material and ϵ is the biaxial strain.

Strain in a semiconductor affects the energy-bands within the material, deforming the valence band dispersion (alteration of heavy- and light-hole effective-mass) and removing the degeneracy at the valence band edge (Γ) between heavy- and light-holes. There is also a small shift in the energy band-gap of the material. The effect is shown in Figure 2.3.

For compressively-strained material (Figure 2.3 (b)) the heavy-hole sub-band becomes the ground state, and increasing strain deforms the density of states to more closely match the conduction band. For tensile strained material (Figure 2.3 (c)) the light-hole sub-band becomes the ground state.

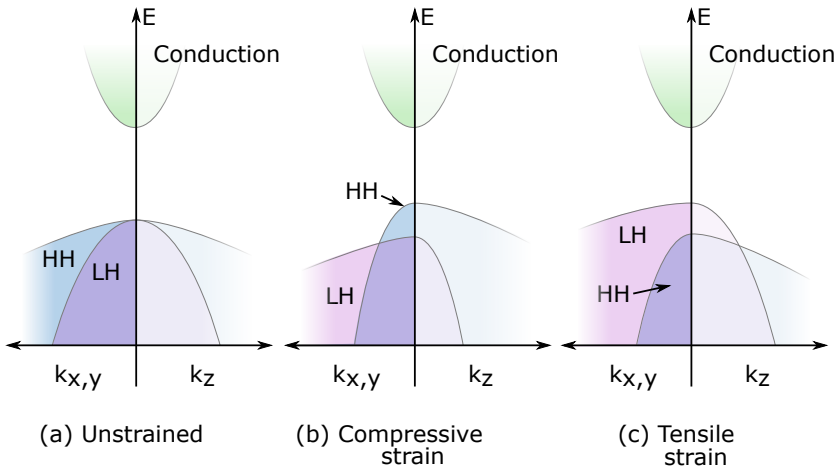

Figure 2.3: Simplified valence band-distortion caused by strain, adapted from [4], for crystal momentum k parallel (x,y) to the sample surface to the left of each plot, and perpendicular (z) to the right (axes as indicated in Figure 2.2). When a material with unstrained band-structure (a) is grown under (b) compressive and (c) tensile strain, there is a change of shape in the heavy and light hole valence bands. Not shown here is the spin-orbit split off valence band.

The deformation of the valence band is advantageous for reducing threshold, as a valence band density of states profile matching the conduction band can allow for the conditions for gain to be met with fewer injected carriers, and thereby increase the efficiency of recombination and reduce the laser threshold. Higher strain reduces the *critical thickness* of the material, which is the maximum thickness that can be grown with high quality without lattice dislocations and material cracking. The magnitude of strain required to achieve conduction and valence band symmetry is such that the layer thickness can only be of the order of a few nm, i.e. a QW, providing an additional advantage for QW gain regions over bulk material. QWs are discussed further in Section 2.3.

Bi-axial strain also has an effect on the polarisation of the optical gain. In relation to the axes defined in Figure 2.2, TE polarisation is when the electric field oscillates in the x-y plane, while for TM polarisation the oscillation is perpendicular to this plane. The band-structure of the semiconductor can be described in terms of atomic orbitals, where the conduction band is an s-type spherical orbital, while the valence bands (consisting of heavy-hole, light-hole and spin-orbit sub-bands) have p-symmetry and are described by the p-orbitals shown in Figure 2.4.

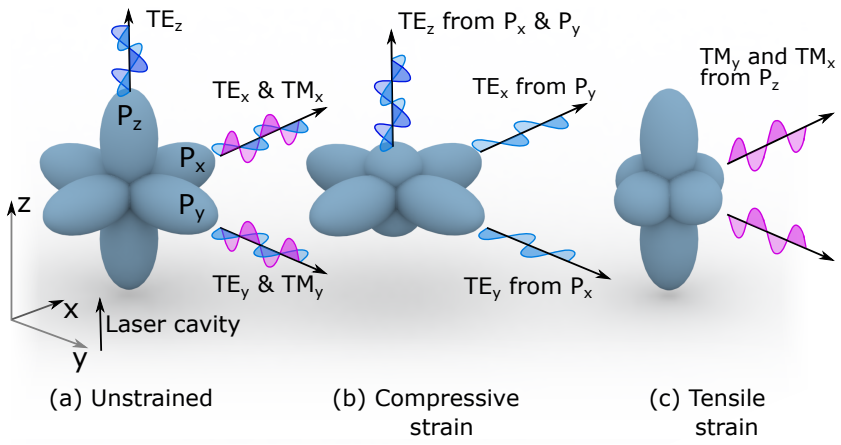

Figure 2.4: P-orbitals of holes at the valence band edge, with the direction of light propagation (laser cavity) indicated for a vertically-emitting semiconductor laser. For VECSEL devices, TE polarised light (indicated blue) propagating along the z-axis is required. Unstrained material (a) provides similar gain for light propagating along each axis, while adding compressive strain (b) is desirable for the maximisation of TE-polarised gain at the expense of TM; while tensile strain (c) enhances the TM-polarised gain (TM polarised light indicated pink).

It can be seen that for an unstrained material that recombination is divided almost equally between x-, y- and z-directions. For vertical cavity lasers, the gain for light propagating along the z-direction should be maximised, and this is shown to be the case for compressive strain in Figure 2.4 (b), where TM polarised gain from the P_z orbital is restricted, enhancing TE polarised gain for both horizontal and vertical emission. Figure 2.4 (c) shows how tensile strain enhances the P_z orbital and favours horizontal emission of TM polarised light, the antithesis of what is required for a vertical emission laser.

The energy shift due to hydrostatic deformation δE_{hy} and shear deformation δE_{sh} can be defined as:

$$\delta E_{hy} = -2a\frac{1 - C_{12}}{C_{11}}\epsilon \tag{2.4}$$

$$\delta E_{sh} = -2b\frac{1 - C_{12}}{C_{11}}\epsilon \tag{2.5}$$

where a and b are the hydrostatic and shear deformation potentials, and C_{11} and C_{12} describe elastic stiffness.

As strain increases in a semiconductor material, at a critical thickness where the elastic

strain energy is above the energy of dislocation formation [5], misfit dislocations and defects within the lattice structure begin to form causing errors in growth, lowering material quality and device lifetime in low quantity, and causing device failure in high quantity. Thus, in order to benefit from the advantages of strain, techniques for the accommodation of strain within the gain structure must be used.

2.2.3 Accommodating strain

Strained QWs are often incorporated into designs to lower threshold and increase differential gain [4,6] by reducing effective mass at the top of the valence band, and reshaping the valence-band p-orbitals to maximise contributing holes in the valence band. This makes strain an important factor to implement into advanced VECSEL designs. Tensile strained QWs favour TM-polarised emission due to the prominence of the light-hole valence band (discussed in Section 2.2.2) which is unusable for vertically-emitting structures [7], while compressive strain favours TE-polarisation. Use of material strain in the active region and overall structure, however, can be detrimental to growth quality and processing, producing cracks and dislocations that act as non-radiative carrier recombination centres.

Strain balancing has been shown to improve both, and involves using material of opposing strain to counteract and balance the material strain introduced by other layers. Strain balancing can also increase device lifetime as the number of defects from growth are reduced [8]. The calculations for strain balancing are discussed by Ekins-Daukes et al. in ref [8], summarised below.

The most basic method of strain balancing is through comparing the strain-thickness products of the compressive and tensile materials, known as the average lattice method. This is extended by adding terms for thickness weighting and differences in elastic constant to be the thickness weighted method, described by Equations 2.6 & 2.7.

$$a_0 = \frac{(A_1 t_1 + A_2 t_2)\, a_1 a_2}{A_1 t_1 a_1 + A_2 t_2 a_2} \tag{2.6}$$

$$0 = t_1 \epsilon_1 + t_2 \epsilon_2 \tag{2.7}$$

where a_0, a_1 and a_2 are the lattice parameters of the substrate material and strained materials respectively, t_1 and t_2 the strained material thicknesses, layer strain ϵ is defined as $\epsilon_x = (a_0 - a_x)/a_x$, and elastic parameter A_x is defined for material x in Equation 2.8 below.

$$A_x = C_{11_x} + C_{12_x} - \frac{2C_{12_x}^2}{C_{11_x}} \tag{2.8}$$

with C_{11_x} and C_{12_x} the material stiffness coefficients.

Ekins-Daukes et al. develop a further 'zero stress' method for achieving zero average in-plane stress in the layer combination. They derive Equations 2.9 & 2.10 below for achieving this.

$$a_0 = \frac{A_1 t_1 a_1 a_2^2 + A_2 t_2 a_2 a_1^2}{A_1 t_1 a_2^2 + A_2 t_2 a_1^2} \tag{2.9}$$

$$0 = t_1 A_1 \epsilon_1 a_2 + t_2 A_2 \epsilon_2 a_1 \tag{2.10}$$

There are two methods of integrating strain balancing of QWs within a multi-QW active region. Using slightly tensile strained barriers around the QWs is the simplest, as strain balancing may be achieved without significantly changing material composition and therefore refractive index or energy band-gap [9–12].

An alternative is to use additional layers with thickness similar to the QWs positioned at the field nodes[13–15]. This uses a higher strain composition material. There is no definitive empirical or theoretical report of the advantages of one strain balancing design technique over the other, however recent publications for VECSEL structures from several research groups working on growth tend towards the use of additional strain balancing layers rather than adding strain to barriers [13,16,17], with the suggestion that these designs increase the ease of the semiconductor growth compared to those with low-strain barrier material.

Strain is also a key concern in any material that will be released from the substrate, and careful management of lattice matching or strain balancing can produce films that retain structural integrity despite having a thickness of <2 μm, as in the thin-film VECSELs discussed in the next chapters.

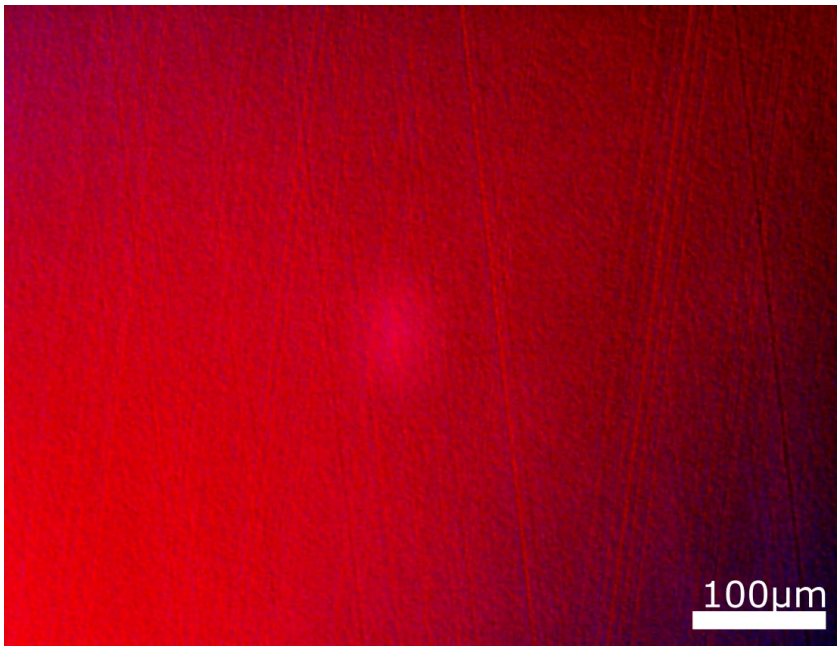

Figure 2.5: Visible microscope image of the surface of a AlP/AlGaAs DBR, with materials designed to be strain balanced. Cross-hatching of surface indicates misfit dislocations.

2.2.4 Temperature dependence

Several properties of semiconductor materials have a temperature dependence, the most intuitive of which is the lattice size a_0 (thermal expansion of materials), which is caused by increased atomic vibration which in turn increases lattice spacing. This can hinder fine strain balancing in semiconductor growth, as growth temperatures in excess of 200 °C can result in material strain during growth such that the critical thickness of the material is exceeded, causing misfit dislocations and growth failure. Such an effect was seen in the attempted growth of a strain balanced AlAsP/AlGaAs distributed Bragg reflector (DBR); a visible microscope image of the resulting wafer is shown in Figure 2.5. The cross-hatched surface indicates growth errors within the lattice structure, caused by the strain introduced by the different thermal expansions of AlAsP and AlGaAs at growth temperature.

Another parameter subject to temperature dependence is the band-gap, both due to the increased lattice spacing and interaction between electrons/holes and lattice phonons.

This shift is described by the empirical Varshni expression [18]:

$$E_{gap}(T) = E_{gap}(0) - \frac{\alpha T^2}{T + \beta} \tag{2.11}$$

where $E_{gap}(T)$ is the band-gap energy at temperature T, and α and $beta$ material parameters.

2.2.5 Refractive index calculation

Fundamental to the design of vertical semiconductor laser structures is the accurate calculation of optical path length, for the correct positioning of layers at nodes/antinodes of the laser mode E-field as required. For this, the refractive index n must be calculated as optical path length is defined as the product of layer refractive index and layer thickness.

As a very rough approximation, refractive index varies inversely to energy band-gap (for photon energy below the band-gap). The reality is significantly more complex, but for a basic visualisation this can suffice – observing the energy band-gaps of binaries in Figure 2.1 shows, for example, the high- and low-n materials within the $Al_xGa_{1-x}As$ material system, notably used for AlGaAs/AlAs DBR mirrors.

Actual refractive index plots are found in the literature from fits to experimental data. For ternary and quaternary materials there may be papers with extrapolated values (e.g. for AlGaAs and [19] InGaAsP [20]) but often it is necessary to interpolate between two or three binaries to find a value for ternary or quaternary materials.

2.3 Quantum well emission

A QW is a layer where the thickness of the potential well is restricted in one dimension to the order of the electron wavelength, causing quantisation of the conduction- and valance-band energy levels. By adjusting the thickness of the QW, on the order of

nanometres, the transition energy of the QW can be designed, with energies higher than the material band-gap.

The standing wave within a QW is described as a simple harmonic oscillator in the time-independent Schrödinger equation, a differential equation that describes quantum systems. In its generalised form, the Schrödinger equation is given as:

$$E\Psi = \hat{H}\Psi \tag{2.12}$$

where the Hamiltonian operator $\hat{H}$ acts on a wave function Ψ, the result is Ψ multiplied by the energy of state Ψ.

For a harmonic oscillator, $\hat{H}$ is described by Equation 2.13

$$\hat{H} = \frac{\hat{p}^2}{2m} + \frac{1}{2}m\omega^2 x^2 \tag{2.13}$$

with m the particle mass, ω angular frequency, x position and $\hat{p}$ the momentum operator given in Equation 2.14.

$$\hat{p} = -i\hbar\frac{\partial}{\partial x} \tag{2.14}$$

2.3.1 Schrödinger equation ground state solution

For an even standing wavefunction the eigenequation for a finite QW, shown in Figure 2.6, can be described by:

$$\alpha = \frac{m_b}{m_w} k \tan\left(\frac{kL}{2}\right) \tag{2.15}$$

where m_b is the effective mass in the barrier material, m_w the effective mass in the QW, L is the QW thickness. α and k are given as:

$$\alpha = \frac{\sqrt{2m_b(\Delta E - E)}}{\hbar^2} \tag{2.16}$$

$$k = \frac{\sqrt{2m_w E}}{\hbar^2} \tag{2.17}$$

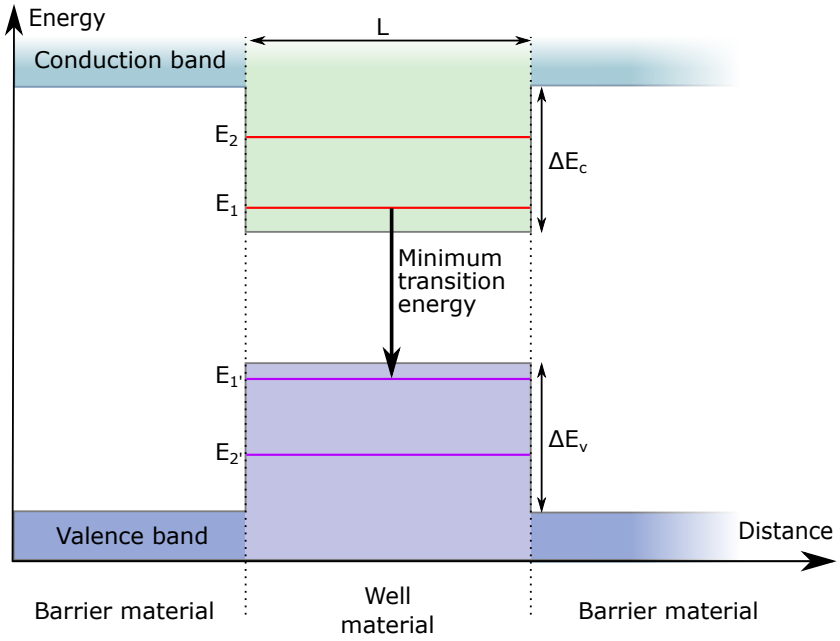

Figure 2.6: Schematic diagram of a finite QW. ΔE_c and ΔE_v are the energy band-gap differences between barrier and well material in conduction and valence bands respectively, L is the thickness of the well, and E_1 and E_2 the first two solutions of the Schrödinger equation for charge carriers in the conduction band (and correspondingly $E_{1'}$ and $E_{2'}$ solutions for carriers in the valence band).

where E is the ground state eigenenergy, ΔE is the depth of the QW and $\hbar$ the reduced Planck constant.

By substituting α and k (Equations 2.16 & 2.17) into Equation 2.15, we can rearrange to an equation from which the solutions provide the eigenenergy for the conduction and valence bands of the QW, with m_b and m_w corresponding to effective masses of electrons or holes for their respective bands:

$$\frac{m_b}{m_w} E \tan^2\left(\sqrt{\frac{m_w E}{2}} L\right) + E - \Delta E = 0 \tag{2.18}$$

Other solutions describe higher energy states, with the first of these (E_2 and $E_{2'}$ for conductive and valence bands respectively) shown in the schematic of the quantum well in Figure 2.6. As discussed in the previous sections, an accurate calculation of the QW transition energy requires the incorporation of material strain and thermal effects, and this is discussed in-depth in Chapter 3 within the context of the II-VI QW simulation. Implementation of this for simulation purposes within Mathcad is given

in Appendix A.

2.4 Multi-layer structures

For the design of the VECSEL structures, the theory of electromagnetic wave propagation through multi-layer stratified dielectric media is used, as described by Born and Wolf [21].

For the calculation, each layer is considered as a thin dielectric film with uniform dielectric constants. The effect on a wave travelling through each layer can be described by a characteristic matrix. For light of wavelength λ entering a layer at incidence angle θ, with thickness t_{layer} and refractive index n_{layer}, this matrix is given by M_{layer}.

$$M_{layer} = \begin{bmatrix} A & B \\ C & D \end{bmatrix} = \begin{bmatrix} \cos(\beta) & -\frac{i}{\eta}\sin(\beta) \\ -i\eta\sin(\beta) & \cos(\beta) \end{bmatrix} \tag{2.19}$$

where $\beta = 2\pi/\lambda n_l t_l \cos(\theta)$, and $\eta = n\sqrt{\epsilon/\mu}$ with ϵ and μ permittivity and permeability respectively.

For multilayer structures, the cumulative effect of the layers can be calculated by the product of their successive characteristic matrices, so for a structure with m layers:

$$M_{multilayer} = \prod_{k=1}^{m} M_k \tag{2.20}$$

From $M_{multilayer}$ the reflection r and transmission t coefficients of the structure can be calculated.

$$r = \frac{(A + Bn_{exit})n_{incidence} - (C + Dn_{exit})}{(A + Bn_{exit})n_{incidence} + (C + Dn_{exit})} \tag{2.21}$$

$$t = \frac{2n_{incidence}}{(A + Bn_{exit})n_{incidence} - (C + Dn_{exit})} \tag{2.22}$$

where $n_{incidence}$ is the refractive index of the material from which the light is incident, and n_{exit} the refractive index of the material after the multilayer structure.

Reflectance R and transmittance T can then be found:

$$R = |r|^2 \tag{2.23}$$

$$T = |t|^2 \tag{2.24}$$

2.4.1 Simulation of stratified media

To design vertical emission structures it is useful to simulate the resultant optical standing wave within the structure, for QW placement in vertical gain structures or the placement of other active region or DBR layers. This is calculated using the characteristic matrices M as defined in Equation 2.20, with M changing as the simulation moves through the system.

To produce a clear image, each layer is split into a number of different identical layers, to increase resolution of the resultant field. A loop performs the calculation for the E-field E_k for each resultant $M_{multilayer}$.

$$E_k = |Q_k|^2 = \left| M_k \cdot M_{k-1} \ldots \cdot M_0 \cdot \begin{bmatrix} (1+r)/n_{incidence} \\ 1-r \end{bmatrix} \right|^2 \tag{2.25}$$

For the k^{th} layer in the stack, the characteristic matrix M is calculated for the entire structure to that point and multiplied by the initial field, a function of r and $n_{incidence}$. Plotting E_k with the corresponding thicknesses provides a spatial view of a standing wave E-field within the stack, e.g. for a DBR, shown in Figure 2.7. An example loop used for the simulation in Mathcad 15 to produce Figure 2.7 is given in Appendix B.

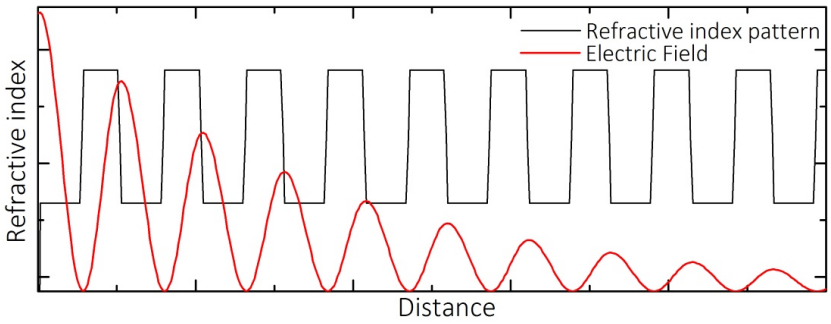

Figure 2.7: Example of the E-field simulation (red) for a DBR (black). Each layer has been split into 20 for the purpose of visualisation, and further division of layers would raise the quality further, decreasing the visible slopes from the refractive index pattern.

2.5 DBR design and limitations

The DBR is one of the simplest sub-wavelength structures, and key to the gain-mirror VECSEL structure. By placing pairs of high and low refractive index material in a stratified structure, each layer being $\lambda/4n$ in thickness, mirrors with reflectivity in excess of 99.9% can be obtained. VECSEL structures are low gain devices and as such are very sensitive to loss, so a high reflectivity mirror must be used to limit the loss of light into the substrate.

DBR mirror reflectivity increases with pair number as the stack's resonances increase. Figure 2.8 shows simulation of a DBR mirror with increasing pair numbers, demonstrating diminishing returns with increasing pair number. It shows how the stop-band shape changes with increasing pair number, shortening in effective wavelength range as it increases in peak reflectivity.

For the simulation, an $Al_{0.45}Ga_{0.55}As$/AlAs DBR was used, with layer thicknesses 49 nm and 56 nm respectively. Refractive index contrast is 0.38 at the stopband centre 675 nm.

Pair numbers required to achieve a certain reflectivity reduce with increased refractive index contrast of the layers, so this should be maximised if possible. Care must be taken however to keep the DBR layer material quality as high as possible, as the active region will (in standard VECSEL growth) be grown on top of the DBR. Material should have as little strain as possible, as there is a significant thickness involved with the

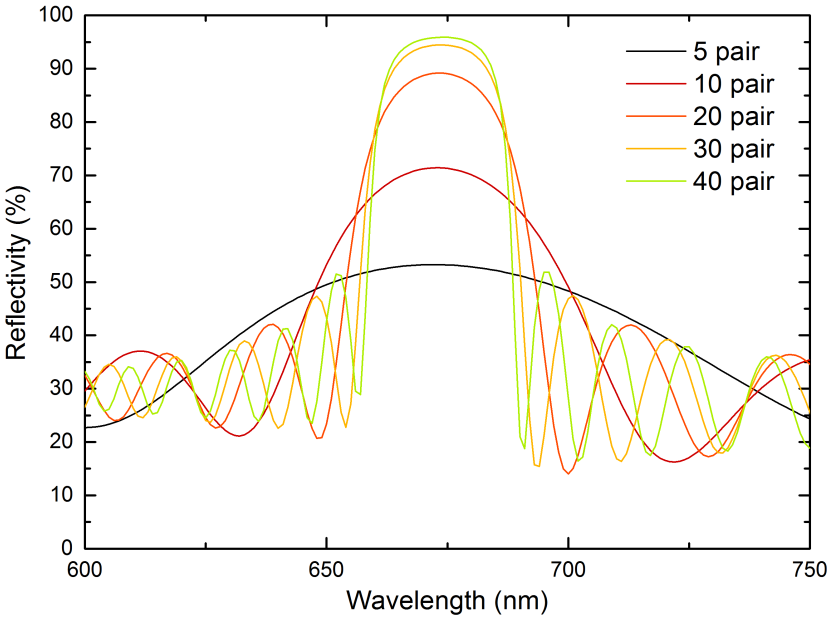

Figure 2.8: Example reflectivity of a DBR for 5, 10, 20, 30 and 40 pairs. The graph shows the diminishing returns with increasing pair number, along with a narrowing of the DBR stopband with increasing pair number.

DBR layers (at risk of being higher than the critical thickness of the material), and without sacrificing lattice structure. The higher refractive index layer must be designed not to absorb the device wavelength, a possibility for layer compositions picked in material systems with limited refractive index availability.

The thickness of a full length DBR depends on the refractive index contrast, but is in the order of multiple micrometres, making up the majority of the VECSEL structure length.

For material systems such as the II-VI ZnCdMgSe, all the above considerations are barriers to the use of full high-reflectivity DBRs. Ensuring that the DBR layers do not absorb the QW emission limits the composition of the high-n layers, and so the maximum refractive index, while the minimum refractive index of the low-n layer is limited by the rock-salt lattice structure of MgSe causing dislocations for high Mg-content material. Growth quality limits the number of layers that can be grown, so an alternative to the gain-mirror VECSEL design must be used for ZnCdMgSe (followed up in Section 2.8 and discussed in Chapter 3).

2.6 VECSEL structures and layer placement

The basic structure of a VECSEL as described in Chapter 1 consists of a number of QWs placed within barriers at positions corresponding to the antinodes of a standing wave of the laser wavelength for resonant periodic gain (RPG). By combining the stratified media simulations described in Section 2.4 with material properties and QW design as described in Sections 2.2 and 2.3 respectively, layer placement can be optimised in the VECSEL design.

The most simplistic design incorporates QWs emitting at wavelength λ, positioned at path lengths of λ/2 apart, with pairs of λ/4 material to act as a DBR mirror.

Incorporating elements such as strained QWs and strain balancing layers, discussed in sections 2.2.2 and 2.2.3, and temperature into the model are crucial for more advanced and efficient designs

2.6.1 The Kuznetsov model of VECSEL performance

The expected output performance for a VECSEL can be calculated and was modelled by Kuznetsov [22], and for known material parameters the model allows for calculation of expected gain, threshold and efficiency of designed structures. Gain g is defined as:

$$g = g_0 \ln\left(\frac{N}{N_0}\right) \tag{2.26}$$

with g_0 the material gain coefficient, carrier density N and transparency carrier density N_0. The laser threshold is reached when gain equals the total losses of the VECSEL structure. The gain at threshold, g_{th}, is thus defined:

$$R_{ext}R_{rear}T_{loss}e^{(2\Gamma g_{th}N_w L_w)} = 1 \tag{2.27}$$

with R_{ext} the reflectivity of the external cavity mirrors, R_{rear} the reflectivity of the rear mirror (normally the DBR), T_{loss} the transmission of the output coupling or loss from

the cavity, Γ the longitudinal confinement factor defined by the RPG configuration [23], N_w the number of QWs in the gain medium, and L_w the QW thickness.

N is dependent on pump power P_{pump} and is described in Equation 2.28:

$$N = \frac{\eta_{abs} P_{pump}}{E_{ph} N_w L_w A_{Pump}} \tau(N) \tag{2.28}$$

where η_{abs} is pump absorption efficiency, E_{ph} photon energy, A_p pump spot area and $\tau(N)$ carrier lifetime, itself a function of carrier density given in Equation 2.29:

$$\tau(N)^{-1} = A + BN + CN^2 \tag{2.29}$$

where A, B and C are the monomolecular, bimolecular and Auger recombination coefficients.

Combining Equations 2.26–2.29 gives expressions for the threshold carrier density N_{th} and for the threshold pump power P_{th}:

$$N_{th} = N_0 \left(\frac{1}{R_{ext} R_{rear} T_{loss}} \right)^{(2\Gamma g_0 N_w L_w)^{(-1)}} \tag{2.30}$$

$$P_{th} = N_{th} \left(\frac{E_p N_w L_w A_{pump}}{\eta_{abs} \tau(N_{th})} \right) \tag{2.31}$$

Output power of the VECSEL is then given as a function of P_{pump}, P_{th}, η_{abs}.

$$P_{VECSEL} = (P_{pump} - P_{th}) \eta_{abs} \eta_{out} \eta_{defect} \tag{2.32}$$

with the output efficiency η_{out}, and the quantum defect efficiency η_{defect} defined in Equations 2.33 & 2.34:

$$\eta_{out} = \frac{\ln(R_{rear})}{\ln(R_{ext} R_{rear} T_{loss})} \tag{2.33}$$

$$\eta_{defect} = \frac{\lambda_{pump}}{\lambda_{VECSEL}} \tag{2.34}$$

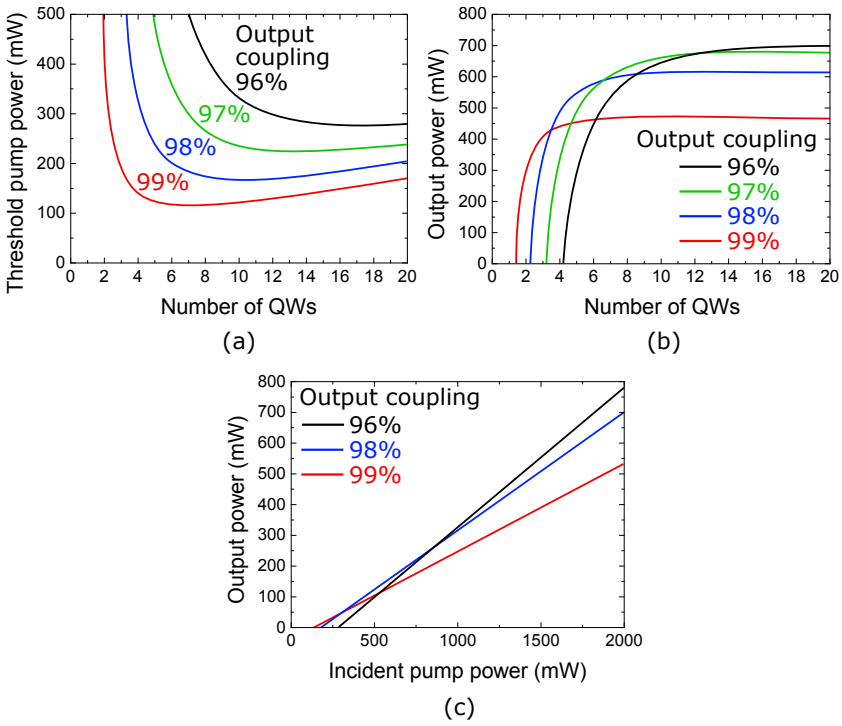

Figure 2.9: Example of the calculations for an InGaAs QW VECSEL based on the example and material specifications in ref. [22]. (a) Threshold pump power for QW numbers for a VECSEL with various output coupling coefficients. (b) VECSEL output power for 1.8 W pump. (c) Power transfers for 96%, 98% and 99% output couplings for a 14 QW VECSEL structure.

For material with known coefficients of gain, transparency carrier density, monomolecular, bimolecular and Auger recombination and pump absorption efficiency, along with a known cavity arrangement, the pump power threshold and output power may be calculated. Through these calculations, the optimal number of QWs and output coupling may be determined for VECSEL devices, and an example of the results of this calculation is shown in Figure 2.9 for an InGaAs QW VECSEL. With threshold reaching a minimum and then increasing with QW number, with a similar effect in output power at a set pump power, a compromise must be reached based on the target output coupling. It can be seen that for this example device operating with 96% or 97% output coupling, an optimum QW number of 12-14 provides a compromise between threshold at lower output couplings and output power.

2.6.2 Designing for temperature effects

Temperature affects semiconductor properties significantly, as described in Section 2.2.4. Previously the effects of this on strain during growth have been given, but in a VECSEL the shift in bandgap with temperature is crucial to model, with the structure temperature increasing when pumped.

Fundamental to designing the VECSEL structure with thermal effects in mind is to understand the shifting properties underlying them. As temperature increases within the structure, both the QW emission wavelength and the RPG wavelength will shift, but at different rates. RPG wavelength is affected mostly by the thermal expansion of the lattice, with the increase in optical path length between wells resulting in an increase in wavelength.

QW peak gain wavelength increases as a result of several factors, the most significant of which is the band-gap shift in the QW material, altering QW transition energy. QW thickness is also altered slightly through the expansion of the lattice.

The QW peak gain wavelength shifts significantly faster than the RPG and sub-cavity resonance wavelengths, so while the temperature increase induced by pumping will redshift both the subcavity resonances and the QW gain, the overlap (and thus observed resonance-enhanced PL) will change with temperature, as shown in Figure 2.10. An increase beyond the temperature of peak operation (shown Figure 2.10 (b)) reduces the overlap between the QW peak emission and the oscillation wavelength of the laser, the RPG and subcavity wavelengths no longer match the material gain and there is a reduction of efficiency until laser action is impossible (Figure 2.10 (c)). This is known in a working laser as thermal rollover and acts as one of the main power limitations for the VECSEL.

If the design does not take this thermal shift into account, this rollover can occur before threshold is reached, causing a non-working laser. To avoid this an offset is introduced to the design, with QW wavelength blue-shifted from the target wavelength [24]. The size of the offset will depend on the QW shift rate with temperature for that material.

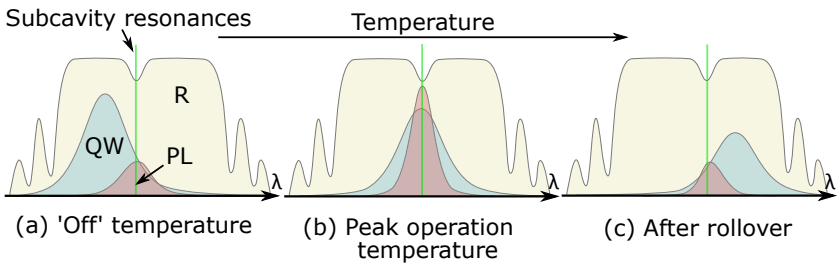

Figure 2.10: The observed PL (red peak) and how it corresponds to the dip in the DBR reflectivity R (yellow area) corresponding to the subcavity resonance, RPG wavelength for a resonant design (green line) and QW emission (blue peak). Under pumping, the QW emission, RPG wavelength and subcavity resonances redshift at different rates, from the positions shown in (a) to the peak operational temperature of (b), and finally to the thermal rollover point (c).

2.6.3 Pump absorption

There are two methods for optical pump absorption in the active region, barrier pumping and in-well pumping [25]. In-well pumping for a vertical gain region is limited by the short absorption length, requiring multi-pass pumping schemes; however VECSELs have been reported using this pumping method (e.g. GaAs QW VECSELs [26,27]). This pump absorption scheme has the significant advantage of decreasing the quantum defect of the device, (i.e. the energy difference between the pump photons absorbed and the photons emitted from the lower energy-states in the potential well). increasing wall-plug efficiency, reducing heat build-up and easing the requirements for thermal management.

The standard approach is barrier pumping of the material, which does introduce a more significant quantum defect, however the pump light is efficiently absorbed within a short distance.

Absorption is modelled as an exponential decay, and the pump absorption length dictates the number of available antinodes in which to situate QWs; ensuring that all wells are pumped sufficiently is essential. If the pump absorption length is too short, there will not be enough antinodes for single or even pairs of QWs, and more wells per antinode are required, e.g. for GaN diode (blue) pumped AlGaInP VECSELs [28].

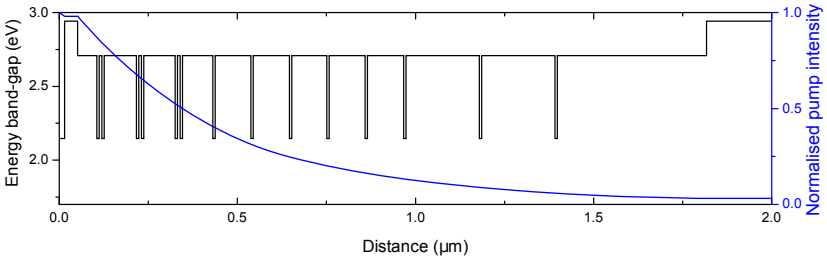

Figure 2.11: Example VECSEL active region with QWs positioned to spread carrier distribution between each well more uniformly. Material parameters are taken from II-VI materials described in Chapter 3. Normalised pump intensity is shown in blue.

The pump absorption profile can inform the non-uniform distribution of QWs through the structure, resulting in a higher number of QWs positioned towards the top surface of the structure for a more equal carrier distribution across the active region. This has been demonstrated to improve efficiency significantly, Baumgärtner et al. reporting a 20% rise when using a front stacked system compared to a uniform QW distribution [13]. Shown in Figure 2.11 is a stacked active region designed for better carrier distribution.

2.6.4 VECSEL design

Each of these features is collected to form the design of the VECSEL gain structure (Fig. 2.11). The design process begins with the choice of QW material that can produce a transition energy at the target wavelength λ_t. Barrier material that is close to being lattice matched to the growth substrate must be available, with an absorption length of several antinodes (10) for the pump light.

The number of QWs is calculated using the Kuznetsov model of VECSEL gain, as discussed in Section 2.6.1. A non-uniform distribution of QWs has been shown to be advantageous, as discussed in Section 2.6.3, although this is not a requirement for a working VECSEL.

QW emission is designed to account for the thermal redshift discussed in 2.6.2, and is normally around 10-15 nm lower in wavelength than λ_t. Barrier layer thickness

$T_{barrier}$ for the QW placement will be:

$$T_{barrier} = \frac{\lambda_t - L_{space}}{2n_b} - \frac{N_{QW}L_{QW}}{n_w} \tag{2.35}$$

where n_b is the barrier layer refractive index, n_w the QW refractive index, L_{space} the QW spacing (if using more than one QW per antinode), N_{QW} the number of QWs per antinode, and L_{QW} the QW layer thickness.

The final layers of the structure to be grown will be the last barrier layer, the carrier confinement window layer (with energy band-gap higher than the barriers) and anti-oxidation cap. The thickness of the carrier confinement window can be adjusted to produce a resonant or anti-resonant subcavity, both of which can have advantages depending on the mode of laser operation. The resonant cavity structure, where the optical standing wave has an antinode at the epitaxial surface, has the advantage of the resonance enhancing the magnitude of the optical field in the subcavity at λ_t, thus reducing the threshold. An anti-resonant structure has a node at the epitaxial surface, and so does not have this enhancement, but benefits by having a broader, more homogeneous gain profile for reduced temperature sensitivity [29] and for wide tuning, desirable for short pulse operation [30,31]. A full discussion of resonant and anti-resonant VECSEL gain structure designs is reported in ref. [32]. The top barrier must have an interface at the node of the standing wave, and thickness is given as half of Equation 2.35, $T_{barrier}/2$. The anti-oxidation cap layer must have sufficient thickness to stop oxidation of the structure but should normally be kept to a minimum as it may be absorptive for λ_t; 10-20 nm is typically used. Finally the window layer has thickness given by Equation 2.36.

$$T_{window} = \frac{q\lambda_t}{4n_{window}} - \frac{T_{cap}}{n_{cap}} \tag{2.36}$$

where T_{cap} and n_{cap} are the cap thickness and refractive index respectively, n_{window} is the window layer refractive index, and q is an odd integer number for a resonant subcavity, and an even integer number for an anti-resonant subcavity.

The substrate-side of the QW region should be long enough to absorb the pump fully,

while not being overly long to transport carriers away from the wells. This region can be split with a carrier confinement window if this is believed to be a concern. The layer should end on an antinode for the beginning of the DBR, and so the thickness is described as:

$$T_{barrier\_end} = \frac{p\lambda_t}{2n_b} - \frac{N_{QW}L_{QW}}{2n_w} \tag{2.37}$$

where p is an integer value.

DBR layers are then included as described by Section 2.5, beginning with the low-n layer in $\lambda_t/(4n_l)$ pairs, with n_l the layer refractive index.

Integrating strain balancing layers initially requires calculation of the required layer thicknesses for strain balancing each QW pair using the zero-stress method described in Section 2.2.3. These layers are then inserted into the subcavity within the barrier material, with appropriate reduction in barrier length. For the addition of a strain-balance layer of thickness T_{SB} in one of the barrier layers, each barrier layer thickness between the QWs should be modified to:

$$T_{barrier2} = \frac{T_{barrier}n_{barrier} - T_{SB}}{2n_{barrier}} \tag{2.38}$$

By combining the calculations in Equations 2.35–2.38, a design for the VECSEL structure can be produced. Shown in Figure 2.12 is a resonant VECSEL subcavity design with strain balancing, 10 pairs ($N_{QW} = 2$) of QWs uniformly distributed, with a window layer below the anti-oxidation cap at the epitaxial surface but no carrier confinement layer towards the DBR.

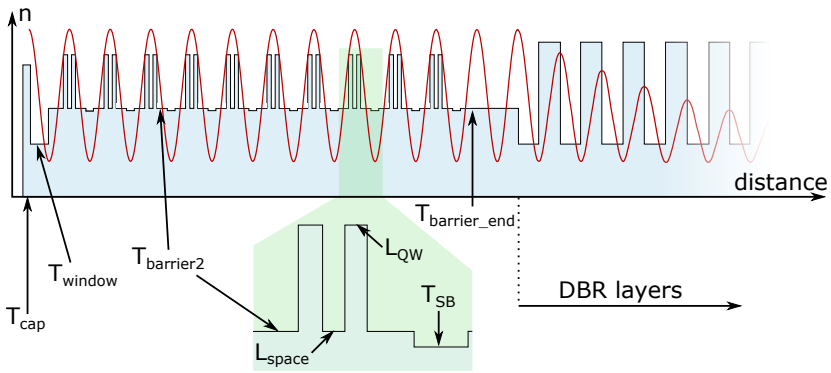

Figure 2.12: Schematic plot of refractive index profile, n, of an example VECSEL structure, with the corresponding thickness parameters from Equations 2.35–2.38 indicated. The structure consists of 20 QWs, placed uniformly in pairs at 10 antinodes. The structure is designed to be resonant, with an antinode placed at the epitaxial surface to the left of the diagram. In this case there is no window layer prior to the DBR.

2.7 Thermal management of VECSEL devices

As described in Section 2.6.1, thermal rollover acts to limit the maximum power output of VECSELs; although, by increasing pump spot and laser mode size while keeping power density constant, this limit can be delayed to an extent. To counter this effect, thermal management schemes to cool the laser region are necessary [33]. There are 3 methods of thermal management currently in use: connecting the substrate to a cooled heat-sink; thinning the substrate and connecting it to a heat-sink to aid in heat extraction (known as a 'thin-device'); and use of a capillary-bonded intracavity heat spreader to spread the heat for extraction from a larger area of substrate. Thinning and heat spreader thermal-management schemes are detailed in Figure 2.13.

The more efficient of the two depends on the material system and cavity layout [34]. For devices with a low thermal conductivity DBR such as those emitting in the visible part of the spectrum, the transparent heatspreader approach is preferable with a high thermal conductivity material such as diamond (high optical transmission and a high thermal conductivity in the order 2 W/(cm K) [35]). For devices which have short pump absorption lengths, the majority of the heat will be deposited near the surface, increasing the efficiency of heat-spreaders over the thin devices. For lasers with a large pump spot and DBR with low thermal resistivity, a thin device thermal management

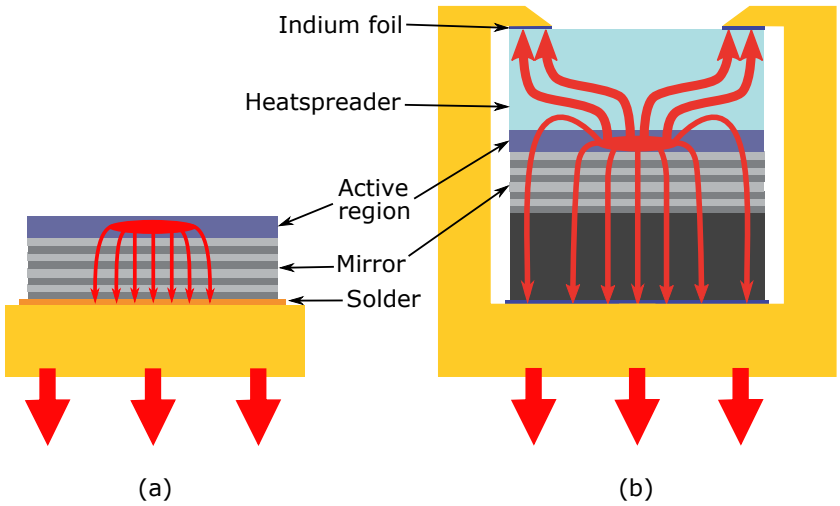

Figure 2.13: Illustration of thermal management schemes, (a) thin-device and (b) heatspreader, with red arrows indicating the transfer of heat. Reproduced from ref. [7]

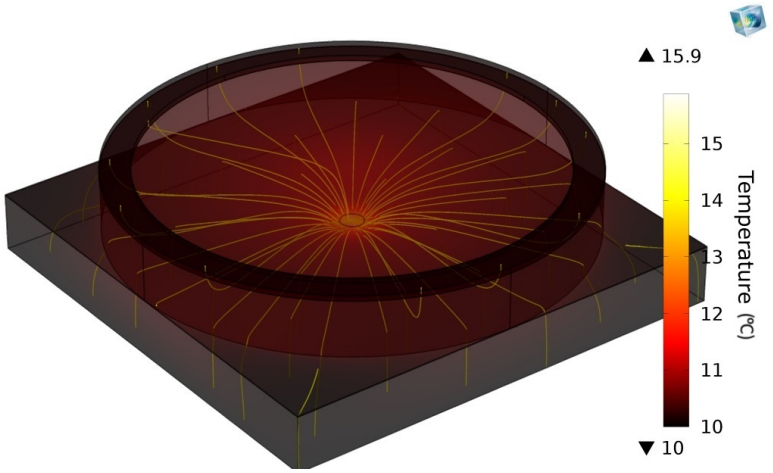

Figure 2.14: Simulation of a 4x4mm square sample of 7 µm-thick AlGaAs on 500 µm-thick GaAs, with a 500 µm thick diamond heatspreader. A mount is simulated by setting the bottom face of the substrate and the rim of the top diamond to 10 °C. Yellow lines indicate the paths that the heat takes to leave the structure, the majority passing down through the substrate. Simulated using COMSOL 5.0

scheme is preferable, as the heat transport is effectively 1 dimensional to the heat-sink [35]. The path of heat extraction for a heatspreader system, as indicated in Figure 2.13 (b), is simulated in Figure 2.14 using finite element analysis for a 4x4mm square sample of 7 µm-thick AlGaAs on 500 µm-thick GaAs, with a 500 µm thick diamond heatspreader.

This simplified model provides comparison for the effects of diamond heat-spreaders,

and shows that the heatspreader has a significant effect on device temperature. Simulation of 1 W of heat provided by a pump laser, radius 50 μm with Gaussian beam profile, is shown in Figure 2.15, where the maximum temperature rise in the gain region is 88, 44, and 16 °C for the heatsink only, thinned device, and diamond heatspreader respectively

Simulations indicate an expected temperature increase of 16 °C for the heat-spreader structures for higher pump powers of 1 W, which would correspond to an offset of 5 nm for InGaAs QWs with a thermal shift of 0.3 nm/°C [36] for optimum operation at this power.

Accounting for realistic heat transfer, imperfect capillary bonding of heatspreader, thermal resistance caused by structure layers etc. means that this temperature increase is likely an underestimate.

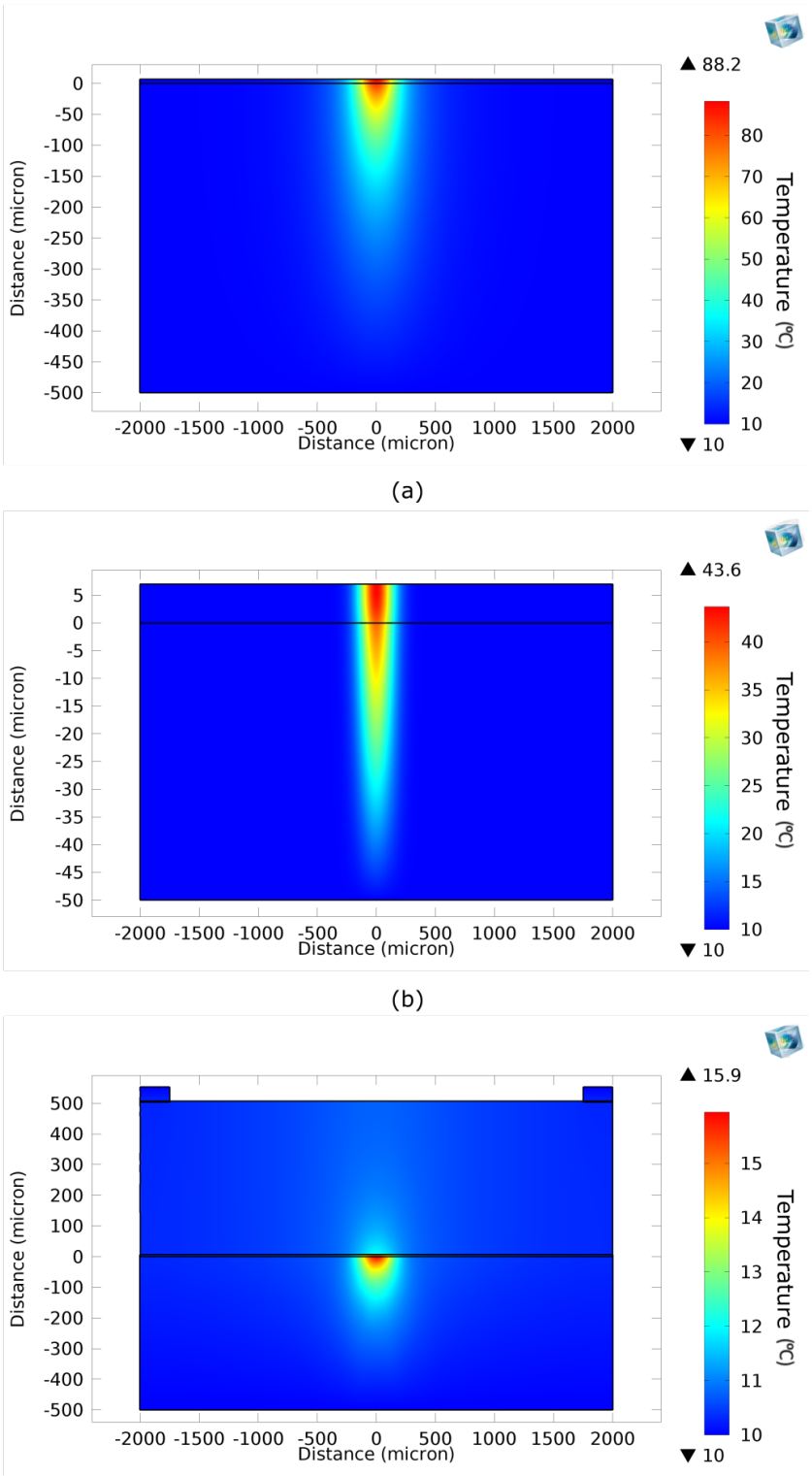

Figure 2.15: COMSOL 5.0 simulation for an AlGaAs layer pumped with 1 W with Gaussian pump spot radius 50 µm. (a) Sample on heat-sink, (b) thin-device sample with substrate thinned to 50 µm, (c) device with an intracavity diamond heatspreader.

2.8 Design challenges and thin-film devices

The material properties of the ZnCdMgSe system are challenging when considering the typical design of VECSEL gain structures, i.e. multi-quantum well gain region and monolithic DBR, as described earlier in the chapter. Challenges in maintaining material growth quality for the high number of periods necessary for a II-VI DBR, potentially 40-50 periods due to a relatively low refractive index contrast available, lead to the compromise that the VECSEL structure designs must consist of only the active region.

Alternatives to the monolithically-grown DBR can be considered: a high reflectivity coated dielectric mirror on the diamond heat-spreader; a dielectric coated mirror on the sample surface – preferably not between heat-spreader and sample as this would impede thermal transfer away from the pumped region of the structure; wafer bonding of a separately grown DBR to the sample surface (ie. through the wafer fusion process as in refs. [37–39]); mirrors entirely separated from the gain region, with the cavity adjusted for mode matching to the pump at the structure.

All three possibilities rely on light propagating through the rear of the epi-layer, however the absorption of InP in the visible spectrum renders this impossible while the substrate is still present. In fact, both the InGaAs and low-temperature ZnCdSe buffer layers also absorb at the design wavelengths. To this end, the epi-layer and at least the InGaAs buffer layer must be removed from the substrate to allow vertical emission from a ZnCdMgSe-based laser.

While thin-films can provide a possible route to the demonstration of a II-VI ZnCdMgSe visible VECSEL, thin-film VECSEL devices in general could potentially provide advantages over the gain-mirror devices:

- access to both ends of the gain region allows for possibilities such as double-end pumping to enable more uniform pumping of the gain region and the spreading of temperature rises;

- rear output coupling, where there is a new usable output to the two- or three-mirror VECSEL cavity and cavity setups may be constrained on one side of the gain region;
- rear output coupling, where there is a new usable output to the two- or three-mirror VECSEL cavity and cavity setups may be constrained on one side of the gain region;
- multi-gain region devices, where rather than multiple gain-mirror devices, layered devices or additional gain regions placed within cavity foci can be used;
- external cavity ring/travelling wave cavities (although demonstrated for gain-mirror VECSELs [40]), used in devices such as optical gyroscopes and intracavity non-linear applications where single passes are desirable, could be achieved using the thin-film as a gain region;
- novel cavity designs that would normally require the VECSEL gain region to be on a low angle fold in the cavity.

2.8.1 Thermal considerations in a thin-film design

The largest challenge for a thin-film VECSEL is thermal management, even more than for a gain-mirror VECSEL which has laminar heat-flow through the semiconductor substrate and simply requires the diamond to spread the heat across the structure. The thin-film VECSEL requires a thermal management system that allows for optical transmission from both surfaces, therefore a cooling mount is used that meets these requirements, shown in Figure 2.16.

A significant difference between the standard cooling schemes and the thin-film cooling scheme is that the thin-film must remove all heat through the contacts at the diamond edges. The high thermal conductivity of diamond however may make this advantageous if the capillary bond is sufficient, similar to using a diamond heat-sink on the base of a thin-substrate device.

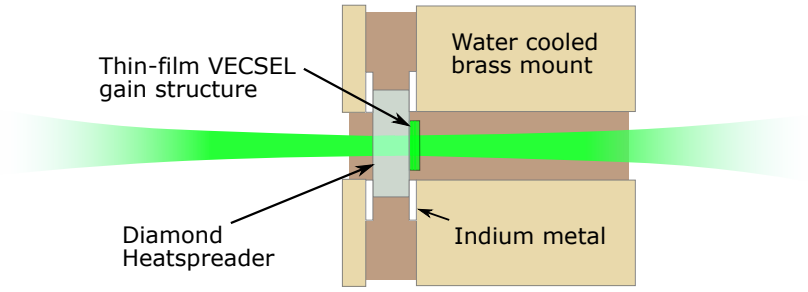

Figure 2.16: Thin-film VECEL cooling mount, allowing transmission from both ends of the sample. There is a lower thermal contact area for this system, and heat cannot pass through the VECSEL substrate as it has been removed and the structure is in contact only with the diamond

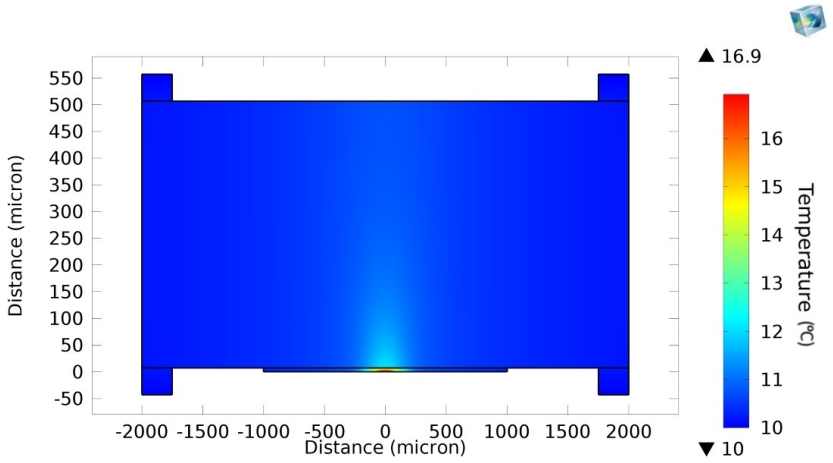

Figure 2.17: Simulation of a pumped AlGaAs structure of thickness 2 µm, bonded to a 500 µm diamond and placed within the brass mount proposed for the thin-film VECSEL structures. Pump is the same as in Figure 2.15, 1 W with 50 µm radius. Heat is extracted from the top and bottom of the diamond through Indium metal contacts.

The removal of the heat through substrate to heat sink does raise questions of the rate of heat extraction. A simulation is shown in Figure 2.17 and for a 2 µm thick AlGaAs layer on a 500 µm thick diamond heatspreader, pumped with 1 W with a Gaussian spot of radius 50 µm. Thermal connections of indium metal contacts (with 0.82 W/(cm K)) are at the top and bottom of the diamond, and the heat-flow is only through these contacts, as shown in Figure 2.18.

The maximum simulated temperature within the structure is 16.9 °C for the thin-film device, which is comparable in performance to the 15.9 °C for the heat-spreader standard VECSEL structure shown in Figure 2.15 (c).

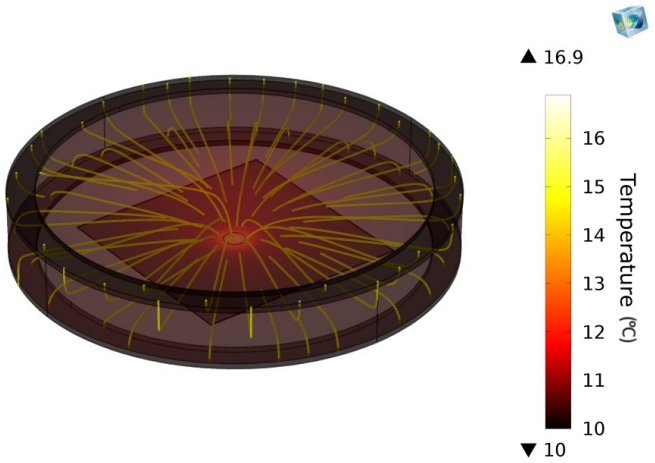

Figure 2.18: Pumped AlGaAs structure as described in Figure 2.17. Yellow lines indicate the paths that the heat takes to leave the structure through the top and bottom Indium contacts

The simulation assumes perfect thermal contact between structure and diamond. This is where the limitation of this system may lie, as the diamond and capillary bond are the only support for the structure. Thermal expansion of the structure at a different rate to the diamond could cause a catastrophic loss of the capillary bond, and so the structural integrity. Thermal expansion of the pumped section of the structure while the surrounding areas remain cool could also cause additional strain and buckling, adding to the challenges of structural and thermal management of these structures on diamond. The investigation of these effects would be the subject of ongoing work.

2.9 Summary

The 'standard' VECSEL design, as presented here, is relatively ubiquitous with basic layouts unchanged from the early devices, even with the large range of III-V material systems now used. VECSEL gain structure design for high-performance devices requires careful consideration and balancing of features. Higher strain QW gain layers can increase efficiency and reduce threshold, but necessitate the use of strain balancing schemes. The addition of strain balance layers and materials may have impact on pump absorption and thermal transfer, requiring additional consideration of offset of the designed QW emission peak from the subcavity resonances, the number of

antinodes that are optimum for operational performance, and the distribution of QWs within these antinodes. The subcavity can be designed to be resonant or anti-resonant, and these both have advantages that must be considered in relation to the device purpose.

The calculation of layer thicknesses has been discussed in Section 2.6.4 for producing a VECSEL gain structure design with the features as desired, and in practice this is aided significantly through the use of simulations of the stratified media, described in Section 2.4.1.

Thin-films have a simpler structure design – the subcavity resonance is much less significant in setting the laser emission wavelength, without the major impact of the DBR layers. For materials with a diamond heatspreader and refractive index close to that of diamond (ZnCdMgSe), this is reduced even further due to the lack of significant Fresnel reflection at the epitaxial surface interface. For these designs and novel materials, the structures become more basic to aid in the first achievement of threshold, and this can be seen in the Chapter 3 where the II-VI designs are reduced to their basic elements of uniform QWs in barrier material. Under uncertain growth conditions where layer thickness may vary from design significantly, overdesigning for QW emission offset and strain balancing can overcomplicate the pursuit of an initial successful test.

Thermal management of VECSELs is shown to be optimum with diamond heatspreaders (with a low pump spot-size), although high thermal conductivity semiconductor material and larger pump spot-sizes can favour the thin-device method. Using bulk AlGaAs in simulation, thin-film VECSEL devices transferred to diamond and relying on the diamond exclusively for heat extraction are shown to have comparable thermal extraction as the heatspreader VECSEL devices, and should therefore be capable of producing comparable maximum output.

The following chapter covers the investigation into the production of II-VI green-emission ZnCdMgSe-based VECSELs, with the ultimate goal to take advantage of the broad visible-spectrum wavelength coverage of ZnCdSe/ZnCdMgSe QWs. As briefly

stated in Section 2.8, ZnCdMgSe-based DBRs provide a challenge for high quality growth, and so a process for epitaxial structure transfer from substrate to produce thin-film VECSEL devices is developed.

2.10 References

[1] W. Li, J.B. Héroux, W.I. Wang, InGaAsSbN: A dilute nitride compound for midinfrared optoelectronic devices, J. Appl. Phys. 94 (2003) 4248–4250. doi:10.1063/1.1606514.

[2] L. Vegard, Die Konstitution der Mischkristalle und die Raumfüllung der Atome, Zeitschrift Für Phys. 5 (1921) 17–26.

[3] I. Vurgaftman, J.R. Meyer, L.R. Ram-Mohan, Band parameters for III–V compound semiconductors and their alloys, J. Appl. Phys. 89 (2001) 5815. doi:10.1063/1.1368156.

[4] A.R. Adams, Strained-layer quantum-well lasers, IEEE J. Sel. Top. Quantum Electron. 17 (2011) 1364–1373. doi:10.1109/JSTQE.2011.2108995.

[5] M. Tabuchi, S. Noda, A. Sasaki, Strain energy and critical thickness of heteroepitaxial InGaAs layers on GaAs substrate, J. Cryst. Growth. 115 (1991) 169–173. doi:10.1016/0022-0248(91)90733-L.

[6] E. Yablonovitch, E. Kane, Reduction of lasing threshold current density by the lowering of valence band effective mass, J. Light. Technol. 4 (1986) 504–506. doi:10.1109/JLT.1986.1074751.

[7] S. Calvez, J.E. Hastie, M. Guina, O.G. Okhotnikov, M.D. Dawson, Semiconductor disk lasers for the generation of visible and ultraviolet radiation, Laser Photonics Rev. 3 (2009) 407–434. doi:10.1002/lpor.200810042.

[8] N.J. Ekins-Daukes, K. Kawaguchi, J. Zhang, Strain-Balanced Criteria for Multiple Quantum Well Structures and Its Signature in X-ray Rocking Curves, Cryst. Growth Des. 2 (2002) 287–292. doi:10.1021/cg025502y.

[9] J.C. Dries, M.R. Gokhale, H. Uenohara, S.R. Forrest, Strain-compensated InGa(As)P-InAsP active regions for 1.3-μm wavelength lasers, IEEE Photonics Technol. Lett. 10 (1998) 42–44. doi:10.1109/68.651096.

[10] C.H. Lin, C.L. Chua, Z.H. Zhu, F.E. Ejeckam, T.C. Wu, Y.H. Lo, et al., Photopumped long wavelength vertical-cavity surface-emitting lasers using strain-compensated multiple quantum wells, Appl. Phys. Lett. 64 (1994) 3395. doi:10.1063/1.111286.

[11] H.Q. Hou, K.D. Choquette, K.M. Geib, B.E. Hammons, High-performance 1.06-μm selectively oxidized vertical-cavity surface-emitting lasers with InGaAs-GaAsP strain-compensated quantum wells, IEEE Photonics Technol. Lett. 9 (1997) 1057–1059. doi:10.1109/68.605498.

[12] S. Hoogland, A. Garnache, I. Sagnes, B. Paldus, K.J. Weingarten, R. Grange, et al., Picosecond pulse generation with 1.5 μm passively modelocked surface-emitting semiconductor laser, Electron. Lett. 39 (2003) 2002–2003. doi:10.1049/el:20030576.

[13] S. Baumgärtner, H. Kahle, R. Bek, T. Schwarzbäck, M. Jetter, P. Michler, Comparison of AlGaInP-VECSEL gain structures, J. Cryst. Growth. 414 (2015) 219–222. doi:10.1016/j.jcrysgro.2014.10.016.

[14] L. Fan, J. Hader, M. Schillgalies, M. Fallahi, A.R. Zakharian, J. V. Moloney, et al., High-power optically pumped VECSEL using a double-well resonant periodic gain structure, IEEE Photonics Technol. Lett. 17 (2005) 1764–1766. doi:10.1109/LPT.2005.853536.

[15] A.C. Tropper, S. Hoogland, Extended cavity surface-emitting semiconductor lasers, Prog. Quantum Electron. 30 (2006) 1–43. doi:10.1016/j.pquantelec.2005.10.002.

[16] A.C. Tropper, S. Hoogland, Extended cavity surface-emitting semiconductor lasers, Prog. Quantum Electron. 30 (2006) 1–43. doi:10.1016/j.pquantelec.2005.10.002.

[17] S. Ranta, T. Hakkarainen, M. Tavast, J. Lindfors, T. Leinonen, M. Guina, Strain compensated 1120nm GaInAs/GaAs vertical external-cavity surface-emitting laser grown by molecular beam epitaxy, J. Cryst. Growth. 335 (2011) 4–9. doi:10.1016/j.jcrysgro.2011.08.044.

[18] Y.P. Varshni, Temperature dependence of the energy gap in semiconductors, Physica. 34 (1967) 149–154. doi:10.1016/0031-8914(67)90062-6.

[19] S. Adachi, GaAs, AlAs, and $Al_xGa_{1-x}As$: Material parameters for use in research and device applications, J. Appl. Phys. 58 (1985) R1–R29. doi:10.1063/1.336070.

[20] S. Adachi, Material parameters of $In_{1-x}Ga_xAs_yP_{1-y}$ and related binaries, J. Appl. Phys. 53 (1982) 8775. doi:10.1063/1.330480.

[21] M. Born, E. Wolf, Principles of Optics, 7th (expanded) edition, 1999, Cambridge University Press.

[22] M. Kuznetsov, F. Hakimi, R. Sprague, A. Mooradian, Design and characteristics of high-power (>0.5-W CW) diode-pumped vertical-external-cavity surface-emitting semiconductor lasers with circular TEM00 beams, IEEE J. Sel. Top. Quantum Electron. 5 (1999) 561–573. doi:10.1109/2944.788419.

[23] S.W. Corzine, R.S. Geels, J.W. Scott, R.H. Yan, L.A. Coldren, Design of Fabry-Perot surface-emitting lasers with a periodic gain structure, IEEE J. Quantum Electron. 25 (1989) 1513–1524. doi:10.1109/3.29288.

[24] N. Schulz, M. Rattunde, C. Ritzenthaler, B. Rosener, C. Manz, K. Kohler, et al., Effect of the Cavity Resonance-Gain Offset on the Output Power Characteristics of GaSb-Based VECSELs, Photonics Technol. Lett. IEEE. 19 (2007) 1741–1743. doi:10.1109/LPT.2007.906054.

[25] J. Wagner, N. Schulz, M. Rattunde, C. Ritzenthaler, C. Manz, C. Wild, et al., Barrier- and in-well pumped GaSb-based 2.3 μm VECSELs, in: Phys. Status Solidi Curr. Top. Solid State Phys., 2007: pp. 1597–1600. doi:10.1002/pssc.200674274.

[26] M. Schmid, S. Benchabane, F. Torabi-Goudarzi, R. Abram, A.I. Ferguson, E. Riis, Optical in-well pumping of a vertical-external-cavity surface-emitting laser, Appl. Phys. Lett. 84 (2004) 4860–4862. doi:10.1063/1.1760887.

[27] S.S. Beyertt, M. Zorn, T. Kübler, H. Wenzel, M. Weyers, A. Giesen, et al., Optical in-well pumping of a semiconductor disk laser with high optical efficiency, IEEE J. Quantum Electron. 41 (2005) 1439–1449. doi:10.1109/JQE.2005.858794.

[28] A. Smith, J.E. Hastie, A.J. Kemp, H.D. Foreman, M.D. Dawson, T. Leinonen, et al., GaN diode-pumping of a red semiconductor disk laser, in: Conf. Proc. - Lasers Electro-Optics Soc. Annu. Meet., 2008: pp. 404–405. doi:10.1109/LEOS.2008.4688661.

[29] M.A. Holm, D. Burns, P. Cusumano, A.I. Ferguson, M.D. Dawson, High-power diode-pumped AlGaAs surface-emitting laser., Appl. Opt. 38 (1999) 5781–5784. doi:10.1364/AO.38.005781.

[30] Z. Zhao, S. Bouchoule, J. Song, E. Galopin, J.-C. Harmand, J. Decobert, et al., Subpicosecond pulse generation from a 1.56 ?µm mode-locked VECSEL, Opt. Lett. 36 (2011) 4377–4379. doi:10.1364/OL.36.004377.

[31] K.G. Wilcox, A.C. Tropper, H.E. Beere, D.A. Ritchie, B. Kunert, B. Heinen, et al., 4.35 kW peak power femtosecond pulse mode-locked VECSEL for supercontinuum generation, Opt. Express. 21 (2013) 1599–1605. doi:10.1364/OE.21.001599.

[32] A. Garnache, A. A. Kachanov, F. Stockel, R. Houdré, Diode-pumped broad-band vertical-external-cavity surface-emitting semiconductor laser applied to high-sensitivity intracavity absorption spectroscopy, JOSA B. 17 (2000) 1589–1598. doi:10.1364/JOSAB.17.001589.

[33] A. MacLean, Power scaling and wavelength control of semiconductor disk lasers, University of Strathclyde, 2008. http://ethos.bl.uk/OrderDetails.do?uin=uk.bl.ethos.487871 (accessed February 5, 2014).

[34] A.J. MacLean, R. Birch, P. Roth, A. Kemp, D. Burns, Limits on efficiency and power scaling in semiconductor disk lasers with diamond heatspreaders, JOSA B. 26 (2009) 2228–2236. doi:10.1364/JOSAB.26.002228.

[35] A.J. Kemp, G.J. Valentine, J.M. Hopkins, J.E. Hastie, S.A. Smith, S. Calvez, et al., Thermal management in vertical-external-cavity surface-emitting lasers: Finite-element analysis of a heatspreader approach, IEEE J. Quantum Electron. 41 (2005) 148–155. doi:10.1109/JQE.2004.839706.

[36] P.J. Schlosser, Vertical External Cavity Surface Emitting Lasers Utilising Quantum Dot Active Regions, University of Strathclyde, 2011.

[37] A. Black, A.R. Hawkins, N.M. Margalit, D.I. Babić, A.L. Holmes, Y.L. Chang, et al., Wafer fusion: Materials issues and device results, IEEE J. Sel. Top. Quantum Electron. 3 (1997) 943–951. doi:10.1109/2944.640648.

[38] J. Rautiainen, J. Lyytikäinen, A. Sirbu, A. Mereuta, A. Caliman, E. Kapon, et al., 2.6 W optically-pumped semiconductor disk laser operating at 1.57-μm using wafer fusion., Opt. Express. 16 (2008) 21881–21886. doi:10.1364/OE.16.021881.

[39] J. Lyytikäinen, J. Rautiainen, L. Toikkanen, 1.3-μm optically-pumped semiconductor disk laser by wafer fusion, Opt. Express. 17 (2009) 9047–9052. doi:10.1364/OE.17.009047.

[40] A. Mignot, G. Feugnet, S. Schwartz, I. Sagnes, A. Garnache, C. Fabre, et al., Single-frequency external-cavity semiconductor ring-laser gyroscope., Opt. Lett. 34 (2009) 97–99. doi:10.1364/OL.34.000097.

Chapter 3

II-VI ZnCdMgSe VECSEL structures

3.1 Introduction

Within the visible spectrum there is a wavelength region encompassing green to orange, where fundamental emission semiconductor devices are complex to manufacture. Most devices operating in this spectral region have fundamental emission elsewhere in the spectrum with the emission converted, whether by simple photoluminescence or fluorescence (e.g. YAG phosphor used in white-light converted GaN LEDs [1]) or by non-linear frequency conversion of lasers. GaN devices have been making progress using novel highly strained material with semi- and non-polar substrates to push the achievable device wavelengths from the blue into the green [2,3] At the same time, there is a push to shorter wavelengths using AlGaInP material, and this material forms the basis of the red VECSEL lasers described in Chapter 4.

Fundamental emission at these wavelengths could not only open the spectrum for higher efficiency devices in the green-orange, but also higher efficiency devices frequency-doubled from these wavelengths into the UV, addressing further gaps in spectral coverage.

In this work we investigate the potential of devices based on the ZnCdMgSe material system, relatively overlooked in favour of InGaN-based devices due to difficulties in

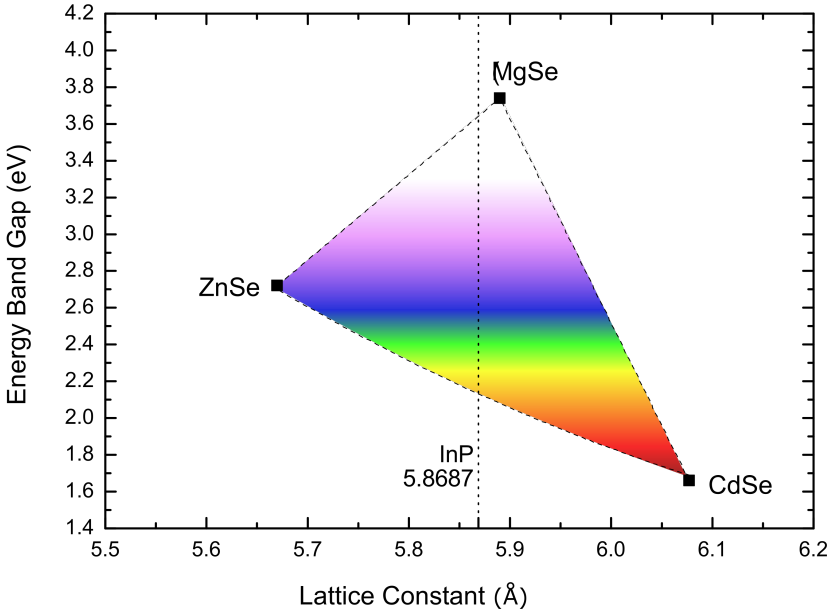

Figure 3.1: Energy band-gap vs. lattice constant for the ZnCdMgSe material system, with the lattice constant of InP marked by a dotted line at 5.8687 Å. II-VI data from Refs. [5–7].

p-type doping [4], which nevertheless offers the possibility of simple optically-pumped devices with fundamental emission across the visible spectrum.

3.1.1 ZnCdMgSe material system

ZnCdMgSe is grown on InP substrates and, through manipulation of the material composition, can be grown lattice-matched to the substrate. Band-gaps of lattice-matched material range from 2.2 eV for the ternary $Zn_{0.48}Cd_{0.52}Se$, up to around 3.4 eV for $(ZnCd)_{0.4}Mg_{0.6}Se$; the upper limit on material fraction a result of the lattice structure of MgSe, to be discussed in Section 3.2.2.1. Figure 3.1 shows a plot of lattice constant against (direct) energy band-gap for the binaries ZnSe, CdSe and MgSe, to illustrate the range of the material system.

Band-gap engineered devices based entirely on the quaternary ZnCdMgSe can be grown, and reported devices include multi-quantum well (QW) edge-emitting structures with blue, green and red laser emission under optical pumping (red requires strained ZnCdSe QWs) [8–11].

The growth of the material is covered in Section 3.2, beginning with an introduction of the growth technique and in-situ characterisation, followed by a detailed description of II VI growth and its challenges in Section 3.2.2.

While there has been a reasonable amount of reported investigation into the ternary alloy ZnCdSe, the optical properties of the quaternary materials have not yet been extensively investigated, and summaries of the most relevant publications and their conclusions on the material properties are in Section 3.3. These studies inform our QW simulation and structure design in Section 3.4. Some of the limitations of this material for complete monolithic structures are also discussed in this section, including those leading to the conclusion that the substrate must be removed from the structure.

Section 3.5.1 discusses the process of substrate removal and device transfer for II VI structures, followed in Section 3.6 by a discussion of the design eVolution. Sections 3.7 and 3.9 discuss characterisation and analysis of each of the II VI structures grown, optical properties and structural quality and strain, respectively.

3.2 II-VI ZnCdMgSe growth

ZnCdMgSe is grown by molecular beam epitaxy (MBE) on 500-µm-thick InP substrates by our collaborators in the Department of Chemistry at CCNY. To improve crystal quality, an initial III-V buffer of InGaAs is grown, followed by a II-VI low temperature buffer of lattice-matched ZnCdSe. In depth discussion on the II-VI growth procedure can be found in section 3.2.2.

3.2.1 Molecular beam epitaxy

MBE is a process through which semiconductor single-crystal structures are grown one atomic layer at a time. Effusion cells for each constituent element are heated to produce an evaporated beam of particles through high vacuum to condense into layers on the target, with the flow controlled by computer operated shutters. The growth is normally slow, less than 3 µm/hour, and consists of the single crystals building up by

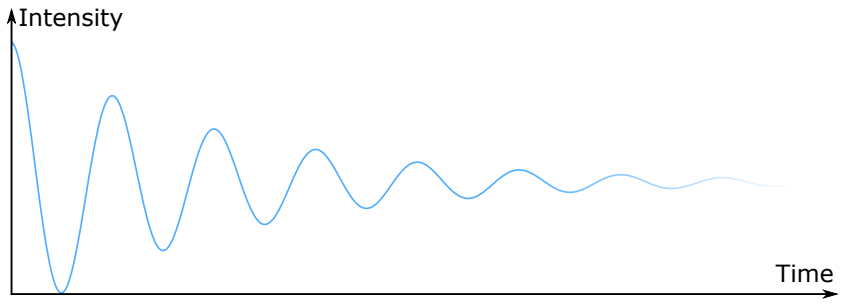

Figure 3.2: The intensity/time relation for a spot of constructive interference within a RHEED pattern, during MBE growth.

one atomic layer at a time. Prior to the actual structure growth, the correct temperature for each effusion cell is estimated theoretically and then adjusted empirically via use of X-ray diffraction (XRD) and photoluminescence (PL) measurements to measure lattice strain and energy-band-gap respectively, allowing for a determination of the crystal alloy composition. The growth rate is determined for each material using reflection high-energy electron diffraction (RHEED), and is used to calculate the growth time for each material, which, in turn, is used in programming the shutter controls for the specific design thicknesses required.

3.2.1.1 RHEED measurement

RHEED is a method through which the surface of the crystal lattice is characterised during growth. Electrons are fired at the sample at a shallow angle, and diffracted by surface atoms. The pattern of constructive and destructive interference can be analysed to determine the lattice structure of the crystal.

In the case of MBE growth, it is the addition of atomic layers to the lattice that is most important for the determination of layer growth times. This can be observed through the change in intensity with time of a single spot, shown in Figure 3.2.

Each period of the oscillation corresponds to the deposition of one crystallographic atomic layer, and so this provides the growth rate for this material required to calculate the growth time for each material to correspond to the structure design.

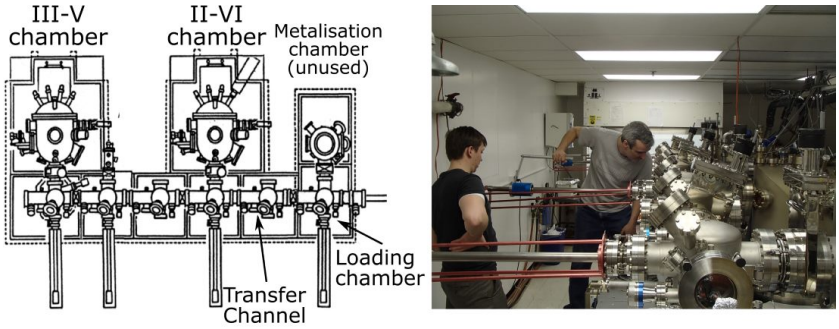

Figure 3.3: RIBER 2300 MBE system, with III-V, II-VI and (unused in this work) metalisation chambers. (a) Schematic of system [12]. (b) Photograph of the insertion of the wafer from the transfer channel to the II-VI chamber.

3.2.2 Structure growth procedure

All of the II-VI samples used for this work were grown in a twin chamber RIBER 2300 MBE system, with both III-V and II-VI growth chambers connected by ultra-high vacuum, shown in Figure 3.3.

Each chamber has effusion cells which, as described in section 3.2.1, have calibrated growth rates for set temperatures of the heating coils, with emission controlled by shutters.

The InP substrates are mounted to molybdenum blocks using Indium prior to transfer into the growth chambers. Once the substrate is placed within the first chamber for III-V deposition, oxide is removed from the surface by heating under an As flux. A lattice-matched InGaAs buffer layer is then grown. This ensures the presence of an As-terminated surface, a good interface for growth of II-VI material [13].

Calibration growths over many runs allow for reasonable confidence in the repeatability of the growth of lattice-matched InGaAs. To measure the growth rate, RHEED is used to observe the formation of the crystal structure over the first few seconds of calibration growth. Growth then continues until a buffer layer of 100–300 nm thickness is produced. The shutters are then closed and the sample is transferred along the UHV connection by a magnetic arm and a track system.

After the substrate is transferred to the II-VI deposition chamber the RHEED measurements of the II-VI layers are performed in order to confirm growth rates, and the planned shutter times adjusted accordingly. A computerised system controls the shutters so that direct user input is not required over the whole growth, which could be many hours in length.

A low temperature ZnCdSe buffer layer of approximately 5 nm is grown onto the InGaAs buffer to act as an interfacial layer and improve the III-V/II-VI interface by promoting two-dimensional nucleation, typically grown 100 °C below the optimal II-VI growth temperature, which is approximately 270 °C [5,14,15].

3.2.2.1 Growth challenges

The material system shown in Figure 3.1 indicates that it could be possible to grow lattice-matched material with a band gap of up to 3.8 eV using the binary MgSe, however MgSe has an unstable zinc-blend lattice structure, and thicker materials revert to a rock salt lattice structure [16] incompatible with the zinc-blende structure of InP, InGaAs and ZnCdSe for high quality material growth. This places a limit on the Mg fraction that can be accommodated in ZnCdMgSe alloys without compromising the crystal growth quality, and based on the growth experience of our collaborators it was decided that $(ZnCd)_{0.4}Mg_{0.6}Se$ would be the highest band-gap material grown for the VECSEL designs. Potential methods of achieving a higher band-gap with higher Mg content material were considered, e.g. using stabilising low Mg content material in a superlattice to provide a high quality pseudo-alloy of higher band-gap, similar to the technique used for the growth of ZnCdSe/MgS superlattices [17]; however, the difficulties discussed below made such a growth of high numbers of multiple quaternary alloys impractical.

Further challenges came from the maximum growth thickness of the structure, which was limited to 2 μm following advice from the growers, after which the growth of the high quality material required would significantly increase in difficulty. This precludes the inclusion of full DBR mirrors within the II-VI VECSELs, although in later growths

we began to grow structures beyond this limit with a test 20-period DBR, helped by improvements in growth quality and lattice-matching by the group at CCNY since 2011 [18].

Finally, accurate growth of the designs was hampered by equipment limitations. Only one Mg effusion cell is contained within the machine, so for designs with multiple quaternary alloys the temperature of the cell must be changed between layers to allow for a change in compositions. This progressively reduces the accuracy of growth rate measurements and the corresponding growth time calculations, and can also be the cause of a drift in the material composition for layers designed to be identical within the structure. An alternative growth method, used to get around this, is the use of quasiquaternary super-lattices to produce pseudo-alloys, as in Morita et al. 1997 [19] (discussed in section 3.3.3), but accurate growth of these pseudo-alloys is still in the early stages of investigation for our collaborators, with a single 'bulk' pseudo-alloy grown by CCNY. The effects of this uncertainty can be seen throughout the characterisation, demonstrated later in Figure 3.35 (b), where SEM measurements confirm differences of >20% in some layers, and in section 3.6.1 where reflectivity measurements show a sample almost half the thickness designed. Within a VECSEL structure, layer thicknesses and refractive indices are carefully designed for quantum well gain, RPG, subcavity resonance and absorption, as described in Chapter 2. The VECSEL is therefore very sensitive to differences between design and growth, and this is the greatest challenge for the pursuit of a ZnCdMgSe VECSEL.

3.3 Material properties

The study of ZnCdSe is a mature research topic, grown under strain on GaAs substrates within structures based on the ZnCdSSe system. For ZnCdSe lattice-matched with *InP*, there are several previous studies of its properties. ZnCdMgSe however is a relatively newly studied material, without significant characterisation data available in the literature.

3.3.1 ZnCdMgSe quaternary characteristics

It is important to note that use of this material is currently very challenging for electrically-pumped devices – inherent properties of the II-VI selenide material systems preclude easy p-type doping of the material. This is not directly relevant for an optically-pumped device, as for optically-pumped vertical gain structures such as VECSELs doping is not required.

The value of the band-gap of zinc-blende MgSe for use in basic bowed band-gap calculations is not easy to determine; various sources give several different values. This is due to the natural rock-salt structure of MgSe, so that it's possible to grow only thin layers in zinc-blende structure [16]. There are three main publications dealing with the MgSe band-gap material:

- Rabah et al. 2003 calculate from theory that the $L_{1c} \rightarrow \Gamma_{15v}$ indirect transition is 4.24 eV (77 K) [20] and the direct gap $\Gamma_{1c} \rightarrow \Gamma_{15v}$ is 2.813 eV, while referring to experimental data from Okuyama et al. 1991 [21] that the direct gap transition is 3.60 eV.
- Charifi et al. 2004 [22] calculate an indirect transition E_{Γ}^{L} of 4.19 eV and a direct band-gap E_{Γ}^{Γ} of 4.21 eV at room temperature (RT).
- Sohel et al. 2004 [5] extrapolate from several experimental data sources [21,23–26] along with their own experimental data to demonstrate a band-gap for zinc blende MgSe of 3.74 eV (77 K). The temperature dependence of the band-gap is demonstrated to be 0.07 eV between 77 K and RT, giving a RT band-gap for MgSe of 3.67 eV.

By comparison, the data by Sohel et al. is the most comprehensive and is taken to be the most accurate. Figure 3.4 shows the plot of ZnMgSe band-gap for the experimental data.

Faced with uncertainty regarding the binary values to use in calculations, it is better to attempt to refer to those reports directly investigating the quaternary material we

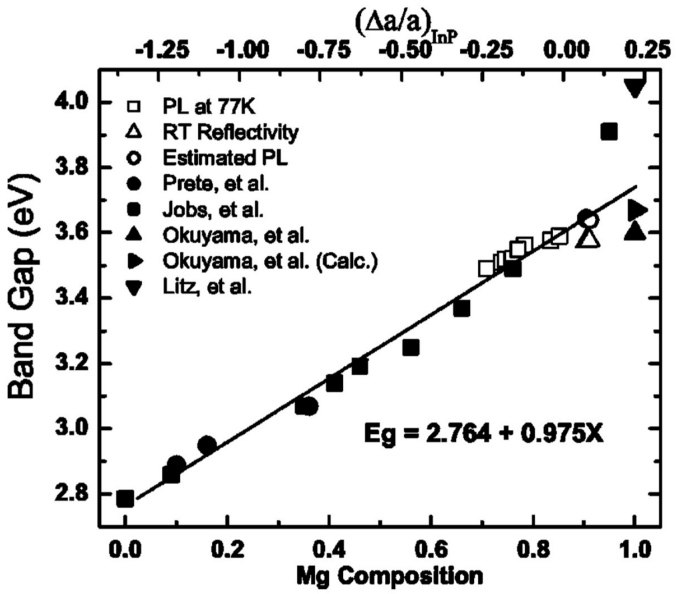

Figure 3.4: Including collected data from [21,23–26], the band-gap of ZnMgSe is described by $E_g = 2.764 + 0.975x$, and the predicted band-gap for MgSe is 3.74 eV at 77 K. Figure reproduced from Sohel et al. 2004 [5].

are using. Summarised below are most of the useful publications with regards to ZnCdMgSe properties and II-VI structure design.

3.3.2 Band-gap and absorption: Hattori et al. 1998

Hattori et al. in 1998 [27] provide absorption coefficient measurements as the Mg fraction within the ZnCdMgSe increases from lattice-matched ZnCdSe. The authors use fitted theoretical values calculated using the density matrix method [28] to determine energy band-gap values from the absorption spectrum for each material, and describe the energy band-gap bowing parameter as negligible within the ZnCdMgSe system, providing a fitted linear relation for Eg with Mg fraction y:

$$E_g = 2.07 + 1.57y \tag{3.1}$$

which gives the room temperature band-gap energy of MgSe as 3.64 eV, which is favourably close to the RT value given by Sohel et al. of 3.67 eV [5].

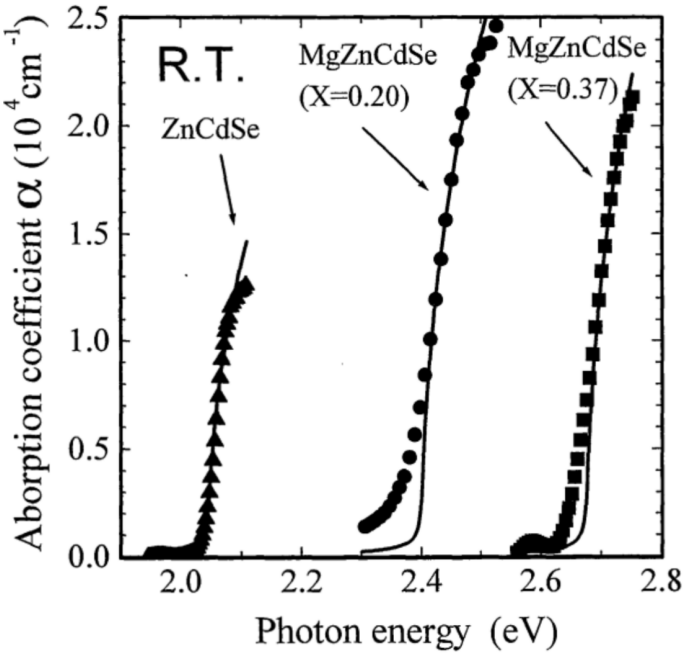

Figure 3.5: Experimental measurements of the absorption edge of $(ZnCd)_{1-y}Mg_ySe$ for y=0 (triangles), y=0.20 (circles) and y=0.37 (squares). The authors of the paper use the fits to estimate energy band-gap of the materials. In reverse, the band-gap of materials can be used to predict the absorption profile. Figure reproduced from Hattori et al. 1998 [27]

Figure 3.5 shows experimental absorption data from the paper for compositions with Mg fractions of 0, 0.2 and 0.37. The composition of 0.37 is used in our designs as the pump-absorbing barrier material for the QWs, so that the recorded data can inform our sub-cavity length.

3.3.3 Band-gap and refractive index: Morita et al. 1997

Another significant paper for use in the design of II-VI heterostructures is by Morita et al. in 1997 [19]. As described in Chapter 2, VECSEL performance is highly dependent upon the correct placement of structure elements within the sub-cavity: QWs are placed at the standing wave antinodes in RPG configuration; electron confinement windows should be placed at the standing wave nodes to reduce the effect of any absorption; the cavity end should be at the antinode of the wave in a resonant cavity, and at the node of the wave in an antiresonant cavity; DBR layer thicknesses must be adjusted for the target reflection wavelength, and must be placed carefully in relation

to the RPG and subcavity resonances. These features all rely on accurate material refractive index information.

The Morita paper references an equation from Samarth et al. (1990) [29] for finding band-gap E_g for $(Zn_{0.48}Cd_{0.52})_{1-y}Mg_ySe$ at a temperature of 15 K, given in Equation 3.2, which the authors use later in their calculation of room temperature direct band-gap and refractive index:

$$E_g = 2.19 + 1.44y \tag{3.2}$$

This equation is, however, for a material at a temperature of 15 K.

The Morita treatment of the refractive index involves experimental recordings of the reflectance of layers, with a simple calculation of refractive index from the resulting reflectance spectrum using Snell's Law, and an example from the paper is shown in Figure 3.6 (a).

By observing that the reflectance of the crest points (at structure resonance) within the spectrum corresponded to that expected of InP from Snell's Law, the trough points off resonance can then be expected to correspond to the refractive index of the epi-layer. The refractive index of ZnCdMgSe with various Mg fractions is given in Figure 3.6 (b). Morita et al. fit the points with calculations based on the modified single effective oscillator (MSEO) method first described by Afromowitz in 1974 [30]. The MSEO method describes refractive index n as a function of dispersion energy E_d, oscillator energy E_0, photon energy E_P and (room temperature) direct band-gap energy E:

$$n^2 - 1 = \frac{E_d}{E_0} + \frac{E_d E_p^2}{E_0^3} + \frac{E_d E_p^4}{2E_0^3(E_0^2 - E_1^2)} \ln\left(\frac{2E_0^2 - E_\Gamma^2 - E_p^2}{E_\Gamma^2 - E_p^2}\right) \tag{3.3}$$

From Equation 3.2 and experimental data for ZnCdSe band-gap, E_Γ is estimated. Equation 3.3 is fitted to the experimental refractive indices (Figure 3.6 (b)), resulting

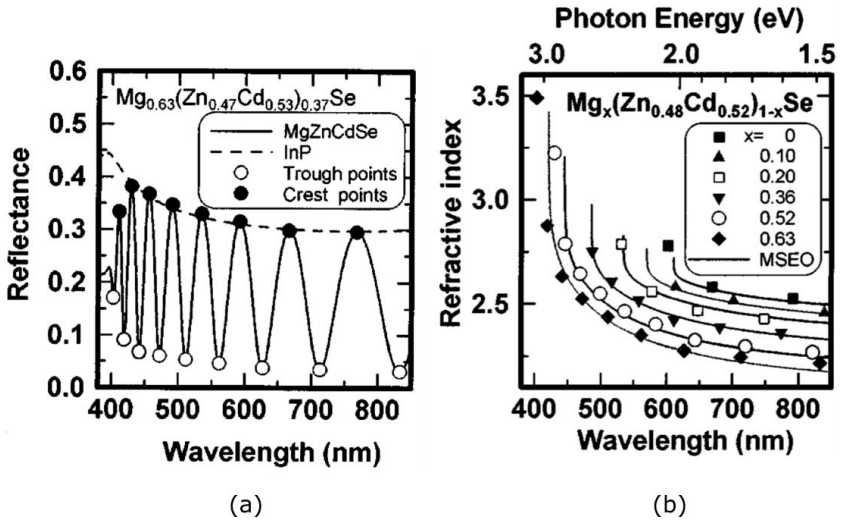

Figure 3.6: (a) Reflectivity spectrum taken of $(Zn_{0.47}Cd_{0.53})_{0.37}Mg_{0.63}Se$ (solid line), compared with the expected reflectivity of the InP substrate (dashed line). (b) Refractive indices of ZnCdMgSe for various Mg fractions. Results are fitted with the MSEO method. Figures reproduced from Morita et al. 1997 [19].

in functions of E_d and E_0 for $(Zn_{0.48}Cd_{0.52})_{1-y}Mg_ySe$ at room temperature:

$$E_d = 24.5 - 15.2y \tag{3.4}$$

$$E_0 = 5.13 - 1.03y \tag{3.5}$$

$$E = 2.03 + 1.45y \tag{3.6}$$

From these, n for any composition of $(Zn_{0.48}Cd_{0.52})_{1-y}Mg_ySe$ can be estimated, although deviation from the Zn/Cd fraction will introduce uncertainty.

While not directly related to characterisation, it is relevant to mention that the Morita paper also reports a 30 pair ZnCdMgSe DBR, with low n layer $(Zn_{0.48}Cd_{0.52})_{0.4}Mg_{0.6}Se$, and high n layer composed of a superlattice of $Zn_{0.48}Cd_{0.52}Se$ and $(Zn_{0.48}Cd_{0.52})_{0.4}Mg_{0.6}Se$ producing a quasiquaternary of $(Zn_{0.48}Cd_{0.52})_{0.9}Mg_{0.1}Se$. The high-n superlattice is used to remove the need for re-calibration of the Mg-source temperature rather than to increase refractive index contrast (as in the reported superlattice DBRs in ref. [17]). This limit of growth also applies to our collaborators at CCNY, as discussed in Section 3.2. Morita et al. report reflectivity of 98.1% at 595 nm.

3.3.4 Conduction band offset

A feature of ZnCdSe/ZnCdMgSe QWs, although not so important for the VECSEL project, is the large conduction band offset (CBO) of the material. The CBO for a $Zn_{0.53}Cd_{0.47}Se/Zn_{0.29}Cd_{0.24}Mg_{0.47}Se$ QW has been measured as $\Delta E_c/\Delta E_0 = 0.82\pm0.02$ [31] which, combined with the wide-bandgap of this material, makes them desirable for inter-subband devices such as mid-IR quantum cascade detectors [32] and lasers [33].

3.4 ZnCdSe/ZnCdMgSe Quantum well design

The basic description of a quantum well is covered in Chapter 2, and consists of a material with low energy band-gap sandwiched between two high energy band-gap materials. The thickness of the low band-gap material determines the minimum transition energy of the quantum well caused by the confinement. To determine the QW transition energy, the following must be taken into account: QW and barrier material band-gaps; conduction band offset; ground energy eigenstate determined by quantum well thickness; and band-gap changes due to strain.

3.4.1 Bulk material band-gap

The quantum wells investigated here are composed of the ternary ZnCdSe within barriers of ZnCdMgSe. For green and blue emission it has been demonstrated that lattice-matched quantum wells of ZnCdSe can be used, but that for red emission higher Cd fraction, i.e. compressively-strained material, is needed to lower the band-gap further [11]. The energy band-gap of ZnxCd1 xSe at temperature T is described [7]:

$$E_{Zn_xCd_{(1-x)}Se)}(x,T) = 2.72 - 1.31(1-x) + 0.33(1-x)^2 - T \cdot 4.5 \cdot 10^{-4} \qquad (3.7)$$

This gives the band-gap of lattice-matched Zn0.48Cd0.52Se as 2.058 eV at RT.

Band-gap calculations for quaternary ZnCdMgSe are performed using simple linear interpolation with no band-gap bowing parameter [27], between the band-gap of ZnCdSe from Equation 3.7 and for MgSe (3.67 eV at RT from ref. [5]), discussed in sections 3.3.2 and 3.3 respectively.

3.5 Quantum well thickness

Described in Chapter 2, for an even wavefunction the eigenequation for a finite quantum well is described by

$$\alpha = \frac{m_b}{m_w} k \cdot \tan\left(\frac{kL_w)}{2}\right) \tag{3.8}$$

where m_b is the effective mass in the barrier material, m_w the effective mass in the QW, and L_w is the QW thickness. α and k are given below:

$$\alpha = \frac{\sqrt{2m_b(\Delta E - E)}}{\hbar^2} \tag{3.9}$$

$$k = \frac{\sqrt{2m_w E}}{\hbar^2} \tag{3.10}$$

where E is the energy of the ground eigenstate, ΔE the 'depth' of the QW, and $\hbar$ the reduced Planck constant. ΔE is modified to include strain effects, as described in section 3.4.3.

By substituting for α and k, and inserting electron effective mass and heavy-hole effective mass, the ground-state eigenenergies of the QW for both the conduction and the valence band can be found by solving:

$$\frac{m_b}{m_w} E \tan^2\left(\frac{\sqrt{m_w E}}{2} L_w\right) + E - \Delta E = 0 \tag{3.11}$$

using the conduction band and valence band offsets (well 'depths') respectively.

3.5.1 Strain effects in a quantum well

The effects of strain in a lattice change the band structure and so have an effect on the transition energy. The bi-axial strain is given by:

$$\epsilon_{xx} = \epsilon_{yy} = \frac{a_0 - a(x)}{a_0} \equiv \epsilon \tag{3.12}$$

where ϵ_{xx} andϵ_{yy} are the strains parallel to the substrate surface, a_0 is the substrate lattice constant, $a(x)$ is the lattice size of the QW material and ϵ is the biaxial strain. The energy shift due to hydrostatic deformation δE_{hy} and shear deformation δE_{sh} can be defined as:

$$\delta E_{hy} = -2a \left[1 - \frac{C_{12}}{C_{11}}\right] \epsilon \tag{3.13}$$

$$\delta E_{hy} = -2b \left[1 - \frac{C_{12}}{C_{11}}\right] \epsilon \tag{3.14}$$

where a and b are the hydrostatic and shear deformation potentials, and C_{11} and C_{12} describe elastic stiffness. When solving for the eigenenergy of the quantum well, the depth of the quantum well ΔE is modified separately for conduction and valence bands to take into account strain, giving $\Delta E_{c'}$, ΔE_{hh} and ΔE_{lh} for the conduction band (electrons), and heavy hole and light hole valence bands respectively.

$$\Delta E_{c'} = Q(E_b - E_w - \delta E_{hy}) \tag{3.15}$$

$$\Delta E_{hh} = (1 - Q)(E_b - E_w - \delta E_{hy} - \frac{1}{2}\delta E_s h) \tag{3.16}$$

$$\Delta E_{lh} = (1 - Q)(E_b - E_w - \delta E_{hy} + \frac{1}{2}\delta E_s h) \tag{3.17}$$

where E_b is the energy band-gap of the barrier, E_w is the energy band-gap of the well and Q the conduction band offset ratio $\Delta E_c / \Delta E_0$. This is shown schematically in Figure 3.7. The vertical emission architecture of the laser determines that we require the heavy-hole transition for TE-polarised optical gain, so ΔE_{lh} can be ignored.

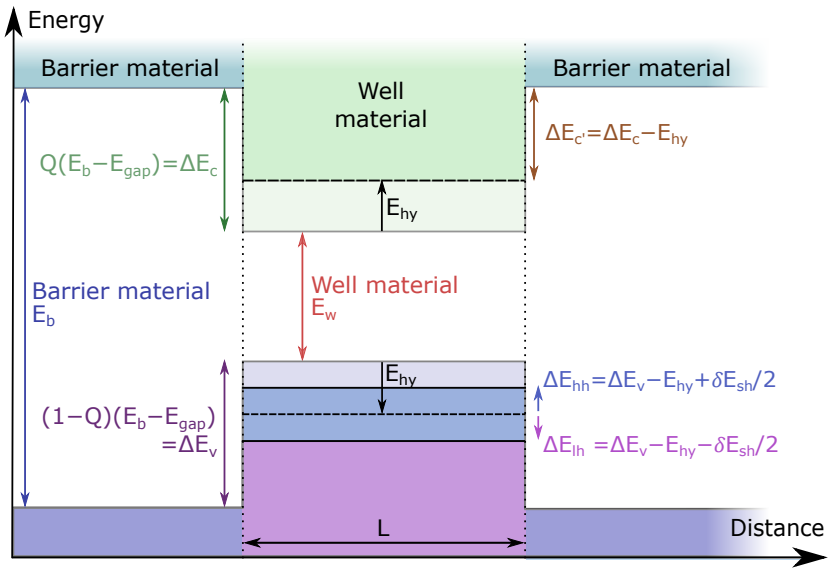

Figure 3.7: Schematic view of bandgap changes due to strain, with $\Delta E_{c'}$, ΔE_{hh} and ΔE_{lh} indicated, and their relations to the barrier and well material bandgaps E_b and E_w.

The relevant quantum well transition energy E_T from $\Delta E_{c'}$ to ΔE_{hh} is then given by

$$E_T = E_w + \delta E_+ \delta E_V \tag{3.18}$$

with δE_C the ground energy eigenstate of the quantum well in the conduction band, from combining Equation 3.14 and Equation 3.10; δE_V the ground energy eigenstate in the valence band from Equation 3.15 and Equation 3.10; and E_w the unstrained ZnCdSe material band-gap as discussed in section 3.4.1 and shown in Figure 3.7.

Where material properties are only available in the literature for the binaries (e.g. we require the effective mass within ZnCdMgSe), linear interpolation between the binaries suffices.

3.5.2 Simulated quantum wells

The relevant values required for the simulation of ZnCdSe/ZnCdMgSe quantum wells are summarised in Table 3.1. Simulations of the quantum well transition energy provide estimated quantum well thicknesses, although during growth calibration the quantum well thicknesses are tuned empirically. Figure 3.8 shows the simulated QW

Relevant material parameters of ZnSe, CdSe, and MgSe			
Coefficient	ZnSe	CdSe	MgSe
Effective electron mass m_e^* (eV/m0)[b]	0.15	0.11	0.23
Effective heavy hole mass m_{hh}^* (eV/m0)[b]	0.66	0.44	0.78
Elastic constant C_{11} (GPa)[c]	85.2	66.7	
Elastic constant C_{12} (GPa)[c]	51.7	46.3	
Hydrostatic deformation potential a (eV)[c]	-4.53	-3.664	
Shear deformation potential b (eV)[c]	1.14	0.8	
Lattice constant (nm)[a]	56.692	60.77	58.90
Energy bandgap (T=300K) E_0 (eV)	2.721[c]	1.66[c]	3.59[a]
Energy bandgap (T=10K) E_0 (eV)	2.82[c]	1.75[c]	3.74[a]
Conduction band offset for ZnCdSe	0.82[b]		

Table 3.1: List of coefficients of ZnSe, CdSe and MgSe for use in ZnCdSe/ZnCdMgSe quantum well simulation. [a] Ref. [13]; [b] Ref. [7]; [c] Ref. [24]

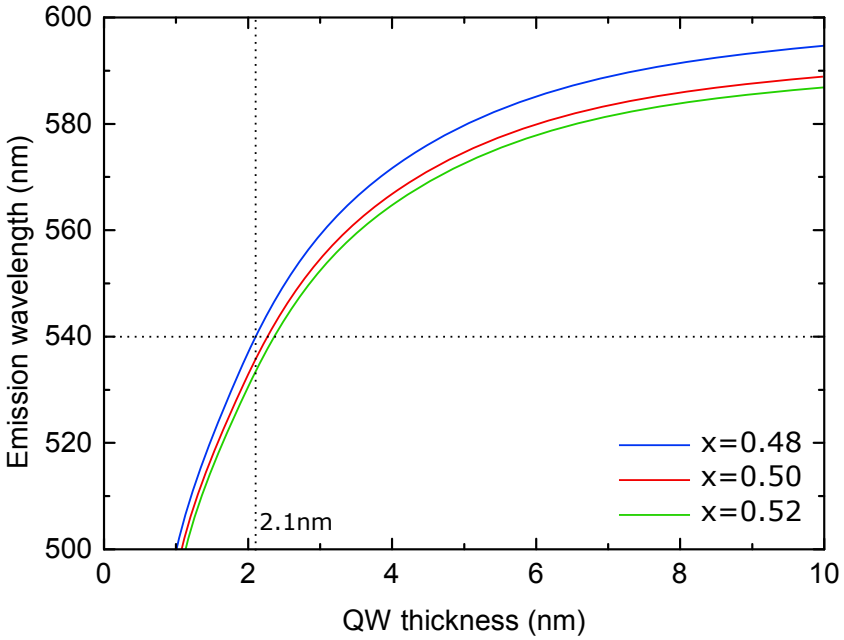

Figure 3.8: Quantum well simulation of ZnCdSe/ZnCdMgSe quantum wells. Transition wavelength vs. well thickness for near lattice-matched $Zn_xCd_{1-x}Se$, x = 0.48, 0.50 and 0.52, showing QW thickness of 2.1 nm for 540 nm emission at room temperature.

transition wavelength with thickness for near lattice-matched $Zn_xCd_{1-x}Se$ with x = 0.48, 0.50 and 0.52, in lattice-matched barriers of $(Zn_{0.52}Cd_{0.48})_{0.63}Mg_{0.37}Se$. For lattice-matched material, the simulation predicts that a QW thickness of 2.1 nm will provide a transition energy for the target emission wavelength of 540 nm. Figure 3.9 compares the simulation (given in Appendix A) with experimental data from Tamargo et al. 2001 [11], showing good agreement for both strained and near-lattice-matched QW samples.

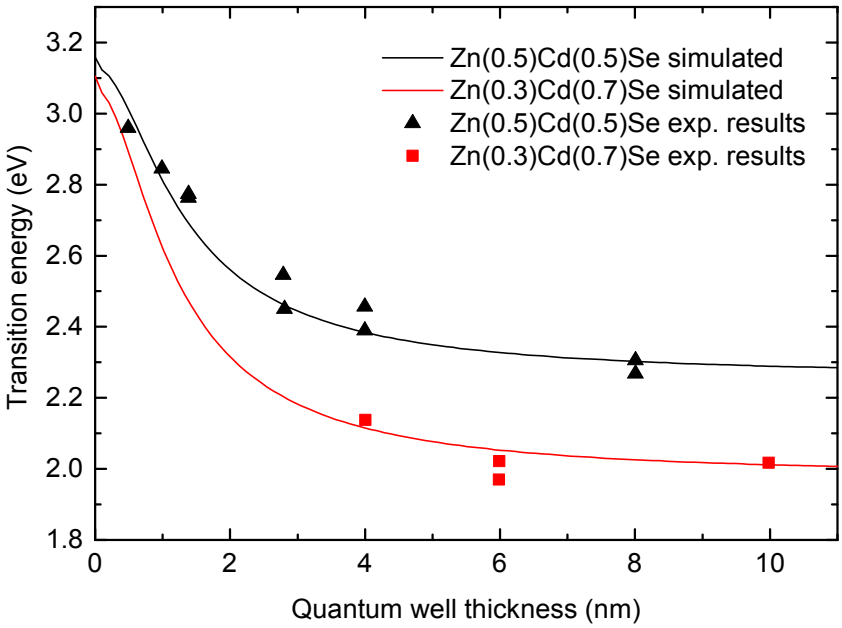

Figure 3.9: A comparison of our QW simulation, calculated using the coefficients given in Table 3.1, with experimental data from ref. [8] for both near-lattice-matched and compressively strained QW samples. The Mathcad simulation is given in Appendix A.

The simulation was altered for low temperatures through the temperature relation of Equation 3.7, along with changing the energy band-gap of MgSe to the value at 77 K from Sohel et al. 2004 [5], for use in the calculation of the ZnCdMgSe band-gap. As a simplification, all other aspects are assumed to be equal at room temperature.

3.6 Thin-film epitaxial lift-off

Discussed in section 3.2.2.1, the material has limitations when considering the standard gain-mirror VECSEL structures as described in Chapter 2. Challenges in growing a DBR lead to the compromise that the VECSEL structure designs consist of only the active region. These active region only thin-film VECSELs can have advantages, and this was also discussed in Chapter 2.

High quality DBRs have been achieved for material lattice-matched to GaAs through the use of superlattice structures to achieve higher refractive index contrast while maintaining growth quality [19,34,35]. As discussed in section 3.3.3, Morita et al. demonstrated a superlattice-based DBR with reflectivity 98.1 %, using selenide material

lattice-matched to InP. Rather than using the superlattice to increase refractive index contrast, it was used to remove the need for additional effusion cells or constant recalibration of cell temperature. Growth of these superlattice structures is highly complex and prone to faults (e.g. shutter failure during growth), and for now the more flexible and immediate solution to the problem of a high quality DBR, is to use either external mirrors or mirror coatings deposited post-growth.

Both possibilities rely on light propagating through the rear of the epi-layer, however the absorption of InP in the visible spectrum renders this impossible while the substrate is still present. In fact, both the InGaAs and low-temperature ZnCdSe buffer layers also absorb at the design wavelengths. To this end, the epi-layer and at least the InGaAs buffer layer must be removed from the substrate for a chance of a vertical emission ZnCdMgSe visible laser. This transfer of the epi-layer from its substrate is known as epitaxial lift-off (ELO).

ELO and transfer of semiconductor structures from their growth substrates provides many advantages; allowing structures, grown lattice-matched on top of a high quality substrate, to be moved to substrates where the lattice mismatch would otherwise prevent high quality growth, to those which would not be suitable for growth, e.g. flexible substrates; or as with the case of visible emitters on InP, the transfer of devices from growth substrates where the device cannot operate.

The investigation into stratified or layered devices, combining monolithically grown heterostructures and non-related bulk substrates, is already an area of active research. ELO and semiconductor transfer is a field of growing importance in research applications [36,37], in the production of thin film transistors [38], light emitting diodes (LEDs) [39], solar cells [40], sensing arrays [41], complementary metal oxide semiconductor (CMOS) circuits [42], etc.

Additional applications of ELO lie in areas where a band-gap engineered transferrable semiconductor film offers advantages over similar methods (e.g. the production of low noise III-V distributed Bragg reflector (DBR) mirrors with significant performance increase over the previous highest performing dielectric SiO_2/Ta_2O_5 mirror [43]).

Standard ELO in III-V and III-N semiconductor devices is performed on structures with a sacrificial layer of fast etching material underneath the device which, once removed, allows for the structure to be lifted and transferred.

For devices based on II-VI semiconductors, ELO has been demonstrated for II-VI materials grown on GaAs with a sacrificial layer of MgS [36,44], but until this project not for II-VI materials grown on InP (reported at the International Conference for Optical, Optoelectronic and Photonic Materials and Applications 2014, [45]).

3.6.1 Development of a processing method for ELO of thin-film II VI ZnCdMgSe structures

The first processing method that we developed for accessing the rear of the epi-layer made use of a via-hole. By allowing the majority of the substrate to remain, it was hoped that strain relaxation effects would be limited. The sample was first capillary-bonded epi-side to diamond, for both structural support and eventual thermal management.

3.6.1.1 Photoresist mask via-hole

The initial method used to produce a via-hole through the InP substrate involved photolithography. The sample substrates are supplied from the grower with indium paste remaining from being mounted in the MBE reactor, and the first step was to remove this through a small amount of mechanical polishing, approximately 100 μm. The following steps are outlined in Figure 3.10. A layer of SiO_2 is first deposited on the exposed InP surface, which acts as the etch mask in the process. The SiO_2 is then spin-coated with S1818 photoresist, shown in Figure 3.10 (a). UV cured S1818 photoresist is used to define an uncured circular region in the centre of the sample (with diameter 1 mm), and developer exposes that centre for etching leaving a cured photoresist circular mask on top of the SiO_2 (Figure 3.10 (b)). Reactive-ion etching is used to remove the exposed circle of SiO_2 (Figure 3.10 (c)), and the surrounding

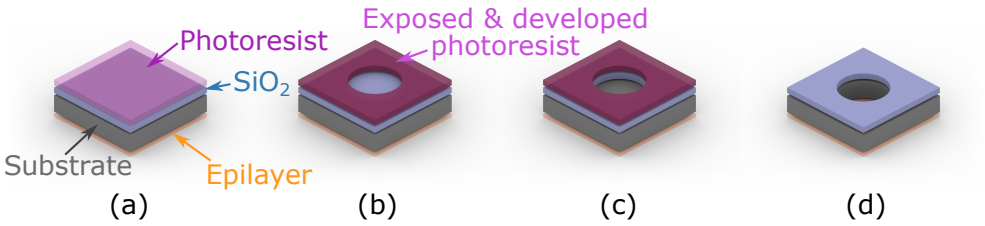

Figure 3.10: Via-hole mask and etch. (a) Substrate (grey) is coated with SiO_2 (blue) and photoresist (pink). (b) The photoresist is exposed to UV with a circular mask, and developed (purple), exposing the SiO_2. (c) Reactive-ion etching selectively removes the circle of SiO_2, and leaves a hole with exposed substrate. Remaining photoresist is removed with acetone and the exposed substrate is wet-etched to produce (d) a via-hole through to the epilayer.

photoresist is then completely removed using an acetone bath. The sample surface for each of these steps is shown in Figure 3.11.

Exposed cleaved edges are then sealed from the diamond edges on the epi-side, using UV-cured wax Norland Optical Adhesive 63 (NOA63) [46] to avoid etching the sample surface and edges, and to prevent the etchant from penetrating and destroying the capillary bond between sample and diamond. This would cause both etch damage to the epi-surface and possible sample destruction from the removal of the mechanical support.

The process steps for the etch through to the II-VI epi-layer are based on information within the publication by Moug et al in 2012 [47]. The sample was etched with $HCl:H_3PO_4$ solution, which etches InP while the InGaAs buffer acts as an etch stop. Gaseous PH_3 is strongly produced by the reaction between the HCl and InP, shown in Figure 3.12.

Cessation of PH_3 bubbling can be used to confirm that all substrate has been removed to the InGaAs etch-stop. The etching of the via-hole through the substrate is shown in the final part of Figure 3.10, (d). With a good quality capillary bond, it was possible to achieve via-holes through the InP substrate, see Figure 3.13 (a).

Once the InGaAs buffer is reached, $H_3PO_4:H_2O_2:H_2O$ is used, in a ratio of 1:1:6 with a selectivity ratio of 1:68 ZnCdSe to InGaAs. The etch rate of the InGaAs is 22.5 nm/sec.

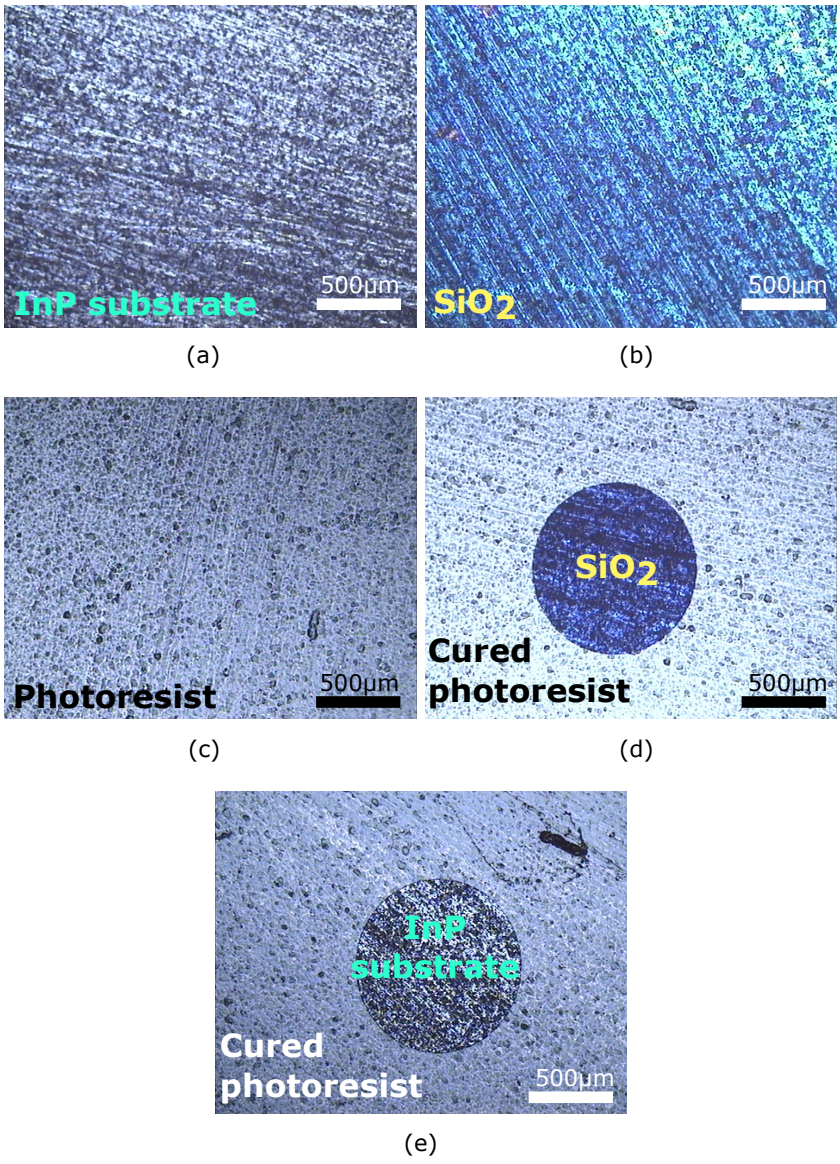

Figure 3.11: Via-hole mask fabrication. (a) Sample with In-paste polished from substrate, (b) SiO_2 deposition on surface, (c) photoresist S1818 coating, (d) via-hole pattern on UV cured photresist, developed, (e) reactive ion etch of SiO_2 makes the via-hole pattern ready for substrate wet etch (corresponds to Figure 3.10 (c)).

Several problems were apparent with this method. First was the InP etch rate and direction. Despite the mask, the prolonged etch time produced highly variable etch-times (from 60–200 minutes), and lateral etching partially negated the thin mask. The robustness of the capillary bond was also an issue, with debonding causing sample loss. More dilute solutions for lower etch rates risked further exacerbating the debonding problem. In addition, cracking of the sample once the substrate was removed caused liquid infiltration of the bond and structure release.

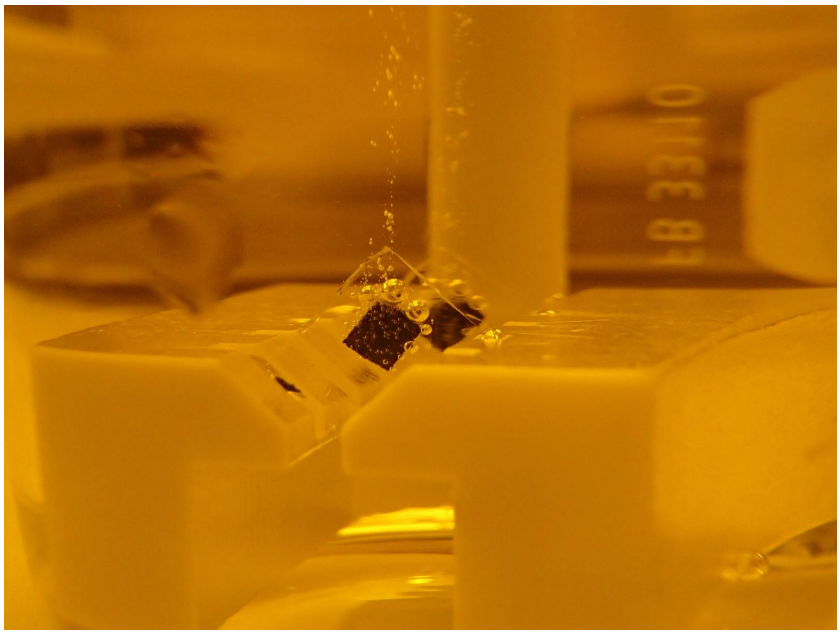

Figure 3.12: Etch of InP using HCl solution, producing gaseous PH3. In this image, samples (size 4×4 mm) have been adhered to glass slides on the epi-side using NOA63.

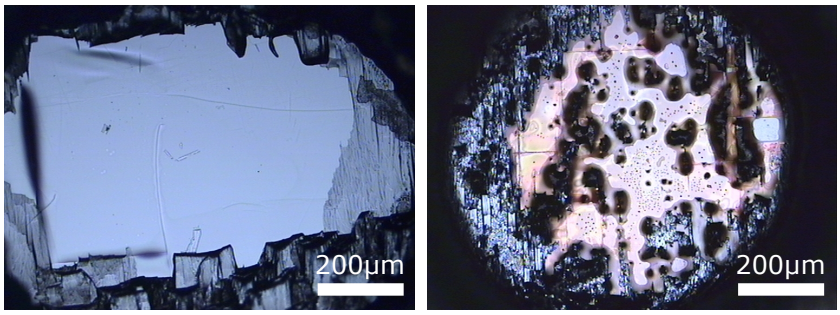

(a) (b)

Figure 3.13: (a) A successful via-hole etch to the InGaAs layer with sample A3087, the best performing (assumed to be least strained) of the first generation samples, using the photoresist mask. Uncertain lateral etching demonstrated. InP remains to the right of the image. (b) A less successful etch which, while maintaining an approximately circular profile, was coated in un-removable material and so destroyed.

The technique had a very low yield overall, with the debonding issue, unpredictable etching, and some unknown issues such as that shown in Figure 3.13 (b) showing a via hole etch where some unknown, un-removable detritus from the etch process has deposited on the InGaAs surface.

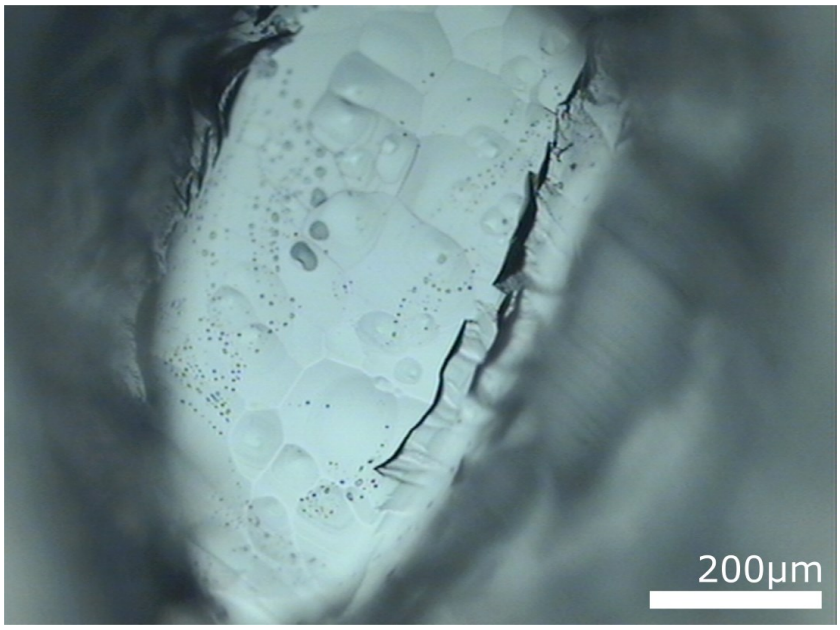

Figure 3.14: Sample etched without photoresist, using an adhesive via-hole. The rippled surface indicates debonding. Some liquid droplets are visible on the surface. View partially obstructed by adhesive hole mask

3.6.1.2 Adhesive mask for via-hole

A potential solution which aided in reducing the overall process time and the number of steps (which was considered a priority to improve the likelihood of capillary bond survival), was to simply use the adhesive (previously used for sealing the bond and edges), sealing completely from the diamond to the edges of the planned via-hole. It was not quite as successful as the photoresist in creating a mask - the etch tended to progress in a non-circular fashion. However in both cases the etch did not proceed at a consistent pace and shaped/skewed holes were common, especially when reaching the InGaAs layer, see Figure 3.14

Both of these methods relied solely on wet etching to remove the substrate, due to the initial step of diamond bonding.

3.6.2 Thin-film transfer method

For structures with sufficiently low strain, the epi-layer can be transferred entirely to a different substrate, in this case a diamond heatspreader. The result is a structure

which does not rely on a capillary bond holding during the wet-etching process, and a useable region with a size of the order of mm. The transfer process is faster than the via-hole process simply due to the reduction in complexity and the number of processing steps required for masking and etching of the via-hole.

One method of transferring epitaxial layers is through the inclusion of a sacrificial layer to allow for under-etching of the structure from the edges, releasing it from the substrate. In some material systems, the etch selectivity of the sacrificial layer is sufficiently large to allow for entire wafer ELO, notably used in the production of solar cells [48]. In the II-VI selenides, a thin layer of MgSe could be used, similar to the MgS sacrificial layer used in the epitaxial lift-off of II-VI material from GaAs [44]. The potential for additional dislocations and lower growth quality meant that this method was deemed too risky for the VECSEL structures. The alternative is full substrate removal, and this technique was developed through several iterations. The basic procedure is the same, with the HCl:H_3PO_4 etch of the substrate, and H_3PO_4:H_2O_2:H_2O etch of the InGaAs. The specifics were a little different, and a number of iterations were investigated before the technique was optimised.

3.6.3 Sample preparation

One of the key issues before was the debonding of the diamond, meaning the destruction of the sample. A solution to this problem was the use of a temporary front substrate, in this case a glass slide. Adhesive was to be used to glue the substrate to the slide, as successful large test samples were achieved through the use of UV-cured wax NOA63 and glass. Before adhering the sample to the glass, both surfaces are cleaned with baths of acetone, methanol and isopropanol, and with standard lens tissue with a drop of the relevant solvent used to remove remaining dirt/artefacts between each step.

Polyethylene glycol (PEG), is an easily removable water soluble wax with a melting point of 60 *irc*C. It is quickly removed in a heated water bath leaving the sample ready

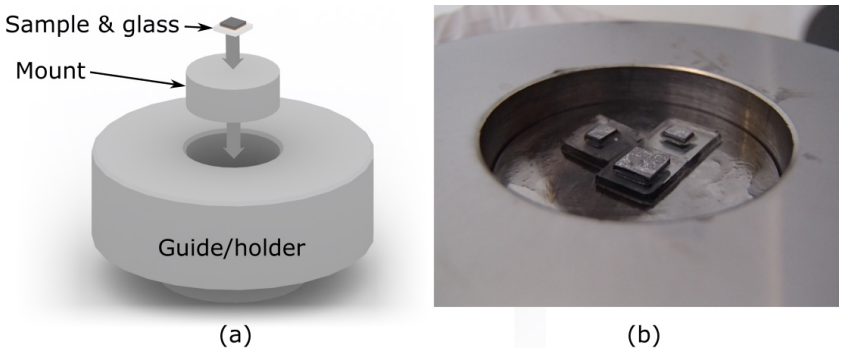

Figure 3.15: (a) Schematic of polishing mount and guide. After using the PEG wax to glue the sample to glass and mount, the mount is held in the larger holder to polish. (b) Photograph of 3 samples awaiting the mechanical polishing step.

for transfer. An issue with the wax is that its ease of removal through dissolution in water can cause premature sample release from the glass (from 30 minutes in solution).

To solve the premature release problem, and to protect the epi-surface from the effects of the substrate etch, the complete etch step must take as short a time as possible. Mechanical polishing was already used as a preparatory step to remove a layer of indium paste used during the growth process. This was used to further thin the sample.

The InP substrate is mechanically polished from its original thickness of 500 µm to a thickness of the order of 100 µm, using SiC paper with a grit size of P1200 (average particle diameter 15.3 µm). Excess wax around the sample aids in accurate polishing by slowing the procedure as the target thickness is approached, as the excess wax around the sample must also be polished as it comes into contact with the SiC paper, acting as a physical buffer. An aluminium mount, within an aluminium guide jig, as shown in Figure 3.15, is used to ensure a level polished surface, and the glass with sample is held on the mount using the same PEG wax as before. Gravity provides adequate force to polish the sample by hand, with observation by eye enough to tell when the target thickness is approximately reached, although the mount also has a fitting for a micrometre screw for accurate thickness targeting. It may be preferable however to allow the small weight of the mount to provide the force rather than the full guide/holder, so as to have a slower polish placing less stress on the samples and wax.

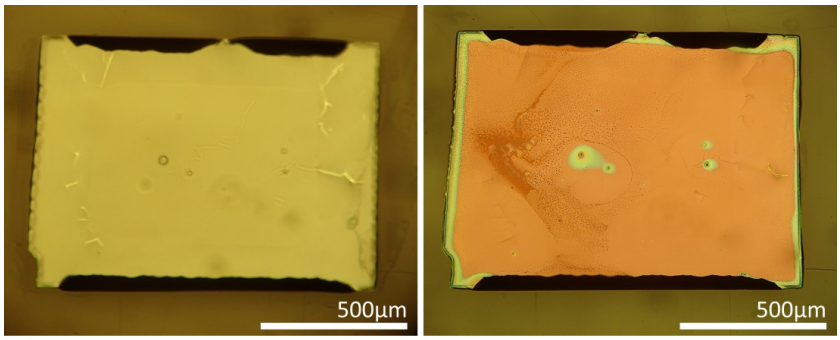

(a) (b)

Figure 3.16: (a) InP etched to InGaAs layer with HCl:H_3PO_4 solution. (b) InGaAs removed with H_3PO_4:H_2O_2:H_2O solution, leaving only II-VI material.

Removal of the glass from the mount also melts the wax on the thinned structures, allowing for re-flow of wax under the samples.

3.6.3.1 Substrate and buffer etch

A significantly shorter process time allows for slower etch rates for a more accurate and predictable etch. HCl:H_3PO_4 (3:1) is used, with an etch rate of 6.6 µm/min. After an etch time of approximately 15 minutes no further gas bubbles are produced, indicating that all of the InP substrate has been removed. Figure 3.16 (a) shows a microscope image of a sample etched to the InGaAs layer. Of note at this stage is the silver colour of this surface, which is easily discernible from the dark InP when viewed under a microscope. The etch selectivity of the solution with InGaAs allows for the sample to remain in the acid until complete substrate removal.

Once the InGaAs is removed, the only remaining material still attached to the glass with the PEG is the II-VI epi-layer. The wax dissolves quickly when the sample is submerged in hot water (approximately 70 °C) and does not damage the epi-layer. After 1–2 minutes in the water the sample is released from the glass.

The InGaAs buffer is then etched as before using H_3PO_4:H_2O_2:H_2O (1:1:6). The sample changes colour over the course of the etch, through red to a translucent yellow-orange (depending on structure reflectivity and transmission characteristics) indicating that the InGaAs is fully removed (see Figure 3.16 (b)). Etch time is 15 seconds for complete

InGaAs removal. It should be noted that the H_3PO_4:H_2O_2:H_2O mixture should be allowed to stand for at least 1 hour before use, to stabilise the etch rate [49] (the solution can be stored for up to a week if necessary without a change in etch behaviour).

The sample does not float to the surface, instead sinking, so can remain on the glass even though the wax is no longer holding it. It can be lifted and printed onto the target substrate via capillary bonding to achieve an optical quality interface. Samples are <3 μm thick, but have been observed to resist cracking under moderate curvature.

3.7 Structure designs

The II-VI samples were grown in batches, or generations, of similar design. Between the generations, characterisation and testing informed design changes for the next growth batch.

The designs can be divided into 3 broad descriptions. The first is the simple design, 5 QWs with carrier confinement layers at either end of the structure. 5 wafers were grown based on this design, which I have described as generation 1. Following this a partial DBR was added, and the QW number increased to 9. 2 wafers were grown initially from this design, although one was without partial DBR layers. I have labelled this generation 2. Following that were further growths of essentially the same design, with minor changes to design layer thicknesses - in general the structures were the same but with higher growth accuracy. These I have labelled generation 2.5, to reflect that the design was essentially unchanged. Generation 3 consists of 3 wafers where the structure included 14 single QWs with no DBR.

This design section is followed by Section 3.7, which summarises the characterisation for each generation, analysing the growth success through PL, XRD and reflectivity measurements and the efforts for substrate removal and epi-layer transfer for each structure (affected by material strain). Following the VECSEL structure characterisation is a brief discussion of a grown 20-period DBR.

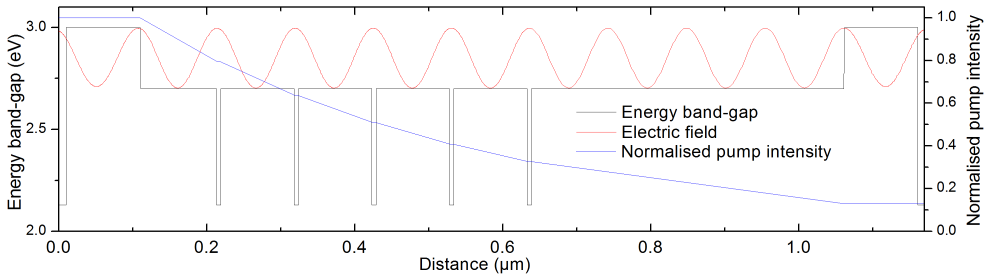

Figure 3.17: Generation 1 design, consisting of 5 quantum wells and a pump absorption region of 10 antinodes. Carrier confinement windows are at either end of the barrier region, and the structure is capped by ZnSe. The pump absorption calculation assumes that the pump light is only absorbed within the barriers.

3.7.1 Generation 1: 5 quantum well structures

Generation 1 consists of one design: 5 quantum wells across 5 antinodes. The structure diagram is shown in Figure 3.17, and the layers detailed in Table 3.2. Contrary to subsequent growth runs, the generation 1 structures had a ZnSe anti-oxidation cap, which was replaced with ZnCdSe to reduce strain in later structures.

Generation 1 Thin-film VECSEL for 540 nm, 5 QWs					
Layer	Material	x	y	Thickness (nm)	Purpose
11	ZnSe	–	–	10	Cap
10	$(Zn_xCd_{1-x})_{1-y}Mg_ySe$	0.53	0.6	100	Carrier confinement
9×4	$(Zn_xCd_{1-x})_{1-y}Mg_ySe$	0.48	0.35	102	Barrier
8×4	$(Zn_xCd_{1-x})_{1-y}Mg_ySe$	0.48	0	4	QW
7	$(Zn_xCd_{1-x})_{1-y}Mg_ySe$	0.48	0.35	101	Barrier
6	$(Zn_xCd_{1-x})_{1-y}Mg_ySe$	0.48	0	4	QW
5	$(Zn_xCd_{1-x})_{1-y}Mg_ySe$	0.48	0.3	109	Pump absorption
4	$(Zn_xCd_{1-x})_{1-y}Mg_ySe$	0.48	0.6	100	Carrier confinement
3	$(Zn_xCd_{1-x})_{1-y}Mg_ySe$	0.48	0	10	Etch-stop/cap
2	$In_xGa_{1-x}As$	0.53	–	200	Buffer layer
1	InP	–	–	–	Substrate

Table 3.2: Generation 1 design layers. Not included: low temperature ZnCdSe buffer layer. Layers 5 and 7 are 4 nm thick QWs, based on empirical data provided by growers, although quantum well thickness was later revised down following simulations.

4 wafers were grown to this design, with designations A3083, A3085, A3086, and A3087. In addition, one further wafer was grown to a similar design but with an anti-resonant sub-cavity, A3088. No offset of RPG wavelength to QW emission is included, to simplify the design.

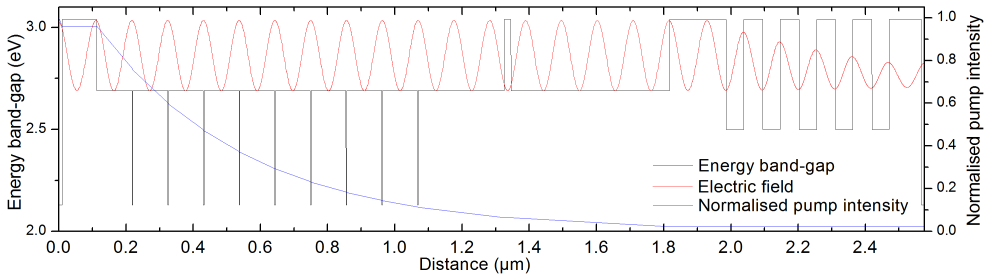

Figure 3.18: Generation 2 design, consisting of 9 QWs and a partial 5.5 period DBR to aid in setting the electric field antinode positions.

Generation 2 Thin-film VECSEL for 540 nm, 9 QWs, 5.5 period DBR					
Layer	Material	x	y	Thickness (nm)	Purpose
17	$(Zn_xCd_{1-x})_{1-y}Mg_ySe$	0.48	0	10	Cap
16	$(Zn_xCd_{1-x})_{1-y}Mg_ySe$	0.56	0.6	103	Carrier confinement
15	$(Zn_xCd_{1-x})_{1-y}Mg_ySe$	0.5	0.32	104	Barrier
14×8	$(Zn_xCd_{1-x})_{1-y}Mg_ySe$	0.48	0	2.1	QW
13×8	$(Zn_xCd_{1-x})_{1-y}Mg_ySe$	0.5	0.32	103	Barrier
12	$(Zn_xCd_{1-x})_{1-y}Mg_ySe$	0.48	0	2.1	QW
11	$(Zn_xCd_{1-x})_{1-y}Mg_ySe$	0.5	0.32	251	Barrier
10	$(Zn_xCd_{1-x})_{1-y}Mg_ySe$	0.56	0.6	20	Carrier confinement
9	$(Zn_xCd_{1-x})_{1-y}Mg_ySe$	0.5	0.32	464	Pump absorption
8	$(Zn_xCd_{1-x})_{1-y}Mg_ySe$	0.56	0.6	113	Transparent window
7×5	$(Zn_xCd_{1-x})_{1-y}Mg_ySe$	0.56	0.6	56.5	Low-n DBR
6×5	$(Zn_xCd_{1-x})_{1-y}Mg_ySe$	0.493	0.25	51.7	High-n DBR
5	$(Zn_xCd_{1-x})_{1-y}Mg_ySe$	0.56	0.6	96	Low-n DBR
4	$(Zn_xCd_{1-x})_{1-y}Mg_ySe$	0.48	0	10	Etch-stop/cap
3	ZnCdSe	–	–	–	Low-T buffer
2	$In_xGa_{1-x}As$	0.53	–	200	Buffer layer
1	InP	–	–	–	Substrate

Table 3.3: Generation 2 design layers, tabulated for growth. Layer 3 thickness for Low-T buffer is unknown, but expected to be <10 nm

3.7.2 Generation 2: 9 quantum well structures with partial DBR

The structure design for generation 2 contains a major structural change when compared to generation 1: the addition of a 5.5 period partial DBR. The design also contains an additional 4 quantum wells for a total of 9, and a pump absorption region of 12.5 antinodes, with an excess-pump absorption region after a carrier confinement layer to avoid absorption and heating within the DBR region. Figure 3.18 and Table 3.3 show the design and layer compositions.

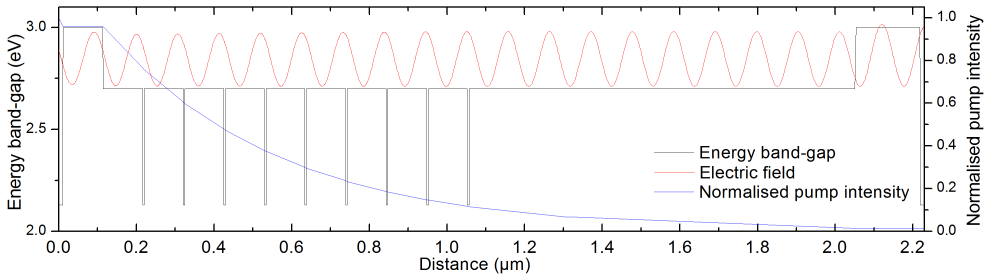

Figure 3.19: A3272 structure layers, which excluded the DBR and mid-structure carrier confinement layers.

Generation 2 Thin-film VECSEL for 540 nm, 9 QWs, no DBR					
Layer	Material	x	y	Thickness (nm)	Purpose
12	$(Zn_xCd_{1-x})_{1-y}Mg_ySe$	0.48	0	10	Cap
11	$(Zn_xCd_{1-x})_{1-y}Mg_ySe$	0.56	0.6	103	Carrier confinement
10	$(Zn_xCd_{1-x})_{1-y}Mg_ySe$	0.5	0.32	104	Barrier
9×8	$(Zn_xCd_{1-x})_{1-y}Mg_ySe$	0.48	0	2.1	QW
8×8	$(Zn_xCd_{1-x})_{1-y}Mg_ySe$	0.5	0.32	103	Barrier
7	$(Zn_xCd_{1-x})_{1-y}Mg_ySe$	0.48	0	2.1	QW
6	$(Zn_xCd_{1-x})_{1-y}Mg_ySe$	0.5	0.32	251	Pump absorption
5	$(Zn_xCd_{1-x})_{1-y}Mg_ySe$	0.56	0.6	20	Carrier confinement
4	$(Zn_xCd_{1-x})_{1-y}Mg_ySe$	0.48	0	10	Etch-stop/cap
3	ZnCdSe	–	–	–	Low-T buffer
2	$In_xGa_{1-x}As$	0.53	–	200	Buffer layer
1	InP	–	–	–	Substrate

Table 3.4: Generation 2 design layers for the structure without DBR. Layer 3 thickness for Low-T buffer is unknown, but expected to be <10 nm

The 5.5 period DBR is made up of alternating quaternary materials: $(ZnCd)_{0.75}Mg_{0.25}Se$ for the high refractive index layer, and $(ZnCd)_{0.4}Mg_{0.6}Se$ for the low. The aim of the DBR layers is to help set the standing wave antinodes to the quantum well positions, as well as providing additional structural support from increased thickness.

Initially, 2 wafers were grown with this structure, designated A3272 and A3273. The design of A3272 corresponds only to the active region, serving as a calibration growth for A3273, and does not include the layers after the first DBR layer, as shown in Figure 3.19 and Table 3.4.

3.7.3 Generation 2.5: 9 quantum well structures with partial DBR

Wafers were grown with similar structure designs to that of generation 2: two nearly identical in design to A3273 with 9 QWs and a 5 period DBR, A3352 and A3361, and following that a sample was attempted using a design with 9 QWs and a 10 period DBR, A3355. The only difference in design between these structures and those of generation 2 was the removal of the final low-n DBR layer (layer 5) and the appropriate increase in size of the final DBR layer to maintain the E-field antinode at the end cap.

3.7.4 Generation 3: 14 QW structures with no DBR

Due to difficulties in growing accurate layer thicknesses, the inclusion of a partial DBR to set the electric field may have been hindering attempts to produce a sample that could reach threshold. This consideration, combined with success in demonstrating a thin-film red VECSEL consisting of only a QW gain region (discussed in Chapter 4), lead to the removal of the DBR from the 3rd generation design. Redistribution of QWs to account for pump absorption profile was considered, however it was decided to retain simplicity in the design. Additional QWs were added to increase gain, with calculations of pump absorption length showing that this would not result in un-pumped QWs. The design is shown in Figure 3.20 and detailed in Table 3.5.

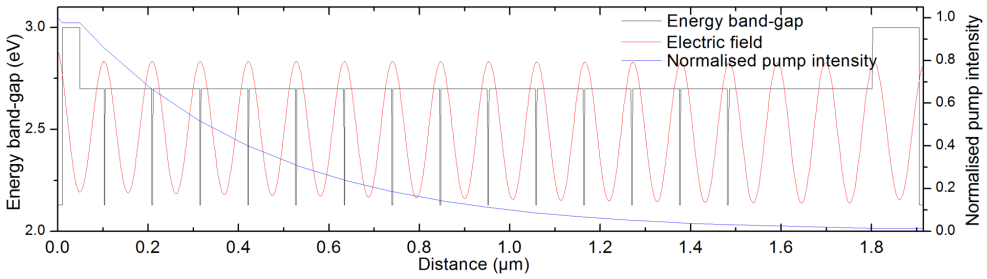

Figure 3.20: Design of the generation 3 structures, with increased QW number, removed DBR and designed for a resonant subcavity. RPG and QW emission wavelengths are both set at 540 nm.

Generation 3 Thin-film VECSEL for 540 nm, 14 QWs, no DBR					
Layer	Material	x	y	Thickness (nm)	Purpose
12	$(Zn_xCd_{1-x})_{1-y}Mg_ySe$	0.48	0	10	Cap
11	$(Zn_xCd_{1-x})_{1-y}Mg_ySe$	0.56	0.6	39	Carrier confinement
10	$(Zn_xCd_{1-x})_{1-y}Mg_ySe$	0.5	0.32	53	Barrier
9×13	$(Zn_xCd_{1-x})_{1-y}Mg_ySe$	0.48	0	2.1	QW
8×13	$(Zn_xCd_{1-x})_{1-y}Mg_ySe$	0.5	0.32	105	Barrier
7	$(Zn_xCd_{1-x})_{1-y}Mg_ySe$	0.48	0	2.1	QW
6	$(Zn_xCd_{1-x})_{1-y}Mg_ySe$	0.5	0.32	323	Final barrier
5	$(Zn_xCd_{1-x})_{1-y}Mg_ySe$	0.56	0.6	102	Carrier confinement
4	$(Zn_xCd_{1-x})_{1-y}Mg_ySe$	0.48	0	10	Etch-stop/cap
3	ZnCdSe	–	–	–	Low-T buffer
2	$In_xGa_{1-x}As$	0.53	–	200	Buffer layer
1	InP	–	–	–	Substrate

Table 3.5: Generation 3 design layers for the structure without DBR.

3.8 Structure photoluminescence & reflectivity studies and SEM thickness measurements.

Photoluminescence (PL) spectra of the structures allows for comparison of material band-gaps and quantum well emission with the design. This is achieved by pumping the sample with a short-wavelength laser and recording the resultant photoluminescence in a spectrometer. As described in Chapter 2, the optical thickness of the layers is crucial in a VECSEL structure, and this is defined as the product of layer length and material refractive index. Surface-PL spectra taken at 77 K allow for peaks corresponding to individual material band-gaps to be distinguished, providing a crucial tool for material composition characterisation. 77 K surface-PL was measured using a grating spectrometer and a He-Cd laser with emission at 325 nm as the excitation source. Surface-PL measurements taken at room temperature, closer to the operating temperature, give indications of structure resonances and their modulation of the quantum well emission, and these were recorded using a Jobin-Yvon HR460 grating spectral analyser (1200 g/mm grating, Si detector) before and after the thin film transfer. PL excitation was provided by a GaN diode emitting at 405 nm, focussed to a spot size of approximately 50 μm radius with power up to 42 mW, corresponding to an

excitation density of approximately 500 W/cm^2.

Edge-PL spectra provide a direct measurement of the QW emission without this modulation. Edge-PL is taken by pumping a cleaved sample near to the edge, and collecting the edge-emitted light directly emitted from the QWs into the spectrometer.

Reflectivity is a further tool to characterise the layer structure of a grown wafer. For a full gain-mirror VECSEL structure, it provides information on the DBR stop-band, structure resonance wavelength and to an extent QW emission. For the thin-device structures, its usefulness is reduced as the reflectivity is dominated by a sinusoidal pattern in the reflectivity/wavelength relationship, from constructive and destructive interference from the Fabry-Pérot etalon set up from the total structure length. Some further information can be found by observing the modulations of this interference due to the layers within the structure, however the causes of the modulations are difficult to categorically identify.

A more helpful tool in the analysis of the structure layer thicknesses is direct measurement through scanning electron microscopy (SEM) of a cleaved edge. This allows for measurement of the thicknesses of some of the visible layers, and approximate modelling of these thicknesses allows for judgment of the device's RPG and subcavity resonances.

Both 77 K spectra and cleaved SEM measurements were undertaken by our collaborators at the City College New York.

Each design generation is discussed individually in this section, and as the growth techniques mature there is a general trend in material composition and QW emission wavelength becoming closer to design.

3.8.1 Generation 1

Before the growth of the wafers of generation 1, equipment failure removed control over the flux ratio so material composition and band-gap drifted over the course of the growths.

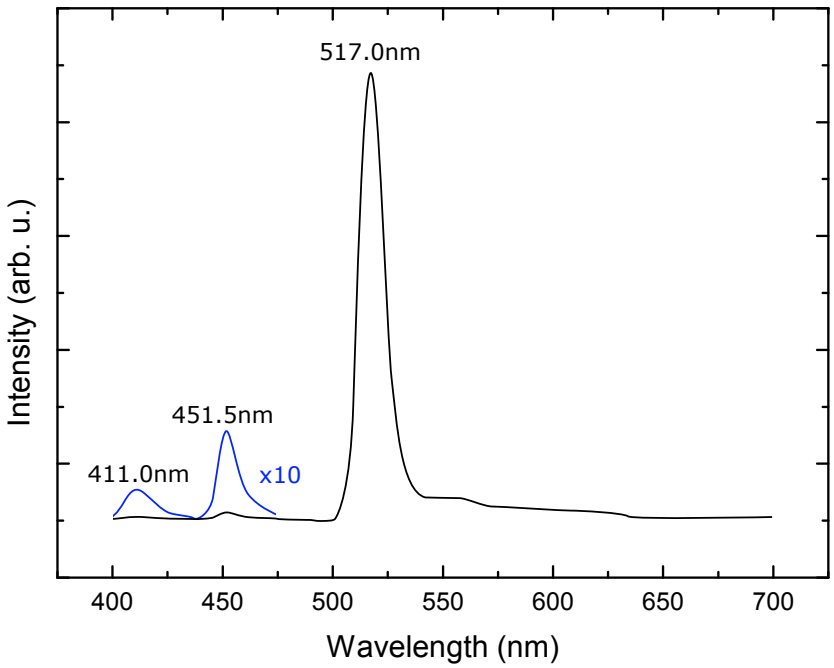

Figure 3.21: A3083 surface-PL at 77 K, with 3 peaks corresponding to the QW emission, pump-absorbing barrier and carrier confinement layers (517 nm, 451 nm and 411 nm respectively).

Figure 3.21 (b) shows the surface-PL of the first grown wafer at 77 K, with peak wavelengths of 411.0 nm, 451.5 nm and 517 nm; corresponding to photon energies of 3.02 eV, 2.74 eV and 2.40 eV respectively. The bandgap of ZnCdMgSe material has been observed to increase by approximately 0.07 eV when cooled from room temperature to 77 K, so the designed values for the layers are 3.07 eV and 2.77 eV for the carrier confinement material and pump absorbing barrier material, with QW transition energy of 2.37 eV. This shows that the material compositions of this first structure were relatively accurate in terms of band-gap design.

Similar characterisations of A3085, A3086, A3087 and A3088 were performed. Surface-PL measurements of the other structures show the band-gaps of the materials progressively drifting from their starting/design values. The quantum well emission for A3087 was at 539.5 nm at 77 K, whereas the design was for QW emission wavelength of 540 nm at room temperature.

Reflectivity measurements of simple structures can provide estimations of thickness from the period of constructive and destructive interference from the Fabry-Pérot

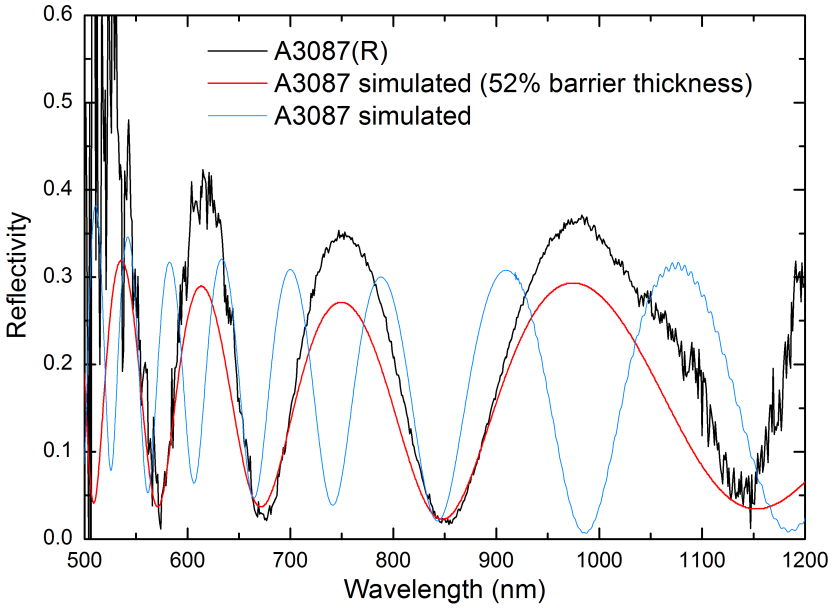

Figure 3.22: Reflectivity spectra for A3087 (black), the simulated A3087 design (blue), and a fitted spectrum with 52% barrier thickness (red).

etalon of the semiconductor film. Reflectivity of A3087, taken at room temperature using a Jobin-Yvon HR460 grating spectral analyser (1200 g/mm grating, Si detector), indicates that the structure is significantly shorter than designed, approximately half thickness, as shown in Figure 3.22.

Reflectivity and PL, along with XRD, measurements show a disparity between design and growth which is concerning, and raise doubts as to the viability of these structures for laser operation in the VECSEL format, which must have specific layer thicknesses. Later generations showed better accuracy in material thickness.

Surface-PL at room temperature was collected using an f=80 mm lens. The collimated light was subsequently focussed into the Jobin-Yvon HR460 grating spectrometer with an f=300 mm lens. At room temperature, the surface-PL shows fewer features, with only the main peak visible.

A3087 shows the strongest PL emission, although it is offset from the RT design wavelength of 540 nm. A3085 was closest to RT design emission with 541 nm.

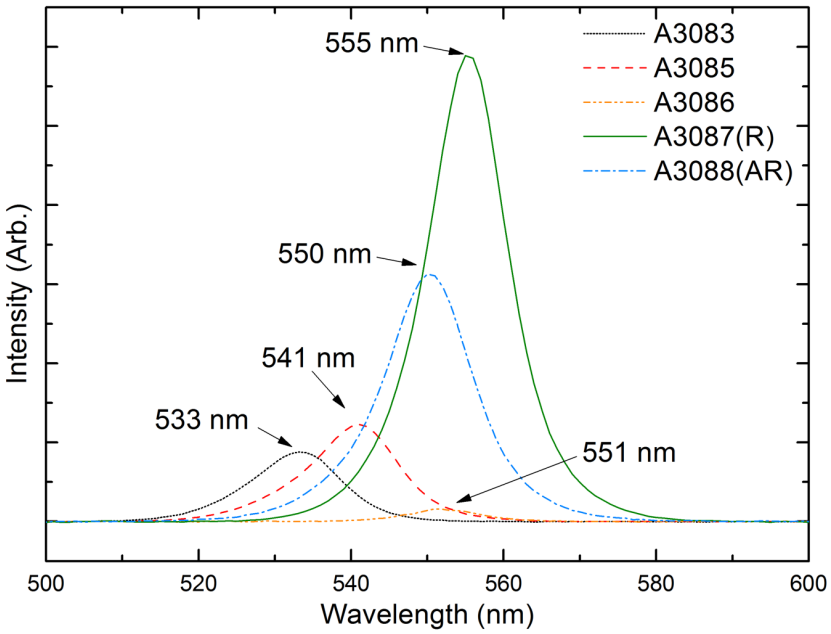

Figure 3.23: Room temperature Surface-PL measurements of the first generation structures, wafer centres.

3.8.2 Generation 2

Generation 2 added additional material compositions due to the 5.5 period DBR. While the carrier confinement layer material of the previous generation was used as the low-n DBR material, a lower band-gap material at 2.5 eV was added for the high n DBR layers. With an additional material composition, the limitations of the II-VI growth described in 3.2.2.1 result in more cell temperature readjustments per growth (to grow the different quaternary compositions) and so more uncertainty in material composition.

Initial 77 K surface-PL characterisations of both A3272 (9 QWs, no DBR layers) and A3273 (9 QWs with 5.5 period DBR) are shown in Figure 3.24 (a) and (b) respectively. The comparison between the recorded values (corresponding to material bandgaps and QW emission) and the design values adjusted for material temperatures of 77 K are given in Table 3.6. Designed values for the layers are 3.07 eV, 2.77 eV and 2.57 eV for the low-n DBR/carrier confinement material, pump absorbing barrier material and high-n DBR material respectively, with QW transition energy of 2.37 eV.

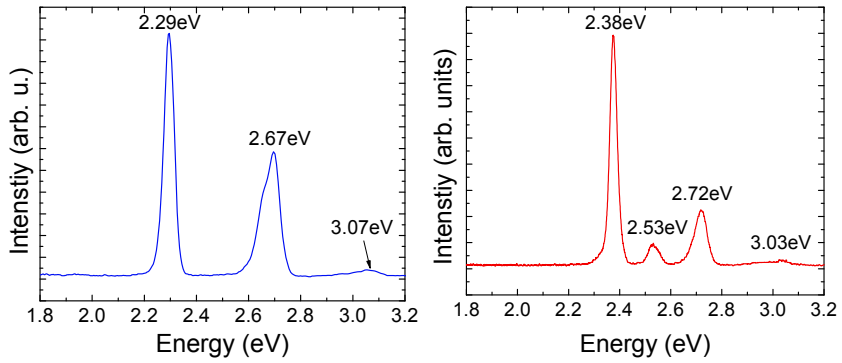

Figure 3.24: 77 K surface-PL measurements (a) A3272, with peaks at 3.07 eV (confinement window material), 2.67 eV (pump absorbing barrier) and 2.29 eV (QW emission, 541 nm). (b) A3273, peaks at 3.03 eV (low-n DBR layer), 2.72 eV (barrier), 2.53 eV (high-n DBR layer), and 2.38 eV (QW emission, 521 nm).

Generation 2: 77 K surface-PL comparison			
Bandgap	Design (estimated)	A3272	A3273
Low-n DBR layer (eV)	3.07	3.07	3.03
Pump absorbing barrier (eV)	2.77	2.67	2.72
High-n DBR layer (eV)	2.57	–	2.53
QW transition (eV)	2.37	2.29	2.38

Table 3.6: Comparison of material band-gaps (at 77 K) for generation 2 structures, from the recorded values in Figure 3.24. A3273 shows a closer match in QW emission and barrier composition, while both show relatively accurate growth of the low-n DBR material, also the carrier confinement layer material.

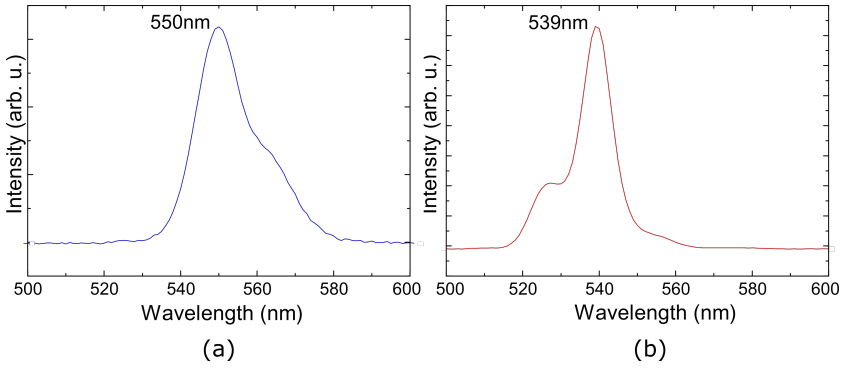

Figure 3.25: Surface-PL of (a) A3272 and (b) A3273. Both show signs of resonance enhancement from the subcavity in their emission spectra.

From Figure 3.24 and Table 3.6, it can be seen that the material compositions of A3273 are closer to the design than A3272. Room temperature surface-PL shown in Figure 3.25 confirms that the QW emission of A3273 is accurate to the design at 539 nm, while A3272 is significantly higher at 550 nm.

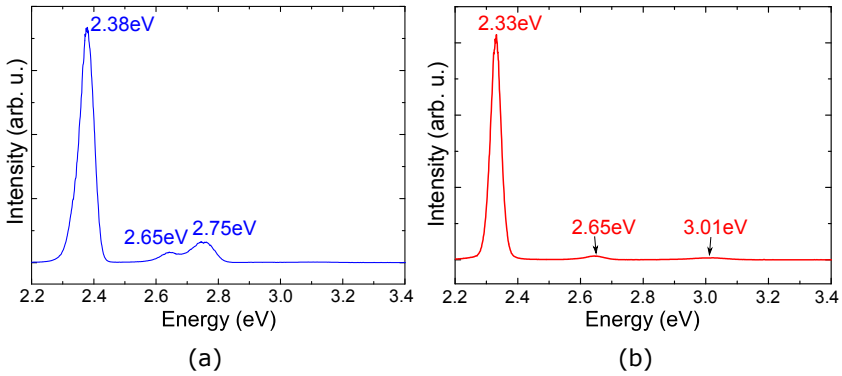

Figure 3.26: Surface-PL at 77 K of (a) A3352 and (b) A3361. Peaks visible are taken to be QW emission (the main peak around 2.3 eV), barrier layers (around 2.6 eV) and low-n DBR layer (around 3.0 eV). A3361 shows closest match to design.

3.8.3 Generation 2.5 – 5-period DBR structures

While the generation 2.5 5-period DBR structures are very similar in design to the generation 2 structures, higher emphasis was placed on material lattice matching to enable robust thin film transfer. Both of the generation 2.5 structures, A3352 and A3361, showed significantly better transfer capabilities (discussed in Section 3.9.3) and so were studied in more detail. A3361 formed the basis of a study into the PL characteristics post-transfer, discussed in this section.

Surface-PL for the two 5.5 period DBR samples (A3352 and A3361) at 77 K are shown in Figure 3.26.

Comparison of the 77 K surface-PL indicates that the material band-gaps of A3352 do not match those of A3361 or the design. Design band-gaps at RT are 2.5 eV, 2.7 eV and 3.0 eV; adjusting for 77 K: 2.57 eV, 2.77 eV and 3.07 eV for high n DBR layer, pump-absorbing barrier and low n DBR layers respectively. The comparison is shown in Table 3.7.

In both materials, the pump-absorbing barrier is accurate to specifications. The short wavelength pump did not penetrate past the first low-n 3.0 eV layer, so the lack of a visible peak at 2.5 eV is not unexpected. This allows us to determine that the material composition accuracy of A3361 is better than that of A3352 for this material for the confinement and DBR layers.

Generation 2.5: 77 K surface-PL comparison			
Bandgap	Design (estimated)	A3352	A3361
High-n DBR layer (eV)	2.57	–	–
Pump absorbing barrier (eV)	2.77	2.65	2.65
Low-n DBR layer (eV)	3.07	2.75	3.01

Table 3.7: Comparison of the observed surface-PL peaks at 77 K for A3352 and A3361. Pump laser expected to be absorbed before reaching the high-n DBR layer, so there is no recordable signal.

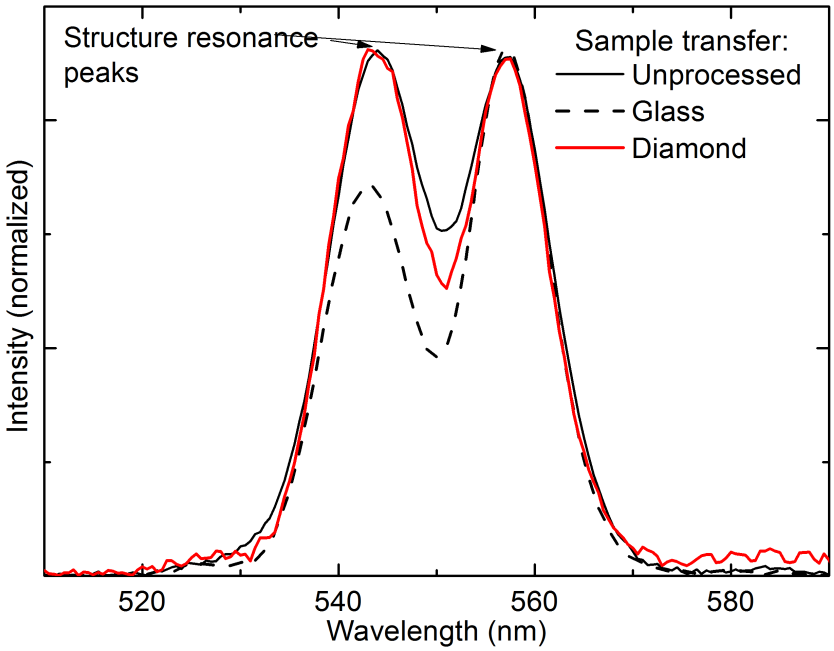

Figure 3.27: Surface photoluminescence at room temperature of a sample before and after processing, both transferred to glass and diamond. The two peaks correspond to sub-cavity resonances. Peak height differences for the glass-substrate structure are explained by the thermal shift of the quantum well emission.

Due to its successful transfer characteristics, a study of the post-transfer optical characteristics of A3361 was carried out. Measurements of PL were recorded using the same setup as previously described, for unprocessed samples and after transfer to both glass and diamond substrates. The sample is mounted on a thermo-electric cooler (TEC) with thermally conductive paste for temperature control. Figure 3.27 shows surface-PL measurements before and after processing for a sample transferred to glass and another to diamond.

The structure contributes two resonance peaks to the emission spectral profile at room temperature, caused by the sum of the Fabry-Pérot etalons set up by the interfaces

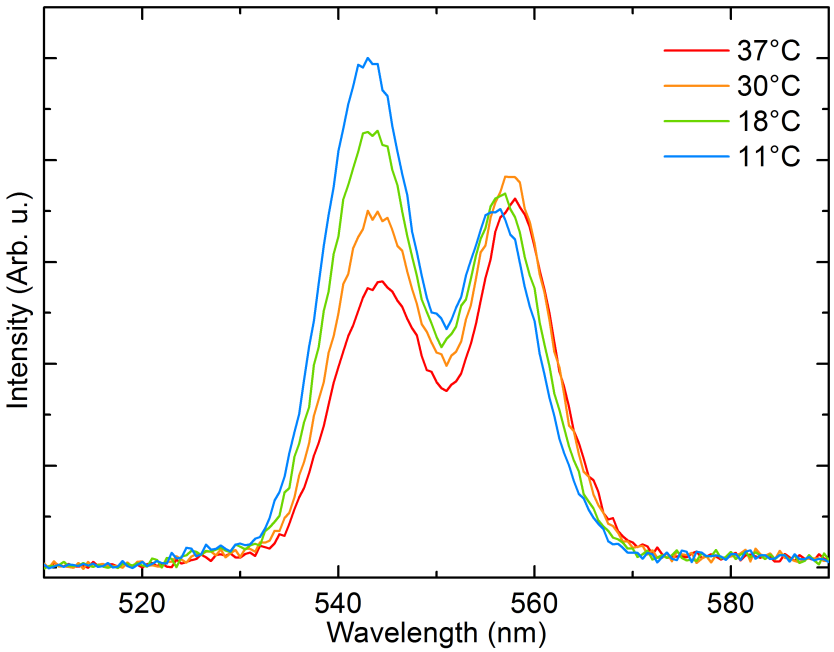

Figure 3.28: Surface Photoluminescence of the sample on diamond as the sample mount temperature is increased. Relative peak height change indicates the redshift of the underlying quantum well emission at increased temperatures.

within the structure, although as with the previous structures with more complex designs (and unknown true layer thicknesses) inaccuracies in the growth mean that these resonances do not match the optical model of the structure.

The absolute values for the processed samples cannot be accurately compared with the unprocessed sample, which includes back-reflection from the InGaAs buffer layer. What is notable, however, is that a distinct difference can be seen in the relative peak heights for the sample on glass. We attribute this to a pump-induced temperature increase being stronger for the sample bonded to glass. By observing the surface-PL of the sample on diamond with a controlled change of sample temperature using the TEC, shown in Figure 3.28, it can be seen that the relative peak heights of the resonances shift due to the underlying redshift of the quantum well PL.

To evaluate the quantum well emission after transfer, Figure 3.29 shows the edge-PL for structures bonded to glass and diamond.

The sample on glass shows a quantum well emission redshift of 200 nm/W, compared to the sample on diamond which shows no measurable change. This pump-induced

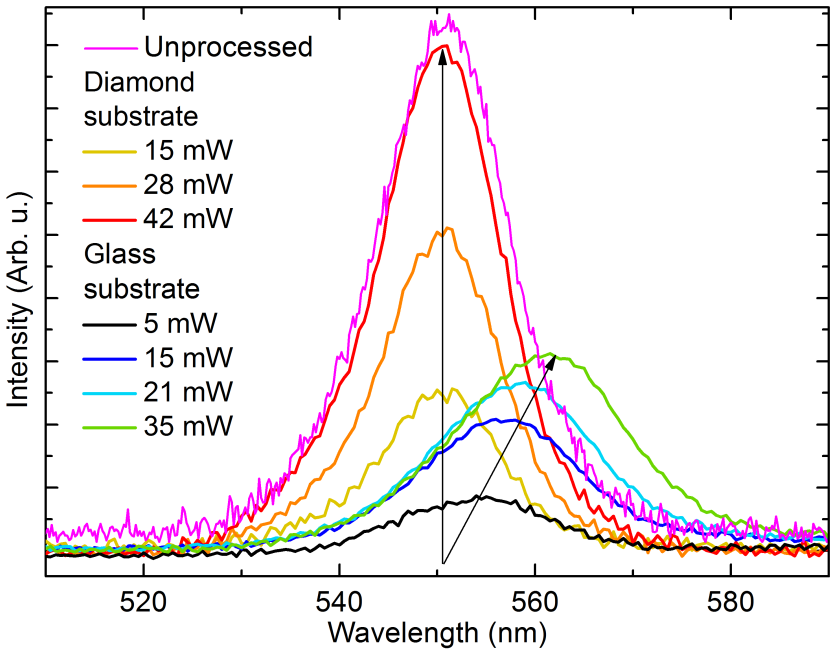

Figure 3.29: Quantum well emission with increasing pump power for structures transferred to diamond and glass. Arrows are included to help guide the eye and indicate wavelength shift with increasing pump power. For the sample bonded to glass, this corresponds to a spot temperature change of 60 K at 35 mW pump.

redshift of the QW emission with pump power explains the observed relative intensity shift of the surface-PL resonance peaks for the sample on glass.

To quantify the thermal shift of the QW emission, the edge-PL for an unprocessed sample is measured at fixed low pump power with varying mount temperatures.

Figure 3.30 shows a 0.13 nm/K redshift in the emission wavelength for the ZnCdSe/ZnCdMgSe multiple QW structure. This compares well to the predicted thermal shift of 0.11 nm/K calculated by the temperature dependence of band-gaps in the quantum well model described in section 3.4 [7]. Thus we estimate that the pump-induced temperature increase in the gain region for the sample bonded to glass was 60 K for only 35 mW pump power.

Structure thickness measurements with SEM for A3352 (Figure 3.31) and A3361 (Figure 3.32) both show significant deviation from the designed thicknesses. This is a significant issue for a VECSEL structure, where the layer interfaces are positioned specifically for RPG wavelength and subcavity resonance wavelength, and especially for these structures where the 5 period DBR is designed to set the electric-field antinodes over

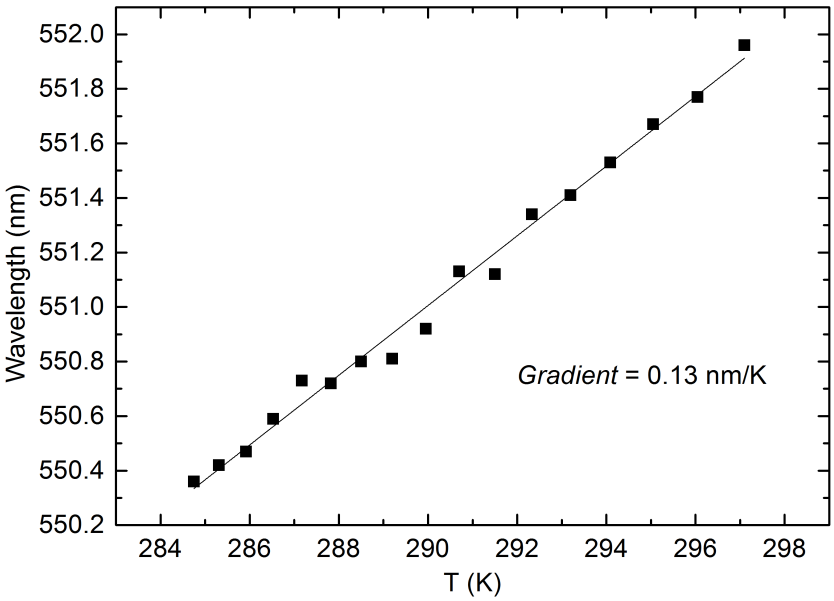

Figure 3.30: The ZnCdSe quantum well emission wavelength redshift with temperature is found to be 0.13 nm/K.

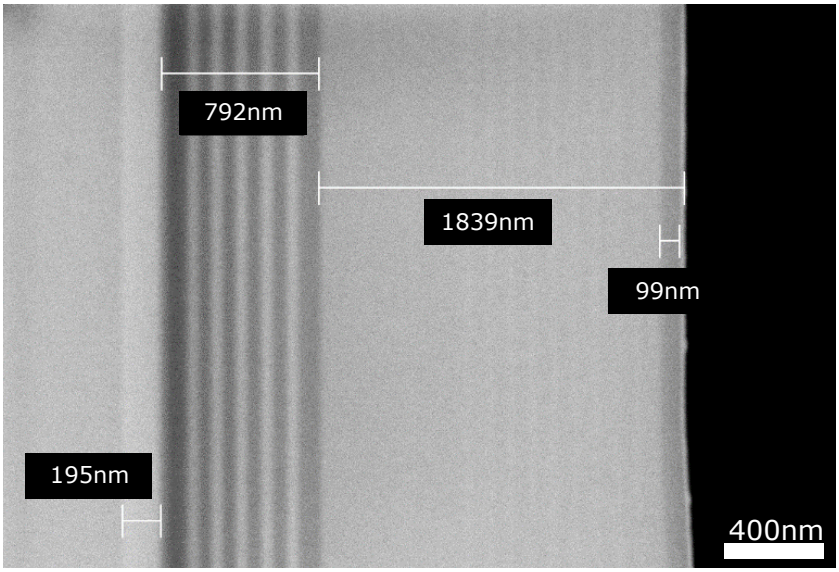

Figure 3.31: SEM of the cleaved edge of A3352. DBR layers are clearly visible and QWs are also well defined.

the QWs. While it appears that there are differences between specific layer thicknesses within sections of the structure (e.g. DBR layer pair thicknesses changing throughout growth), it is informative to compare the full section thicknesses with design, given in Table 3.8 for A3352 and A3361.

Significant deviation from designed thicknesses are shown in both A3352 and A3361. With changes in the layer thicknesses for both DBR and active region sections, the

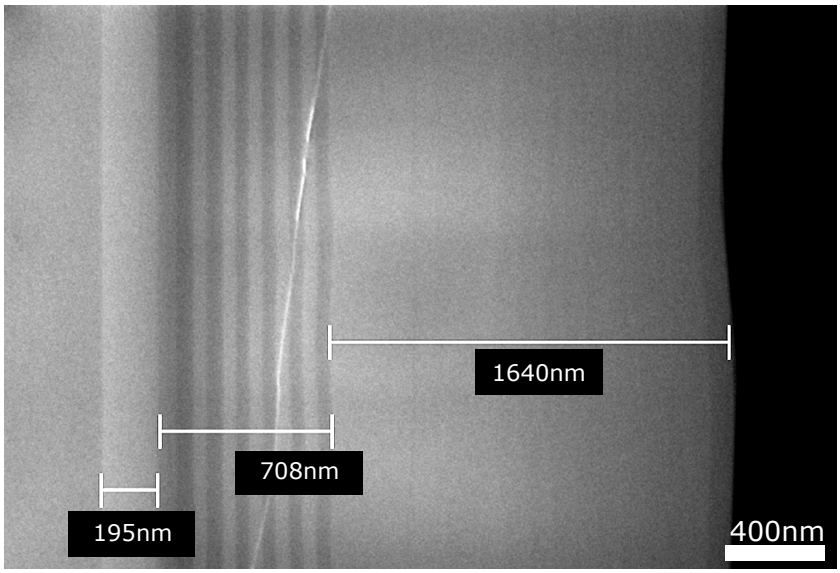

Figure 3.32: SEM of the cleaved edge of A3361. Structure shows surface distortion which is confirmed by a subsequent AFM measurement showing features of similar depth and width on the surface.

Generation 3: SEM layer thickness comparison			
Section	Design (nm)	A3352 (nm)	A3361 (nm)
InGaAs buffer	200	195	195
DBR	644	792	708
Active region	1913	1839	1640
QW separation (Average)	104	115	96

Table 3.8: Comparison of material 77 K band-gaps for generation 2 structures, from the recorded values in Figure 3.22. A3273 shows closer match in QW emission and barrier composition, while both show relatively accurate growth of the low-n DBR material, also the carrier confinement layer material.

alignment of DBR to QW position is wrong for both A3352 and A3361, with further difficulties introduced in the variation within the QW separation/RPG wavelength.

A non-flat epitaxial surface is shown in the SEM of A3361 in Figure 3.32, and to confirm that this is not an artefact of SEM, the epitaxial surface is measured using Atomic Force Microscopy (AFM) using a Park XE-100 atomic force microscope. The surface was shown to have ripples of up to 40 nm depth on a micron-scale.

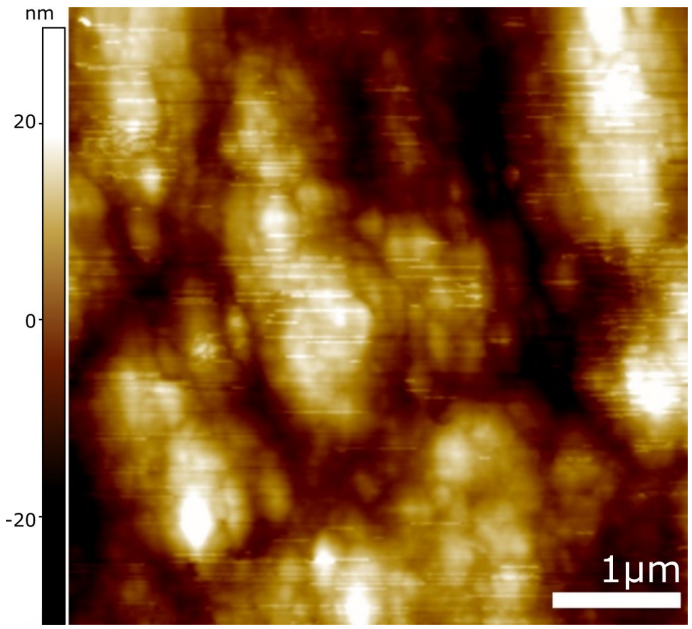

Figure 3.33: AFM measurement of A3361 surface, confirming the surface 'ripples' indicated by SEM.

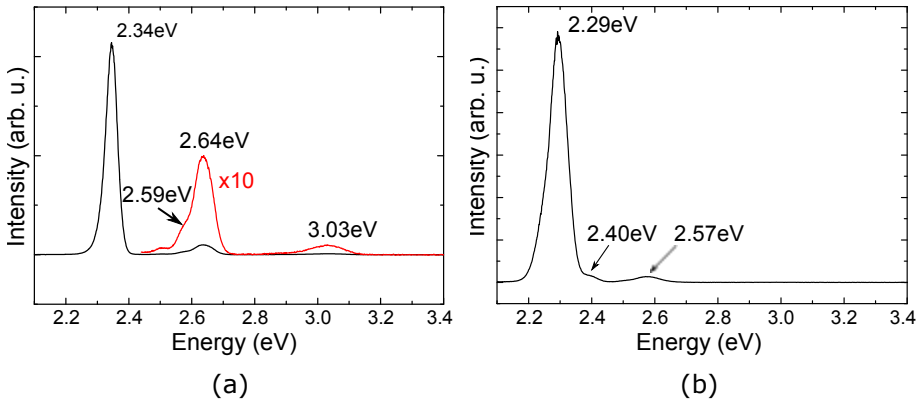

Figure 3.34: A3355 characterisation: Surface-PL at (a) 77 K and (b) room temperature. The (resonance enhanced) quantum well emission and the pump-absorbing barrier material are observed to have the correct energy band-gaps. Both DBR layer materials have slightly higher than designed band-gaps.

3.8.4 Generation 2.5 – 10 period DBR structures

As well as the two 5.5 period DBR samples, one structure was grown with 10.5 DBR pairs. In other aspects the design is the same as before. The increased pair number was to enhance the resonance effects and investigate progress towards a standard VECSEL structure with full DBR. 77 K surface-PL in Figure 3.34 (a) shows accurate emission for the QWs, with reasonably accurate material band-gaps.

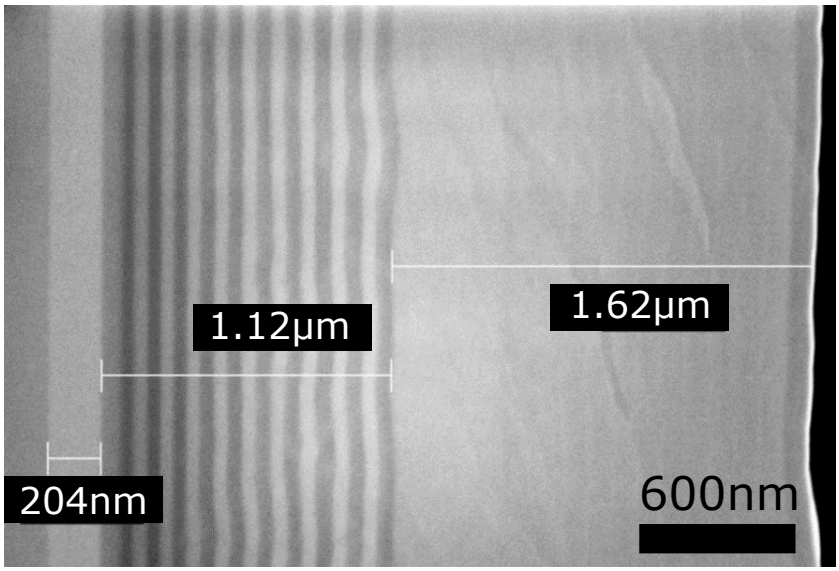

Figure 3.35: SEM image of A3355, showing ripples during material growth. Also noticeable is the increasing thickness of the DBR layers as growth progressed (from left to right).

Room temperature surface-PL confirms accurate main peak wavelength at 540 nm in Figure 3.34 (b). The peak shape is comparable to the main peak seen in the 77 K measurement.

An SEM of the cleaved edge provides layer thickness characterisation in Figure 3.35. DBR layer thickness can be seen to increase as growth progressed, although in other respects the section thicknesses match relatively well to design compared to other structure growths, with a 5% shorter DBR and 4% shorter active region and QW separation when compared with the design.

3.8.5 Generation 3: 14 QW no-DBR structures.

Due to the variation in layer thickness of the previous structure growths, and the successful demonstration of the red thin-film VECSEL (discussed in Chapter 4), generation 3 returned to a more simplistic design to remove some of the possible problems brought on by the partial DBR. 3 wafers were grown to this design, A3602, A3611 and A3612. 77 K surface-PL for these structures, shown in Figure 3.36, have very similar layer peaks, each demonstrating lower band-gap material than designed with barrier material at approximately 2.51 eV and confinement layer material 2.85 eV, compared

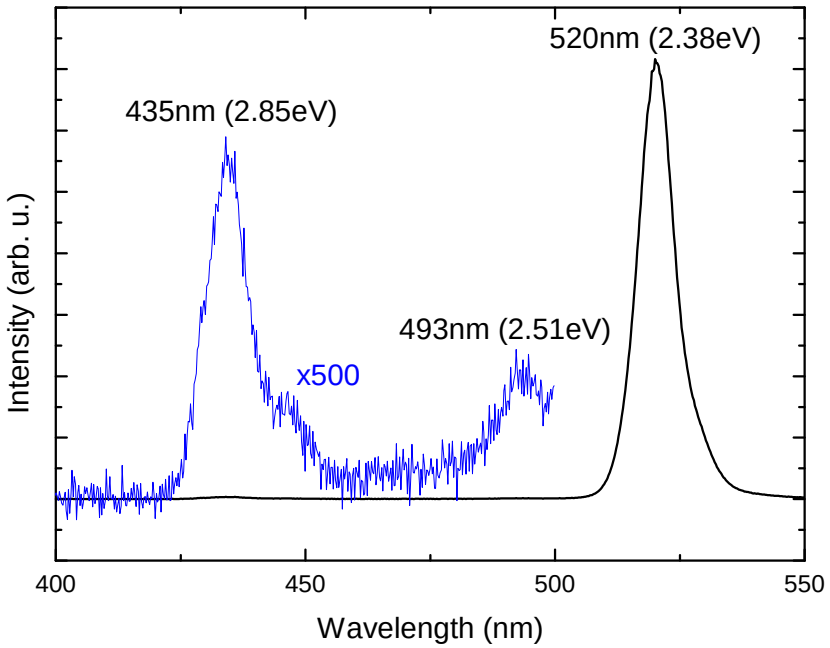

Figure 3.36: Surface-PL at 77 K for A3602. Carrier confinement and barrier layers are indicated at 2.85 eV and 2.51 eV respectively, both about 0.2 eV below design. Similar lower bandgap material is observed for A3611 and A3612.

to the designed 2.77 eV and 3.07 eV respectively. QW emission wavelength varies between the structures, with the room temperature PL showing emission wavelengths of 530 nm, 546 nm and 527 nm in A3602, A3611 and A3612 respectively, as shown in Figure 3.37.

SEM measurements of the structures indicate that they are shorter than designed with shorter spacing between QWs, an average spacing of 98.0 nm for both A3602 and A3611, and 100.8 nm for A3612. An example is given in Figure 3.38 for A3611. This reduction in RPG wavelength combined with the longer wavelength emission of A3611 makes this structure unsuitable for a VECSEL device.

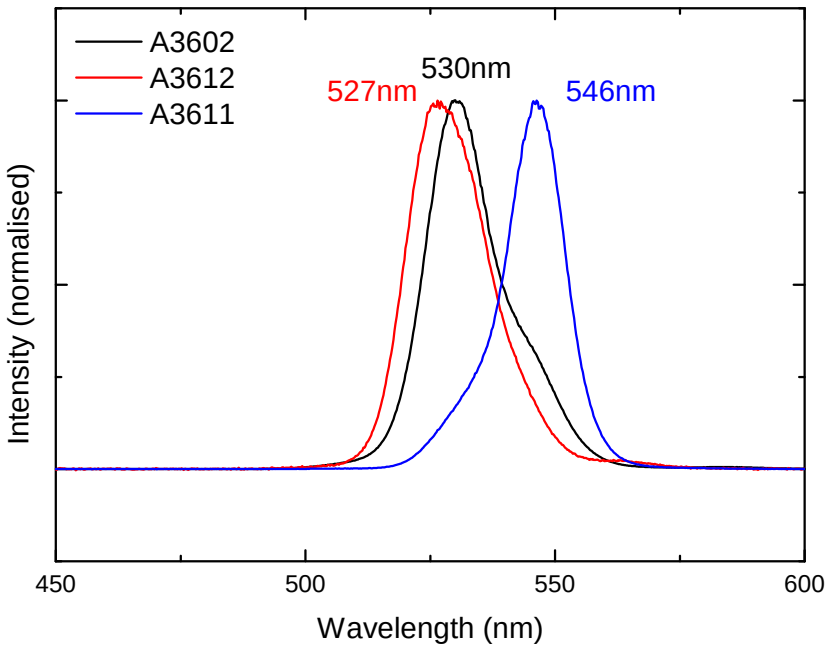

Figure 3.37: Surface-PL at room temperature for A3602 (black), A3611 (blue) and A3612 (red), showing A3611 with longer wavelength emission at 546 nm.

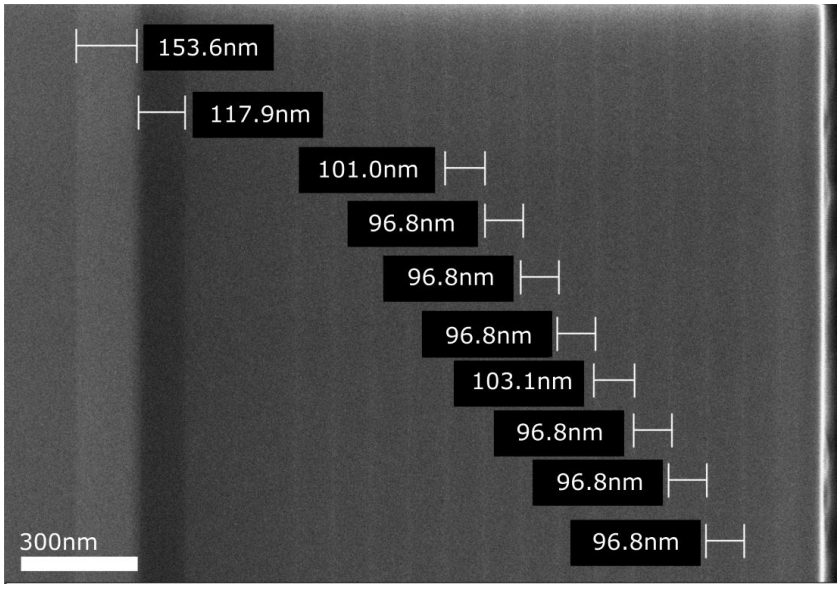

Figure 3.38: SEM image of A3611, showing QW spacing that averages to 98.0 nm, equal to that of A3602 and close to the 100.8 nm of A3612.

3.9 20 period DBR

Grown prior to generation 2.5, a 20 period DBR was designed and grown to investigate possibilities in development of full VECSEL structures with grown DBRs. The design is a simple expansion of the partial DBRs of the generation 2 structures: two alternating quaternary materials, with top and bottom ZnCdSe caps, and is shown in Figure 3.39.

The peak reflectivity was designed for 540 nm, however fluctuations in growth rate altered this in the grown structure to be closer to 560 nm.

The different features of the measured DBR reflectance spectrum, shown in Figure 3.40 compared with the calculated reflectivity, can be partially explained. The flattening of the reflectivity below 500 nm is caused by the absorption of the high n material, band-gap 2.5 eV. The reflectivity below 480 nm is therefore entirely from the Snell's law interface reflection for light passing from air to ZnCdSe (from n=1 to n=2.4), and can be used to calibrate the magnitude of the recorded reflectivity. The reduction in reflectivity on the red side of the main stop band is caused by absorption from the ZnCdSe end caps, (2.1 eV).

Aspects of the spectrum such as the asymmetric peaks to the red and blue side are more difficult to characterise, with changes in the layer thicknesses throughout growth adding uncertainty to the periodicity. The enhancement to the blue-side peaks and the suppression of the first red-side peak indicates that the reduction in the peak reflectivity is combined with unknown side-peaks due to these changing layers. The simulation shown in Figure 3.40 is for a DBR with 7 nm thicker high-n DBR layers, and

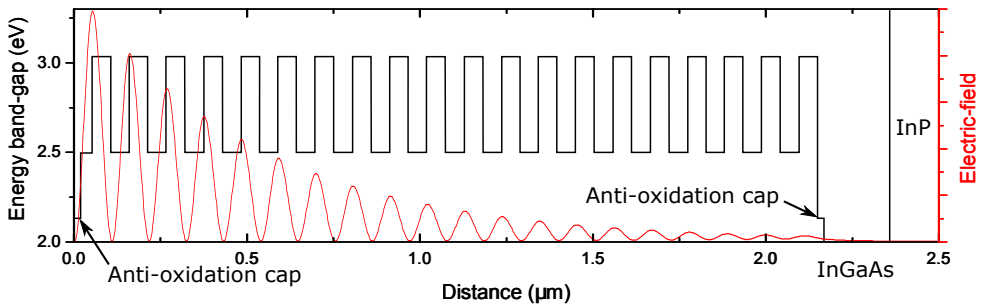

Figure 3.39: Design for a 20 period ZnCdMgSe DBR. Anti-oxidation cap on substrate-side to allow for epi-layer transfer.

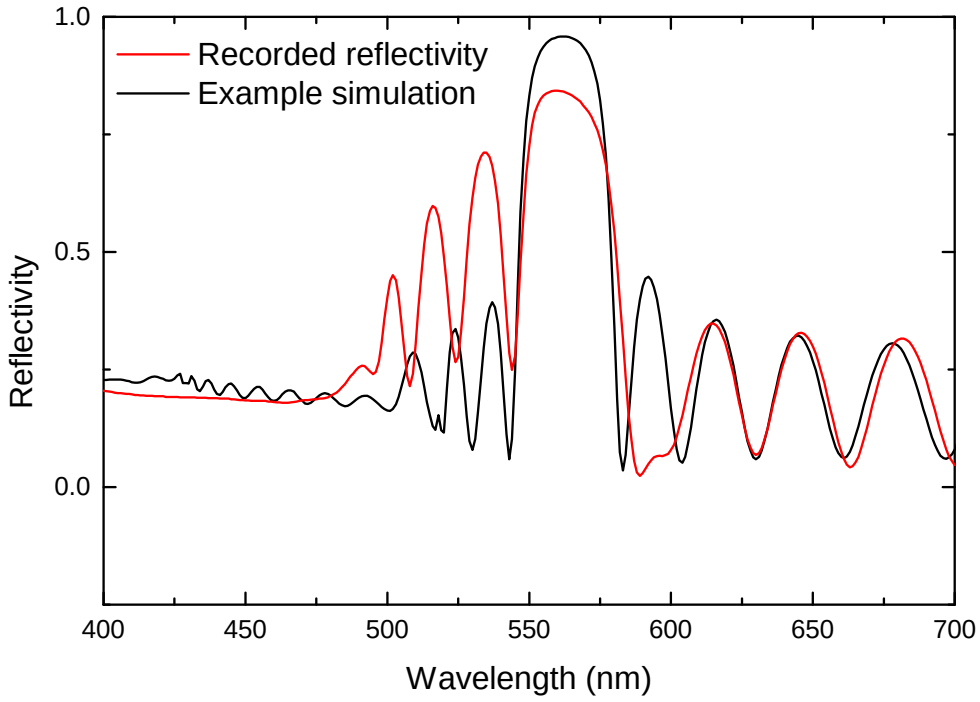

Figure 3.40: Measured reflection spectrum with simulation partially fitted. The match of the Fabry-Perot oscillation indicates correct structure thickness, but deviation from design in the details.

matching of the Fabry-Pérot oscillation in wavelength allows for total II-VI structure thickness confirmation.

3.10 Structure strain and transfer

While photoluminescence spectra can show the material band-gaps and QW emission of the material, crucial to the thin-film devices are the transfer characteristics – directly related to the material strain and overall strain of the device. X-ray diffraction (XRD) measurements , carried out by our collaborators at City College New York, allow for the strain in a structure to be measured, with each material within a structure contributing a peak with magnitude increasing relative to its thickness. The main peak in each measurement is that of InP, and material peaks at lower angles indicate compressively strained material ($\Delta a/a_0 > 0$ as defined in Chapter 2) and at higher angles tensile strained material ($\Delta a/a_0 < 0$). HRXRD was performed for the structures using a Bruker D8 DISCOVER [50].

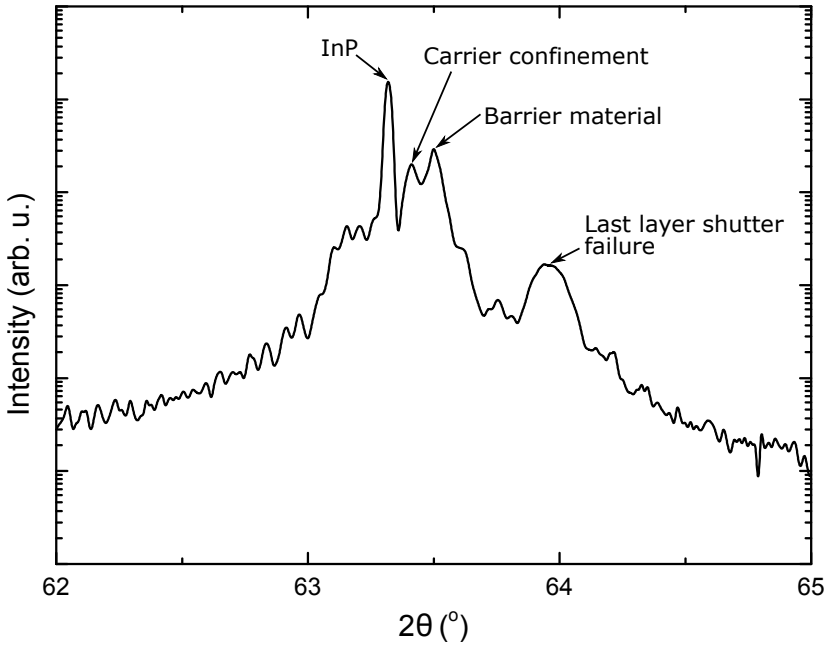

Figure 3.41: XRD measurement for A3083, with estimated peak causes indicated

3.10.1 Generation 1

The ternary alloy ZnCdSe is expected to be lattice-matched and produce a peak that coincides with InP. Thus, the other main peaks are taken to be the quaternary alloys for the window and pump-absorbing barrier materials

Figure 3.41 shows the XRD measurement for A3083. The Zn shutter stuck during the growth of the final capping layer, so A3083 contains a strained layer with composition far from the lattice-matched $Zn_{0.48}Cd_{0.52}Se$. This is clearly visible in the strong peak to the right of Figure 3.41 at approximately 64 ° . Well defined fringes at such a high angle imply good crystal growth quality. Peak intensity in XRD is proportional to the volume of scattering centres, so the higher peak corresponds to the higher total material thickness. Therefore we can determine that the pump absorbing barrier material (2.6 eV) is that of the higher secondary peak, while the lower of the secondary peaks is that of the carrier-confinement window layers.

As with the surface-PL described in Section 3.7.1, XRD measurements were made for all structures in the growth generation. The drift of the material properties caused by

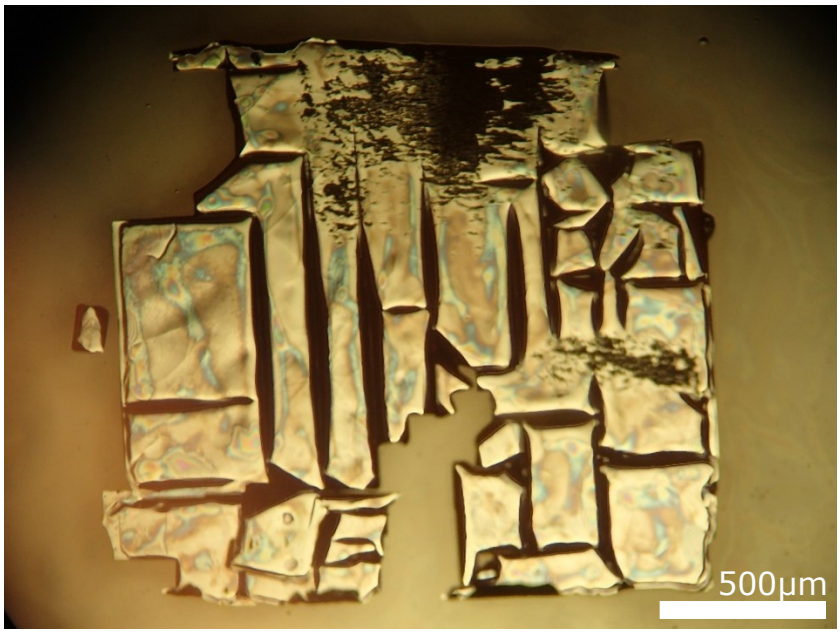

Figure 3.42: A3087 sample following processing to remove the substrate. The InP is mostly removed (residual InP is visible at the top and to the right) but strain has caused catastrophic fracturing across the sample.

equipment failure produces a shift of the material peaks tending to move away from the main InP peak, corresponding to increased tensile material strain over time.

This strain in the structures meant that the only viable processing method was the via-hole method, A3083 and A3085 being used during the development of the procedure. Shown in Figure 3.42 is an attempt at full substrate removal of an A3087 sample, etched to the InGaAs layer.

It is visible that the strain has not caused cracking where residual InP substrate is present (at the top of the sample), and it is only once the substrate is removed that the tensile strain of the structure causes cleaving throughout the sample.

3.10.2 Generation 2

For the generation 2 structures, A3272 with no DBR appears balanced in the XRD measurement in Figure 3.43 (a) with equal peaks of equal magnitude to the tensile and compressive sides of the central peak, while A3273 with DBR shows tensile strain.

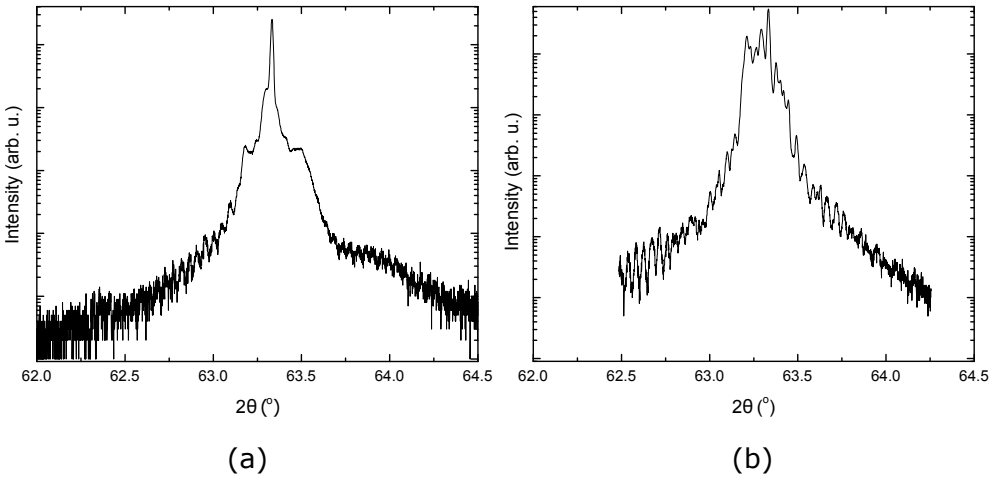

Figure 3.43: (a) A3272 XRD, showing low strain in the structure. (b) A3273 XRD, showing slight compressive strain.

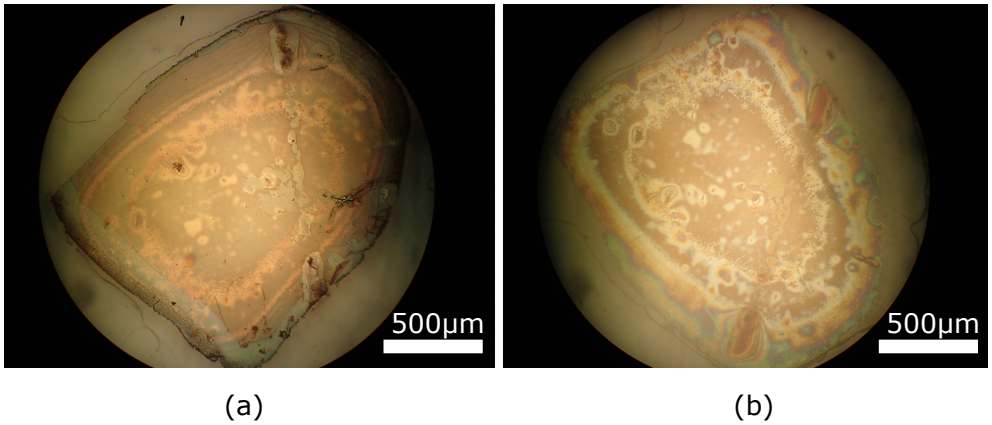

Figure 3.44: A3272 sample transferred to diamond, damaged by pump beam translated across the sample. (a) Rear side of the structure (substrate removed) (b) Epi-side of structure, through diamond.

A3272 was able to be transferred from substrate, and a major part of the transfer development was performed using this structure.

Removal of the structures from substrate was performed using the transfer method, with more success with A3272 than A3273. Pumped A3272 samples transferred to diamond are shown in Figure 3.44.

It can be seen from Figure 3.44 that a bond in the centre of the sample has been achieved; the rust-brown is the sample transmittance colour unchanged by interference fringes, indicating optical contact. The lighter patches are areas where the bond is less good, and the other colour bands indicate where the sample is no longer bonded to the

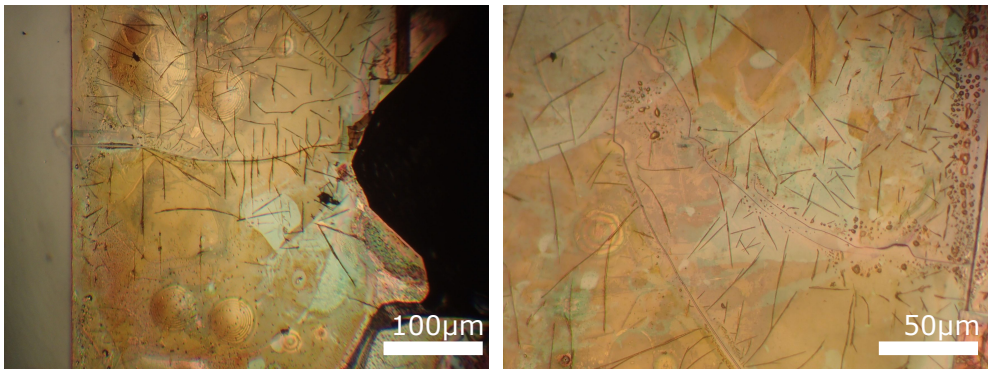

Figure 3.45: A3273 transferred to diamond. (a) To the right is residual substrate, and the left the cleaved sample edge. Sample shows strain fractures across the surface. (b) Fractures in detail.

surface. On the edge of the structure where the bond has many colour bands, the damage caused by the pump spot is catastrophic, the material having been physically ruptured by the heat and the surrounding area bonds disrupted. In the centre of the structure the damage is minimal, with the diamond able to remove much of the heat. The structure is still damaged, with significant drop in emitted PL intensity, however the surrounding area is unaffected.

A3273 could not be so easily transferred without suffering from strain effects, and when transferred the sample surface showed signs of significant damage, shown in Figure 3.45.

3.10.3 Generation 2.5

The same as the structures of the generation 2 growth were samples designated A3352 and A3361, both with the same design as in Figure 3.18. XRD measurements shown in Figure 3.46, demonstrate a distinctly higher strain in A3352 than in A3361, with highest material mismatches $\Delta a/a_0$ of 0.32% (compressive) and -0.15% (tensile) respectively.

The XRD measurement of the 10 period DBR structure is inconclusive for A3355, with broad material peaks indicating low quality material.

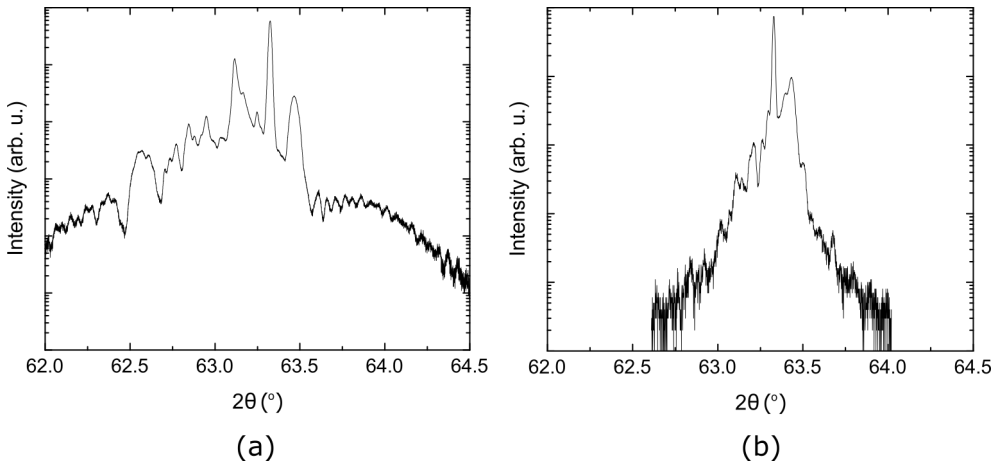

Figure 3.46: Generation 2.5 (a) A3352 and (b) A3361 XRD measurements. Significantly greater mismatch for material in A3352 than A3361.

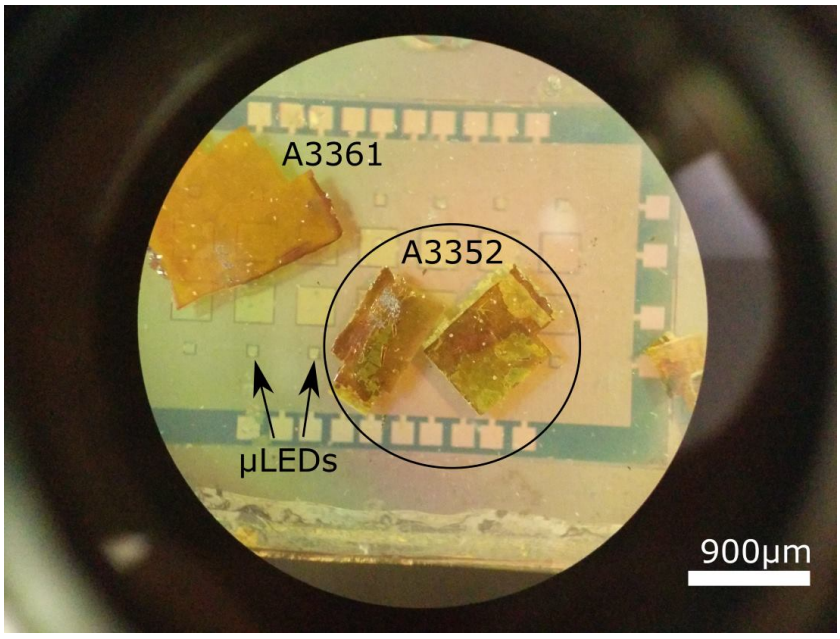

Figure 3.47: A3361 (left sample) and A3352 samples (centre and right samples) transferred to a sapphire substrate to act as colour converter for the μLED array fabricated on the other side of the substrate (discussed in Chapter 5). A3352 cracked into pieces upon lift from glass, and the remaining fragments are cracked. A3361, while not remaining whole, has an undamaged surface.

The difference in strain between A3352 and A3361 was observed in the transfer characteristics of the samples, with A3352 cracking during processing, whereas A3361 was transferrable without significant problems: a comparison of the transfer capability can be seen in Figure 3.47 for samples transferred onto GaN μLEDs for colour conversion (discussed in Chapter 5).

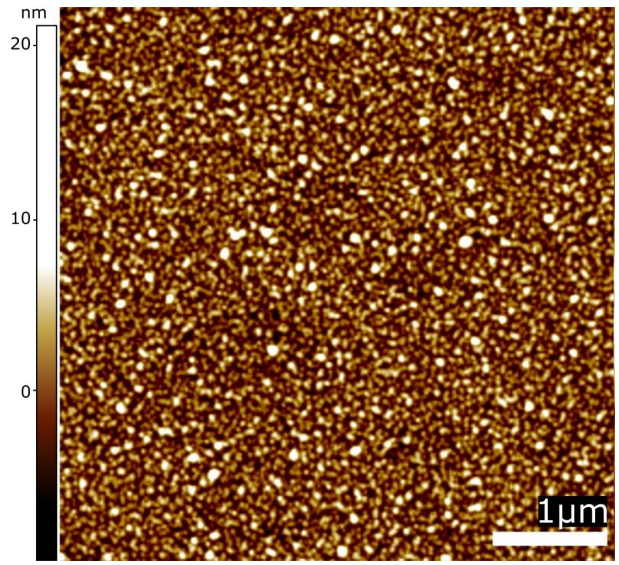

Figure 3.48: AFM measurement of the etched face of A3361, InP and InGaAs removed, with an average RMS roughness of 3.6 nm.

For A3361, transfer was possible for large samples, with unbroken sections of lengths up to 3 mm transferred. The sample in Figure 3.47 is broken due to premature lifting of the sample before it had entirely released in the water bath. In contrast, the A3352 samples were from the same 3x3 mm processed square, which fractured into several samples. Both structures showed significantly lower strain than in earlier generations, e.g. compare with generation 1 A3087 in Figure 3.42.

AFM measurements of the etched side of the A3361 II-VI material were performed, with the target area selected to avoid any cracks. The root-mean-square roughness was measured to be 3.6 nm, averaged across a 10x10 µm square surface on the sample, shown in Figure 3.48.

3.10.4 Generation 3

The final structure growths of the project had to be grown with a partially blocked Cd cell, potentially compromising the composition of the layers. XRD measurements of the 3 wafers shows that A3602 has a low amount of compressive strain, $\Delta a/a_0 = 0.22\%$ while A3611 and A3612 were both tensile strained with a higher magnitudes of -0.59% and -0.32%, shown in Figure 3.49.

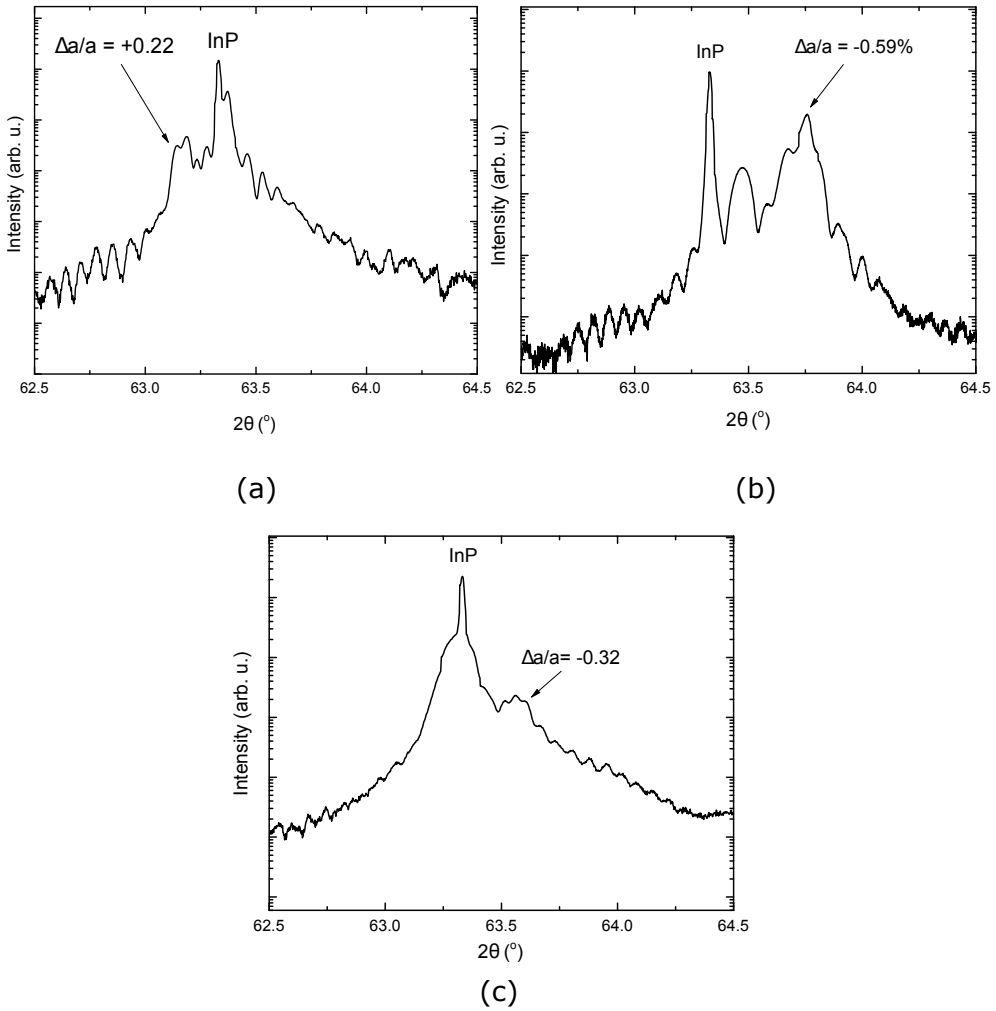

Figure 3.49: XRD measurements showing (a) compressive strain in A3602, (b) high tensile strain in A3611, and (c) lower tensile strain in A3612.

Of the three structures in Generation 3, A3602 has the best transfer characteristics, with large area transfer possible as shown in Figure 3.50. The compressive material strain of A3602 is only slightly higher in magnitude than the lowest strain in the project, the -0.15% tensile strain of A3361, and this is confirmed by the similar transfer characteristics. A3611 and A3612 have less successful etch and transfer properties, with the structures fracturing during the etching stages due to strain (shown in Figure 3.51), as expected from the XRD measurements in Figure 3.49 indicating tensile strain.

A3602 was pumped in a three-mirror cavity with 445 nm and 450 nm GaN pump diodes at powers up to 1 W with a 50 μm diameter pump spot. While its structure thicknesses correspond well with the design as described in Section 3.7.5, laser threshold was not achieved . Assuming that the QW emission was correctly aligned with the RPG

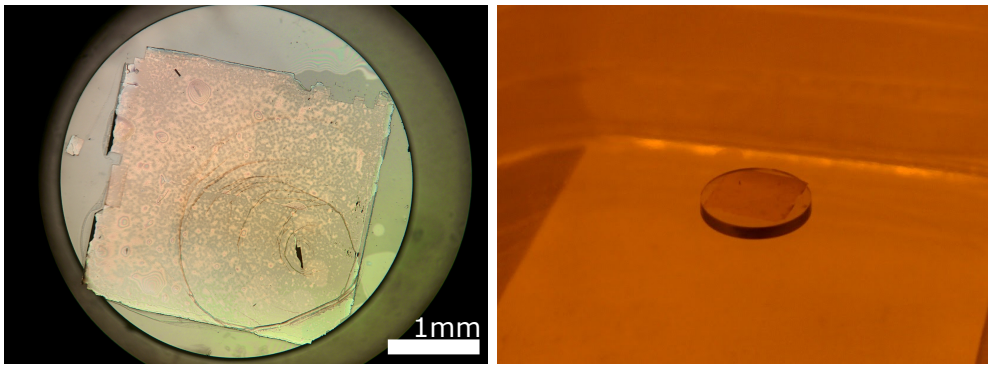

(a) (b)

Figure 3.50: A3602 transferred to diamond, (a) microscope image of sample transferred to diamond. Rings visible are liquid residue. (b) Photograph of the transferred sample. Large areas of the structure are able to be transferred.

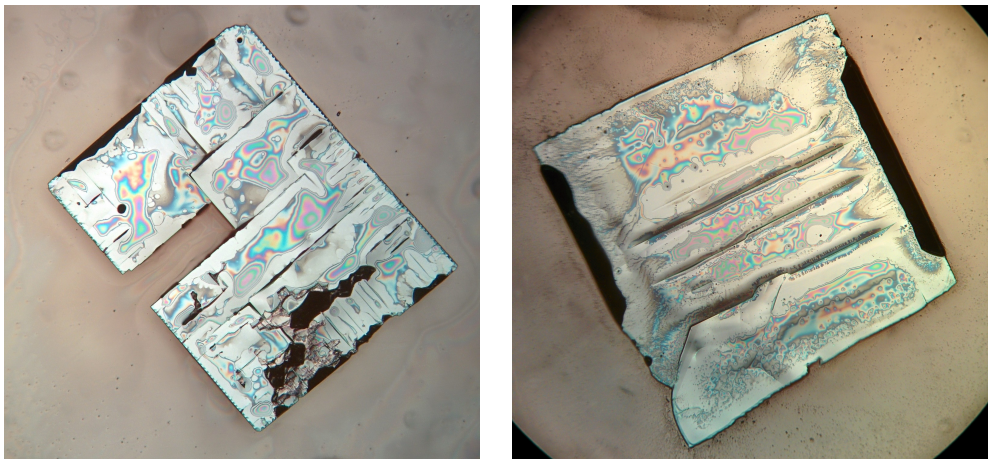

(a) (b)

Figure 3.51: Fracturing behaviour during etch of (a) A3611 and (b) A3612, showing the effects of the tensile strain of the structures indicated by XRD.

wavelength, which is implied from the SEM images described in Section 3.7.5, this can be due to a poor contact with diamond causing thermal rollover before threshold is reached, or a lack of pump power such that the VECSEL does not reach threshold even when the cavity is aligned. The former is solved through continued growth improvements, while the latter requires a pump source with higher power, e.g. high power GaN diodes or an Argon ion gas laser. Alternative possibilities are significantly cooling the structure or pulse-pumping the VECSEL to reach threshold.

3.11 Conclusions and future work

In this chapter we have introduced the II-VI selenide system grown on InP and its growth via MBE. Previously published work on the material properties was investigated for use in the design of II-VI VECSELs, and the problems in growing the DBRs in standard VECSEL designs were discussed. QW transition wavelength was modelled for ZnCdSe/ZnCdMgSe, agreeing well with experimental results.

A method for epitaxial lift-off of the structures has been developed from initial attempts involving via-hole etching, later taking advantage of higher quality and closer lattice-matching of material to allow for the transfer of wide-area II-VI InP grown devices, shown for sample sizes up to 5x5 mm (used in the colour conversion discussion in Chapter 5).

Sample designs for each growth generation are shown, and structures are characterised optically (PL studies, reflectivity) and both indirectly (XRD) and directly (film transfer) for device strain . The effects of this device strain have been shown to be significant in the successful transfer of devices

As generation 1 suffered from low emission and material strain, it was decided to introduce partial DBRs to help set the electric field maxima positions, enhance resonances within the subcavity and help provide structural support by increasing device thickness. Growth problems with layer thickness accuracy and limitations of the effusion cells (meaning that temperatures had to be changed multiple times mid-growth) meant that these design changes led to further complications.

Generations 2 and 2.5 showed progress in material composition accuracy and significant improvements on strain, allowing for transfer of the structures completely to diamond. Laser threshold was, however, not reached.

Nevertheless, progress in crystal quality and lattice-matching of the materials allowed for repeatable and reliable substrate removal. The successful laser emission from a III-V InGaP-based active region (described in Chapter 4) which contained only quantum wells arranged for RPG, transferred to diamond and pumped in a fully external 3

mirror cavity, caused a re-think of the need to include partial DBRs in the II-VI devices. From this it was taken that a simple II-VI ZnCdMgSe structure is a sensible target, optimising the growth for consistency in quantum well emission and spacing for RPG.

Generation 3 of the structure design consisted of a higher QW count, and removed the partial DBR of generation 2. By simplification of the design back to a simple active-region only structure, without the necessity of changing effusion cell temperatures mid-growth, it was hoped that accurate unstrained structures could be grown, maximising the chances of successful transfer and laser action. Laser threshold was not achieved, with unwanted layer thickness and material composition variation still a barrier to successful VECSEL structures from this material system.

3.12 References

[1] S. Tanabe, S. Fujita, S. Yoshihara, A. Sakamoto, S. Yamamoto, YAG glass-ceramic phosphor for white LED (II): luminescence characteristics, Proc. SPIE. 5941 (2005) 594112–594116. doi:10.1117/12.614681.

[2] S.-H. Park, Crystal orientation effects on electronic properties of wurtzite InGaN/-GaN quantum wells, J. Appl. Phys. 91 (2002) 9904. doi:10.1063/1.1480465.

[3] Y. Enya, Y. Yoshizumi, T. Kyono, K. Akita, M. Ueno, M. Adachi, et al., 531 nm Green lasing of InGaN based laser diodes on semi-polar 2021 free-standing GaN substrates, Appl. Phys. Express. 2 (2009) 82101. doi:10.1143/APEX.2.082101.

[4] W. Lin, S.P. Guo, M.C. Tamargo, I. Kuskovsky, C. Tian, G.F. Neumark, Enhancement of p-type doping of ZnSe using a modified (N+Te)δ-doping technique, Appl. Phys. Lett. 76 (2000) 2205. doi:10.1063/1.126297.

[5] M. Sohel, M. Muñoz, M.C. Tamargo, Molecular beam epitaxial growth and characterization of zinc-blende ZnMgSe on InP (001), Appl. Phys. Lett. 85 (2004) 2794. doi:10.1063/1.1804611.

[6] I. Hernandez-Calderon, Optical properties and electronic structure of wide band gap II-VI semiconductors, in: M.C. Tamargo (Ed.), II-VI semiconductor materials and their applications, 2002: pp. 113–170.

[7] Y. Wu, Structure-Dependent Threshold Current Density for CdZnSe-Based II-VI Semiconductor Lasers, IEEE J. Quantum Electron. 30 (1994) 1562–1573. doi:10.1109/3.299488.

[8] L. Zeng, B.X. Yang, A. Cavus, W. Lin, Y.Y. Luo, M.C. Tamargo, et al., Red-green-blue photopumped lasing from ZnCdMgSe/ZnCdSe quantum well laser structures grown on InP, Appl. Phys. Lett. 72 (1998) 3136–3138. doi:10.1063/1.121571.

[9] Y. Luo, S. Guo, O. Maksimov, Patterned three-color ZnCdSe/ZnCdMgSe quantum-well structures for integrated full-color and white light emitters, Appl. Phys. Lett. 4259 (2000) 10–13. doi:10.1063/1.1330229.

[10] M.C. Tamargo, W. Lin, S.P. Guo, Y. Guo, Y. Luo, Y.C. Chen, Full-color light-emitting diodes from ZnCdMgSe/ZnCdSe quantum well structures grown on InP substrates, J. Cryst. Growth. 214 (2000) 1058–1063. doi:10.1016/S0022-0248(00)00274-8.

[11] M.C. Tamargo, S. Guo, O. Maksimov, Y.C. Chen, F.C. Peiris, J.K. Furdyna, Red-green-blue light emitting diodes and distributed Bragg reflectors based on ZnCdMgSe lattice-matched to InP, in: J. Cryst. Growth, 2001: pp. 710–716. doi:10.1016/S0022-0248(01)00808-9.

[12] M.C. Tamargo, Wide Bandgap II-VI Selenides on InP for Short Wavelength Quantum Cascade Lasers, in: Int. Quantum Cascade Lasers Sch. Work., 2010.

[13] M.C. Tamargo, II-VI semiconductor materials and their applications, CRC Press, 2002.

[14] M.N. Perez-Paz, X. Zhou, M. Muñoz, H. Lu, M. Sohel, M.C. Tamargo, et al., CdSe self-assembled quantum dots with ZnCdMgSe barriers emitting throughout the visible spectrum, Appl. Phys. Lett. 85 (2004) 6395–6397.

[15] J. De Jesus, T.A. Garcia, S. Dhomkar, A. Ravikumar, C. Gmachl, G. Chen, et al., Characterization of the three-well active region of a quantum cascade laser using contactless electroreflectance, J. Vac. Sci. Technol. B. 31 (2013) -. doi:10.1116/1.4803838.

[16] H.-M. Wang, J.-H. Chang, T. Hanada, K. Arai, T. Yao, Surface reconstruction and crystal structure of MgSe films grown on ZnTe substrates by MBE, J. Cryst. Growth. 208 (2000) 253–258. doi:10.1016/S0022-0248(99)00451-0.

[17] S. Klembt, H. Dartsch, M. Anastasescu, M. Gartner, C. Kruse, High-reflectivity II-VI-based distributed Bragg reflectors for the blue-violet spectral range, Appl. Phys. Lett. 99 (2011) 1–4. doi:10.1063/1.3644955.

[18] T. Axtmann Garcia, S. Hong, M. Tamargo, J. de Jesus, V. Deligiannakis, A. Ravikumar, et al., Improved electrical properties and crystalline quality of II–VI heterostructures for quantum cascade lasers, J. Vac. Sci. Technol. B. 31 (2013) -. doi:http://dx.doi.org/10.1116/1.4803837.

[19] T. Morita, H. Shinbo, T. Nagano, I. Nomura, A. Kikuchi, K. Kishino, Refractive index measurements of MgZnCdSe II–VI compound semiconductors grown on InP substrates and fabrications of 500–600 nm range MgZnCdSe distributed Bragg reflectors, J. Appl. Phys. 81 (1997) 7575. doi:10.1063/1.365301.

[20] M. Rabah, B. Abbar, Y. Al-Douri, B. Bouhafs, B. Sahraoui, Calculation of structural, optical and electronic properties of ZnS, ZnSe, MgS, MgSe and their quaternary alloy $Mg_{1-x}Zn_xS_ySe_{1-y}$, Mater. Sci. Eng. B. 100 (2003) 163–171. doi:10.1016/S0921-5107(03)00093-X.

[21] H. Okuyama, K. Nakano, T. Miyajima, K. Akimoto, Epitaxial growth of ZnMgSSe on GaAs substrate by molecular beam epitaxy, Japanese J. Appl. Physics, Part 1 Regul. Pap. Short Notes Rev. Pap. 30 (1991) 1620–1623.

[22] Z. Charifi, H. Baaziz, N. Bouarissa, Predicted electronic properties of zinc-blende Zn1–xMgxSe alloys, Mater. Chem. Phys. 84 (2004) 273–278. doi:10.1016/S0254-0584(03)00377-8.

[23] B. Jobst, D. Hommel, U. Lunz, T. Gerhard, G. Landwehr, E0 band-gap energy and lattice constant of ternary $Zn_{1-x}Mg_xSe$ as functions of composition, Appl. Phys. Lett. 69 (1996) 97. doi:10.1063/1.118132.

[24] M.T. Litz, K. Watanabe, M. Korn, H. Ress, U. Lunz, W. Ossau, et al., Epitaxy of $Zn_{1-x}Mg_xSe_yTe_{1-y}$ on (001)InAs, J. Cryst. Growth. 159 (1996) 54–57.

[25] P. Prete, N. Lovergine, L. Tapfer, C. Zanotti-Fregonara, A.M. Mancini, MOVPE growth of MgSe and ZnMgSe on (100)GaAs, J. Cryst. Growth. 214 (2000) 119–124. doi:10.1016/S0022-0248(00)00045-2.

[26] H. Okuyama, Y. Kishita, A. Ishibashi, Quaternary alloy $Zn_{1-x}Mg_xS_ySe_{1-y}$, Phys. Rev. B. 57 (1998) 2257–2263. doi:10.1103/PhysRevB.57.2257.

[27] H. Hattori, I. Nomura, T. Nagano, H. Shimbo, M. Haraguchi, T. Morita, et al., Absorption coefficient measurements of MgZnCdSe II-VI compounds on InP substrates and quantum confined stark effect in ZnCdSe/MgZnCdSe multiple quantum wells, Japanese J. Appl. Physics, Part 1 Regul. Pap. Short Notes Rev. Pap. 37 (1998) 1465–1469. doi:10.1143/JJAP.37.1465.

[28] M. Yamada, H. Ishiguro, H. Nagato, ESTIMATION OF THE INTRA-BAND RELAXATION TIME IN UNDOPED AlGaAs INJECTION LASER., Jpn. J. Appl. Phys. 19 (1980) 135–142. doi:10.1143/JJAP.19.135.

[29] N. Samarth, H. Luo, J.K. Furdyna, R.G. Alonso, Y.R. Lee, A.K. Ramdas, et al., Molecular beam epitaxy of Zn1–xCdxSe epilayers and $ZnSe/Zn_{1-x}Cd_xSe$ superlattices, Appl. Phys. Lett. 56 (1990) 1163. doi:10.1063/1.102550.

[30] M.A. Afromowitz, Refractive index of $Ga_{1-x}Al_xAs$, Solid State Commun. 15 (1974) 59–63. doi:10.1016/0038-1098(74)90014-3.

[31] M. Muñoz, H. Lu, X. Zhou, M.C. Tamargo, F.H. Pollak, Band offset determination of $Zn_{0.53}Cd_{0.47}Se/Zn_{0.29}Cd_{0.24}Mg_{0.47}Se$, Appl. Phys. Lett. 83 (2003) 1995. doi:10.1063/1.1606875.

[32] A.P. Ravikumar, T.A. Garcia, J. De Jesus, M.C. Tamargo, C.F. Gmachl, High detectivity short-wavelength II-VI quantum cascade detector, Appl. Phys. Lett. 105 (2014) 061113. doi:10.1063/1.4893359.

[33] J. De Jesus, G. Chen, L.C. Hernandez-Mainet, A. Shen, M.C. Tamargo, Strain compensated CdSe/ZnSe/ZnCdMgSe quantum wells as building blocks for near to mid-IR intersubband devices, J. Cryst. Growth. (2014). doi:10.1016/j.jcrysgro.2014.12.021.

[34] C. Kruse, S.M. Ulrich, G. Alexe, E. Roventa, R. Kröger, B. Brendemühl, et al., Green monolithic II–VI vertical-cavity surface-emitting laser operating at room temperature, Phys. Status Solidi. 241 (2004) 731–738. doi:10.1002/pssb.200304126.

[35] M.C. Tamargo, W. Lin, S.P. Guo, Y. Guo, Y. Luo, Y.C. Chen, Full-color light-emitting diodes from ZnCdMgSe/ZnCdSe quantum well structures grown on InP substrates, J. Cryst. Growth. 214 (2000) 1058–1063. doi:10.1016/S0022-0248(00)00274-8.

[36] M. Madsen, K. Takei, R. Kapadia, H. Fang, H. Ko, T. Takahashi, et al., Nanoscale semiconductor “x” on substrate “y” - Processes, devices, and applications, Adv. Mater. 23 (2011) 3115–3127. doi:10.1002/adma.201101192.

[37] A. Carlson, A.M. Bowen, Y. Huang, R.G. Nuzzo, J.A. Rogers, Transfer printing techniques for materials assembly and micro/nanodevice fabrication, Adv. Mater. 24 (2012) 5284–5318. doi:10.1002/adma.201201386.

[38] E. Menard, K.J. Lee, D.Y. Khang, R.G. Nuzzo, J.A. Rogers, A printable form of silicon for high performance thin film transistors on plastic substrates, Appl. Phys. Lett. 84 (2004) 5398–5400. doi:10.1063/1.1767591.

[39] S.H. Park, H. Jeon, Microchip-type InGaN vertical external-cavity surface-emitting laser, Opt. Rev. 13 (2006) 20–23. doi:10.1007/s10043-006-0020-y.

[40] J. Yoon, A.J. Baca, S.-I. Park, P. Elvikis, J.B. Geddes, L. Li, et al., Ultrathin silicon solar microcells for semitransparent, mechanically flexible and microconcentrator module designs., Nat. Mater. 7 (2008) 907–915. doi:10.1038/nmat2287.

[41] Y.M. Song, Y. Xie, V. Malyarchuk, J. Xiao, I. Jung, K.-J. Choi, et al., Digital cameras with designs inspired by the arthropod eye., Nature. 497 (2013) 95–99. doi:10.1038/nature12083.

[42] D.H. Kim, Y.S. Kim, J. Wu, Z. Liu, J. Song, H.S. Kim, et al., Ultrathin silicon circuits with strain-isolation layers and mesh layouts for high-performance electronics on fabric, vinyl, leather, and paper, Adv. Mater. 21 (2009). doi:10.1002/adma.200900405.

[43] G.D. Cole, W. Zhang, M.J. Martin, J. Ye, M. Aspelmeyer, Tenfold reduction of Brownian noise in high-reflectivity optical coatings, Nat. Photonics. 7 (2013) 644–650. doi:10.1038/nphoton.2013.174.

[44] C. Bradford, A. Currran, A. Balocchi, B.C. Cavenett, K.A. Prior, R.J. Warburton, Epitaxial lift-off of MBE grown II-VI heterostructures using a novel MgS release layer, in: J. Cryst. Growth, 2005: pp. 325–328. doi:10.1016/j.jcrysgro.2005.01.019.

[45] B.E. Jones, P.J. Schlosser, J. De Jesus, T.A. Garcia, M.C. Tamargo, J.E. Hastie, Characterisation of II-VI selenide multi-quantum well thin films transferred to transparent substrates, in: Int. Conf. Opt. Optoelectron. Photonic Mater. Appl., Leeds, 2014.

[46] Norland Products, Norland Optical Adhesive 63, (n.d.). http://norlandprod.com/adhesives/NOA63.html.

[47] R. Moug, A. Alfaro-Martinez, L. Peng, T. Garcia, V. Deligiannakis, A. Shen, et al., Selective etching of InGaAs/InP substrates from II-VI multilayer heterostructures, Phys. Status Solidi. 9 (2012) 1728–1731. doi:10.1002/pssc.201100716.

[48] J.J. Schermer, P. Mulder, G.J. Bauhuis, M.M.A.J. Voncken, J. van Deelen, E. Haverkamp, et al., Epitaxial Lift-Off for large area thin film III/V devices, Phys. Status Solidi. 202 (2005) 501–508.
doi:10.1002/pssa.200460410.

[49] A.G. Baca, C.I.H. Ashby, Fabrication of GaAs Devices, IET, 2005.

[50] Bruker, D8 DISCOVER, (n.d.).
http://www.bruker.com/products/x-ray-diffraction-and-elemental-analysis/x-ray-diffraction/d8-discover/overview.html (accessed September 15, 2014).

Chapter 4

III-V AlGaInP thin-film VECSEL

4.1 Introduction

AlGaInP lattice-matched to GaAs allows for bandgap energies from the green to the red, while GaInP/AlGaInP quantum wells with moderate strain tailored from tensile to compressive can be engineered for emission wavelengths from orange to red. The GaInP/AlGaInP material system shown in Figure 4.1 has been used to fabricate red-emission VECSELs operating at or near room temperature with increasingly better performance, from the first demonstration of pulsed operation in 2002 [1], continuous-wave (CW) in 2003 [2], and demonstrations of high-power output over the past decade [3–5].

Building from the thin-film device transfer methods developed for the II-VI materials described in Chapter 3, we have pursued a similar form of thin-film VECSEL, excluding a DBR from the design and leaving only the active region, for this material system. This chapter discusses the progression from establishing material characteristics and strain balancing, substrate removal and transfer, structure design incorporating strain balanced quantum wells and barriers, through to initial structure and laser characterisation. The effects of quantum-well strain balancing on device transfer are investigated, and the challenges of thermal management are discussed.

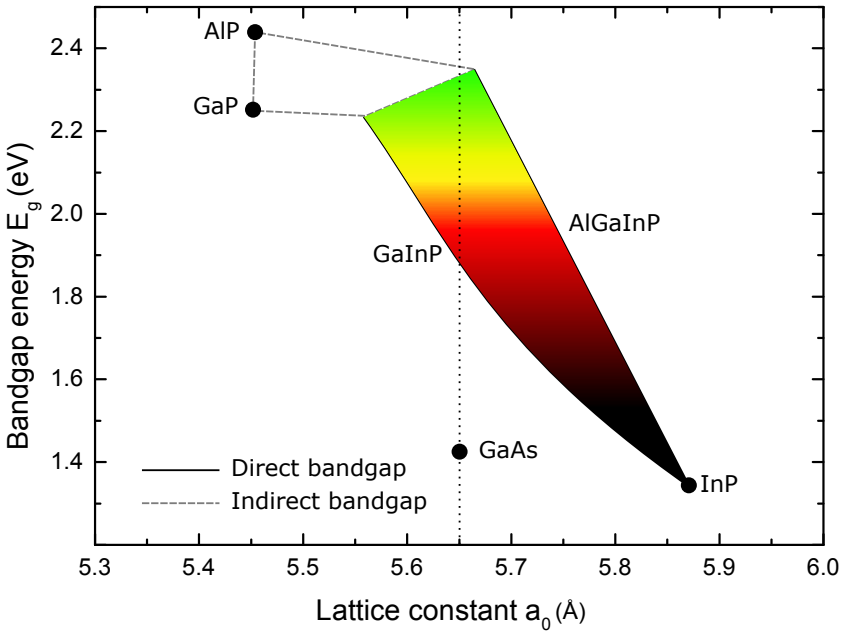

Figure 4.1: A plot of lattice constant a_0 for energy band-gap E_g of the binaries AlP, GaP, InP and their ternaries. The area shaded indicates where the quaternary AlGaInP has direct band-gap. Joining lines indicate whether the energy band-gap is direct or indirect. GaAs lattice constant indicated by a dashed line for use as substrate. Figure adapted from [6].

4.1.1 III-V structure growth

The III-V structures described in this chapter were grown via metal organic chemical vapour deposition (MOCVD) at the EPSRC National Centre for III-V Technologies in Sheffield [7]. The structures are grown on 2" diameter GaAs substrates in a two-wafer horizontal Semicon MR350 low flow channel MOCVD reactor. MOCVD growth proceeds by a horizontal flow of gas being maintained across the substrate from which the epitaxial material grows. The growth wafer is placed on a heated susceptor to bring it to growth temperature while the gas is heated in the chamber. The susceptor is non-rotating, so substrates are not rotated during deposition resulting in a thickness gradient across the sample, while temperature non-uniformity of the susceptor can result in inhomogeneity of growth. In contrast to commercial growth, where variations of growth result in discarded material and unacceptable waste, for a research device a variation of the structure across the wafer can be beneficial, with photoluminescence (PL) and reflectivity maps providing guidance to the wafer position most optimal for device performance.

4.2 Material characteristics for design

For the design and simulation of VECSEL structures, a number of parameters are needed to describe the binary materials, along with the characteristics of ternary (and sometimes quaternary) compounds such as band-gap bowing parameters. These are described in Chapter 2, with the relevant Equation 2.2 modified for the generalised calculation of ternary and quaternary parameters as described in Section 2.2.1.

The VECSEL designs discussed in this chapter are based upon GaInP QWs, within AlGaInP barriers and with DBR structures based on AlGaAs. An overview of lattice constant/band-gap relation of relevant binaries and ternaries was given in Figure 4.1, and the relevant material parameters needed for GaP, InP, AlP, AlAs, and GaAs are given in Table 4.1.

Binary parameters relevant for AlGaInP-based VECSEL gain structures						
Material	Lattice constant (Å)	Energy band-gap (eV)	α	β (10^3dyne/cm)	C_{11} (GPa)	C_{12} (GPa)
GaAs	5.65325	1.424	32.153	9.37	1221	566
AlAs	5.6611	2.168	–	–	1250	534
AlP	5.4635	2.45	–	–	1330	630
GaP	5.4512	2.26	36.249	10.697	1405	620.3
InP	5.8688	1.35	26.2	6.602	1011	561
InAs	6.0583	0.354	21.674	5.76	832.9	452.6

Table 4.1: Binary material parameters relevant to AlGaInP-based VECSEL gain structures, relating to lattice constant, energy band-gap and strain calculation. α and β are Varshni coefficients for calculating band-gap shift with temperature, and C_{11} and C_{12} the material elastic stiffness coefficients. Data from Vurgaftman et al. 2001 [9].

For refractive index the value is wavelength-dependant, so this is taken from literature sources; see Schubert et al. 1999 [11] for AlGaInP, Adachi 1985 [12] for AlGaAs.

4.3 Thin-film processing and considerations

As with the II-VI VECSEL structures discussed in Chapter 3, AlGaInP thin-film gain structure VECSELs offer an alternative to the traditional rear-DBR VECSEL. Access to both ends of the gain region allows for such possibilities as double-end pumping, rear output coupling, multi-gain region devices, ring/travelling wave cavities, and novel cavity designs that would normally require the VECSEL gain region to be on a low

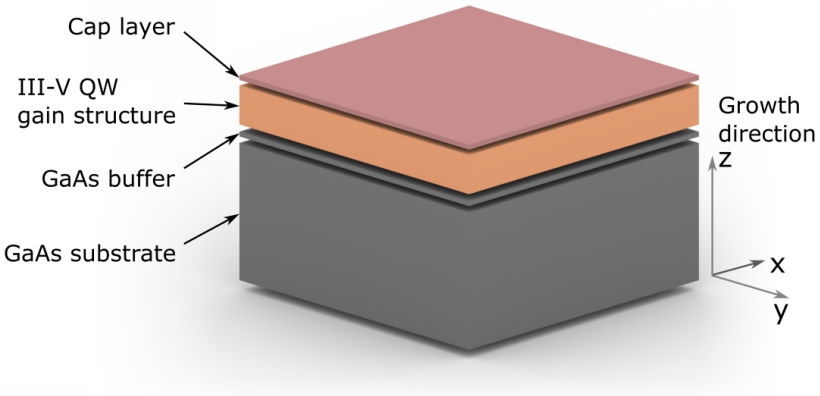

Figure 4.2: Basic layout of the grown III-V thin-film structures, from GaAs substrate a GaAs buffer layer is grown to improve epitaxial layer quality, followed by the quantum well gain structure and a capping layer.

angle fold in the cavity. Extended tuning ranges through the removal of the influence of the DBR reflection band could become possible, potentially extended to the red through angling of the structure to increase the RPG wavelength, or for the operation of multi-wavelength devices without the need for a more complex multi-wavelength DBR.

The first gain structures used to investigate thin-film VECSELs were originally grown as calibration structures for the active region of the standard VECSEL structures, for emission at 675 nm. They consist of 10 GaInP quantum well pairs designed for emission at 660 nm at room temperature, totalling 20 quantum wells, spaced in AlGaInP barriers for RPG at 675 nm. A top capping layer of GaInP stops oxidation of the structure on the epi-side. The structures are grown on a GaAs buffer layer, on a GaAs substrate. A generalised schematic of the semiconductor structure is shown in Figure 4.2. Detail of the thin-film VECSEL structures can be found later in Section 4.4.

As no sacrificial layer is present, the GaAs substrate and buffer layers must be completely removed to release the VECSEL structure, rather than an under-etch procedure as in [13,14]. As with the standard VECSELs with DBR included, the no-DBR VECSELs must have thermal management via a capillary-bonded diamond heatspreader, and so the structures must emerge from the the processing with a sufficiently low surface roughness and the ability to be transferred/printed.

4.3.1 Substrate removal and transfer

The removal of the GaAs substrate is based on the transfer of II-VI material as described in Chapter 3. Throughout the removal of GaAs substrate from the sample, the epi-side is fixed to a glass temporary substrate, epi-side down, with a low melting-point water soluble wax, Polyethylene glycol (PEG). PEG has a melting point of approximately 60 °C.

Both glass and sample are cleaned with solvent baths (acetone, methanol) before bonding them together with the wax, to ensure a clean surface for transfer post-etch. Prior to wet-etch, the substrate is polished from its initial 500 µm thickness to approximately 100 µm using SiC paper with a grit of 1200. Excess wax around the sample aids in accurate polishing both by acting as an indicator of thickness and by slowing the polishing rate as the target thickness is approached (the wax must be polished as well). The polishing step reduces etch time, increases homogeneity of the wet etch and also reduces the chance of the sample releasing prematurely in the acid – the reduction in etch time from polishing to smaller thicknesses is observed to consistently increase the chance of transfer success.

An aluminium mount, within an aluminium guide jig, as shown in the II-VI processing section in Chapter 3, is used to ensure a level polished surface, and the glass with sample is held on the mount using the same PEG wax as before. Gravity provides adequate force to polish the sample by hand, with observation by eye enough to tell when the target thickness is approximately reached, although the mount also has a fitting for a micrometre screw for accurate thickness targeting. The substrate is etched with H_3PO_4:H_2O_2:H_2O (3:4:3) with an estimated etch rate of 6 µm/min, and an expected etch time of 15–20 minutes for 100 µm. The etch proceeds from the sample edges to the centre, shown in Figure 4.3.

The acid solution does not etch AlGaInP at a high rate, so the structure barriers can effectively be considered an etch stop after the GaAs buffer layer. GaInP slows the etch further, and this is partially the reason for the addition of a GaInP anti-oxidation and etch stopping layer in design B, discussed in section 4.6.2.

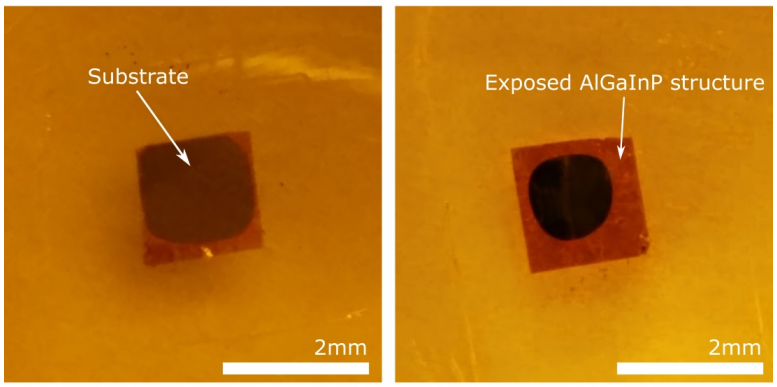

Figure 4.3: Demonstration of substrate etch from edges to centre of sample, showing the residual substrate (black) as it recedes exposing the AlGaInP structure at (a) 6 minutes, and (b) 12 minutes.

Once the sample is completely etched so that only the GaInP/AlGaInP epi-layers remain on the glass, both are placed in 70 °C de-ionised water to remove the sample from the substrate. As the structure is released, the water should be changed to avoid any residual wax from remaining on the structure. For well cleaned glass- and structure-surfaces a bond may hold them together without wax, and water baths for an extended time can be used to release this bond. Once the sample is no longer held by wax or bond, it can be lifted using a flexible membrane. This is best accomplished by dragging the sample laterally from the glass, which does increase the risk from any surface dirt or debris around the structure but allows the breaking of the bond between structure and glass at the edge.

The target diamond for transfer is cleaned thoroughly through ultrasonic, acetone and methanol baths, followed by a 3 min etch in H_2SO_4:H_2O_2 (3:1), known as piranha solution. This final piranha etch not only cleans the sample but hydroxylates the surface, temporarily giving the diamond surface hydrophilic properties, conducive to capillary bonding.

The complete processing of the structure is summarised in brief below:

- Clean sample and glass with acetone, methanol and isopropanol
- Glue with PEG wax (60 °C melting point) to glass

- Polish substrate to approx. 100 µm thickness
- Etch with H_3PO_4:H_2O_2:H_2O (3:4:3) (estimated 6 µm/min). Etch time: 15-20 minutes
- Bath in DI water at 65 °C for 10 minutes
- Lift and transfer onto diamond (piranha cleaned, 3:1 H_2SO_4:H_2O_2)
- Liquid capillary bond sample with DI water

4.3.2 Strain balancing

In contrast to the II-VI structures where each layer was designed to be lattice-matched, the GaInP QWs of the red VECSEL gain structures are designed to be compressively strained. Strain balancing of the structures is desirable to increase device lifetime as discussed in Chapter 2. The zero-stress method is used to calculate the correct strain balancing layer thicknesses in the structure designs, to compensate the quantum well strain.

As discussed in Chapter 2, the zero stress method achieves the best results for achieving zero average in-plane stress in the layer combination [15], using Equations 4.1 & 4.2 below for achieving this:

$$a_0 = \frac{A_1 t_1 a_1 a_2^2 + A_2 t_2 a_2 a_1^2}{A_1 t_1 a_2^2 + A_2 t_2 a_1^2} \tag{4.1}$$

$$0 = t_1 A_1 \epsilon_1 a_2 + t_2 A_2 \epsilon_2 a_1 \tag{4.2}$$

where a_0,a_1 and a_2 are the lattice parameters of the substrate material and strained materials respectively, t_1 and t_2 the strained material thicknesses, layer strain is defined for material x as $\epsilon_x = (a_0 - a_x)/a_x$, and elastic parameter A_x is defined in Equation 4.3.

$$A_x = C_{11_x} + C_{12_x} - \frac{2C_{12_x}^2}{C_{11_x}} \tag{4.3}$$

with C_{11_x} and C_{12_x} the material elastic stiffness coefficients.

4.4 Thin-film structure designs

The structure designs for thin-film VECSEL devices are similar to the gain-mirror structures but without the DBR mirror. In addition, anti-oxidation layers are added to the specially designed structures to protect the etched surface after epitaxial layer transfer.

4.4.1 Structure design A

The first structure used to demonstrate a thin-film VECSEL was originally a calibration structure for a standard gain-mirror VECSEL structure with DBR, and will be described as design A. The active region consists of 10 pairs of 6 nm $Ga_{0.46}In_{0.54}P$ QWs within slightly tensile strained $(Al_{0.53}Ga_{0.47})_{0.54}In_{0.46}P$ barriers to counter the compressively strained quantum wells. The structure design is shown in Figure 4.4, and detailed in Table 4.2.

This structure does not contain an anti-oxidation layer/etch-stop on the substrate side of the sample (to the right of Figure 4.4), as the design was grown simply as the active region of a gain-mirror VECSEL. This means that there may be issues with over-etching and post-etch oxidation, discussed in section 4.7.2.

Thin-film VECSEL for 675 nm, (10×2) QWs, QW emission: 660 nm; RPG: 675 nm; Subcav. Res: 675 nm					
Layer	Material	x	y	Thickness (nm)	Purpose
8	$Ga_xIn_{1-x}P$	0.51	–	10.0	Cap
7	$(Al_xGa_{1-x})_yIn_{1-y}P$	0.53	0.54	86.0	Strained Barrier
6×10	$Ga_xIn_{1-x}P$	0.46	–	6.0	QW
5×10	$(Al_xGa_{1-x})_yIn_{1-y}P$	0.53	0.54	7.0	Strained Barrier
4×10	$Ga_xIn_{1-x}P$	0.46	–	6.0	QW
3×10	$(Al_xGa_{1-x})_yIn_{1-y}P$	0.53	0.54	82.5	Strained Barrier
2	$(Al_xGa_{1-x})_yIn_{1-y}P$	0.53	0.54	109.0	Strained Barrier
1	GaAs	–	–	–	Substrate

Table 4.2: Table 4.2: Design for the active-region calibration growth; quantum well emission 660 nm, RPG wavelength 675 nm, described as ‘design A’.

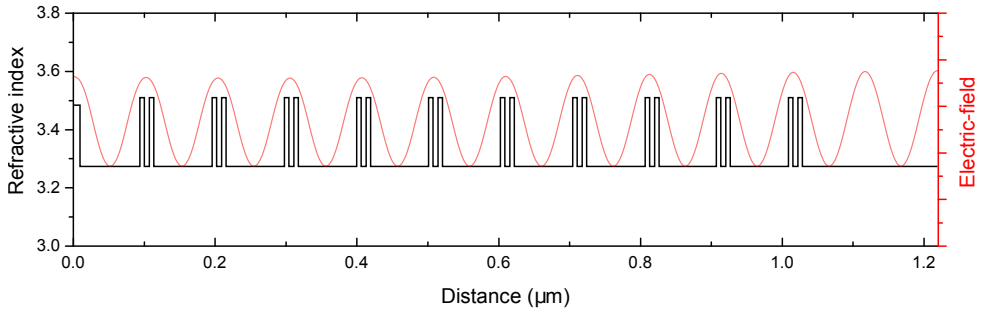

Figure 4.4: Design A, 10 pairs of quantum wells with strain balanced barrier layers.

4.4.2 Structure design B

After successful laser action of design A, a new design specifically for a strain balanced active-region only laser structure for thin-film transfer was designed and grown, as part of a growth campaign featuring new designs for thin-film and gain-mirror VECSELs at 675 nm and 689 nm. Differing from the previous structure, design B contains strain balancing layers within lattice-matched barriers, which other groups working on optimising growth now favour instead of tensile strained barriers, as discussed in Chapter 2. The tensile strain in each strain-balance layer is designed to be large enough to be calibrated with XRD. In addition, an anti-oxidation capping layer was added as the first layer grown, both to act as an etch-stop, and to protect the surface post-transfer.

Using a non-uniform distribution of QWs could have been beneficial for matching QWs with carrier density as discussed in Chapter 2, but in consideration of the novel architecture of these devices, the addition of other (non-relevant to thin-film) features to the gain-mirror VECSELs that these were grown alongside, and a lack of in-house growth has restricted the number of sensible structure changes per growth campaign. For this campaign it was decided that an investigation into strain balancing would be more important, the effects of which on the thin-device transfer had so far been untested. The strain balancing $(Al_{0.51}Ga_{0.49})_{0.54}In_{0.46}P$ layers are designed to match the refractive index of the lattice-matched $(Al_{0.6}Ga_{0.4})_{0.525}In_{0.475}P$ barrier layers, and the thickness of the strain balancing layers is calculated using the zero-stress method outlined in Section 4.3.2.

Thin-film VECSEL for 675 nm, (10×2) QWs, QW emission: 660 nm; RPG: 675 nm; Subcav. Res: 675 nm					
Layer	Material	x	y	Thickness (nm)	Purpose
11	$Ga_xIn_{1-x}P$	0.515	–	10.0	Cap
10	$(Al_xGa_{1-x})_yIn_{1-y}P$	0.60	0.525	85.0	Barrier
9×10	$Ga_xIn_{1-x}P$	0.46	–	6.0	QW
8×10	$(Al_xGa_{1-x})_yIn_{1-y}P$	0.60	0.525	7.0	Barrier
7×10	$Ga_xIn_{1-x}P$	0.46	–	6.0	QW
6×10	$(Al_xGa_{1-x})_yIn_{1-y}P$	0.60	0.525	26.0	Barrier
5×10	$(Al_xGa_{1-x})_yIn_{1-y}P$	0.51	0.54	31.0	Strain Balance
4×10	$(Al_xGa_{1-x})_yIn_{1-y}P$	0.60	0.525	26.0	Barrier
3	$(Al_xGa_{1-x})_yIn_{1-y}P$	0.6	0.525	99.0	Barrier
2	$Ga_xIn_{1-x}P$	0.515	–	10.0	Cap
1	GaAs	–	–	–	Substrate

Table 4.3: Design for active-region VECSEL growth, 10×2 quantum wells with emission 660 nm, RPG wavelength 675 nm. Described as 'design B'.

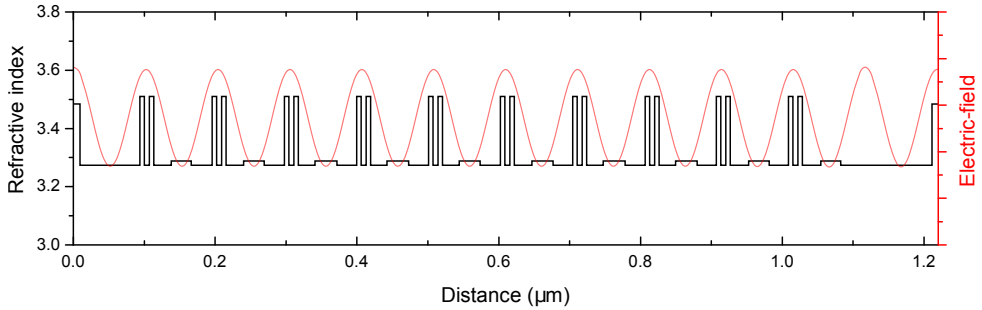

Figure 4.5: Design B, including strain balancing layers between QW pairs. Refractive index of the strain balance layers is designed to be the same as the pump-absorbing barrier layers, via band-gap matching, but is set displayed as different to help distinguish the layers within the schematic.

The design, given in Table 4.3, consists of the same 10 pairs of 6 nm $Ga_{0.46}In_{0.54}P$ QWs as in structure design A, but with slightly altered barrier thicknesses, and the addition of the strain balancing layers at the nodes of the electric field, shown in Figure 4.5. For QW pairs of $Ga_{0.46}In0.54P$ totalling 12 nm per E-field antinode, the thickness needed for a strain balancing layer of $(Al_{0.6}Ga_{0.4})_{0.54}In_{0.46}P$ was found using Equations 4.1 & 4.2 to be 31 nm per pair.

Thin-film VECSEL for 689 nm, (10×2) QWs, QW emission: 674 nm; RPG: 689 nm; Subcav. Res: 689 nm					
Layer	Material	x	y	Thickness (nm)	Purpose
11	$Ga_xIn_{1-x}P$	0.515	–	10.0	Cap
10	$(Al_xGa_{1-x})_yIn_{1-y}P$	0.60	0.525	82.6	Barrier
9×10	$Ga_xIn_{1-x}P$	0.44	–	8.2	QW
8×10	$(Al_xGa_{1-x})_yIn_{1-y}P$	0.60	0.525	7.0	Barrier
7×10	$Ga_xIn_{1-x}P$	0.44	–	8.2	QW
6×10	$(Al_xGa_{1-x})_yIn_{1-y}P$	0.60	0.525	12.0	Barrier
5×10	$(Al_xGa_{1-x})_yIn_{1-y}P$	0.51	0.54	56.5	Strain Balance
4×10	$(Al_xGa_{1-x})_yIn_{1-y}P$	0.60	0.525	12.0	Barrier
3	$(Al_xGa_{1-x})_yIn_{1-y}P$	0.6	0.525	103	Barrier
2	$Ga_xIn_{1-x}P$	0.515	–	10.0	Cap
1	GaAs	–	–	–	Substrate

Table 4.4: Design for thin-film VECSEL growth, 10×2 quantum wells with emission 674 nm, RPG and subcavity resonance wavelength 689 nm. Described as ‘design C’.

4.4.3 Structure design C

In addition to the structures emitting at 675 nm, structures designed with higher-strain 8.2 nm thick $Ga_{0.46}In_{0.54}P$ quantum wells for operation at 689 nm were designed and produced, both with and without strain compensation layers. These were part of the growth campaign for both gain-mirror VECSELs and thin-film structures. The design is detailed in Table 4.4 and shown in Figure 4.6. The structures without the $(Al_{0.51}Ga_{0.49})_{0.54}In_{0.46}P$ strain balancing layers simply have layer 4 as lattice-matched $(Al_{0.6}Ga_{0.4})_{0.525}In_{0.475}P$, as the strain balancing material was chosen to have the same refractive index. Strain balance layers are thicker than those in design B, to accommodate the higher strain in the quantum well material. These structures are designated design C.

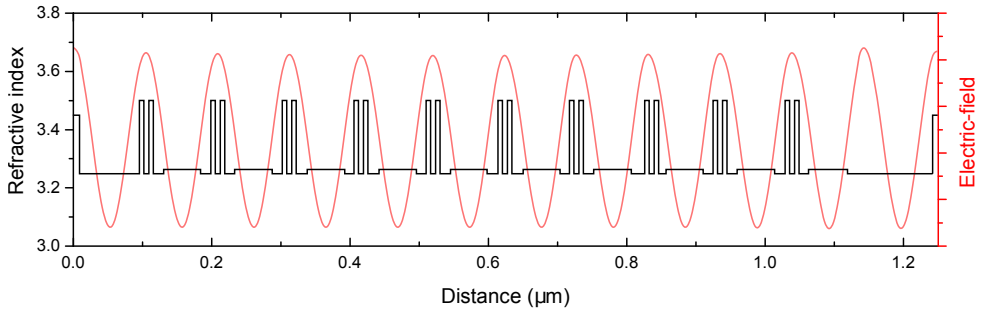

Figure 4.6: Design C, including strain balancing layers between QW pairs. Refractive index of the strain balance layers is designed to be the same as the pump-absorbing barrier layers, via band-gap matching, but is set displayed as different to help distinguish the layers within the schematic.

4.5 VECSEL mount and cavity

The sample mount for the thin-film VECSEL must have an aperture for the light on both sides of the sample while extracting heat from the structure and heatspreader composite. The mount used is water-cooled and contains a central hole for the laser mode to pass through, as described in Chapter 2. The chiller unit for the mount is set to cools the water to 5 °C. Indium metal is used to improve the thermal contact between the diamond and the brass.

The basic thin film VECSEL cavity used for initial experiments is similar to the standard 3 mirror gain-mirror VECSEL arrangement described in Chapter 1, although future cavities could be constructed to take advantage of the novel possibilities of a thin-film VECSEL with no DBR. Two $f = 100$ mm curved mirrors are used to provide the mode focus at the sample, with a plane end mirror completing a near-collimated second cavity arm. Figure 4.7 shows the cavity layout with the lengths $L1 = 99$ mm from curved end mirror to sample, $L2 = 59$ mm from sample to curved folding mirror, and $L3 = 250$ mm from folding mirror to plane end mirror. The optics for the $lambda = 532$ nm, Coherent Verdi pump laser contain a half-wave plate and polarising beam splitter combination to allow for power adjustment, and a lens of $f = 250$ mm focusses the pump beam to a spot size of diameter 70 μm, approximately matching the intracavity mode of the VECSEL cavity within the structure (mode-matching).

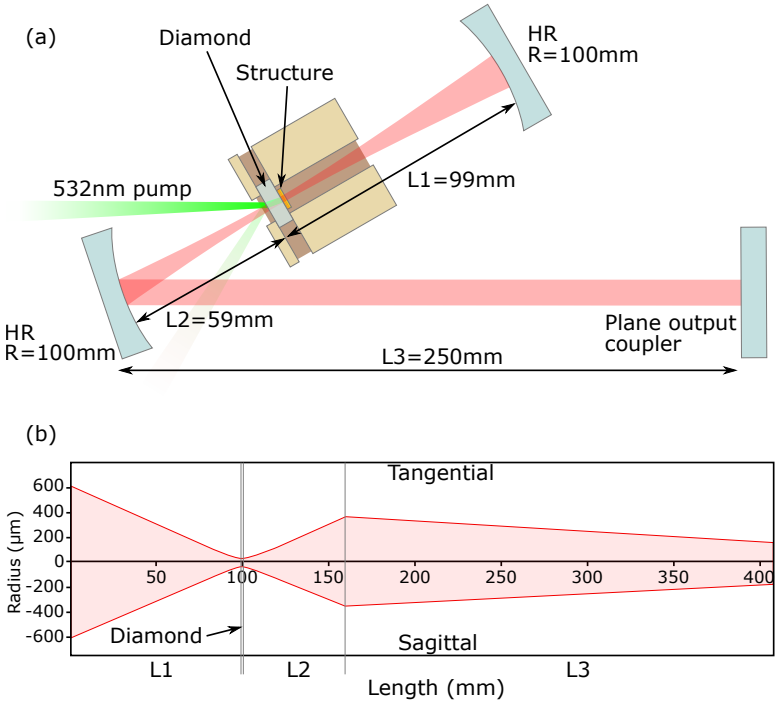

Figure 4.7: (a) 3 mirror standing-wave cavity setup for 70 μm mode size at sample. Diamond-bonded sample is held in a water-cooled brass mount, and lengths L1 and L2 are taken from the diamond surface. Length L3 is from the folding mirror to the plane end mirror. (b) Simulation of cavity mode size for the lengths specified in (a). Tangential and Sagittal intracavity beam radii are equal to within a small margin due to a minimisation of folding angle to under 10°.

4.6 Structure characterisation

After growth, reflectivity and PL measurements are used to analyse the accuracy of the structure growth in comparison with the design, and determine whether anything must be changed for the next growth, e.g. quantum well emission. The non-uniformity of the structures across the wafer surface also leads to some areas of the sample matching the design better than others. The initial characterisation with reflectivity and PL allow for the positions on the sample most likely to provide high performance to be determined.

In standard gain-mirror VECSEL structures, the reflectivity provides detailed information on the DBR stop-band, along with absorption from quantum wells providing an indication of subcavity resonances. In the thin structures, the pattern is determined mostly by a combination of the maxima and minima caused by the Fabry-Pérot etalon

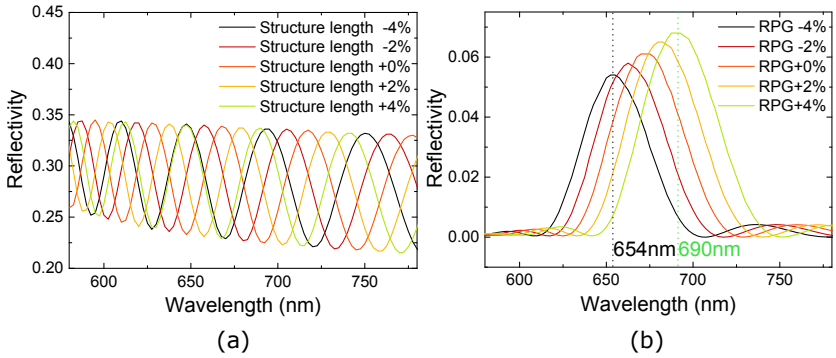

Figure 4.8: Simulated change in reflectivity for: (a) a single layer of AlGaInP buffer material on GaAs, top interface with air, with structure length increased and decreased by up to 4%; (b) 10 QW pairs of thickness 6 nm, separation 7 nm, barrier layer 82.5 nm, with no top or bottom interfaces, with barrier layer (and by extension RPG wavelength) increased and decreased by up to 4%.

[16] of top and bottom surfaces, shown in Figure 4.8 (a) for a single layer of AlGaInP starting at 1220 nm; and the constructive and destructive interference from the Fresnel reflections at each layer interface within the structure. In these structures, the main feature which can alter the Fresnel reflection profile from the layer interfaces is the RPG wavelength, i.e. the distance between quantum well pairs, and the effect of thickness changes to the barrier layers is shown in Figure 4.8 (b) for a structure with no air or substrate interfaces. These simulations are based on the calculation of reflectivity using the theory of electromagnetic wave propagation through multi-layer stratified dielectric media [17], as described in Chapter 2 and shown in Appendix B.

Figure 4.8 demonstrates that while the main reflectivity peak positions is dominated by the Fabry-Pérot etalon of the structure thickness, that deviation from the sinusoidal spectrum is due to the reflectivity peak from the QW layer placement. The small increase observed in the simulated reflectivity for longer RPG wavelength is attributed to the QWs in the pair being offset from the RPG wavelength antinode position, with the pair separation relative to RPG wavelength becoming smaller for higher wavelengths. The QW positions and the structure thickness are linked, the majority of the structure thickness being the barrier layers between quantum wells, so both the etalon peaks and the QW reflection peak will approximately move together.

There will also be a small contribution from the quantum well emission to the measured reflected spectrum in the form of a small peak feature at the PL emission wavelength.

The surface-PL measured spectrum gives the QW emission, potentially modulated by structure resonances, and for all structures is found to be mostly homogenous across the wafer surface. Sub-peaks within the emission can be due to additional transitions other than the QW ground state conduction band to the heavy-hole valence band ground state – band-filling effects, higher energy levels within the quantum well and transitions to the light-hole valence band contributing additional transitions.

Both the reflectivity and PL spectra are difficult to analyse conclusively for these structures, not having the easily identifiable reflectivity features of the gain-mirror structures as described in Chapter 2.

4.6.1 Initial characterisation: Design A

The initial characterisation of the design A structure shows that PL is relatively uniform across the structures, although some slight variation of wavelength is present, along with a stronger variation in intensity across the wafer. Reflectivity is found to have a significant difference across the wafer as expected from the MOCVD growth discussed in Section 4.1.1.

Surface-PL measurements show quantum well emission modulated by the resonances of the structure. For structures with DBR mirrors, the modulation of quantum well emission outside the DBR stop-band can cause this to be radically altered (see Chapter 2 for a discussion of DBR offset and why the emission could be outside of the stop-band), but for structures without the DBR mirrors the modulation is simplified to the RPG wavelength (barrier thickness) and Fabry-Pérot (structure thickness). The surface-PL measurement for the centre of a structure of design A is shown in Figure 4.9.

The broad surface-PL peak is at 659 nm, with a secondary shoulder peak at around 650 nm. The shoulder is not due to structure resonances such as the RPG wavelength-/QW spacing, as a similar shape with the shoulder on the blue side is visible for a single quantum well structure grown to calibrate a design B structure, shown in Figure 4.10, determining that the QW emission is of this form. Both the first excited heavy-hole

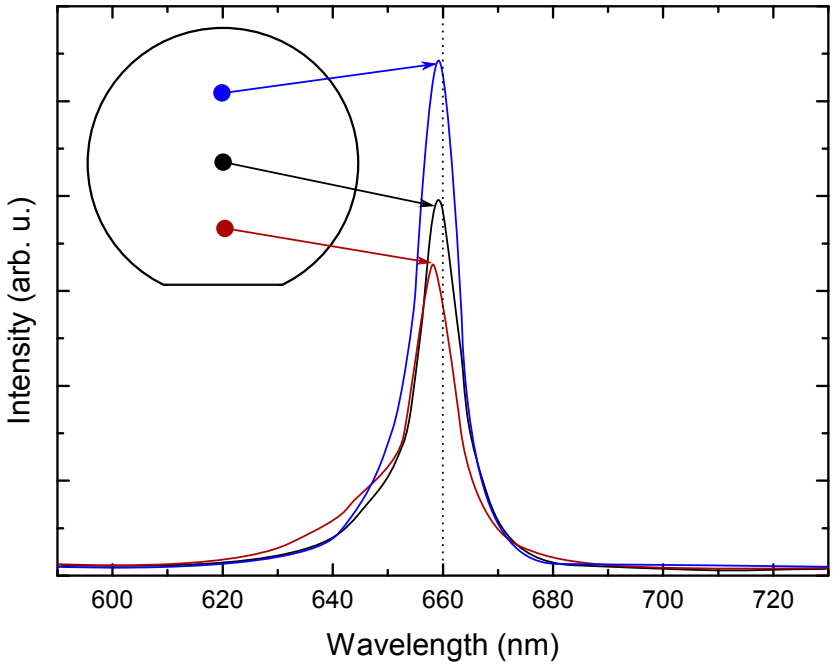

Figure 4.9: Surface-PL of design A structure, with a 'shoulder' visible around 650nm. Multiple measurements taken from positions specified on the inset wafer map showing the full 2 " wafer, with major flat indicated. Peak wavelength is essentially the same across the wafer. Dotted line indicates design wavelength.

transition and the ground state light-hole transition energies are expected to produce peaks at approximately 648 nm so these are consistent with the QW shoulder feature.

The reflectivity for the centre of design A is given in Figure 4.11. The key feature of this reflectivity profile is the large peak and trough indicating resonance of the quantum well positions as previously discussed, and therefore the spacing between QW pairs and the RPG wavelength.

The oscillation visible in Figure 4.11 indicates structure thickness, and the main peak and trough deviating from this the QW pair separations, as shown in Figure 4.8 and as previously explained. The slight shoulder at 655–659 nm in each spectrum shown corresponds to the peak PL emission.

Different positions on the wafer show varied closeness of fit to the simulated reflectivity, with one position 14.1 mm from centre matching the trough wavelength of 690 nm and overall oscillation well. Other positions vary further to the blue, with the trough reducing as far as 660 nm (RPG of approximately 650 nm according to simulation) for

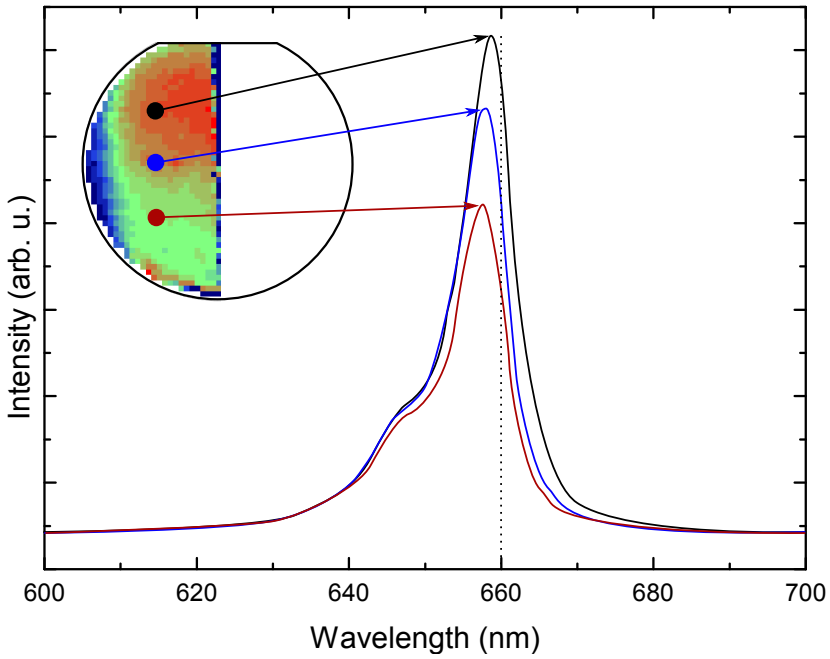

Figure 4.10: Single GaInP quantum well for calibration of the quantum well emission for structure B, shows the same shape as for the multi-QW structures. This demonstrates that RPG is not contributing to PL shape. Multiple measurements taken from positions specified on the inset PL intensity wafer map (red areas show higher recorded intensity), indicate a nearly homogeneous emission wavelength. Dotted line indicates design wavelength.

the position marked with a blue spot on the inset wafer map. The agreement between the simulation and the recorded spectrum at the position indicted by the red spot on the inset wafer map shows that the structure barrier thicknesses are accurately grown to the design at this position. The variation is due to the thickness variation caused by the flow of gas in MOCVD growth with a stationary substrate, which can be seen in Figure 4.11 as the decrease in thickness for positions further from the major flat, and thermal inhomogeneity of the sample during growth.

4.6.2 Initial characterisation: Design B

Reflectivity and surface PL for structure B are very similar to that of A, due to the similarity in design. Figure 4.12 shows surface-PL of the first strain balanced growth of design B, showing the same shape as the calibration single-QW structure surface-PL spectrum (Figure 4.10), and that of design A growths. The reflectivity spectrum for

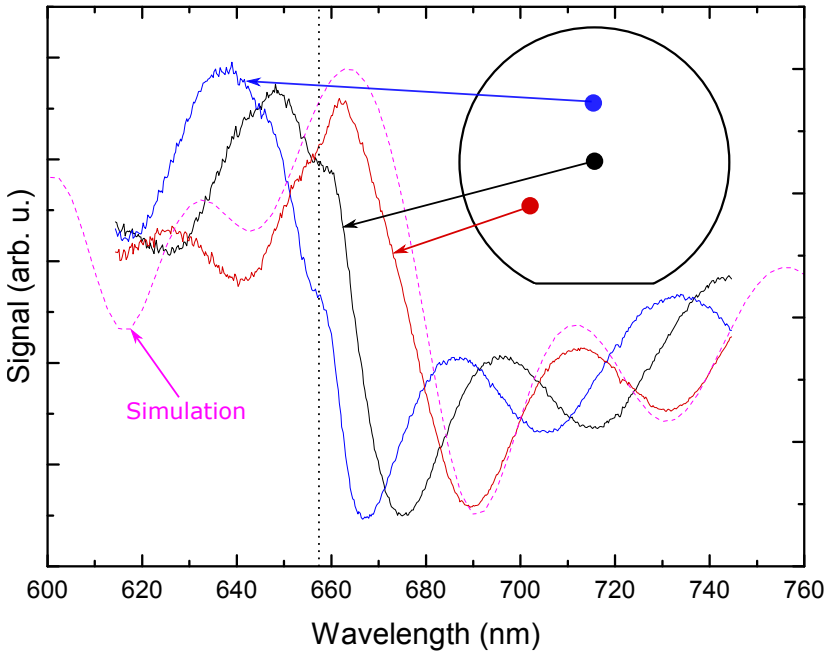

Figure 4.11: Design A, simulated design (dashed pink) and measured (with positions indicated, inset) reflectivity spectra. Two of the positions shown do not match the simulation, indicating thinner structure further from the major flat, while the position indicated by the red spot gives good agreement to the simulation. Dotted black line indicates peak PL wavelength.

design B in Figure 4.13 shows the same small feature corresponding to the PL peak wavelength, this time at the top of the peak at 657 nm. The reflectivity spectra show the same overall oscillation with a large deviating peak and trough. As with the design A structures, a position closer to the major flat shows the best match to the simulation of the design, shown in pink, indicating that this is the most likely area on the wafer for high laser performance.

4.6.3 Initial characterisation: Design C

Design C has again a similar design to B, but for a longer target wavelength. It should therefore be expected that the surface PL and reflectivity should also demonstrate the same features as those seen in Sections 4.6.1 and 4.6.2. This can be seen to be the case in the surface-PL spectra in Figure 4.14, where the same emission peak shape is observed with the shoulder on the blue side.

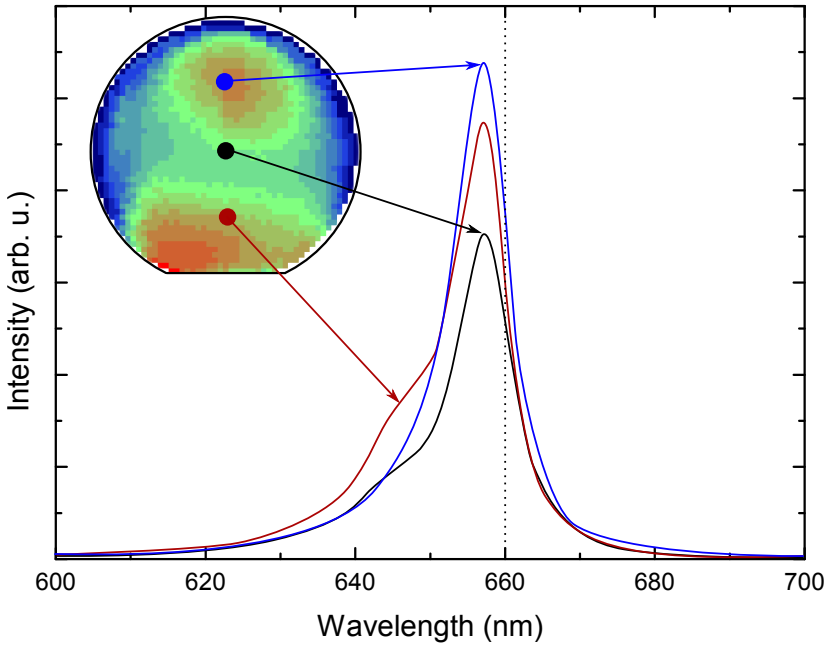

Figure 4.12: Design B surface-PL (MR3716), shape is very similar to both the single quantum well calibration, and that of structure A. Multiple measurements taken from positions specified on the inset PL intensity wafer map (red areas are higher intensity), with major flat indicated, show homogeneous peak wavelength across the wafer. The dotted line indicates the design wavelength.

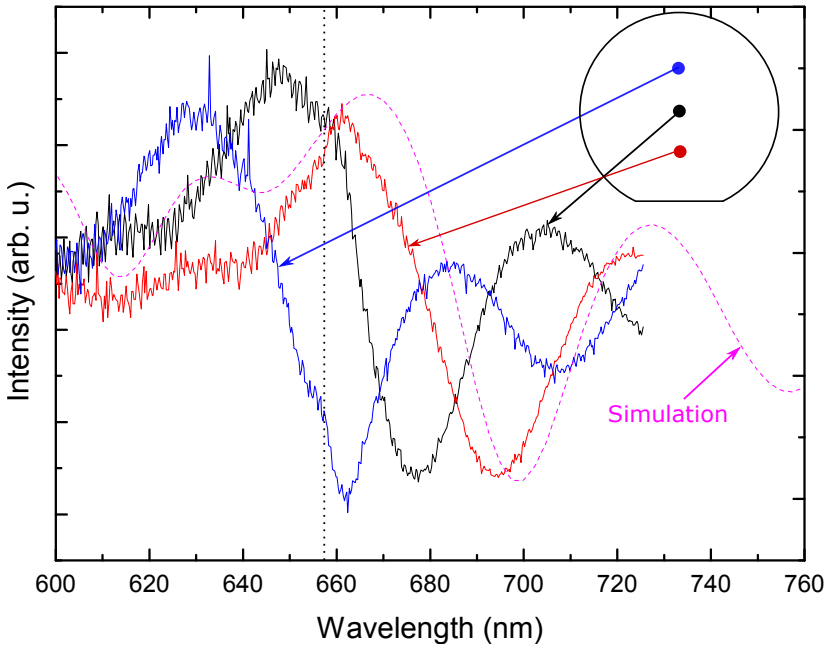

Figure 4.13: Design B, simulated design (dashed pink) and measured (with positions indicated, inset) reflectivity spectra. Two of the positions shown do not match the simulation, indicating thinner structure further from the major flat, while the position indicated by the red spot gives good agreement to the simulation. Dotted black line indicates peak PL wavelength.

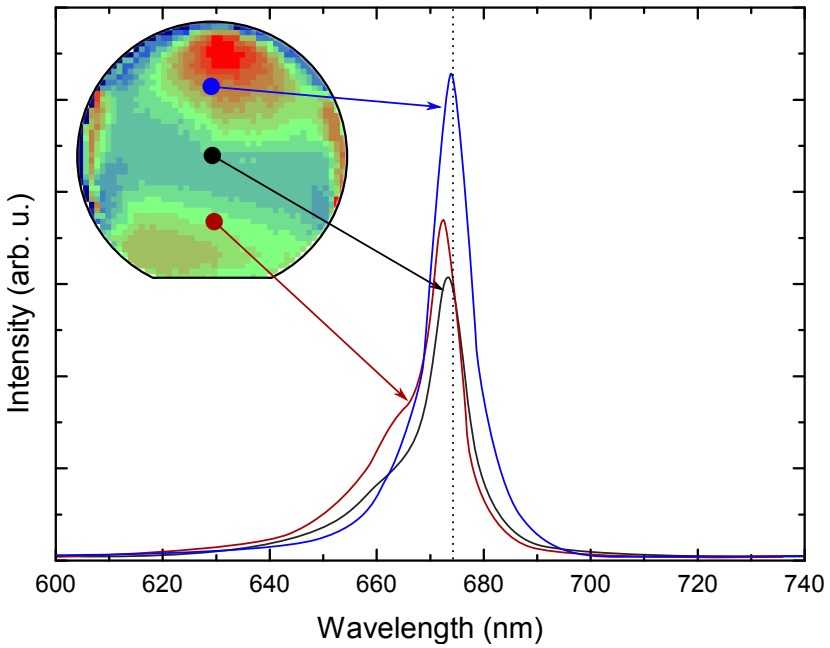

Figure 4.14: Design C surface-PL (MR3751), shape is similar to both the single quantum well calibration, and that of structures A & B, but at longer wavelengths. Multiple measurements taken from positions specified on the inset PL intensity wafer map (red areas are higher intensity), with major flat indicated, show homogeneous peak wavelength across the wafer. Indicated by the dotted line is the design wavelength of 674 nm.

The reflectivity spectrum is shown in Figure 4.15. Unlike the other wafers previously discussed, the position where the recorded reflectivity spectrum matches the simulated spectrum is closer to the centre, and the expected position is indicated by a pink circle on the wafer map inset in Figure 4.15.

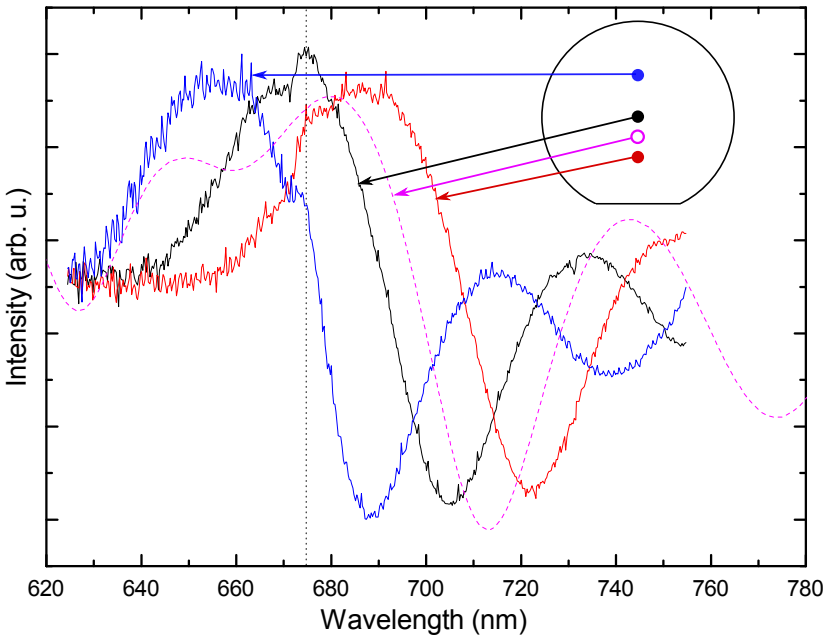

Figure 4.15: Design C (MR3751), simulated design (dashed pink) and measured (with positions indicated, inset) reflectivity spectra. None of the positions shown match the simulation, with the design simulation located between the red and black positions on the wafer. The position that corresponds to the design layer thicknesses is therefore estimated to be between the two, indicated by the pink circle on the inset wafer map (approximately 5 mm from centre). Dotted black line indicates peak PL wavelength.

4.7 Laser and transfer characterisation

After initial characterisation and analysis of the wafers, each structure is cleaved and processed using the method described in Section 4.3.1. Laser characterisation was achieved for multiple structures in the cavity described in Section 4.5, but was often too short-lived for recording. An in depth analysis of the transfer success is discussed in Section 4.7.4. The two most successful lasers were obtained from designs A and C, and these are discussed in this section. Figure 4.16 shows a photograph of the working thin-film VECSEL from the design A structure.

4.7.1 Processed laser gain regions

Each processed region is less than 1.5 µm thick, and the first CW film VECSEL was from design A: a 2×2 mm square from near the optimal position specified in Figure 4.11,

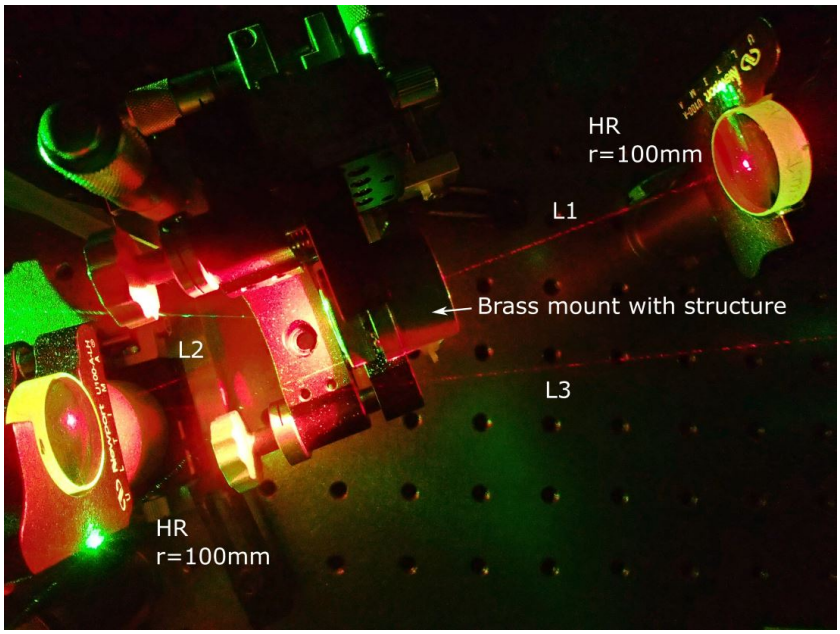

Figure 4.16: Demonstration of a thin-film VECSEL. Cavity lengths are indicated as shown schematically in Figure 4.7.

capillary bonded to a 4 mm radius, 500 µm thick CVD grown ultra-low birefringence diamond.

Figure 4.17 shows the processed sample on diamond, and the surface quality and bond appears poor in several places. There are however several places in which the bond is good (signified by the smooth red areas on the through-diamond view) and it is these spots which are pumped and provide the strongest SPL emission at low pump powers. The laser performance of this structure is described in Section 4.7.3.

4.7.2 Power loss issues

A consistent feature in these laser samples has been the relatively rapid power loss for pumped spots. This is either due to spot de-bonding causing overheating and burning, or of a more gradual process such as thermal annealing, or a combination of the two. This issue manifests for different amounts of time for different samples, although it tends to be the case that after the first spot 'burns out', the others will follow more quickly, indicating that it is debonding that is the problem, and that it spreads weakening the bond across the surface with each spot.

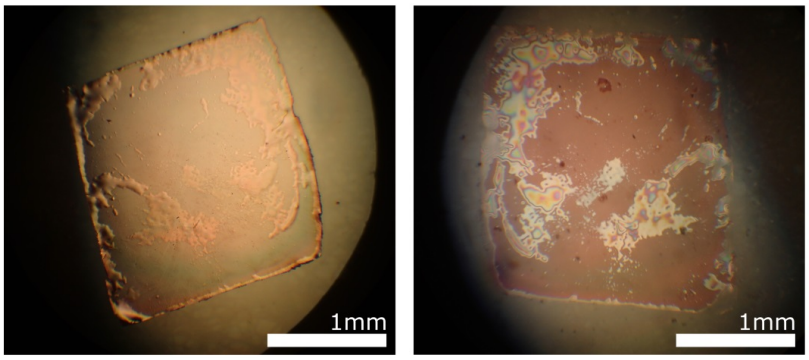

Figure 4.17: Diamond bonded sample (design A) before pumping, (a) rear side of sample transferred to diamond (b) microscope image of the capillary bond through diamond prior to pumping. Flat red areas indicate high bond quality spots to be pumped.

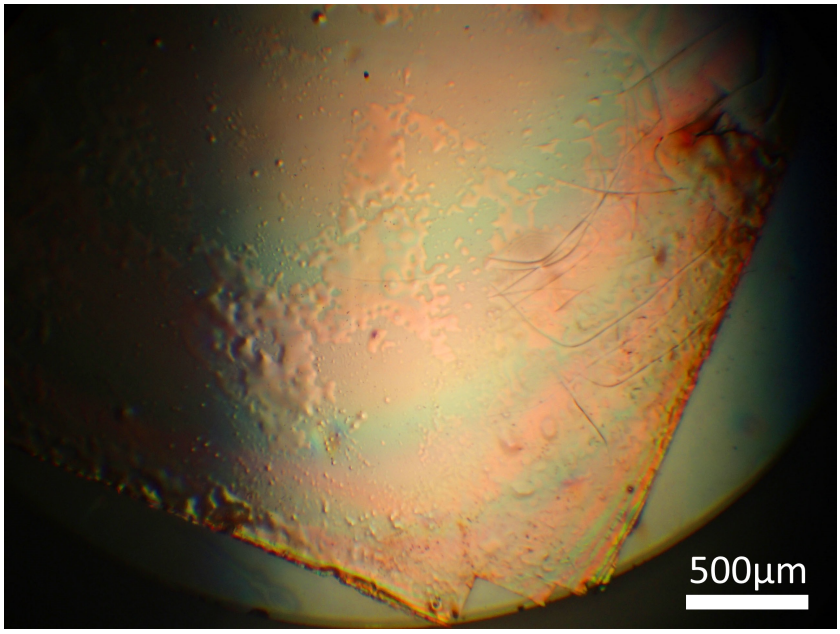

Figure 4.18: Interference fringes visible on the outer areas of a large (3 mm square) sample capillary bonded to diamond. Structure is design A.

Potential solutions are to simply achieve a better bond between sample and diamond (hence the introduction of piranha cleaned diamonds for example), and the use of a heatspreader sandwich. A potential issue with the heatspreader sandwich is the etch progression shown in Figure 4.3, the longer period the outer areas of the sample are exposed to the etchant may produce a rounded surface meaning that the bonding of planar material on both sides may be difficult or impossible, see Figure 4.18 for an example of interference fringes caused by the changing structure thickness .

This over-etch complication is one that the addition of a GaInP etch stop in the second structure design was to address.

Due to the short lifetime of the samples, complete laser tests have been challenging. The best sample spot worked for several hours, and this is the structure used for power transfers and the initial spectral measurement. The second best working sample enabled measurement of a tuning curve through the insertion of a 4 mm birefringent filter (BRF).

Quasi-CW pumping with a chopped pump at 50 Hz does not appear to extend the lifetime of these lasers. A pattern was observed where the switching off of the laser caused the spot to cease working for the next attempt, suggesting that in the event that the pump heating does not cause de-bonding, the cooling may do so anyway.

One possibility to aid in both heat extraction and holding the bond is the potential of a diamond sandwich bond, however this is hindered by the surface curvature demonstrated in Figure 4.18. .

4.7.3 Laser characterisation: design A

Structure A was grown as the calibration structure for a 675 nm gain-mirror VECSEL with tensile strained balancing barrier layers, and as such does not contain an anti-oxidation layer.

A spectral measurement was taken before the laser was fully optimised, with the free-running laser spectrum containing 4 peaks centred at 670.5 nm, shown in Figure 4.19. The separation of the peaks matches the expected free-spectral range of the etalon set up by the intracavity diamond heatspreader. The free-spectral range of the structure is significantly larger, of the order 50 nm, and will not influence the recorded spectrum .

Power transfer curves were then taken with different mirrors as the output coupler, with mirrors of <0.01%, 0.05% and 0.2% transmission measured, shown in Figure

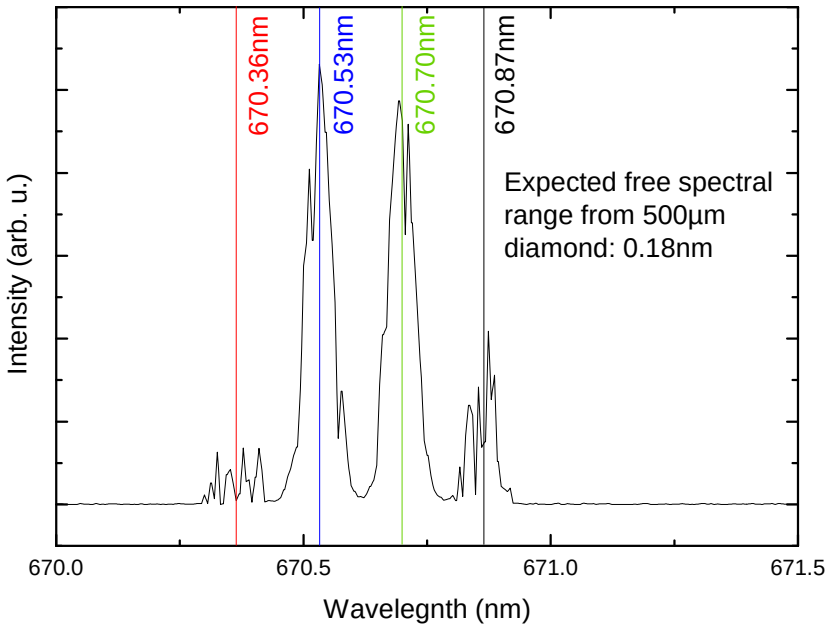

Figure 4.19: Recorded spectrum of free-running laser emission. Laser operates around 670 nm. Peak separation corresponds to the etalon of the 500 µm thick diamond heatspreader.

4.20. Before further higher transmission output couplers (OCs) could be tested, laser oscillation ceased.

For these measurements the brass mount was cooled to 10 °C. Maximum output power was obtained with 0.2% OC: 21.5 mW for 3.2 W pump power, with rollover occurring at higher pump powers. Cavity optimisation was performed while pumping at 1 W each time. Threshold remained approximately the same for each output coupler used, 0.36 W, as expected for such low output couplings, considering the logarithmic dependency of threshold gain g_{th} on carrier density N_{th} in Equation 2.26. This threshold is lower than most published red VECSEL results, and is more comparable to the diode-pumped red VECSEL reported in ref. [18], although this is likely due to the published power transfer curves being for higher output coupling with the cavity optimised for high power operation rather than low threshold.

Another sample cleaved from the wafer, from a position next to the previously described laser, enabled measurement of a tuning curve for the VECSEL via rotation of an intracavity 4 mm-thick birefringent filter (BRF) before ceasing operation, shown in Figure 4.21.

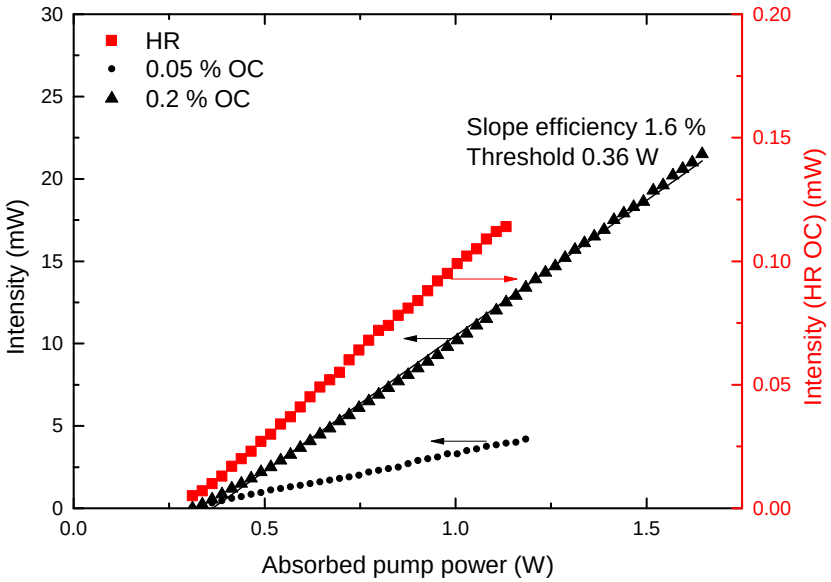

Figure 4.20: Power transfers of the laser, maximum power 21.5 mW with 0.2% OC, transfers also taken for 0.05% OC, and for an HR cavity. Threshold is approximately 0.36 W in all cases. Error bars are not shown as fluctuations in recorded values was low with respect to the output powers.

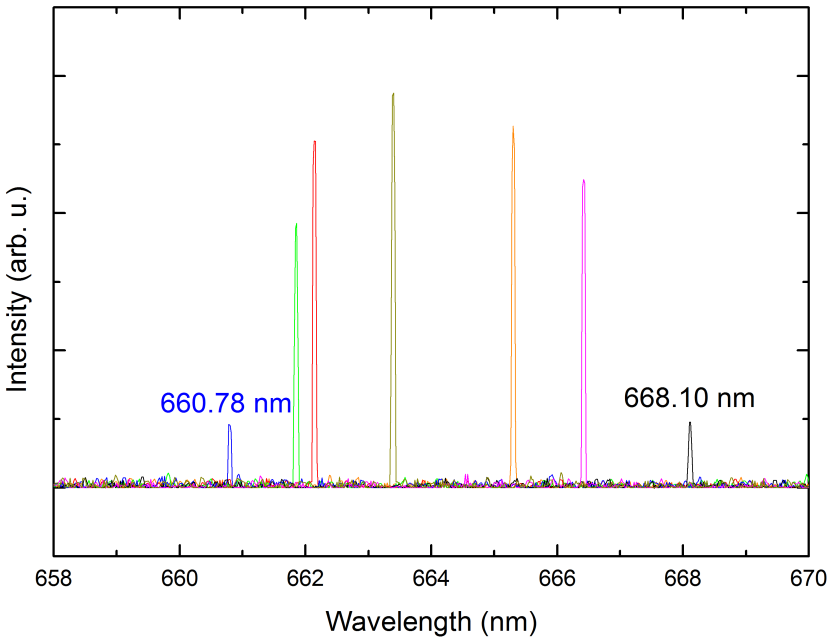

Figure 4.21: Tuning of the calibration structure thin-film VECSEL. Each colour indicates a measurement made with a different BRF angle. Tuning range is 8 nm, which is similar but slightly lower than that expected from an equivalent 675 nm gain-mirror VECSEL.

The tuning range of the thin-film VECSEL is >8 nm for a 4 mm BRF, similar to that of a standard VECSEL [3]. Use of a thinner BRF could increase the tuning range, but would potentially broaden each individual spectrum to include multiple peaks; the equivalent gain-mirror VECSEL structure with a 1 mm BRF producing tuning ranges of up to 20 nm.

The structure design had RPG wavelength at 675 nm, so the laser operating at a wavelength as low as 660 nm indicates that the RPG is shorter at this position. Referring back to the reflectivity characterisation, Figure 4.11, the blue-shift of the major peaks by 10–15 nm may indicate an RPG shift of the same, however the spectrum shown in Figure 4.19 demonstrates that RPG must vary across the sample as a result of the MOCVD growth.

4.7.4 Etch & transfer tests: designs B and C

Both designs B and C incorporate strain balance layers within the barriers, with the potential to allow for more accurate calibration of strain balancing material composition during growth. As discussed in Chapter 2 there are performance and device lifetime advantages to including strain balancing layers in VECSEL structures with a potential for easier growth. To characterise the effects of strain balancing on the epitaxial layer transfer, equivalent structures to designs B and C were also grown without the strain balancing layers.

For design B, 3 wafers were grown, 1 with strain balancing and 2 unbalanced. Design C growths consisted of 2 strain balanced and 1 unbalanced. For the test of structure etch and transfer to diamond, 5 samples of cleaved size 2.5×2.5 mm from each wafer were tested, taken from the centre of each wafer.

The summary of structures grown and the success of transfer and operation are given in Table 4.5. Examples of the etch characteristics are given in the microscope images in Figure 4.24 for the unbalanced design C structure MR3751 showing the buckling behaviour caused by strain, and in Figure 4.25.

Thin-film VECSEL structures & transfer				
Structure	Design (λ)	Balanced	Transfer characteristics	Laser action
MR3716	B (675 nm)	Yes	Etched with no distortion or cracking, large area transfer possible (>2x2mm).	Yes
MR3717	B (675 nm)	No	Significantly fractures during etch, unable to be transferred	–
MR3732	B (675 nm)	No	Etched with no distortion or cracking and transferred to diamond	No
MR3749	C (689 nm)	Yes	Etched with minor distortion and transferred to diamond	No
MR3750	C (689 nm)	Yes	Surface shows partial fractures during the etch, but the majority of the structure remains transferable	No
MR3751	C (689 nm)	No	Distorts during etch, which can cause fractures during transfer.	Yes

Table 4.5: Tabulated summary of etch and transfer tests for III-V thin-film VECSEL structures. Laser action of structures is also indicated. Little correlation is observed between the inclusion of strain balancing layers and the etch/transfer success.

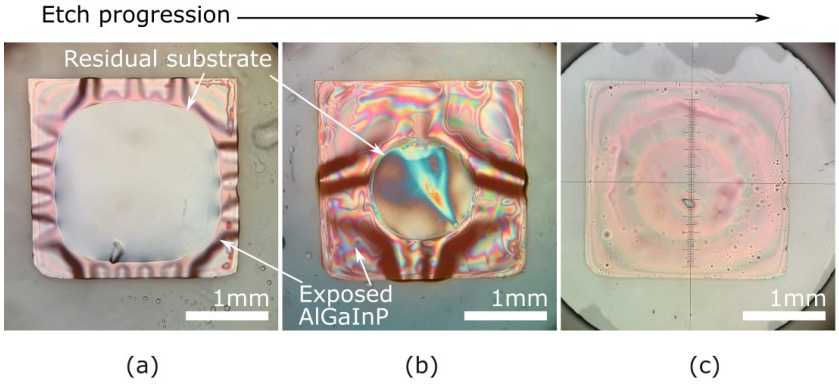

Figure 4.22: Etch progression of MR3751, unbalanced design C structure. Note the buckling/distortion of the structure as the substrate is removed, but that it does not fracture. (a) 10 minutes etch time; (b) 15 minutes etch time (with approximately 1 minute remaining); (c) structure transferred to diamond and flattened. Visible are the newton rings indicating partial structure etch (non-parallel surfaces).

From the etch and transfer tests, there appears to be no advantage in transferability for structures designed to be strain balanced; however, XRD measurements are required to determine whether or not the strain balancing was achieved as designed. Different structures display different characteristics as the substrate is removed, some with the epitaxial cracking and others with buckling, indicative of tensile and compressive strain respectively as with the II-VI structures [19].

The laser tests discussed in Section 4.7.5 below show that the most successful and

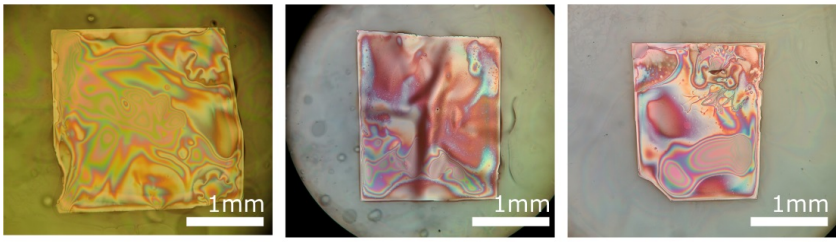

Figure 4.23: Etched samples of (a) MR3732, unbalanced design B; (b) MR3749, balanced design C; and (c) MR3750, balanced design C.

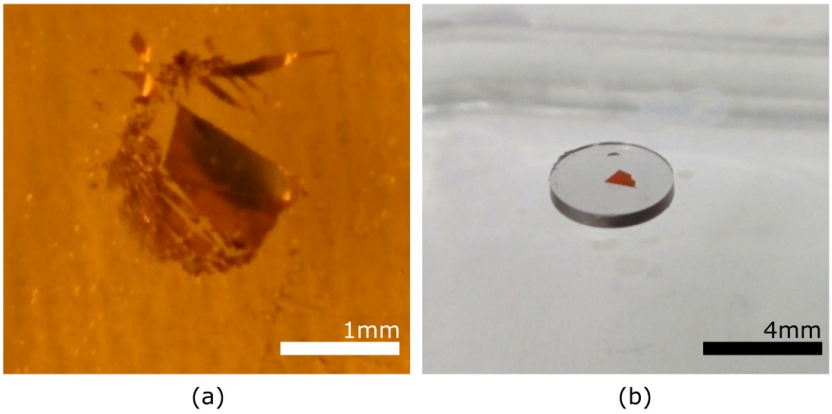

Figure 4.24: MR3751 structure transferred to diamond, producing the longest lasting laser operation. (a) Structure on glass, removal from acid and water bath has damaged the buckled outer areas of the structure, while the centre remained attached with wax to the glass. (b) Centre piece transferred to diamond to be pumped in the laser cavity.

long-lasting laser structure is MR3751, an unbalanced design C structure with higher strained QWs. This should have been the highest strain structure grown, and this is upheld by the rippling during etch and resultant fracturing on lift-off from the glass. However this structure produced the most successful laser operation of the growth campaign with the transfer of a fractured piece to diamond. The structure during lift-off and transferred to diamond is shown in Figure 4.24.

It is found that these structures still suffer from the debonding issues described in Section 4.7.2, with operation failing after approximately 7 hours operation. This is contrasted with the laser action observed from samples of MR3716, which ceased operation within 20 minutes of operation with constant reduction in efficiency. Care was taken not to over-pump the structures to extend device lifetime as far as possible.

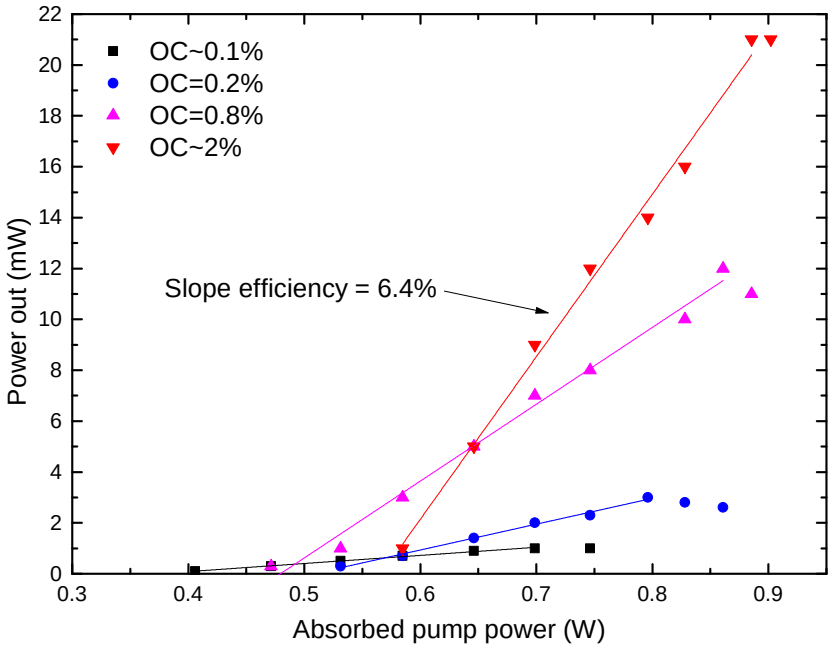

Figure 4.25: Power transfer curves for the design C laser MR3751, with output coupling of 0.1%, 0.2%, 0.8% and approximately 2% (reflectivity approximate at this wavelength). Slope efficiency of 6.4% was recorded for the 2% OC, with a maximum power of 21 mW for 0.9 W absorbed pump power. Lowest recorded threshold for 0.1% output coupling was 0.4 W.

4.7.5 Laser characterisation: design C

The 3-mirror cavity was set up as before, described in Section 4.5. Output couplers of 0.1%, 0.2%, 1% and 2% were used to provide the power transfer plots as shown in Figure 4.25.

Maximum output power of 21 mW was found for 2% output coupling for absorbed pump power of 0.9 W, with a threshold of 0.57 W and slope efficiency 6.3%. The lowest threshold was when in operation with 0.1% output coupling at 0.4 W absorbed pump power. An even higher power of 31 mW for 0.9 W of absorbed pump power was briefly observed with an output coupling of approx. 3%, but rapidly reduced to 12 mW within seconds due to thermal rollover.

Higher output power was achieved with the unbalanced design C laser than for the design A laser. This was due however to the higher output coupling, and thermal rollover was significantly lower for this laser. The two lasers cannot be directly

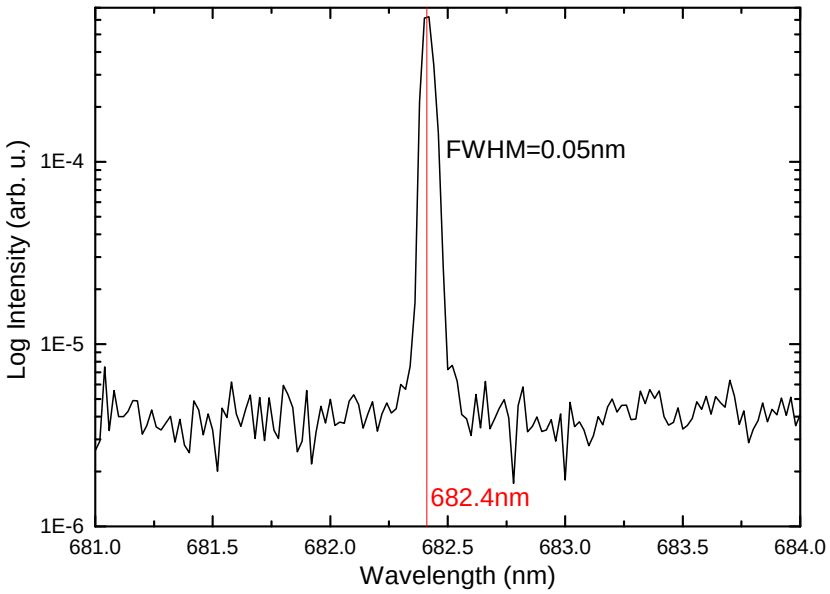

Figure 4.26: Spectral measurement of the free-running design C laser, with peak centre 682.4 nm and FWHM 0.05 nm.

compared, as their design and output wavelengths are quite different. The spectral emission for the design C MR3751 laser is shown in Figure 4.26. Laser action failed before the cavity could be optimised with an inserted BRF to measure tuning.

4.8 Summary and future work

Through a method of substrate etch and structure transfer adapted from the II-VI materials work discussed in Chapter 3, thin-film VECSELs have been demonstrated as viable devices, but requiring continued and intensified work with growth groups to progress them beyond short-lived novel devices to useful and reliable devices for application. Continuing challenges include overcoming the debonding/device lifetime limitation which severely limits their characterisation and application. Results indicate the potential to match the performance of gain-mirror VECSELs if these challenges can be overcome.

Three designs for thin-film VECSELs have been described, the strain-balancing barrier layers in design A, the strain-balance layers within lattice matched barriers of design B and the long wavelength design C. Designs B and C also had structure growths without balancing (layers replaced with lattice-matched barrier material) to investigate

the impact of QW strain on the thin-device transfer. This was found to be minimal, or at least the accuracy of the strain balancing not sufficiently repeatable for a confident determination of the effects. 'Balanced' structures would be unable to transfer successfully, and 'unbalanced' structures etching and transferring without problem. This is demonstrated by the arbitrary success and failure demonstrated in Table 4.5. High-resolution X-ray diffraction measurements would need to be made and analysed for a complete picture of the structure strain before determining how strain balancing of the QWs affects the transfer characteristics.

Laser action was achieved with multiple structures, but for the most part was short-lived, falling prey to thermal management issues, resulting in damage and debonding which only further exacerbated the thermal problems. Two laser devices were operational for long enough for a partial characterisation, showing properties which, while not equal to the red gain-mirror VECSEL results in refs. [3–5,20,21], could result in high performance devices. Through further development of the transfer technique, more protection could be given in future to the top surface of the structure during etch, reducing the curvature of the surface (evidenced by the interference fringes visible in transferred structures) and so introducing the potential for diamond-sandwich devices to clamp the structure and both hold the bond and to extract heat more effectively. When compared to the early room temperature (cooled to 0 °C) continuous-wave red VECSEL in ref. [3], perhaps a fair comparison due to the novel nature of the thin-film VECSEL, the design A laser described in Section 4.7.3 could be pumped to nearly comparable levels before thermal roll-over, with a lower threshold recorded and similar tuning ranges (10 nm in ref [3], compared to 8 nm). Not compared is the output beam quality, with the thin-devices possibly operating highly multimode.

While initial laser results have been performed with the thin-film structures in approximately the same cavity as the full VECSEL structures with grown DBRs, thin-film active-region-only VECSEL structures open possibilities for novel cavity designs and pump arrangements. Double-end pumping can increase uniformity of pump absorption and carrier distribution throughout the quantum wells – the distribution of quantum wells with respect to pump absorption has been demonstrated to have a

significant effect on efficiency, so removing this effect could have performance advantages. Vertical external-cavity travelling-wave ring cavities can be attempted using these thin-film semiconductor gain regions, a relatively new area of investigation with a small number of recent reports [22], which could provide advantages for processes where unidirectional oscillation is desirable, e.g. intra-cavity modulators.

4.9 References

[1] M. Müller, N. Linder, C. Karnutsch, W. Schmid, K.P. Streubel, J. Luft, et al., Optically pumped semiconductor thin-disk laser with external cavity operating at 660 nm, in: Proc. SPIE, 2002: pp. 265–271. doi:10.1117/12.469242.

[2] M. Müller, C. Karnutsch, J. Luft, W. Schmid, K. Streubel, N. Linder, et al., Optically pumped vertical external cavity semiconductor thin-disk laser with CW operation at 660nm in, in: Compd. Semicond. 2002, 2003: pp. 427–430.

[3] J. Hastie, S. Calvez, M. Dawson, T. Leinonen, A. Laakso, J. Lyytikäinen, et al., High power CW red VECSEL with linearly polarized TEM00 output beam., Opt. Express. 13 (2005) 77–81. doi:10.1364/OPEX.13.000077.

[4] T. Schwarzbäck, M. Eichfelder, W.M. Schulz, R. Roßbach, M. Jetter, P. Michler, Short wavelength red-emitting AlGaInP-VECSEL exceeds 1.2W continuous-wave output power, Appl. Phys. B Lasers Opt. 102 (2011) 789–794. doi:10.1007/s00340-010-4213-5.

[5] T. Schwarzbäck, R. Bek, F. Hargart, C.A. Kessler, H. Kahle, E. Koroknay, et al., High-power InP quantum dot based semiconductor disk laser exceeding 1.3 W, Appl. Phys. Lett. 102 (2013) 092101. doi:10.1063/1.4793299.

[6] E.F. Schubert, Light-Emitting Diodes, 2nd ed., Cambridge University Press, 2006.

[7] EPSRC National Centre for III-V Technologies, Our Facilities, (2015). http://www.epsrciii-vcentre.com/working-us/facilities/ (accessed April 2, 2015).

[8] I. Vurgaftman, J.R. Meyer, L.R. Ram-Mohan, Band parameters for III–V compound semiconductors and their alloys, J. Appl. Phys. 89 (2001) 5815. doi:10.1063/1.1368156.

[9] M. Schubert, J.A. Woollam, G. Leibiger, B. Rheinla, I. Pietzonka, V. Gottschalch, et al., Isotropic dielectric functions of highly disordered $Al_xGa_{1-x}InP$ (0<x<1) lattice matched to GaAs, J. Appl. Phys. 86 (1999) 2025–2033. doi:10.1063/1.371003.

[10] S. Adachi, GaAs, AlAs, and AlxGa1–xAs: Material parameters for use in research and device applications, J. Appl. Phys. 58 (1985) R1–R29. doi:10.1063/1.336070.

[11] E. Yablonovitch, T. Gmitter, J.P. Harbison, R. Bhat, Extreme selectivity in the lift-off of epitaxial GaAs films, Appl. Phys. Lett. 51 (1987) 2222. doi:10.1063/1.98946.

[12] C. Bradford, A. Currran, A. Balocchi, B.C. Cavenett, K.A. Prior, R.J. Warburton, Epitaxial lift-off of MBE grown II-VI heterostructures using a novel MgS release layer, in: J. Cryst. Growth, 2005: pp. 325–328. doi:10.1016/j.jcrysgro.2005.01.019.

[13] N.J. Ekins-Daukes, K. Kawaguchi, J. Zhang, Strain-Balanced Criteria for Multiple Quantum Well Structures and Its Signature in X-ray Rocking Curves, Cryst. Growth Des. 2 (2002) 287–292. doi:10.1021/cg025502y.

[14] C. Fabry, A. Perot, A multipass interferometer, in: Ann. Chim. Phys., 1899.

[15] M. Born, E. Wolf, Principles of Optics, 7th (expanded) edition, 1999, Cambridge University Press.

[16] A. Smith, J.E. Hastie, A.J. Kemp, H.D. Foreman, M.D. Dawson, T. Leinonen, et al., GaN diode-pumping of a red semiconductor disk laser, in: Conf. Proc. - Lasers Electro-Optics Soc. Annu. Meet., 2008: pp. 404–405. doi:10.1109/LEOS.2008.4688661.

[17] R. Moug, A. Alfaro-Martinez, L. Peng, T. Garcia, V. Deligiannakis, A. Shen, et al., Selective etching of InGaAs/InP substrates from II-VI multilayer heterostructures, Phys. Status Solidi. 9 (2012) 1728–1731. doi:10.1002/pssc.201100716.

[18] T. Schwarzbäck, M. Eichfelder, W. Schulz, R. Roßbach, M. Jetter, P. Michler, Short wavelength red-emitting AlGaInP-VECSEL exceeds 1.2 W continuous-wave output power, Appl. Phys. B. 102 (2010) 789–794. doi:10.1007/s00340-010-4213-5.

[19] S. Baumgärtner, H. Kahle, R. Bek, T. Schwarzbäck, M. Jetter, P. Michler, Comparison of AlGaInP-VECSEL gain structures, J. Cryst. Growth. 414 (2015) 219–222. doi:10.1016/j.jcrysgro.2014.10.016.

[20] A. Mignot, G. Feugnet, S. Schwartz, I. Sagnes, A. Garnache, C. Fabre, et al., Single-frequency external-cavity semiconductor ring-laser gyroscope., Opt. Lett. 34 (2009) 97–99. doi:10.1364/OL.34.000097.

Chapter 5

II-VI quantum well films for colour conversion

Sections 5.1 to 5.4 offer a discussion of colour conversion for visible light communication as an application of the thin-film transfer technique. This research was performed in collaboration with fellow student Joao M. M. Santos, who led the emission and modulation bandwidth experiments on the hybrid GaN/II-VI μLED devices throughout Section 5.4, the results of which were reported in [1].

Section 5.6 introduces transfer of GaN LEDs to a processed II-VI thin-film, for rear emission through the structure; a collaboration with another fellow student António J. Trindade.

5.1 Introduction to visible light communication

Visible light communications, also known as Li-fi, is a method by which information is sent wirelessly using the visible spectrum [2]. The light is modulated to carry information through air, and the goal of such a system is to integrate wireless networking into spot- and room-lighting for a simplified and intuitive system for end consumers. Additional applications include providing networking in areas where electro-magnetic interference must be avoided, such as in mines or hospitals, or where radio-frequency communication is impossible, such as underwater. Privacy and security of a network can also be increased if the light leakage is avoided, and secure connections can be

made via a directed beam. A visible light source is therefore needed with light output that meets white-light specifications for pleasant room lighting, while maintaining high modulation band-widths.

5.2 White light generation

The common method of producing a white-light-emitting LED is to coat a blue-emission GaN device with phosphors to down-convert to a broad white spectrum. Phosphor converted devices, however, have a low modulation bandwidth due to long excited-state lifetimes in the micro-second regime [3]. Semiconductor solutions provide significantly higher modulation bandwidths while potentially fulfilling the conversion aspect for use within room lighting and white-light situations; the LED emission data rate from an unconverted InGaN-based device providing bandwidths up to 400 MHz [4]. By mixing multiple wavelengths an approximation of white light is reached, as defined in the chromaticity diagram shown in Chapter 1, Figure 1.5 (a).

Investigations so far have concentrated on organic semiconductors (e.g. [5,6]) and colloidal quantum dots (e.g. [7]). Both the organic semi-conductors and quantum dots require encapsulation to operate without environmental optical change, i.e. material changes caused by exposure to light, humidity, oxidation and heat [7]. Inorganic semiconductor quantum well laser structures, on the other hand, routinely withstand optical pumping at intensities significantly higher than those emitted by LEDs, and so are viable for long device life-times, and potentially high bandwidths.

5.3 Characterisation for colour conversion

To assess the suitability of II-VI quantum wells for colour conversion, the decay time of the gain structures described in Chapter 3 was measured – material lifetime of quantum well based semiconductors is one of the main advantages over the short device-lifetime of organic colour converters.

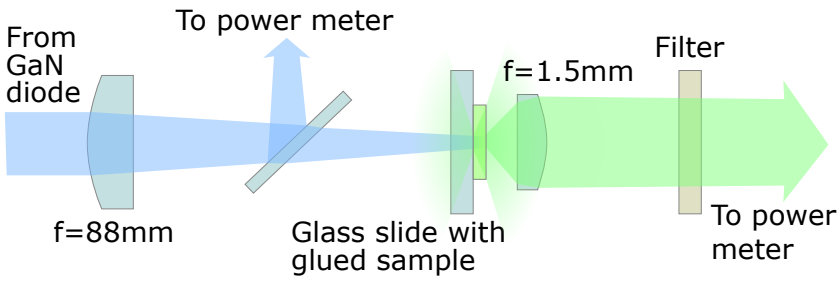

Figure 5.1: Decay measurement setup. A GaN laser diode pumps a processed sample through the glass slide, with pump power measured using a partial reflection. Surface-PL is collected using an f=1.5 cm lens, residual pump light is filtered, and the power is measured using an optical power meter.

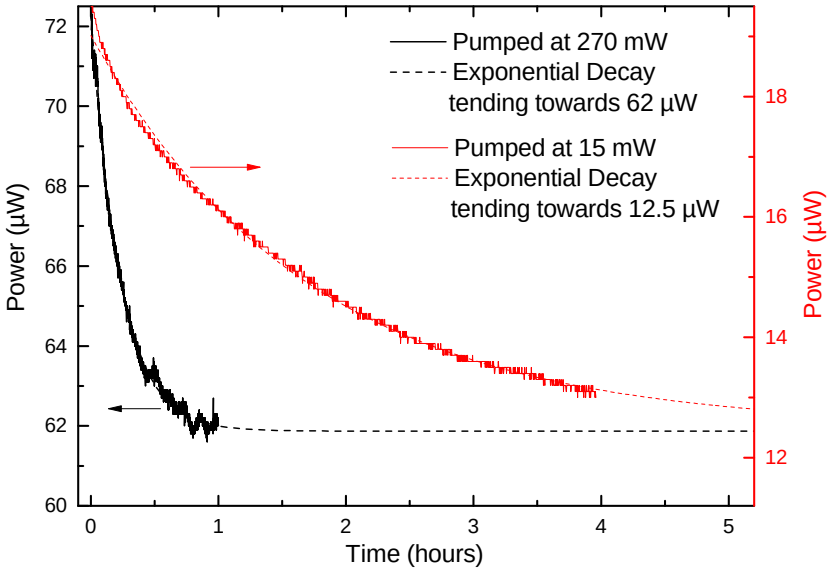

Figure 5.2: Power/time measurements for 15 mW and 270 mW pump power, with fitted exponential decay curves.

Using a sample of A3273, the first structure of Generation 2, with substrate and buffer removed, glued using NOA63 wax to glass and pumped with a continuous wave GaN laser diode, material decay with time was investigated. Very little heat-extraction is expected through the wax and glass.

Via the setup shown in Figure 5.1 below, 445 nm light from the GaN laser diode is focussed onto the sample to a spot of diameter <1 mm. The sample was pumped continuously with 15 mW or 270 mW, although the expected maximum power of the LEDs for this spot size is only 1.5 mW.

Figure 5.2 (a) shows the decay over 4 hours with 15 mW pump power, and (b) for 270 mW pump power at a different spot on the same sample. For 15 mW pump the

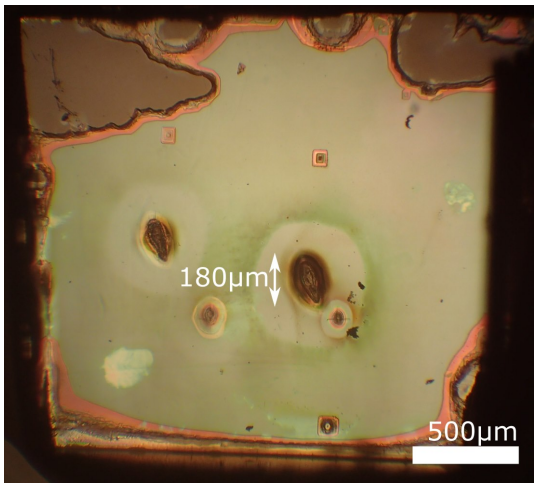

Figure 5.3: Pumped colour conversion sample A3273, imaged through the glass slide. Large spots indicate the locations of the high pump powers, small spots for the low pump powers. Each spot contains areas of higher damage in the centre, corresponding to the pump spot profile. The small square features are not pump related but are artifacts from the growth revealed during processing.

exponential decay tends towards a stable 12.5 µW emission, while for 270 mW pump it tends towards 62 µW.

After pumping of the sample, a microscope image shows damage to the surface caused by the two powers, Figure 5.3. Different features are visible on the surface, the most obvious of which are the dark burn patches. Higher powers have produced wider patches, although the largest is only 180 µm wide for a pump size of nearly 1 mm (at $1/e^2$) due to the non-uniform pump spot profile. The light areas surrounding these spots are caused by the heating effect on the wax, in effect re-curing the spots further and allowing for more transmission. The decay curve for each sample will likely still remain valid, as there would be little change in temperature after the initial thermalisation. It suggests that there is a form of thermal annealing within the II-VI layers.

5.4 Transfer and testing of II-VI films

Transfer of the II-VI film from substrate is performed as described in Chapter 3, but in this case to the sapphire substrate of the GaN micro-scale (<200 µm) LEDs (µLEDs). The II-VI films tested were all from the second growth of Generation 2, which were

found to have the best transfer capabilities. The characterisations for these structures are described in Section 3.8.3.

5.4.1 Power and efficiency

Efficiency of the II-VI colour-conversion from Generation 2 was not expected to be optimal, the design having limitations for this purpose due to its intended use as a VECSEL structure. A major limiting factor was the absorption edge of the barrier material: the µLED emission wavelength at 450 nm was higher than the excitation wavelength for which the structure was designed, thus significantly reducing the absorption of the pump light. Further, the 5.5 period distributed Bragg reflector (DBR) would reduce transmission of the light generated by the quantum wells. Finally, the lack of anti-reflection layers on these initial samples reduced the pump absorption through Fresnel reflection loss when passing from air or sapphire to II-VI material with refractive index of qpproximately 2.5, and refractive index contrast at the II-VI/air interface introduces additional loss through back reflection . The composition of the II-VI barriers is such that 85±1% of the broad (FWHM 23 nm) emission spectrum of the µLED is absorbed. Figure 5.4 shows the normalised spectra of the bare µLED, hybrid µLED (µLED with a bonded colour conversion film), hybrid µLED filtered with a long-pass dichroic mirror and the absorption edge of the II-VI film. It can be observed that the peak at 475 nm in the hybrid µLED spectrum is due to un-absorbed µLED-emitted light. The II-VI film contributes a peak at 540 nm.

Figure 5.5 shows the recorded transmitted powers for a II-VI sample bonded to the µLED sapphire substrate, pumped with the GaN µLED (the bare µLED power output also shown for comparison). The power conversion efficiency is 1±0.1%, confirming the expectation that this structure would have low conversion efficiency.

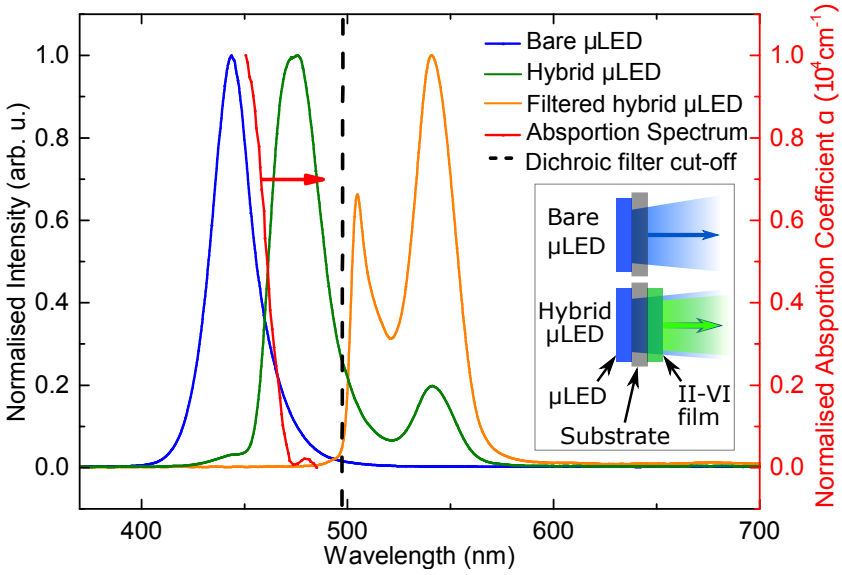

Figure 5.4: Normalised spectra of the bare µLED, hybrid µLED and filtered hybrid µLED for II-VI emission. Indicated in red is the absorption edge of the QW barrier material, and the dashed line indicates the cut-off of the long-pass dichroic filter. Inset: schematic of bare and hybrid µLED.

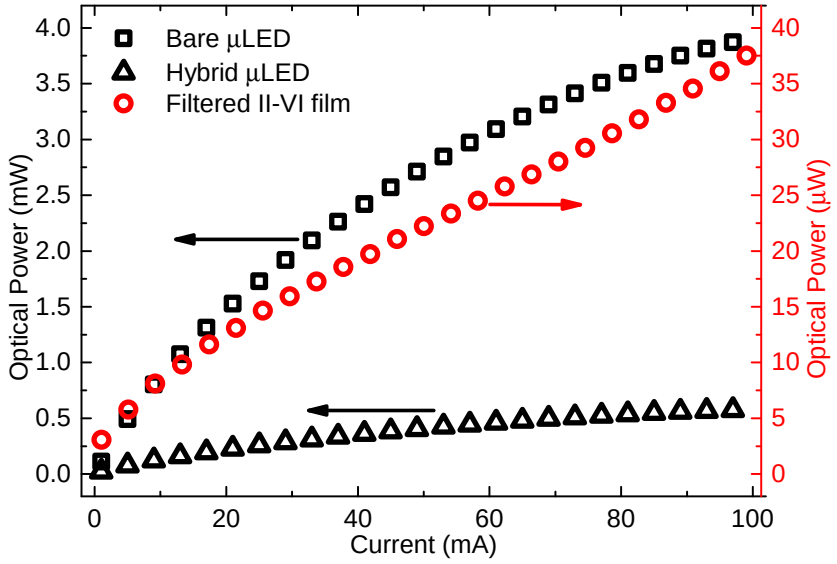

Figure 5.5: Recorded optical powers for the bare µLED, hybrid µLED and dichroic-filtered II-VI film. [1]

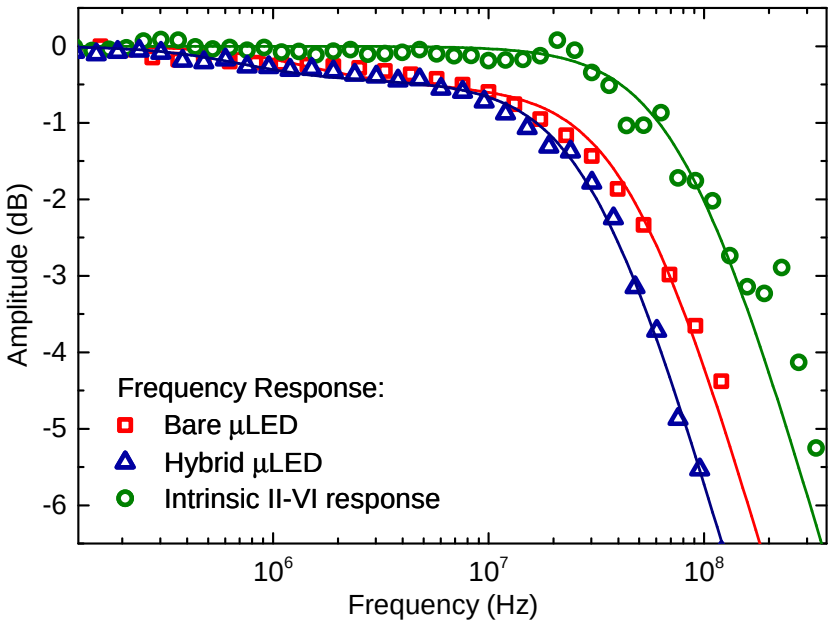

Figure 5.6: Bi-exponentially fitted frequency responses for the bare and hybrid µLED, and intrinsic II-VI film frequency response from the difference. [1]

5.4.2 Bandwidth measurements

How the modulation properties of the µLED are affected by the addition of the II-VI material is key for judging the potential of II-VI QW structures for visible light communication. An Agilent HP 8753ES Network Analyser produced the µLED modulation signal and compared the frequency response measured using a fast photoreceiver (with bandwidth 1.4 GHz). The frequency responses of the bare µLED and hybrid µLED are given in Figure 5.6, along with a calculated value for the intrinsic II-VI response curve from the difference between them.

The optical bandwidth of the bare and hybrid µLED, with intrinsic II-VI bandwidth, are plotted in Figure 5.7. In this case, the µLED is the limitation on the modulation bandwidth of the hybrid µLED, with a value of 51 MHz.

The power-density dependence of the II-VI modulation bandwidth was measured, both for a glass-bonded structure, with the µLED light focussed by a pair of lenses onto the structure, and for the hybrid µLED, shown in Figure 5.8.

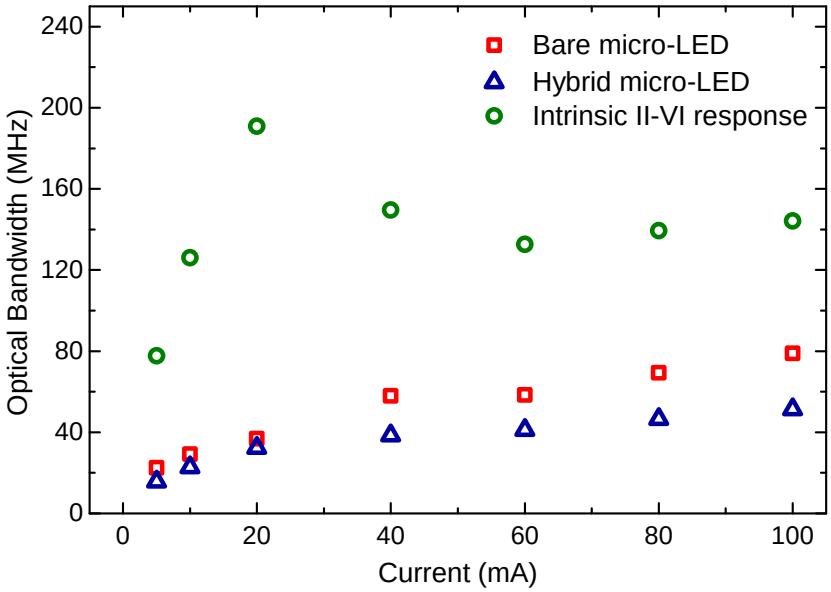

Figure 5.7: Bandwidths of the bare and hybrid μLEDs, and intrinsic II-VI bandwidth for −3 dB in (a). [1]

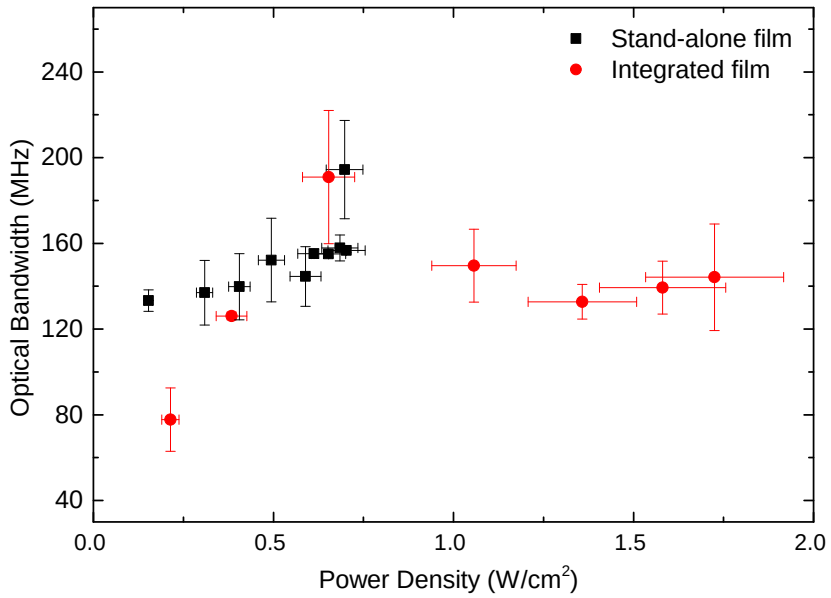

Figure 5.8: Bandwidth dependence on pump power density for the II-VI film both as a stand-alone film on glass, and integrated into the hybrid μLED. [1]

The trend for the hybrid μLED matches that for the separate glass-bonded structure. The pumped spot size for the hybrid μLED is estimated to be 330±20 μm. For 1–1.75 Wcm^2 the average intrinsic bandwidth is 145 MHz, corresponding to an effective photoluminescence lifetime of 1.9 ns using Equation 5.1:

$$f_{co} = \frac{\sqrt{3}}{2\pi\tau_i} \tag{5.1}$$

where f_{co} is the optical bandwidth and τ_i the photoluminescence lifetime. The optical bandwidth of the II-VI film is twice that of phosphors, and this combined with a long device lifetime offers the potential for visible light communications. The II-VI structure design must be adapted to optimise for efficiency.

5.5 Designing for colour conversion

One of the key features of a colour conversion design is the absorption length of the structure. To produce white-light, multiple wavelengths must be combined. The blue from the LED can be used for this task, along with red and green from the converter, so the blue component can be fine-tuned through design of the structure absorption length. Calculation of absorption length was discussed in Chapter 3. Both red and green emission can be obtained using II-VI material [8,9], either from separate layered devices or integrated into one structure, through the manipulation of quantum well thickness and composition, as discussed in Chapter 3. This allows for devices that fully convert the blue LED light to white light at a position of choice on the chromaticity plot.

The first step to enhancing the conversion efficiency is of course to omit the DBR layers, as in the design of the Generation 3 II-VI structures. Further steps can be the introduction of grown anti-reflection layers to improve the transmission of the incoming blue light from sapphire to II-VI, although care would need to be taken that the composition of these layers would not absorb the pump. Coating the sapphire with

a dielectric anti-reflection coating before II-VI transfer could be a preferable solution to this.

Modulation bandwidth could be increased further in the II-VI material by removing the resonant design, which was beneficial for the VECSEL structures but increases photon lifetime within the structure.

5.6 Transfer printed LEDs

An alternative to transfer of the II-VI material from the native substrate to the LED substrate is the direct transfer of LEDs onto a II-VI film transferred to glass. By under-etching µLED structures, arrays are transferred by pick-and-placing them with patterned PDMS material, as described in [10].

After the LEDs have been placed onto the II-VI material, via capillary bonding, metal contacts are deposited to power and address each µLED. A simplified schematic is shown in Figure 5.9.

Investigation into the transfer printed method was limited by problems in the production of working LEDs, but resulted in the largest unbroken II-VI platelet transfer of 5×5 mm^2 of Generation 2.5 A3362 (5.5 period DBR), shown in Figure 5.9. It is the final stage where problems arise, with the metal track deposition failing to maintain

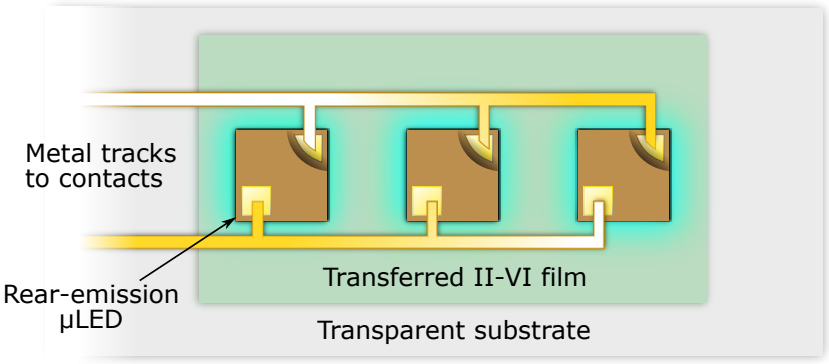

Figure 5.9: Simplified schematic of an array of transferred rear-emission µLED devices on a II-VI thin-film for colour conversion. For small-area colour conversion films, metal tracks must cross the edge to reach the electrical contacts, and it is this interface which must be smooth to allow for deposition.

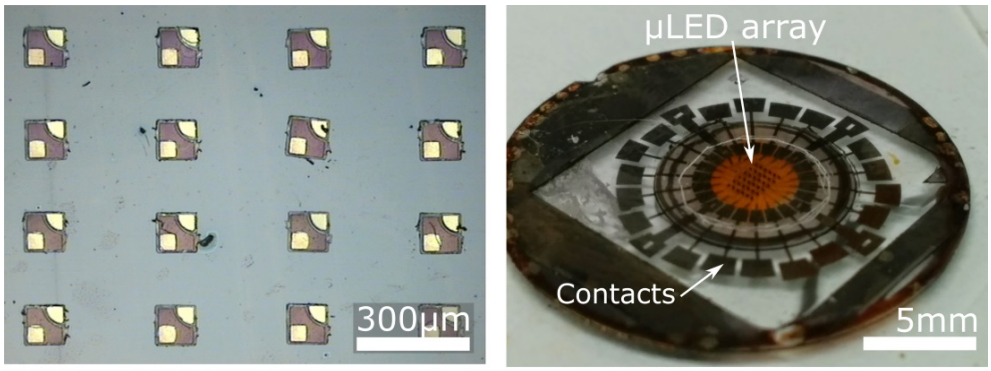

Figure 5.10: (a) Transferred micro-LED array on II-VI thin-film material, itself transferred to a glass substrate (before metal track deposition). (b) Micro-LEDs and metal tracks on Generation 2.5 sample A3361. The step at the edges of the II-VI material cause the metal tracks for powering the LEDs to not connect properly, a fault requiring further development.

a connection across the II-VI material edge. One potential solution was to smooth the interface with spin-coated adhesive, however this was unsuccessful and required further development. At this point the investigation was put on hold in favour of the previously discussed II-VI transfer colour converters.

5.7 Conclusions

By using the transfer technique developed for the II-VI VECSEL project in Chapter 3, the use of the ZnCdMgSe multi-QW structures as colour conversion films was investigated. For the purposes of visible light communication, the blue light from GaN diodes (at 445 nm) must be converted to white, while maintaining both high modulation speed for transmission of data, and maintaining long term performance in the device.

The most well-studied candidates for conversion materials are organics and quantum dots, with organics having higher modulation speeds but shorter lifetime than the dots, requiring additional preparation such as encapsulation. Inorganic ZnCdSe/ZnCdMgSe semiconductor quantum well structures are shown to have high modulation bandwidths and long device lifetimes, potentially bringing the best aspects of both organics and quantum dots.

Transfer of the ZnCdMgSe thin-films to the sapphire substrate of rear-emission micro-LEDs is performed in the same way as the laser structure transfer to diamond. High quality wide area films are possible and could easily cover multiple LEDs in an array. Measurements of power show a low conversion efficiency, although this is partially due to a non-optimum design, a structure from generation 2.5 described in Chapter 3. The design contains a DBR which hinders light extraction, as well as absorption that is not designed for this specific wavelength. Bandwidth is shown to match or exceed that of the GaN LED making this material ideal for colour conversion application if the efficiency can be increased.

A potential technique to aid this, reducing reflection due to refractive index contrast from LED-sapphire-ZnCdMgSe is to transfer the micro-LEDs directly onto the II-VI and use that as the substrate. While the target 5×5 mm^2 ZnCdMgSe film was etched and prepared to a high standard, the challenges involved in the layering of metal-tracks across the edge of the II-VI for powering/addressing the micro-LEDs meant that the transferred LEDs could not be powered. This was not overcome within this project, but could be through smoothing the interface using spin-coated photoresist or wax, or through the use of wider-area II-VI material.

5.8 References

[1] J.M.M. Santos, B.E. Jones, P.J. Schlosser, S. Watson, J. Herrnsdorf, B. Guilhabert, et al., Hybrid GaN LED with capillary-bonded II-VI MQW colour-converting membrane for Visible Light Communications, (2014).

[2] H. Haas, Harald Haas: Wireless data from every light bulb, TED Talks Dir. (2011). http://www.ted.com/talks/harald_haas_wireless_data_from_every_light_bulb (accessed March 18, 2015).

[3] J. Grubor, S. Randel, K.-D. Langer, J.W. Walewski, Broadband Information Broadcasting Using LED-Based Interior Lighting, Light. Technol. J. 26 (2008) 3883–3892. doi:10.1109/JLT.2008.928525.

[4] J.J.D. McKendry, D. Massoubre, S. Zhang, B.R. Rae, R.P. Green, E. Gu, et al., Visible-Light Communications Using a CMOS-Controlled Micro-Light- Emitting-Diode Array, J. Light. Technol. 30 (2012) 61–67. doi:10.1109/JLT.2011.2175090.

[5] C.R. Belton, G. Itskos, G. Heliotis, P.N. Stavrinou, P.G. Lagoudakis, J. Lupton, et al., New light from hybrid inorganic-organic emitters, J. Phys. D. Appl. Phys. 41 (2008) 94006. doi:10.1088/0022-3727/41/9/094006.

[6] H. Chun, P. Manousiadis, S. Rajbhandari, D.A. Vithanage, G. Faulkner, D. Tsonev, et al., Visible Light Communication Using a Blue GaN μLED and Fluorescent Polymer Color Converter, Photonics Technol. Lett. IEEE. 26 (2014) 2035–2038. doi:10.1109/LPT.2014.2345256.

[7] N. Laurand, B. Guilhabert, J. McKendry, A.E. Kelly, B. Rae, D. Massoubre, et al., Colloidal quantum dot nanocomposites for visible wavelength conversion of modulated optical signals, Opt. Mater. Express. 2 (2012) 250. doi:10.1364/OME.2.000250.

[8] L. Zeng, B.X. Yang, A. Cavus, W. Lin, Y.Y. Luo, M.C. Tamargo, et al., Red-green-blue photopumped lasing from ZnCdMgSe/ZnCdSe quantum well laser structures grown on InP, Appl. Phys. Lett. 72 (1998) 3136–3138. doi:10.1063/1.121571.

[9] M.C. Tamargo, S. Guo, O. Maksimov, Y.C. Chen, F.C. Peiris, J.K. Furdyna, Red-green-blue light emitting diodes and distributed Bragg reflectors based on ZnCdMgSe lattice-matched to InP, in: J. Cryst. Growth, 2001: pp. 710–716. doi:10.1016/S0022-0248(01)00808-9.

[10] A.J. Trindade, B. Guilhabert, D. Massoubre, D. Zhu, N. Laurand, E. Gu, et al., Nanoscale-accuracy transfer printing of ultra-thin AlInGaN light-emitting diodes onto mechanically flexible substrates, Appl. Phys. Lett. 103 (2013) 253302. doi:10.1063/1.4851875.

Chapter 6

Conclusions and outlook

This thesis discusses the progress towards thin-film VECSEL devices for emission in the visible spectrum. Materials investigated were ZnCdMgSe for emission in the green (with an eye on the potential for this material to target emission throughout the visible spectrum), a material system with which VECSEL devices have not been demonstrated, and AlGaInP for emission in the red – developed from the already mature AlGaInP gain-mirror VECSELs. Our ZnCdMgSe gain structure designs were grown via molecular beam epitaxy (MBE) by our collaborators at City College New York, and our AlGaInP-based structures were grown via metal organic chemical vapour deposition (MOCVD) at the EPSRC National Centre for III-V Materials at the University of Sheffield. Methods for epitaxial lift-off (ELO) of the structures were developed in-house for both ZnCdMgSe structures grown on InP, and for AlGaInP devices grown on GaAs, allowing for the multi-QW gain regions to be removed from their absorptive substrates and placed on to high thermal conductivity diamond. While the ELO added challenges for structure design and growth, requiring low strain or strain-balanced structures to allow for successful processing, the basic premise of the novel laser architecture was justified upon the achievement of laser threshold with the AlGaInP thin film VECSEL devices. The lift-off procedure for both materials allows for grown structures to be transferred without the inclusion of sacrificial layers, and this was used effectively to demonstrate colour conversion with a II-VI film as part of a hybrid micro-LED.

6.1 II-VI ZnCdMgSe thin-film VECSELs

The ZnCdMgSe material system offers the possibility of devices designed with quantum wells (QWs) emitting throughout the visible spectrum, with structures reported containing red, green and blue emission QWs within a single epitaxial growth [1]. A significant disadvantage of the material is the difficulty in doping, required for electrically-pumped devices, the lack of which has resulted in GaN devices dominating blue/green research over the II-VI materials. VECSELs, however, are optically-pumped, and with the advent of high power GaN laser diodes suitable as pumps, there is an opportunity to re-visit the II-VI materials for this versatile laser format. What does cause difficulties when considering a ZnCdMgSe-based VECSEL is the low refractive index contrast possible with this material, and therefore the challenges in producing accurate and thick structures with sufficient numbers of distributed Bragg reflector (DBR) pairs to achieve the high reflectivity required for an integrated VECSEL end-mirror.

The growth substrate is InP, absorptive in the visible spectrum, so development of II-VI ZnCdMgSe VECSELs can progress along two paths:

- The grown DBR can be further developed, with progress made in material quality and growth accuracy to accommodate the demanding long growth required. This ideally needs a growth chamber capable of growing multiple quaternary materials without the limitations of temperature control, with sufficient numbers of effusion cells to allow for this. One possible way to make this more achievable is through the use of pseudo-alloys produced through superlattices, either to achieve higher refractive index contrast maintaining material quality as in ref. [2], or to overcome a lack of effusion cells by creating a superlattice of ZnCdSe and high-bandgap ZnCdMgSe as in ref. [3]. In this work we made initial investigations with our collaborators, designing and fabricating a ZnCdMgSe-based DBR with 85% reflectivity [4]; however, further progress in DBR growth is dependent upon advances in MBE capability by the semiconductor growth groups.

- The epitaxial layer can be removed from the substrate, allowing for light to pass through without absorption, and for external or coated mirrors to be used for VECSEL cavity end-mirrors. This latter method was the main focus of this work, as described in Chapter 3.

Initial attempts involving via-hole etching demonstrated the possibility of accessing the rear of the epitaxial structure, with the selective wet etch recipes based on ref. [5]. Higher quality growth and closer lattice-matching of II-VI material later allowed for the transfer of wide-area II-VI InP grown devices.

Designs for thin-film ZnCdMgSe-based VECSELs went through an evolution of 3 generations based on an increasing understanding of the challenges for achieving these devices. Initial designs were for a small number of QWs, but structure fracturing when producing via-holes and no successful laser operation led to the increase of structure thickness along with the inclusion of a partial DBR to enhance the sub-cavity resonances over the QW positions. With this structure design epitaxial layer transfer became possible, with sample sizes of 2–4 mm transferrable. SEM images showed that the impediment to laser action was now likely layer thickness inaccuracy, such that the carefully designed overlapping resonances and layer placement was not achieved. The final design, generation 3, reduced complexity by removing the DBR layers, while maintaining structure thickness through increased gain region length (and increased QW number).

Gain structure strain has been shown to be significant in the successful transfer of devices. As generation 1 suffered from low emission and material strain, it was decided to introduce partial DBRs to help set the electric field maxima positions, enhance resonances within the subcavity and help provide structural support by increasing device thickness. Growth problems with layer thickness accuracy and limitations of the effusion cells (meaning that temperatures had to be changed multiple times mid-growth) meant that these design changes led to further complications.

Generations 2 and 2.5 showed progress in material composition accuracy and significant improvements on strain, allowing for transfer of the structures completely

to diamond. Laser threshold was not however reached. Nevertheless, progress in crystal quality and lattice-matching of the materials allowed for repeatable and reliable substrate removal. The successful laser emission from a III-V AlGaInP-based active region (described in Chapter 4) which contained only quantum wells arranged for RPG, transferred to diamond and pumped in a fully external 3 mirror cavity, caused a re-think of the need to include partial DBRs in the II-VI devices. From this it was taken that a simple II-VI ZnCdMgSe structure is a sensible target, optimising the growth for consistency in quantum well emission and spacing for RPG.

Generation 3 of the structure design consisted of a higher QW count, and removed the partial DBR of generation 2. By simplification of the design back to a simple active-region only structure, without the necessity of changing effusion cell temperatures mid-growth, it was hoped that accurate unstrained structures could be grown, maximising the chances of successful transfer and laser action. Laser threshold was not achieved, with unwanted layer thickness and material composition variation still a barrier to successful VECSEL structures from this material system.

Once ZnCdMgSe/InP MBE is capable of producing layers with thickness and composition accuracy sufficient to allow for unstrained films with correct optical thicknesses, laser action in ZnCdMgSe VECSELs should be achieved. The design can then be optimised, compressively strained QWs can be introduced and balanced with tensile strained ZnCdMgSe barriers, and QW number and placement adjusted to take the pump-absorption profile into account. Beyond optimisation, we could then take advantage of the visible-spectrum coverage of ZnCdSe/ZnCdMgSe QW emission, either in separate devices providing a choice of spectral coverage from blue to red, or with novel multi-wavelength designs with broad tuning or multiple lasers from a single chip.

6.2 III-V AlGaInP thin-film VECSELs

AlGaInP is a material system that has been used in the demonstration of high-power red-emission gain-mirror VECSELs, with recent reports showing outputs of 1.1 W at

room temperature [6]. Partially as a demonstration of the possibilities of the thin-film architecture, but also to advance and inform future design for the II-VI ZnCdMgSe VECSEL structures, an active-region only AlGaInP gain structure, originally grown for the purposes of calibration of a 'standard' VECSEL, was processed using a similar substrate removal technique to that developed for the ZnCdMgSe epitaxial layer removal.

Laser threshold was reached with a strain-balanced active region in a 3-mirror external cavity, although laser action was short-lived due to de-bonding of the structure from the diamond-heatspreader, causing catastrophic destruction of the pumped spot. This was to be the main limitation of these lasers, with maximum device lifetime of 5–7 hours operation. This was most likely caused by a transfer issue, which could be improved through development of the transfer method, or by the reduction and balancing of structure strain to improve the mechanical characteristics of the epitaxial film after release from the substrate.

Three designs for thin-film AlGaInP-based VECSELs have been described with different strain balancing techniques: the strain-balancing QW barriers in design A, the strain-balance layers within lattice-matched barriers of design B and the long wavelength design C. Designs B and C also had structure growths without balancing (layers replaced with lattice-matched barrier material) to investigate the impact of QW strain on the thin-device transfer and laser performance. This investigation was inconclusive, with the accuracy of the strain balancing not sufficiently repeatable for a confident determination of the effects and some of the structures grown to the balanced design displaying cracking or distortion from tensile or compressive strain respectively.

The highest output power achieved was for a structure operating at 682 nm, with output power of 21 mW for an input of 0.9 W, with a slope efficiency of 6.4%, for 2% output coupling.

While confirming the potential of thin-film VECSELs and informing the design of the generation 3 ZnCdMgSe VECSELs, the demonstration of thin-film red-emission VECSELs opens possibilities for novel cavity designs and pump arrangements without

the restrictions of the DBR. Double-end pumping can increase uniformity of pump absorption and carrier distribution throughout the quantum wells – the distribution of quantum wells with respect to pump absorption has been demonstrated to have a significant effect on efficiency, so removing this effect could have performance advantages. The removal of the DBR also opens the potential for broadband operation devices, without the spectral limitations of a high-reflectivity DBR. VECSEL operation within a ring cavity is a relatively new area of investigation with a small number of recent reports where, to-date, a 'standard' VECSEL structure is positioned at a cavity fold [7]. A thin device that could be incorporated at any position within a ring cavity could provide advantages for processes where unidirectional oscillation is desirable, e.g. intra-cavity modulators or nonlinear conversion.

6.3 Colour conversion

The transfer of II-VI ZnCdMgSe films, while developed for the II-VI VECSEL project, also enables the use of this material system for other applications. This was demonstrated through the transfer of the ZnCdMgSe multi-QW structures for use as colour-conversion films on GaN-based micro-LEDs for the purposes of visible light communication (VLC). Blue light from GaN diodes (at 445 nm) must be converted to an approximation of white light through the addition of green and red wavelengths, so that the VLC device can be integrated into room lighting while maintaining both high modulation speed for transmission of data, and long term performance in the device.

Transfer of the ZnCdMgSe thin-films to the sapphire substrate of rear-emission micro-LEDs to form hybrid devices consisting of the LEDs and a conversion film was performed in the same way as the laser structure transfer to diamond. High quality wide area films can easily cover multiple LEDs in an array. Power measurements showed a low conversion efficiency from the first embodiment of these devices; however, this was largely due to the fact that the films had not been optimised for this purpose (designed as a VECSEL gain region).

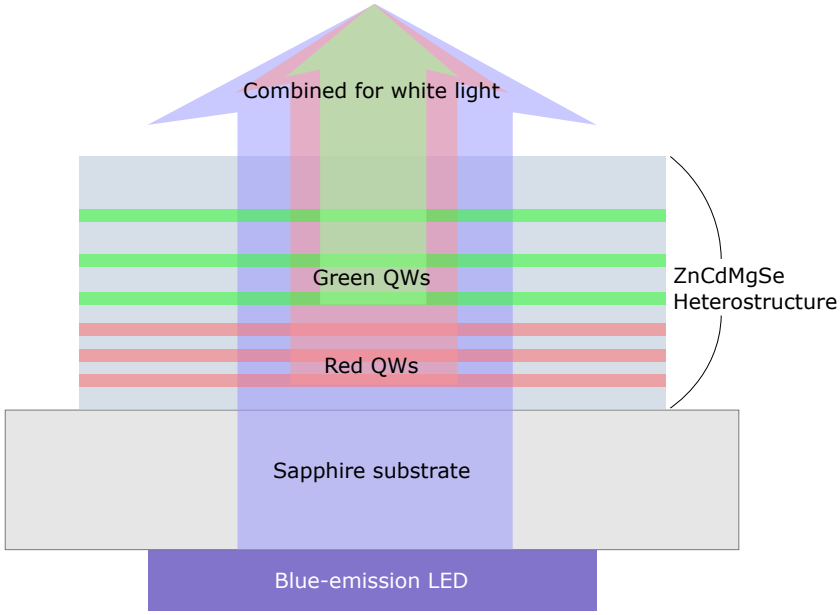

Figure 6.1: Schematic of a proposed multiple-QW ZnCdMgSe thin-film for colour conversion of blue emission GaN LEDs to produce white light. The red-emitting quantum wells are closest to the LED to avoid re-absorption of the green light.

Of critical importance was that the modulation bandwidth of the II-VI colour conversion film was shown to match or exceed that of the GaN LED. This material is therefore potentially ideal for colour conversion applications if the efficiency can be increased via optimised structure designs, thus providing a more robust alternative to currently-used organic semiconductors [8].

Future continuation of the research will be in the growth and testing of purpose-designed and grown II-VI colour conversion structures, with optimised absorption length and QW number for the correct conversion ratio to combine transmitted blue light and emitted green. The addition of strained red-emitting QWs, either in a patterned structure similar to that reported in ref. [9] or through the addition of multiple QW layers to a monolithic structure, as shown in Figure 6.1, would enable the fabrication of high modulation bandwidth white LEDs with one, stable, colour conversion film.

6.4 References

[1] M.C. Tamargo, S. Guo, O. Maksimov, Y.C. Chen, F.C. Peiris, J.K. Furdyna, Red-green-blue light emitting diodes and distributed Bragg reflectors based on ZnCdMgSe lattice-matched to InP, in: J. Cryst. Growth, 2001: pp. 710–716. doi:10.1016/S0022-0248(01)00808-9.

[2] C. Kruse, S.M. Ulrich, G. Alexe, E. Roventa, R. Kröger, B. Brendemühl, et al., Green monolithic II–VI vertical-cavity surface-emitting laser operating at room temperature, Phys. Status Solidi. 241 (2004) 731–738. doi:10.1002/pssb.200304126.

[3] T. Morita, H. Shinbo, T. Nagano, I. Nomura, A. Kikuchi, K. Kishino, Refractive index measurements of MgZnCdSe II–VI compound semiconductors grown on InP substrates and fabrications of 500–600 nm range MgZnCdSe distributed Bragg reflectors, J. Appl. Phys. 81 (1997) 7575. doi:10.1063/1.365301.

[4] J. De Jesus, T.A. Garcia, V. Kartazaev, B.E. Jones, P.J. Schlosser, S.K. Gayen, et al., Growth and characterization of ZnCdMgSe-based green light emitters and distributed Bragg reflectors towards II–VI based semiconductor disk lasers, Phys. Status Solidi. (2014).

[5] R. Moug, A. Alfaro-Martinez, L. Peng, T. Garcia, V. Deligiannakis, A. Shen, et al., Selective etching of InGaAs/InP substrates from II-VI multilayer heterostructures, Phys. Status Solidi. 9 (2012) 1728–1731. doi:10.1002/pssc.201100716.

[6] J.E. Hastie, L.G. Morton, A.J. Kemp, M.D. Dawson, A.B. Krysa, J.S. Roberts, Tunable ultraviolet output from an intracavity frequency-doubled red vertical-external-cavity surface-emitting laser, Appl. Phys. Lett. 89 (2006) 061114. doi:10.1063/1.2236108.

[7] A. Mignot, G. Feugnet, S. Schwartz, I. Sagnes, A. Garnache, C. Fabre, et al., Single-frequency external-cavity semiconductor ring-laser gyroscope., Opt. Lett. 34 (2009) 97–99. doi:10.1364/OL.34.000097.

[8] J.M.M. Santos, B.E. Jones, P.J. Schlosser, S. Watson, J. Herrnsdorf, B. Guilhabert, et al., Hybrid GaN LED with capillary-bonded II-VI MQW colour-converting membrane for Visible Light Communications, (2014).

[9] Y. Luo, S. Guo, O. Maksimov, Patterned three-color ZnCdSe/ZnCdMgSe quantum-well structures for integrated full-color and white light emitters, Appl. Phys. Lett. 4259 (2000) 10–13. doi:10.1063/1.1330229.

Appendix A

Quantum well transition energy simulation

The quantum well ground-state transition energy is simulated in MathCad 15, for strained material. After appropriate initialisation with material parameters as defined in Chapter 3, Table 3.1, the following code will produce the transition energy:

Energy difference due to strain

Strain: $\varepsilon(x) := \dfrac{a_{InP} - a_{ZnCdSe}(x)}{a_{InP}}$

Change in energy gap: [4]

$$\delta E_{hy}(x) := -2 \cdot a_{Hyd.ZnCdSe}(x) \cdot \left(1 - \frac{C_{12.ZnCdSe}(x)}{C_{11.ZnCdSe}(x)}\right) \cdot \varepsilon(x)$$

$$\delta E_{sh}(x) := -2\, b_{ZnCdSe}(x) \cdot \left(1 + \frac{C_{12.ZnCdSe}(x)}{C_{11.ZnCdSe}(x)}\right) \cdot \varepsilon(x)$$

$$\zeta(x) := \frac{1}{2}\, \delta E_{sh}(x)$$

Depth of well in the conduction band:

$$\Delta E_c(x,z,y,Temp) := Q\left(E_{0ZnCdMgSe}(z,y,Temp) - E_{0ZnCdSe}(x,Temp) - \delta E_{hy}(x)\right)$$

Height of well in the (hh) valence band:

$$\Delta E_v(x,z,y,Temp) := (1 - Q)\left[\left(E_{0ZnCdMgSe}(z,y,Temp) - E_{0ZnCdSe}(x,Temp) - \delta E_{hy}(x)\right) - \zeta(x)\right]$$

Figure A.1: Computing the depth of a strained QW for the conduction band and heavy-hole (hh) valence band

Electron subband energy

The eigenequations for an even wave function give:

$$fe(Ec,L,x,z,y,Temp) := \left[Ec - \Delta E_c(x,z,y,Temp) + \frac{m_{e.ZnCdMgSe}(z,y)}{m_{e.ZnCdSe}(x)} \cdot Ec \cdot \left(\tan\left(\sqrt{\frac{2 \cdot m_{e.ZnCdSe}(x) \cdot Ec}{h^2}} \cdot \frac{L}{2} \right) \right)^2 \right]$$

Solve for the eigenenergy:

$Ec := 0 \cdot eV$

Given

$fe(Ec,L,x,z,y,Temp) \cdot 10^{25} = 0J$

$EC(L,x,z,y,Temp) := Minerr(Ec)$

Heavy hole subband energy

The eigenequations for an even wave function give:

$$fh(Ev,L,x,z,y,Temp) := \left[Ev - \Delta E_v(x,z,y,Temp) + \frac{m_{hh.ZnCdMgSe}(z,y)}{m_{hh.ZnCdSe}(x)} \cdot Ev \cdot \left(\tan\left(\sqrt{\frac{2 \cdot m_{hh.ZnCdSe}(x) \cdot Ev}{h^2}} \cdot \frac{L}{2} \right) \right)^2 \right]$$

Solve for the eigenenergy:

$Ev := 0 \cdot eV$

Given

$fh(Ev,L,x,z,y,Temp) \cdot 10^{25} = 0J$

$EV(L,x,z,y,Temp) := Minerr(Ev)$

ET(L,x,z,y,Temp) Explanation: L is QW length, x is for $Zn_{(1-x)}Cd_{(x)}Se$, z and y are for $(Zn_{(1-z)}Cd_{(z)})_{(1-y)}Mg_{(y)}Se$. Temp is temperature, if the Eg calculation with it in is used.

Transition energy

$$ET(L,x,z,y,Temp) := \left(EC(L,x,z,y,Temp) + EV(L,x,z,y,Temp) + E_{0ZnCdSe}(x,Temp) \right)$$

Figure A.2: Calculation of the ground-state transition energy ET

Appendix B

Simulation of E-field propagation in stratified media

Based on the theory of light propagation in stratified media, found in Born and Wolf, Principles of Optics, 7th (expanded) edition, (1999) Cambridge University Press.

The following code allows for the calculation of reflectivity spectra and the standing wave E-field of a structure, for structures consisting of material of known refractive index.

Characteristic matrix for stack of homogeneous dielectric films for normal incidence

$$M(\lambda, t, comp) := \left| \begin{array}{l} M_{stack} \leftarrow identity(2) \\ \text{for } j \in 1..N_{layer} \\ \quad \left| \begin{array}{l} M_r \leftarrow M_{stack} \\ p \leftarrow n\left(\lambda, comp_{j-1}\right) \\ \beta \leftarrow \frac{2\cdot\pi}{\lambda}\cdot p\cdot t_{j-1} \\ M_{layer} \leftarrow \begin{pmatrix} \cos(\beta) & -\frac{i}{p}\cdot\sin(\beta) \\ -i\cdot p\cdot\sin(\beta) & \cos(\beta) \end{pmatrix} \\ M_{stack} \leftarrow M_r\cdot M_{layer} \end{array} \right. \\ M_{stack} \end{array} \right.$$

$$p_{init}(\lambda) := n\left(\lambda, x_{top}\right)$$

$$p_{exit}(\lambda) := n\left(\lambda, x_{substrate}\right)$$

Figure B.1: Calculation of the characteristic matrix for the structure, for layer thicknesses t_j and corresponding refractive indices n_j (from array $comp_j$)

.

Reflectivity and transmission

$$r(\lambda,t,comp) := \frac{\left(M(\lambda,t,comp)_{0,0} + M(\lambda,t,comp)_{0,1}\cdot p_{exit}(\lambda)\right)\cdot p_{init}(\lambda) - \left(M(\lambda,t,comp)_{1,0} + M(\lambda,t,comp)_{1,1}\cdot p_{exit}(\lambda)\right)}{\left(M(\lambda,t,comp)_{0,0} + M(\lambda,t,comp)_{0,1}\cdot p_{exit}(\lambda)\right)\cdot p_{init}(\lambda) + \left(M(\lambda,t,comp)_{1,0} + M(\lambda,t,comp)_{1,1}\cdot p_{exit}(\lambda)\right)}$$

$$t_z(\lambda,t,comp) := \frac{2\cdot p_{init}(\lambda)}{\left(M(\lambda,t,comp)_{0,0} + M(\lambda,t,comp)_{0,1}\cdot p_{exit}(\lambda)\right)\cdot p_{init}(\lambda) + \left(M(\lambda,t,comp)_{1,0} + M(\lambda,t,comp)_{1,1}\cdot p_{exit}(\lambda)\right)}$$

$$R(\lambda,t,comp) := \left(\left|r(\lambda,t,comp)\right|\right)^2$$

$$T(\lambda,t,comp) := \left(\left|t_z(\lambda,t,comp)\right|\right)^2 \cdot \frac{p_{exit}(\lambda)}{p_{init}(\lambda)}$$

Figure B.2: Reflectivity and transmission coefficients r(λ) and t(λ), and the reflectivity and transmission R(λ) and T(λ)

$$\begin{aligned}
&field(\lambda,t,comp) := \\
&\quad reflec \leftarrow r(\lambda,t,comp) && \text{Initialise inputs.}\\
&\quad \varepsilon_r \leftarrow p_{init}(\lambda)\\
&\quad Q_{init} \leftarrow \begin{bmatrix} \frac{1+reflec}{\varepsilon_r} \\ (1-reflec) \end{bmatrix} && \text{Define input wave as a 1x2 matrix.}\\
&\quad N_{stack} \leftarrow identity(2) && \text{Initialise characteristic matrix with 2x2 identity.}\\
&\quad nnmax \leftarrow N_{qual} && \text{Set number of divisions per layer.}\\
&\quad zcurrent \leftarrow 0\\
&\quad \text{for } j \in 1..N_{layer} && \text{Loop over layers.}\\
&\qquad N_r \leftarrow N_{stack}\\
&\qquad p \leftarrow n\left(\lambda, comp_{j-1}\right) && \text{Set layer refractive index.}\\
&\qquad \text{for } nn \in 1..nnmax && \text{Loop per division for quality.}\\
&\qquad\quad thick \leftarrow \frac{nn\cdot t_{j-1}}{nnmax} && \text{Division thickness.}\\
&\qquad\quad \beta \leftarrow \frac{2\cdot\pi}{\lambda}\cdot p\cdot thick\\
&\qquad\quad N_{stack} \leftarrow \begin{pmatrix} \cos(\beta) & \frac{i}{p}\cdot\sin(\beta) \\ i\cdot p\cdot\sin(\beta) & \cos(\beta) \end{pmatrix}\cdot N_r && \text{Multiply previous characteristic matrix to find new M.}\\
&\qquad\quad Q \leftarrow N_{stack}\cdot Q_{init}\\
&\qquad\quad Res_{0,(j-1)\cdot nnmax+nn} \leftarrow zcurrent + \frac{thick}{m} && \text{Multiply characteristic matrix with previous E-field magnitude to find new.}\\
&\qquad\quad Res_{1,(j-1)\cdot nnmax+nn} \leftarrow \left(\left|Q_0\right|\right)^2\\
&\qquad zcurrent \leftarrow zcurrent + \frac{t_{j-1}}{m} && \text{Add thickness and go to next.}\\
&\quad Res_{0,0} \leftarrow 0\\
&\quad Res_{1,0} \leftarrow \left(\left|Q_{init_{0,0}}\right|\right)^2
\end{aligned}$$

Figure B.3: Annotated calculation of the standing electric field

List of Publications

Brynmor E. Jones, Peter J. Schlosser, Joel De Jesus, Thor A. Garcia, Maria C. Tamargo, and Jennifer E. Hastie, "Processing and characterisation of II-VI thin film gain structures," *accepted for publication in the Journal of Thin Solid Films (2015)*

Joao M. M. Santos, **Brynmor E. Jones**, Peter J. Schlosser, Scott Watson, Johannes Herrnsdorf, Benoit Guilhabert, Jonathan J. D. McKendry, Joel De Jesus, Thor A. Garcia, Maria C. Tamargo, Anthony E. Kelly, Jennifer E. Hastie, Nicolas Laurand, and Martin D. Dawson, "Hybrid GaN LED with capillary-bonded II-VI MQW color-converting membrane for visible light communications," *Semiconductor Science and Technology* ***30*** *035012 (2015) doi:10.1088/0268-1242/30/3/035012* ***Cover Image***

Joel De Jesus, Thor A. Garcia, Vladimir Kartazaev, **Brynmor E. Jones**, Peter J. Schlosser, Swapan K. Gayen, Jennifer E. Hastie, and Maria C. Tamargo, "Growth and characterization of ZnCdMgSe-based green light emitters and distributed Bragg reflectors towards II-VI based semiconductor disk lasers," *Physica Status Solidi A,* doi:10.1002/pssa.201431439 (2014)

Joao M. M. Santos, **Brynmor E. Jones**, Peter J. Schlosser, Johannes Herrnsdorf, Benoit Guilhabert, Joel De Jesus, Thor A. Garcia, Maria C. Tamrgo, Jennifer E. Hastie, Nicolas Laurand, and Martin D. Dawson, "Hybrid InGaN LEDs with capillary-bonded MQW color-converting membranes," *presented at the IEEE International Photonics Conference, San Diego, USA, Paper WC3.4 (2014)*

Brynmor E. Jones, Peter J. Schlosser, Joel De Jesus, Thor A. Garcia, Maria C. Tamargo and Jennifer E. Hastie, "Characterisation of II-VI selenide multi-quantum well thin

films transferred to transparent substrates," *presented at International Conference of Optical, Optoelectronic and Photonic Materials and Applications (ICOOPMA), Leeds 2014*

Joao M. M. Santos, **Brynmor E. Jones**, Peter J. Schlosser, Johannes Herrnsdorf, Benoit Guilhabert, Joel De Jesus, Thor A. Garcia, Maria C. Tamargo, Jennifer E. Hastie, Nicolas Laurand, and Martin D. Dawson, "Hybrid GaN LED with II-VI colour-converting platelet for visible light communications," *presented at the International Conference of Optical, Optoelectronic and Photonic Materials and Applications (ICOOPMA), Leeds 2014*

Joel De Jesus, Thor A. Garcia, Vladimir Kartazaev, Swapan K. Gayen, **Brynmor E. Jones**, Peter J. Schlosser, Jennifer E. Hastie, and Maria C. Tamargo, "ZnCdMgSe-based green light emitters and distributed Bragg reflectors – design, growth and characterisation," *presented at the North American Molecular Beam Epitaxy Conference, Banff, Canada (2013)*